Rossby Waves and Mean Currents in the Southern Ocean

Ellis R Ash

Doctor of Philosophy
The University of Edinburgh
2000

Acknowledgements

Firstly, a very big thankyou goes to my supervisors Keith Haines in Edinburgh, and Chris Hughes at the Proudman Oceanographic Laboratory for their support and guidance throughout the project, and for their patience in training an Engineer to become a Physical Oceanographer.
Many members of the Meteorology Department have helped provide an excellent working environment, as well the moral and technical support required to complete a task like this.
Life in Edinburgh has been highly enjoyable because of many friends, and many adventurous weekend excursions with them. A special mention goes to Rond for her love and understanding over the past two years.
Finally, an extra special thanks must go to my parents, Jen and Stuart, who have been so supportive in everything I have done.
This work was funded by the Natural Environment Research Council and a CASE award from the Proudman Oceanographic Laboratory, Merseyside.

Abstract

Dynamics in the Southern Ocean are dominated by the Antarctic Circumpolar Current (ACC), and this large eastward current has an important influence on the earth's climate. This thesis presents a study of Rossby waves and eddy activity near the surface of the Southern Ocean. Diagnostics are derived from the time-varying component of the surface geostrophic current, which is conveniently measured by modern satellite altimeters. The mean currents, however, cannot be measured using altimetry, because the earth's gravitational field at the sea surface (the geoid) is not yet known to sufficient accuracy. Rossby waves and eddy activity are known to interact with the mean flow, so it should be possible to infer information about the mean flow if suitable relationships with these quantities can be established.

Output from the last six years of the Fine Resolution Antarctic Model, where the mean flow is known, is used to develop techniques for quantifying Rossby waves and eddy activity. Some eastward jets in the mean flow are found to act as waveguides for Rossby waves. Phase speeds are found to increase linearly with frequency, but do not vary with the strength of mean flow. The reason for this is demonstrated using the dispersion relation, but it is shown that Rossby waves cannot be used to measure mean flows in the ACC without a further understanding of the theory involved. A property of the time-average eddy activity, known as the eddy orientation angle, is shown to indicate the axes of the prominent eastward jets in the mean flow. This shows that eddies are acting to force these jets.

Five years of measurements from the TOPEX/POSEIDON satellite mission are used to identify Rossby waves in the real ocean. Coherent Rossby wave propagation is again confined to localised regions, some of which act as waveguides. Phase speeds are measured in these regions, and shown to be consistent with previous measurements of Rossby waves. An improved resolution dataset, combining TOPEX/POSEIDON and ERS altimetry measurements, is used to analyse the time-average eddy activity and associated forcing on the mean flow in unprecedented detail. Current data from cruises of the World Ocean Circulation Experiment are used in conjunction with altimetry data to estimate the mean flow at locations along ship tracks. Using these estimates, and the position of temperature fronts as an indication of prominent jets in the mean flow, the eddy forcing is shown to be different to that observed in FRAM. Instead of forcing the mean flow, eddies are being generated within the jets which are likely to be maintained by topographic forcing.

Contents

Chapter 1

Introduction

The Southern Ocean is of major importance in oceanography due to its role in connecting the three main ocean basins and determining oceanic heat fluxes in the Southern Hemisphere. Because of its hostility and remoteness, the Southern Ocean is less well observed than other oceans. The advent of satellite measurement systems, however, has enabled continuous monitoring of surface quantities over the entire ocean. This thesis investigates the Southern Ocean using five years of sea surface height (SSH) data from the TOPEX/POSEIDON and ERS satellite altimeters. The research focuses on the analysis of Rossby wave activity and the relationship between wave activity and the mean flow, thereby seeking to retrieve information about the mean flow from time dependent quantities. This is important because the earth's gravitational field at the sea surface (the geoid) is not currently known to sufficient accuracy to enable direct measurement of mean flows by satellite altimeters (though future satellites should establish a better geoid, and enable back-calculation of mean flows).

A unique feature of the Southern Ocean is a zonally unbounded band of latitude, defined by the Drake's passage, which permits the existence of a significant current known as the Antarctic Circumpolar Current (ACC). The ACC is an eastward flowing, recirculating current, driven by strong westerly winds and internal density gradients, and influenced by the complicated bathymetry. Southern Ocean dynamics are dominated by the ACC which, with estimated transport 110Sv (Nowlin and Klinck, 1986), is the largest of ocean currents. Knowledge of the be-

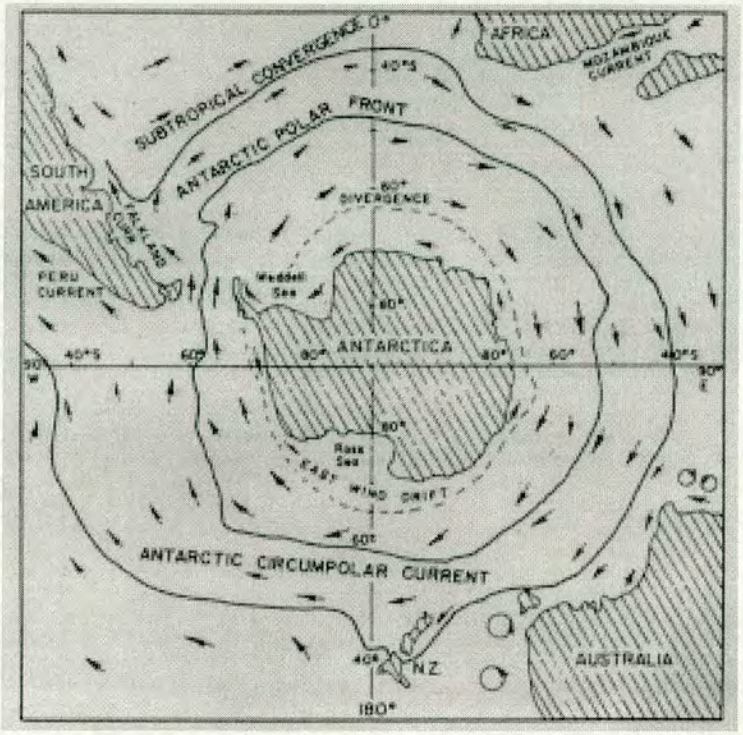

Figure 1.1: Schematic of the ACC, from Pickard and Emery (1990).

haviour of this current is fundamental to our understanding of the climatological role of that region, which is still largely undetermined (Vassie et al., 1994). It is appropriate to begin with a more detailed description of the ACC.

1.1 The Antarctic Circumpolar Current

A simplified schematic of the ACC is shown in figure 1.1. The axis of the ACC is associated with the Polar Front (also known as the Antarctic Convergence Zone), which has long been known about (Meinardus, 1923). Here, cold and relatively fresh Antarctic Surface Water meets warmer water from the North. The latitude of the Polar Front varies from about 50°S, in the South Atlantic, to about 65°S in the Southeast Pacific. Recent studies of the mean position of the Polar Front are brought together by Moore et al (1999), who compare observations using satellite sea surface temperature data to previous work. The boundaries of the ACC are delineated by the subtropical convergence to the North, and divergence (dashed line in figure 1.1) to the South. The strongest currents, however, are confined

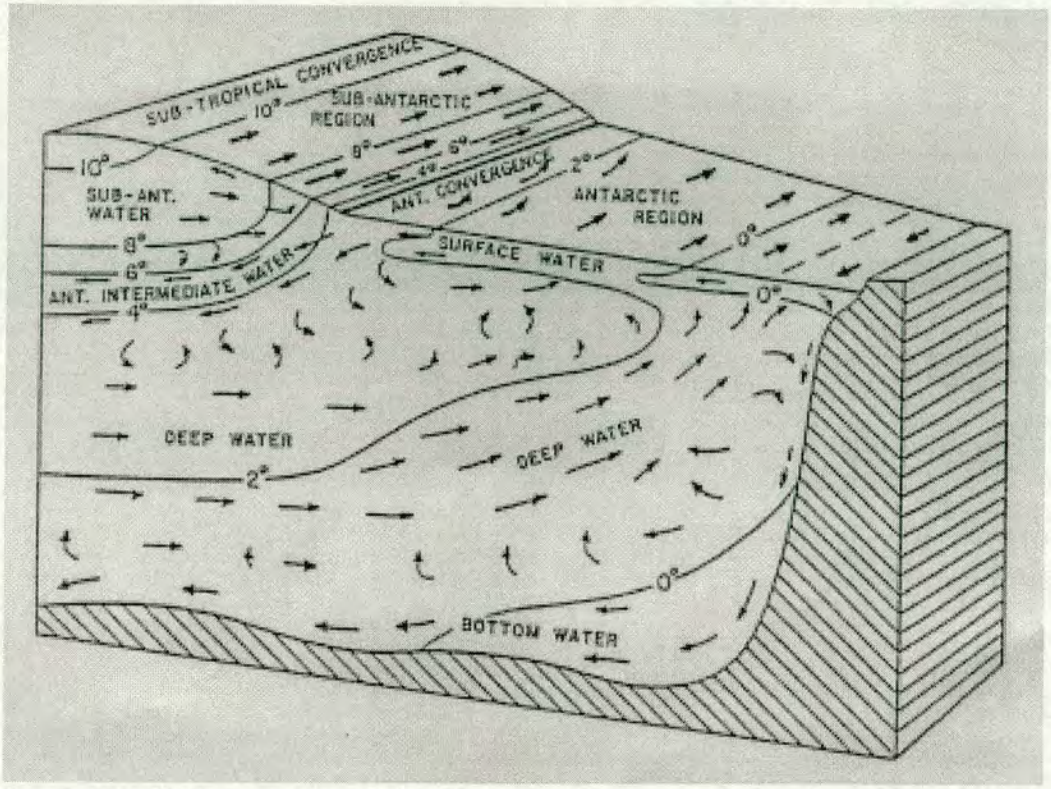

Figure 1.2: Water masses of the Southern Ocean, from Sverdrup et al (1942).

to a narrower band between about 5° North and South of the Polar Front, in a region known as the Antarctic Polar Frontal Zone.

The internal structure of the ACC and Southern Ocean was first described by Sverdrup et al (1942), using measurements from whaling and sealing vessels. This is illustrated in figure 1.2, which shows zonally averaged currents and temperature contours. A good description of water masses in the Southern Ocean is given by Harris (1996) and this will be summarised here. The deepest water is known as Antarctic Bottom Water (ABW). This cold, dense water extends north to between 40° and 50°S (Tchernia, 1980), and is the major source of cold water for the worlds oceans (Mantyla and Reid, 1983). ABW is thought to be produced mainly in the Weddell Sea region, with smaller production sites in the Ross Sea and off East Antarctica (Tchernia, 1980; Gordon and Tchernia, 1972). It then flows down the continental shelf to the abyssal plains, where it moves north and east along the bottom. Above the ABW is the Circumpolar Deep Water (CDW) which extends all round Antarctica and is the largest water mass of the Southern Ocean. The CDW is warmer and saltier than ABW, and transports heat, salt

and nutrients southwards. The lower CDW is thought to originate from North Atlantic Deep Water, and the upper CDW from mid-depth water of the Indian and Pacific oceans (Sievers and Nowlin, 1984; Orsi et al, 1993; Roether et al, 1993). Some CDW becomes ABW at the edge of Antarctica while the rest mixes and cools without sinking, and forms the northward flowing Antarctic Surface Water (ASW). At the Polar Front, some ASW is thought to mix with warmer water to form Antarctic Intermediate Water (AIW) (see figure 1.2). AIW is also thought to be formed by the winter cooling of the warmer Subantarctic Surface Water and Subantarctic Mode Water. It is the Antarctic Intermediate Water which is the dominant water mass of the ACC (Rintoul, 1988).

The dynamics of the ACC are unlike that of other strong currents, such as the Gulf Stream, which are found in the subtropical gyres. In a typical ocean basin, such as the North Atlantic, the dynamics can be understood in terms of a simplified model developed by Stommel (1948). In this model, a sinusoidal wind-stress is applied to a rectangular basin with a linear north to south variation in coriolis force. The wind supplies negative relative vorticity to the gyre, causing increased anticyclonic circulation. As the gyre speeds up, friction at the western boundary leads to a gain in positive relative vorticity due to shear in the flow. To reach a steady state, the positive relative vorticity gain due to shear at the western boundary must balance the negative relative vorticity input by the wind. The result is an anticyclonic circulation with an intense northward current at the western boundary, explaining currents such as the Gulf Stream. In the Southern Ocean, however, there is only a boundary to the South, and Stommel's gyre model does not apply.

Although the internal water structure has an influence, the ACC is known to be driven primarily by the overlying wind field. Many models have shown the persistent westerly winds to provide sufficient stress at the surface to drive the current. Calculations show, however, that frictional dissipation at the lateral boundaries of the current is not sufficient to balance the input of angular momentum due to wind stress at the surface (Munk and Palmén, 1951) . This implies the ACC should accelerate rather than remain a steady current. Munk and Palmén were first to address this problem, and deduced that stresses at the ocean bottom were

required to oppose the surface wind stress. This has since been confirmed in a number of modelling studies (Treguier and McWilliams, 1990; Wolf et al., 1991; Killworth and Nanneh, 1994; Wells and DeCuevas, 1995; Krupitsky et al., 1996) although the mechanisms and locations of interaction of the current with bottom topography are not fully understood.

The ACC is not a broad, uniform current, as might be assumed from figures 1.1 and 1.2. Instead, the flow is split into narrow jets associated with various frontal zones (Nowlin and Klinck, 1986). The presence of multiple zonal fronts in the Southern Ocean has been studied by Orsi et al (1995), who presented positions of five major fronts calculated from hydrographic data. The northern most of these, the subtropical front, is situated around 40°S and defines the northern limit of the ACC region. The other fronts extend continuously round the globe. Moving polewards, these are the Subantarctic Front, the Polar Front (discussed above), the Southern ACC front and the Southern boundary of the ACC. In Drake Passage, these four fronts are distinct and are about 50 to 150km wide. They tend to be more widely separated at other longitudes.

Work aimed at understanding the formation of jets in the ACC can be traced back to Rhines (1975). Rhines undertook a theoretical and numerical study of two-dimensional turbulence and eddies on a β-plane (linear variation of coriolis parameter, f, with latitude ($\beta = df/dy$)). The turbulence was found to cascade energy into larger scale eddies, whose growth was then inhibited by wave propagation. A zonal jet flow structure was established with a natural meridional scale given by $(2U/\beta)^{1/2}$, where U is a measure of the jet velocity. This scale is known as the Rhines scale, and has a typical value of 70km in the ocean. The work of Rhines was followed up by Williams (1978) who used the results to explain jets in the atmospheres of both the Earth and Jupiter. More recently, Treguier and Panetta (1994) used numerical modelling to study the formation of zonal jets in the ACC. A mechanism associated with the development of fronts in wide, baroclinically unstable regions (Panetta, 1993) is applied to a wind-forced channel model of the ACC. The resulting scales and strength of jets are shown to compare well with observations.

Associated with jets in the ACC is a large amount of baroclinic (depth dependent) eddy activity, which is known to transfer zonal momentum downwards and is also responsible for most of the pole-ward heat flux (Marshall et al., 1993). Having said this, the ACC is more barotropic than other ocean currents, with less temperature differential between the surface and deep waters.

One of the more comprehensive model studies of Southern Ocean dynamics was the Fine Resolution Antarctic Model (FRAM, FRAM group, 1991). FRAM is described in chapter 3 and results from the model are used as a basis for much of this thesis. In such a model, a set of dynamical equations are solved numerically by time-marching with appropriate boundary conditions. Ocean modelling is a popular technique for estimating the time dependent flow in the oceans, and does not rely on substantial ocean measurements. Success has also been had in deriving the circulation of the Southern Ocean from observations, though they are sparse in places (for example Harris, 1996). This technique, known as inverse modelling, gives steady state solutions for the flow, but does not give information about the eddies that are known to be important in many processes.

The bottom topography of the Southern Ocean is known to be very important in ACC dynamics. Figure 1.3 (taken from Hughes et al, 1997) shows the bottom topography (from the DBDB5 dataset), together with contours of mean sea surface temperature (SST) (measured by the Along-Track Scanning Radiometer on the ERS-1 satellite). This representation on a rectangular grid will be used throughout the thesis. The SST contours reflect the large-scale circulation at the surface, though the contour interval of $1.5°C$ is too large to resolve the exact positions of the fronts discussed earlier. This figure is included for reference, but also shows how the topography is influencing the surface circulation in many places. Topography is discussed further in chapter 4.

1.2 Structure of the thesis

The remainder of the thesis will be structured as follows. Chapter 2 contains a description of previous research relating to Rossby waves, particularly in the

ocean. The theory of Rossby waves, modelling studies and Rossby wave observations are covered in separate sections. Chapter 3 describes the analysis of output from the FRAM model of the Southern Ocean. After a description of the model, the spatial distribution and the frequency of Rossby wave activity are studied. This leads on to the calculation of Rossby wave phase speeds, and then a study of the time-averaged effect of the Rossby wave activity. Chapter 4 expands on some of the results of chapter 3 by looking at the relationship between Rossby waves and the mean flow in FRAM. The use of simplified models in relating Rossby waves to the mean flow, and the relevance of bottom topography to the dynamics observed at the surface are also discussed. Chapter 5 describes the analysis of data from the TOPEX/POSEIDON satellite mission. The satellite and data are described and the methods of analysis used in chapter 3 are applied, wherever possible. An assessment of the errors involved is presented where appropriate. Chapter 6 expands on the analysis of eddies and introduces data in the form of mapped anomalies of sea surface height, combined from the TOPEX/POSEIDON and ERS satellite missions. Ship cruise measurements from the World Ocean Circulation Experiment (WOCE) are used to estimate the position and strength of jets in the mean flow. The relationship between eddies and the mean flow is studied by calculating a quantity known as the Reynold's stress. This is related to the estimates of mean flow, and compared with results from FRAM. Finally, chapter 7 summarises and discusses the principal results, and then puts forward suggestions for further work.

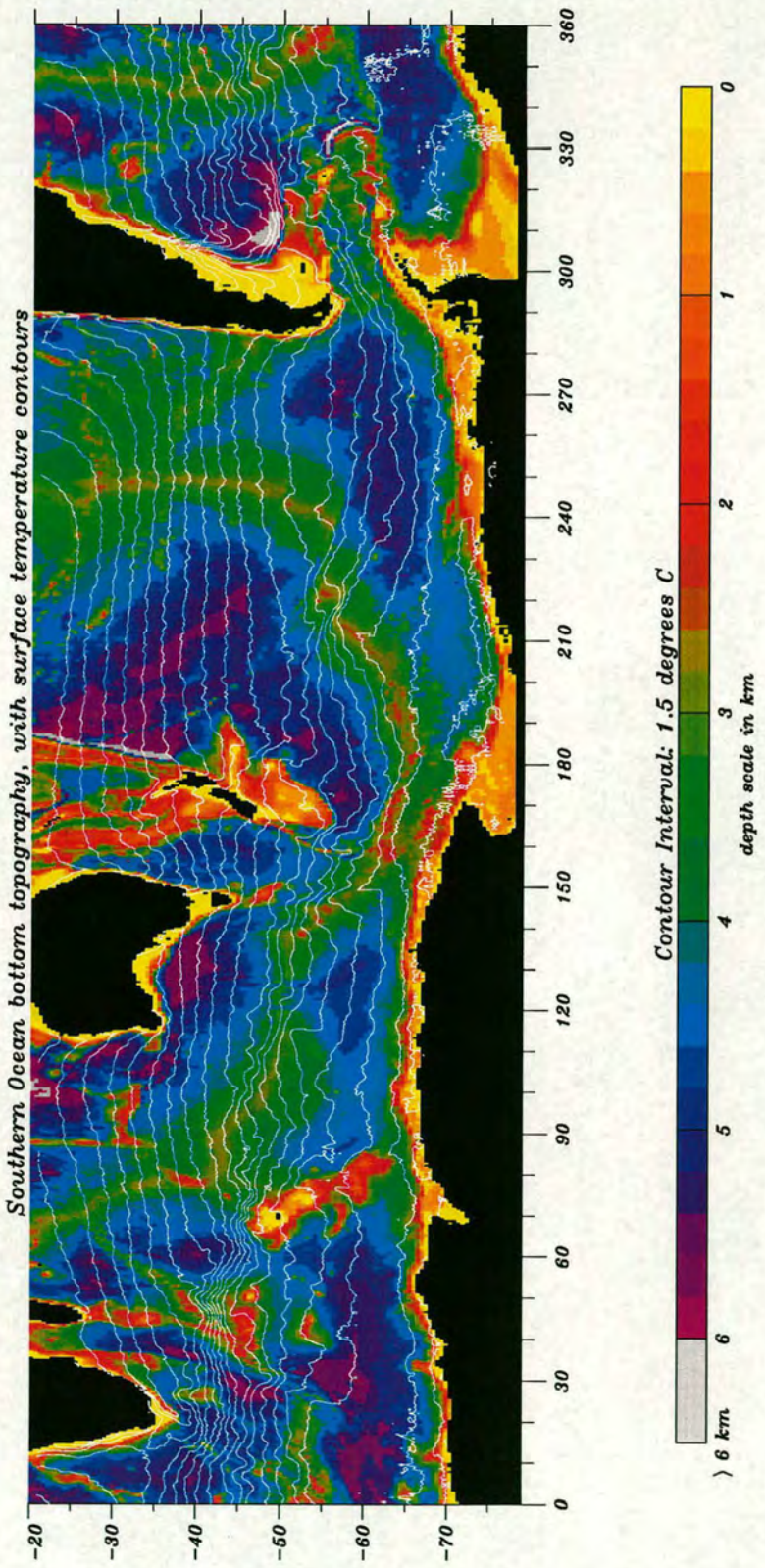

Figure 1.3: Bottom topography and surface temperature contours in the Southern Ocean (from Hughes et al, 1997). The contour interval is $1.5°C$ and the depth scale is in km.

Chapter 2

Theory and observations of Rossby waves

Rossby waves, also known as planetary waves, are found in geophysical fluid media due to the Earth's rotation and resulting latitudinal gradient in planetary vorticity. This provides a restoring force for fluid parcels when displaced North or South, due to the conservation potential vorticity in the absence of external forces. Rossby waves are large scale, with typical wavelengths of a few thousand kilometres in the atmosphere and a few hundred kilometres in the ocean. They propagate with phase speeds of several m/s in the atmosphere and several cm/s in the ocean, and are low frequency, with periods of days in the atmosphere and months in the ocean. Rossby waves are recognised as the fundamental mechanism for adjustment of both the atmosphere and oceans in response to changes in forcing over timescales of a few days or more (Anderson and Gill, 1975; Anderson and Killworth, 1977).

Figure 2.1 shows a simplified schematic for the propagation of Rossby waves. The periodic displacement of the contours of constant pressure (which is analogous to constant dynamic height in the ocean) gives rise to changes in relative vorticity shown by the positive and negative rotational arrows. The resulting motion is shown by the arrows in the y (North-South) direction and acts to propagate the wave to the West. Rossby waves always propagate westward relative to the mean flow, and this will be confirmed by the theory presented in 2.1.

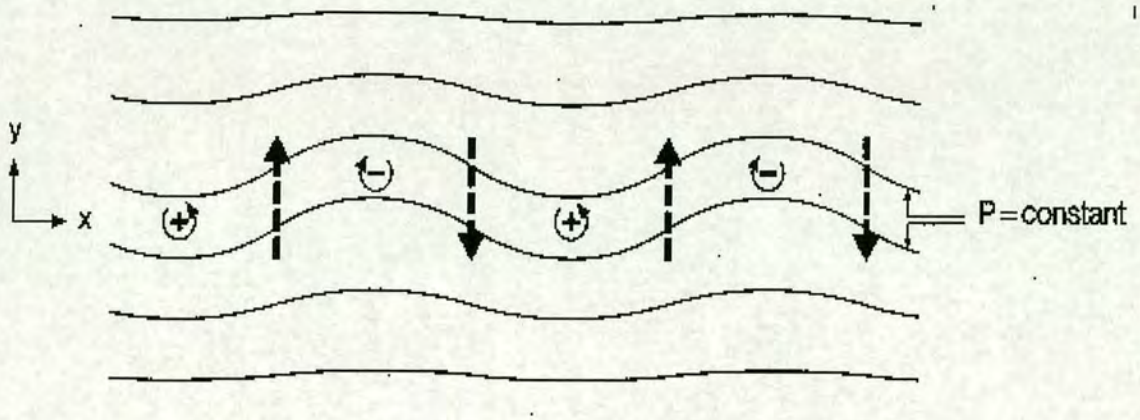

Figure 2.1: Schematic of Rossby wave propagation

This chapter reviews previous research relating to Rossby waves. Rossby waves in the atmosphere are mentioned, but the chapter focuses on oceanic Rossby waves. Section 2.1 gives an introduction to the theory of Rossby waves. Section 2.2 describes studies of Rossby wave behaviour in the presence of mean currents. Section 2.3 describes previous observations of Rossby waves in the ocean and section 2.4 reviews some recent theory which takes account of these observations.

2.1 Linear Rossby wave theory

2.1.1 Early developments

The theory of Rossby waves was first developed by Rossby (1939, 1940), following his analysis of several years of meteorological charts which, in the 1930's, had included measurements of the upper westerlies for the first time. It is worth noting that some time earlier Margules (1893) wrote about waves with periods proportional to rotation rate in his paper on air motion in a rotating spherical shell. Also, in the same decade, Hough (1897, 1898) wrote about mean flows following paths of constant potential vorticity following his analysis of Laplace's equations in relation to the theory of tides. It was not until some forty years later, however, that Rossby related these results to observations and provided a physical explanation.

Rossby's work, and the developments in the years after, were elegantly reviewed in a lecture by Platzman (1968), who emphasised the importance of this work and its profound effect on our understanding of atmosphere and ocean dynamics. In particular, Rossby's concept of the beta plane enabled derivation of an equation relating phase speed to mean flow velocity and wave length-scale, from the governing physical equations. The beta plane approximation was studied further, and shown to be useful, in some important work by Longuet-Higgins (1964-65).

In the decade following Platzman's review, Rossby wave theory continued to be an active area of research with particular progress being made using the linear perturbation approach. In studies of the atmosphere, new work looked at vertical propagation of Rossby waves (e.g. Dickinson, 1969a; Garcia and Geisler, 1974) and the interactions between Rossby waves and zonal flows (e.g. Dickinson, 1969b). In the ocean, Rossby waves with behaviour characterised by linear theory were positively identified (Thompson, 1971), and the theory used to provide insight into oscillatory features of ocean currents. An excellent review of the progress made at this time, focusing on linear-perturbation theory and its use in describing long-period geophysical fluid motions, is provided by Dickinson (1978).

2.1.2 Rossby wave dispersion relation

The absolute vorticity in an ocean of uniform depth is given by the sum of the relative and planetary vorticities:

$$q = \zeta + f \tag{2.1}$$

A dispersion relation for free Rossby wave propagation in a barotropic mean flow may be derived by linearising the planetary vorticity using the β plane approximation,

$$f = f_0 + \beta y \tag{2.2}$$

and applying the principal of Lagrangian conservation of potential vorticity in the absence of external forces, given by

$$\frac{Dq}{Dt} = \frac{\partial q}{\partial t} + \mathbf{v}.\nabla q = 0, \tag{2.3}$$

$$\text{where} \quad \mathbf{v} = (u, v) \quad \text{and} \quad \nabla = \left(u\frac{\partial}{\partial x} + v\frac{\partial}{\partial y} \right). \tag{2.4}$$

A uniform zonal flow, $\overline{u}$ is assumed with small horizontal perturbations:

$$u = \overline{u} + u', \quad v = v'. \tag{2.5}$$

For uniform zonal flow ($\overline{u}$ constant), ζ is given by

$$\zeta = \left(\frac{\partial v}{\partial x} - \frac{\partial u}{\partial y} \right) = \left(\frac{\partial v'}{\partial x} - \frac{\partial u'}{\partial y} \right). \tag{2.6}$$

A streamfunction, $\psi = \overline{\psi} + \psi'$, is defined by

$$\overline{u} = -\frac{\partial \overline{\psi}}{\partial y}, \quad u' = -\frac{\partial \psi'}{\partial y}, \quad v' = \frac{\partial \psi'}{\partial x} \tag{2.7}$$

which gives $\zeta = \nabla^2 \psi'$, where ∇^2 is the horizontal Laplacian. The potential vorticity in terms of ψ' and β becomes

$$q = \nabla^2 \psi' + f_0 + \beta y. \tag{2.8}$$

Substitution into 2.3 and expansion using the perturbation velocities 2.5, neglecting products of perturbation quantities, gives

$$\left(\frac{\partial}{\partial t} + \overline{u}\frac{\partial}{\partial x} \right) \nabla^2 \psi' + \beta \frac{\partial \psi'}{\partial x} = 0. \tag{2.9}$$

Wave solutions are sought, of the form:

$$\psi' = \mathrm{Re}[\Psi e^{i(kx+ly-\omega t)}] \tag{2.10}$$

where k and l are the zonal and meridional wavenumbers respectively and ω is the angular frequency. Substitution of 2.10 into 2.9 yields the dispersion relation:

$$c_x = \frac{\omega}{k} = \overline{u} - \frac{\beta}{k^2 + l^2} \tag{2.11}$$

where c_x is the zonal phase speed.

Modification for zonal shear flow

In the case of a zonal flow which varies North-South, ζ becomes

$$\zeta = \left(\frac{\partial v'}{\partial x} - \frac{\partial u'}{\partial y} - \frac{\partial \overline{u}}{\partial y} \right) \tag{2.12}$$

and the dispersion relation 2.11 is modified by replacing β by β_e, the effective β, where

$$\beta_e = \beta - \frac{\partial^2 \overline{u}}{\partial y^2}. \tag{2.13}$$

Modification for stratification

In the case of a stratified ocean, the potential vorticity on a β plane with a barotropic zonal flow which varies North-South can be shown to be (e.g. Pedlosky, 1987)

$$q = \nabla^2 \psi' - \frac{\partial \overline{u}}{\partial y} + f_0 + \beta y + \left(\frac{\partial}{\partial z} \frac{f_0^2}{N^2} \frac{\partial}{\partial z} \right) \psi' \tag{2.14}$$

where N is the Brunt-Väisälä or buoyancy frequency.

Breaking down the potential vorticity into time mean and perturbation parts and linearising 2.3 gives

$$\frac{Dq}{Dt} = \frac{D(\overline{q}+q')}{Dt} = \frac{\partial q'}{\partial t} + \overline{u}\frac{\partial q'}{\partial x} + v'\frac{\partial \overline{q}}{\partial y} \tag{2.15}$$

$$\text{where from 2.14} \quad q' = \nabla^2\psi' + \left(\frac{\partial}{\partial z}\frac{f_0^2}{N^2}\frac{\partial}{\partial z}\right)\psi' \tag{2.16}$$

$$\text{and} \quad \frac{\partial \overline{q}}{\partial y} = \beta - \frac{\partial^2 \overline{u}}{\partial y^2} - \left(\frac{\partial}{\partial z}\frac{f_0^2}{N^2}\frac{\partial}{\partial z}\right)\overline{u}. \tag{2.17}$$

Seeking solutions of the form $\psi' = \mathrm{Re}[\Psi e^{i(kx+ly+mz-\omega t)}]$ results in the dispersion relation

$$c_x = \frac{\omega}{k} = \overline{u} - \frac{\beta_e}{k^2 + l^2 + \frac{f_0^2 m^2}{N^2}}. \tag{2.18}$$

This equation shows that, for positive β_e, $\overline{u} - c_x$ will be positive and so the Rossby waves always propagate westward relative to the mean flow. If β_e becomes zero or negative (possible in regions of strong jet type flows), a critical layer develops, where Rossby waves cannot propagate. This is due to the instability which occurs when there is a change in sign of the North-South gradient in potential vorticity, which is dominated by the gradient of background vorticity, β_e. Critical layers are of fundamental importance to a study of Rossby waves and are discussed in section 2.2.2.

For an ocean with a flat bottom, the vertical wavenumber term, $\frac{f_0^2 m^2}{N^2}$, is equivalent to R_0^{-2} where R_0 is the Rossby deformation radius. In a continuously stratified ocean there will be an infinite set of Rossby deformation radii, which, for an ocean in a state of rest, give rise to a corresponding set of Rossby wave modes with different phase speeds. The fastest of these modes is the barotropic mode which crosses ocean basins with a time scale of a few days. The remaining modes are baroclinic whose eastward phase speeds decrease with increasing R_0. First baroclinic mode Rossby waves have a phase speed of a few cm/s and it is this

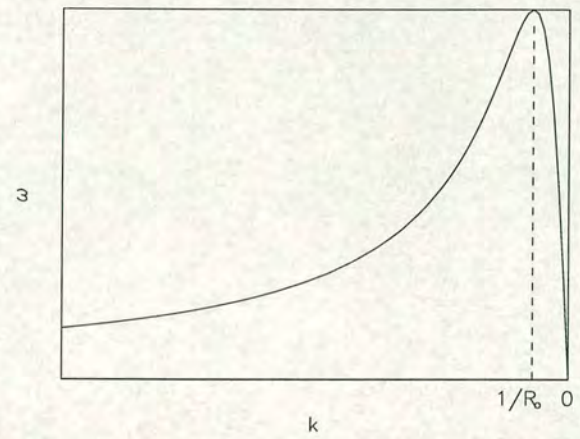

Figure 2.2: ω against k from the Rossby wave dispersion relation.

class of Rossby wave that is most readily observable in the real ocean. In ocean models such as FRAM and OCCAM, only the barotropic and first baroclinic mode Rossby waves are resolved.

Figure 2.2 shows the dispersion relation plotted for the case of zero flow and fixed meridional wavenumber, l. By convention, k is shown negative to indicate westward propagation. A turning point occurs at $k = 1/R_0$ and this maximum value of the frequency, ω, depends on the value of β, which varies with latitude. In the long wave limit, with k much less than $1/R_0$, the frequency, ω, is proportional to k and the waves are non-dispersive. For short waves, ω is proportional to $1/k$ and the phase speed increases with frequency and wavelength.

Rossby waves can be treated as a class of general waves for the purpose of understanding and interpreting the dispersion relation. The dispersion relation relates frequencies to wavelengths without any consideration of how different waves might interact with each other. In a real propagation situation there will be a complicated mixture of waves with different spatial and temporal scales. Two approaches are commonly used for simplifying the problem of real wave propagation. The first is known as WKBJ theory, after G. Wenzel, H.A. Kramers, L. Brillouin and H. Jeffreys (Morse and Feshbach, 1953). WKBJ theory is an approximation for short waves (in the dispersive regime) which applies when the background conditions (typically mean U) change very little over several wave-

lengths. In these circumstances, the dispersion relation can be used to obtain separate solutions for single waves. These may then be combined linearly to produce a general solution.

The other approach is known as ray tracing and a good description of this is found in Lighthill (1978). With this method, individual sinusoidal waves are traced along paths of constant frequency. As with WKBJ theory, the background conditions must change slowly on scales of a few wavelengths, and there is assumed to be no interference between waves of different frequency. This is a useful approach for two reasons. Firstly, it leads to information on the spatial distribution of the wavenumber at a given frequency. Secondly, because the wave energy moves along rays, the tracing can be used to determine the distribution of wave amplitude.

2.2 Rossby waves in mean flows

2.2.1 Propagation in zonal flows

Linear Rossby wave theory holds for waves of small amplitude in an ocean with uniform depth in a state of rest, or with a uniform zonal velocity, U. A modification for a uniform shear in the zonal velocity has been introduced, but it then becomes unclear how to define U. WKBJ theory and ray tracing help with the application of linear theory to more realistic (though constrained) circumstances, but the real ocean has a complicated flow structure for which a general theory of Rossby wave propagation has not been established. Numerical and observational studies of Rossby wave propagation have begun to bridge the gap between theory and reality. Many atmospheric studies exist, such as those of Dickinson (1968) and Mekki and McKenzie (1977). In the ocean, progress has been made using quasi-geostrophic modelling of Rossby wave propagation in various zonal flow structures.

Quasi-geostrophic approach

Quasi-geostrophic modelling makes use of a simplified set of dynamical equations which describe the behaviour of motion in mid-latitudes quite adequately for many purposes.

One major study of Rossby waves propagating in a zonal shear flow is that of Killworth (1979). Killworth used quasi-geostrophic modelling to explore the behaviour of baroclinic Rossby waves in the presence of weak mean flows. He looked at barotropic and baroclinic flows and their affects on the vertical wave modes as well as the time evolution of baroclinic waves.

The first of these initial value experiments studied the propagation of free Rossby waves across a zonally orientated jet. The experiment was conducted for both an eastward and a westward jet, with jet orientation being the only difference between the two cases. The jet was of $sech^2$ form with a maximum speed of 1.8 cm/s. Rossby waves were generated continuously by a wavemaker to the North of the jet in a region of zero flow. With the eastward jet, waves propagated southwards until the jet velocity reached approximately one tenth of its maximum, where they were reflected northwards. This result is shown in the top part of figure 2.3 which shows time-space contours of streamfunction in a channel of width 2400km. The initial wavelengths are 377km, with a period of 1.06 years. The waves begin reflection after 8 years and a steady pattern is reached after 16 years. With the westward jet, the waves propagated southwards until the jet velocity reached about half its maximum, where they were absorbed due to the presence of a critical layer (see section 2.2.2).

A second set of experiments looked at the dispersion of energy following an impulsive input of wave activity into the same type of jet at t=0. The experiment was performed for four combinations of long and short horizontal wavelengths in an eastward jet, and for short wavelengths in a westward jet. In the eastward jet with short waves, the waves were distorted by the shear and propagated away from the shear to set up a standing wave. This result is shown in the bottom part of figure 2.3. Initial wavelengths are 377km (E-W) and 400km (N-S) and

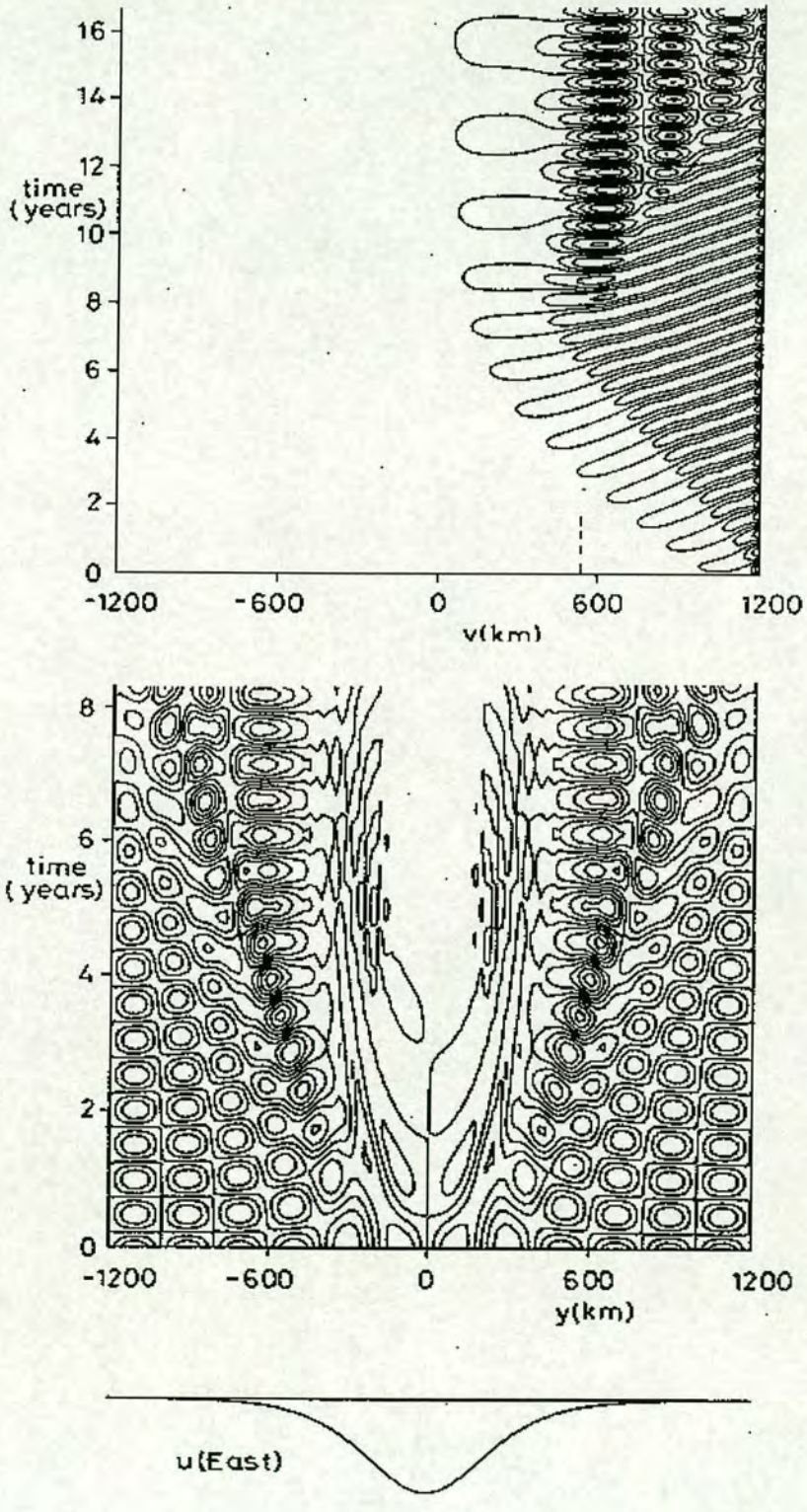

Figure 2.3: Time-space contours of streamfunction from results of two numerical experiments by Killworth (1979), discussed in the text. In each case, waves are propagating in an Eastward mean flow given by the profile, which has a maximum velocity of 1.8 cm/s.

the maximum jet velocity is 1.8 cm/s, as before. Waves are seen to spread from the centre of the jet until, after 4 years, there is very little activity where the flow is greater than about half the maximum. With a long N-S wavelength (2400km), propagation followed a very similar pattern to the short wave case, but on a slightly longer timescale. With long E-W waves (1885km), the effect of shear was much less and there was little amplitude distortion. This implied that long waves would be more detectable in the real ocean than short waves. With a westward jet, the short waves are trapped within the shear region, where their amplitude and phase is altered on time scales of a few months.

A final experiment traced the evolution of wave activity with short wavelengths in a sinusoidal gyre system. This showed rapid decay of waves except near the maximum of the westward jet, implying that short waves would not survive for long in oceanic gyre systems. Killworth's work has demonstrated some interesting properties of simplified Rossby wave propagation in the presence of weak mean flows, but it must be noted that mean flows in the real ocean may have velocities an order of magnitude greater than those modelled in this study.

Pedlosky (1977) used a 2-layer quasi-geostrophic model to look at the effect of vertical shear on the propagation of different Rossby wave modes. Propagation was found to depend on the phase speed compared to the local current velocity, which is the criticality of the vertical shear of the flow. A westward shear flow was found to act as a barrier to eastward propagation, but permitted the northward transmission of westward propagating disturbances.

Other approaches

Drazin et al (1982) used analytical methods, supported by numerical results, to study properties of Rossby waves in basic horizontal shear flows. They showed the dispersion relation and spatial structure of the waves to be significantly modified by the shear for cases of quite general velocity profiles.

Matano and Philander (1994) used a shallow-water model to study the decay of meanders in eastward currents. The fast decay of meanders moving away

from a western boundary was attributed to shear in the flow, which resulted in the presence of critical layers. These then inhibited the meridional passage of currents containing Rossby wave activity. Their analysis did not account for interaction between Rossby waves and the mean flow, but this was considered and implied that the eastward currents might act as a waveguide for the Rossby waves. Several more studies are concerned with Rossby wave propagation in the presence of a critical layer, and these are discussed in section 2.2.2.

2.2.2 Rossby wave critical layers

A Rossby wave critical layer occurs when the zonal phase speed matches the zonal flow speed, giving rise to a singularity in the dispersion relation. Under such conditions, the wave frequency is Doppler-shifted to zero and the Rossby waves cannot propagate. Instead, energy is cascaded into smaller scales and transferred to the mean flow. Critical layers can occur in eastward shear flows when the North-South gradient of background vorticity (β_e) becomes zero.

Critical layer theory is an important branch of theoretical fluid mechanics and not just a geophysical fluid dynamics phenomenon. A general review of critical layer theory is provided by Maslowe (1986) who included applications to geophysical fluid dynamics, focusing on the exchange of energy between Rossby waves and the mean flow.

Critical layers have been studied for many years, particularly in application to stability properties of the atmosphere (e.g. Kuo, 1949). The importance of critical layers as a constraint on Rossby wave propagation, both latitudinally and vertically, is widely recognised (Dickinson, 1968). Behaviour at a critical layer is highly nonlinear, but it is possible to demonstrate the essential mathematical features of the critical layer using the linearised barotropic vorticity equation. This problem was treated by Dickinson (1970) in application to atmospheric motions, who discussed the time dependent behaviour of eddy velocities near a critical layer. The importance of nonlinearity at a critical layer has been studied numerically by Haynes (1989) who looked at wave absorption under conditions of barotropic instability.

The evolution of a nonlinear critical layer was studied in experiments by Warn and Warn (1976, 1978) and more analytically by Stewartson (1978). The effect of the critical layer on Rossby wave propagation has been studied numerically by Geisler and Dickinson (1974). They found that the zonal flow profile would adjust to bring the background vorticity gradient, β_e, to zero at the critical layer. This resulted in total reflection of the waves and no further interaction with the mean flow. This work was extended by Killworth and McIntyre (1985) who studied the mathematical details of Rossby waves impinging on a critical layer. Their work confirmed that critical layers absorb the wave activity initially, but absorb decreasingly with time such that the waves are reflected in the long term.

It is clear that critical layers play a fundamental role in the propagation of Rossby waves. The awareness of critical layer regions will therefore be important in the analysis of Rossby wave activity in the real ocean. Critical layers are an example of wave-mean flow interaction, which is a broader area of study (e.g. Dickinson, 1969c; McIntyre and Norton, 1990).

2.2.3 Propagation in non-zonal flows

The problem of Rossby wave propagation is further complicated if the mean flow is not zonal. Killworth (1979) looked at the case of flow with a meridional component and found that such flows would deflect waves but not inhibit their propagation. Critical layers in non-zonal flow were found to affect only very short, baroclinic waves. Kang et al (1982) used analytical techniques and simplified modelling to study Rossby waves in non-zonal shear flows. They considered flows at 45° to the zonal direction and concluded that any non-zonal shear flow would be unstable for disturbances on scales larger than the Rossby deformation radius (mode 1).

Rossby wave behaviour in non-zonal flow has also been studied by Kamenkovich and Pedlosky (1996). They used barotropic and two layer quasi-geostrophic models to analyse the stability of wave activity in jets inclined between 5° and 30° to the zonal direction. Unlike zonal jets, non-zonal jets could be unstable when the gradient of potential vorticity was single signed. Radiating properties of the

non-zonal jets were studied and found to be very different from those of zonal currents. Eastward zonal currents would not support radiating instabilities, but flows with a meridional component were capable of radiating long waves. This was considered to be a mechanism for the generation of eddies in regions away from energetic ocean currents.

2.2.4 Waveguides for Rossby waves

If waves are seen to propagate along a certain path without spreading tranversely, then they can be considered to be trapped within a waveguide. Established zonal jets might act as a waveguide for Rossby waves if bounded North and South by a critical layer. Several authors have looked at wave-guiding phenomenon in geophysical flows.

In an atmospheric study, Hoskins and Ambrizzi (1993) used a linearised barotropic model to look at teleconnection patterns in the upper troposphere. Their results provided evidence for the existence of a strong waveguide in the Asian jet and weaker waveguides in the North Atlantic and Southern Hemisphere jets.

Annenkov and Shrira (1992) used a QG model to study the effect of the mean circulation on wave activity in the ocean. They found that the N-S propagation of Rossby waves was strongly inhibited by the meridional instability of large-scale flows. Baroclinic waves propagating westward, as well as meridionally, were reflected from the core of eastward flows in the mid-latitudes to form, as they describe, "sub-polar" and "sub-equatorial" waveguides. Baroclinic waves propagating eastwards were seen to follow waveguides bounded by critical layers.

Using output from the FRAM model, Hughes (1996) studied Rossby wave propagation in the Southern Ocean. Animations of zonal gradient of residual SSH showed clear eastward propagation within the ACC and westward propagation elsewhere. Cross-spectral analysis was used to quantify phase speeds and the results showed sharp divides between eastward and westward propagation, indicating a wave-guiding effect for eastward propagating waves. Lines of meridional minima of β_e were superimposed on a snapshot of the zonal gradient of SSH,

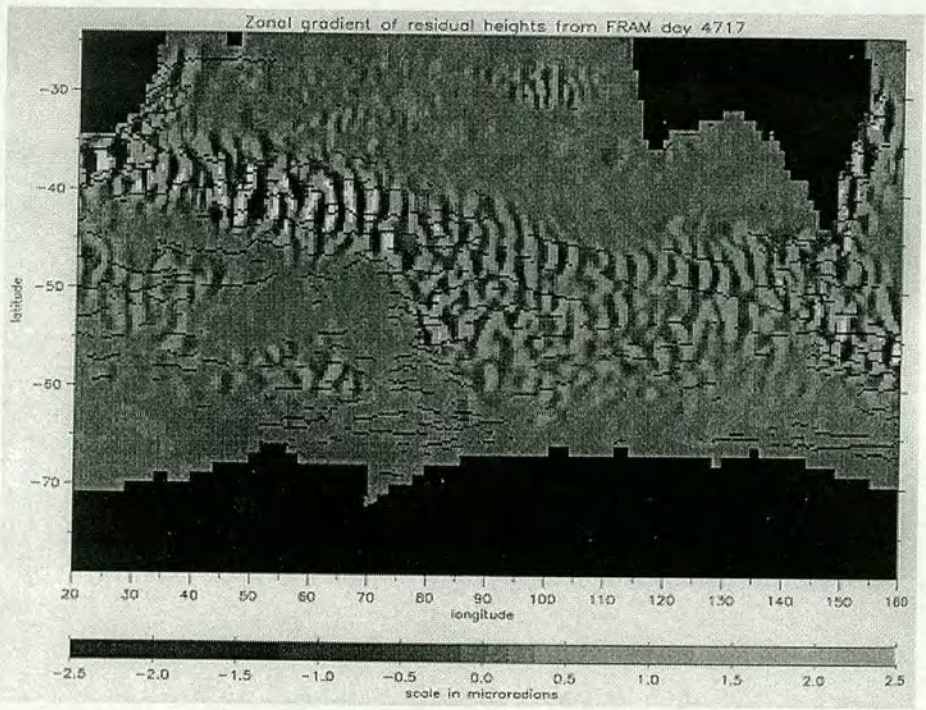

Figure 2.4: Figure from Hughes (1996) showing a snapshot of zonal gradient of SSH from FRAM with meridional minima of β_e marked in black where the minimum value is negative.

showing some waves to be channelled between those lines. This comparison is shown in figure 2.4 for the Indian sector of the Southern Ocean, where the channelling is evident in many places. The lines represent theoretical critical lines which have been seen to bound wave propagation in previous studies (see section 2.2.2). The existence of Reynolds stresses at these lines, however, implied absorption of wave activity and so imperfect wave-guiding. Despite the use of model output, these results implied that the analysis of Rossby waves might provide useful information about the mean flow in the real Southern Ocean.

2.3 Rossby wave observations

2.3.1 Early observations

Because of the importance of atmospheric measurements for meteorological forecasting, Rossby waves have been observed in the atmosphere for some time. In

the oceans there is not the same network of in situ measurement stations. Despite this, several authors have reported evidence of first mode baroclinic Rossby waves from hydrographic data, both for the North Pacific (e.g., Emery and Magaard, 1976; White and Saur, 1983; White, 1985; Kessler, 1989) and the North Atlantic (e.g., Mcwilliams and Flierl, 1976; Price and Magaard, 1986; Spall, 1992). Identification of Rossby waves in patchy hydrographic data, however, is not easy (White, 1977, 1985; Kessler, 1990), and it is only since the launch of satellite altimeters that suitable data for extensive Rossby wave observation have been available.

2.3.2 Satellite altimeters

Satellite altimeters use radar to measure the distance between the altimeter and the sea surface. The mean sea surface height is measured independent of wind-driven wave activity, which is on a much smaller scale than the footprint of the altimeter (though the nature of the return signal enables winds and surface waves to be quantified separately). The satellite orbital position is known very accurately and measurement corrections are applied to reduce other sources of error. As a result, the height of the sea surface relative to a reference ellipsoid is measured by modern altimeters to an accuracy of centimetres (Shum et al., 1995). Surface currents signifying Rossby wave activity are detected by the dynamic topography, which is the difference between the sea surface height and the geoid. The geoid is where sea surface would be in an ocean of no motion (which depends on the local gravity field, which is not well known). The dynamic topography varies by a few metres globally and so height measurements to an accuracy of a few centimetres are sufficient for quantitative Rossby wave observation. A typical Rossby wave causes SSH changes of 5 to 20cm over timescales of a few months, and the measurement of changes in SSH does not rely on knowledge of the geoid.

2.3.3 Observations from Geosat

The first satellite altimeter to measure the SSH with sufficient accuracy and coverage for Rossby wave observation was launched on the Geosat mission in

1985. Tokmakian and Challenor (1993) used Geosat data to find evidence of Rossby wave propagation in the Azores region of the North Atlantic. Geosat data was also used by Le Traon and Minster (1993) who studied wave activity in the South Atlantic between 15° and 35°S. They divided this part of the ocean into four bands of longitude and for each band calculated statistical quantities such as the variability, 17 day decorrelation, along track wavenumber spectrum and frequency-wavenumber spectrum. The frequency-wavenumber spectra contained a significant semiannual signal which compared favourably to semiannual Rossby waves.

In the Southern Ocean, Morrow et al (1994) calculated the Reynolds stress components at Geosat crossover points in order to determine the surface eddy momentum flux. This was presented as velocity variance ellipses for three more active regions of the Southern Ocean; the Agulhas region, southeast of Australia and southwest Atlantic. The results are an indication of the spatial distribution of eddy and Rossby wave activity and interaction with mean currents. This work is an important reference for some of the results presented in this thesis. It will be discussed further in chapter 6.

Unfortunately, the Geosat data set was found to suffer from tidal signal interference, (Schlax and Chelton, 1994), which limited the extent to which Rossby waves could be identified. The follow-up satellite to Geosat, TOPEX/POSEIDON, was launched in 1992 and had an orbit designed to enable easy distinction between tidal and Rossby wave signals. TOPEX/ POSEIDON has now been observing the ocean surface for over five years, providing an unprecedented facility for Rossby wave observation. The TOPEX/POSEIDON mission and measurements will be discussed more fully in chapter 5.

2.3.4 Observations from TOPEX/POSEIDON

North Atlantic and Pacific

TOPEX/POSEIDON data has been used by several authors to study Rossby wave activity in the North Atlantic and Pacific. Wang and Koblinsky (1995)

used the TOPEX/POSEIDON data to identify Rossby waves in the Kuroshio and Gulf Stream regions. Rossby waves in the Gulf stream have also been observed by Rogel et al. (1997). Cipollini et al (1996, 1997a,b) looked at the North Atlantic by interpolating SSH anomalies onto a 1° grid and analysed FFT and Radon transforms of longitude/time diagrams. They found a prominent band of zonal propagation at around 33° – 34°N and were able to make approximate measurements of wave speeds and amplitudes in this region. Two major peaks were identified in Fourier space, and these corresponded to periods of 330 days and 200 days, with wavelengths of 1440km and 580km respectively. The westward phase speeds for these waves are 5.1cm/s and 3.4cm/s.

Polito and Cornillon (1997) used 1° gridded data to calculate SSH autocorrelation matrices on a 5° grid, which were analysed to show westward propagation in the North Atlantic up to 50°N. They looked separately at annual and semi-annual spectral bands, the first with periods between 280 and 450 days and the second with periods 120 and 280 days. Values of phase speed and zonal wavelengths were obtained for these bands, with the annual band showing dominant signals. Typical westward phase speeds, averaged between 40° and 70°W, were 4.6cm/s at 27.5°N, 4.2cm/s at 32.5°N, and 3.7cm/s at 37.5°N. Wavelengths decreased with latitude, from about 2000km at 10°N to about 500km at 40°N. The results were compared with previous observations and numerical model output, which suggested that the waves observed at mid-latitudes were generated by fluctuations of the wind stress curl at the eastern boundary.

Non-gridded TOPEX/POSEIDON data were used by Glazman et al (1996) to look at two regions of the North Atlantic between 30° and 40°N. They used a technique to estimate spatial-temporal autocorrelation functions, which contained information on baroclinic Rossby wave propagation. Mean phase speeds in that region were found to be 2.8cm/s westward.

In an early evaluation, Nerem et al. (1994) used TOPEX/POSEIDON to estimate the phase speed of westward propagating anomalies between 21°S and 21°N in the Pacific. They identified first-mode baroclinic Rossby waves away from an equatorial band (5°S to 5°N). In the northern hemisphere, westward phase speeds

increased from 0cm/s at 21°N to over 50cm/s at 5°N. In the southern hemisphere, phase westward speeds were slightly higher, increasing from 10cm/s at 21°S to 50cm/s at 7°S. The uncertainty in these measurements, however, was 4cm/s, due to smoothing used in the gridding process.

Southern Ocean

In the Southern Ocean, Hughes (1995) has looked at Rossby wave activity derived from 16 months of TOPEX/ POSEIDON SSH measurements and compared this to results derived from FRAM model output. The zonal gradient of SSH was extracted at satellite crossover points, which has an advantage over gridded SSH anomalies in reducing the long wavelength errors due to orbit inaccuracy and tides. The disadvantage of using crossover data is the zonal resolution, but where waves are coherent over several degrees of latitude, the diamond pattern of crossover points can be used to double the zonal resolution. Hughes used the technique of Complex Principal Components analysis (Barnett, 1983) to quantify propagation, particularly in the Pacific sector. Wave parameters were derived from the analysis and compared to those derived from FRAM output using the same technique. The wave parameters presented were fairly sparse (covering approximately 20% of the ocean) and varied over the Southern Ocean. Wavelengths were typically between 300 and 500km and phase speeds between 5cm/s westwards and 5cm/s eastwards. In the Pacific sector, eastward phase speeds were mainly between 1 and 4cm/s. Wave periods varied from a few months to over a year. Rossby wave activity in the Southern Ocean has also been observed using the ERS1 satellite (see section 2.3.5).

Global

Chelton and Schlax (1996) studied more than three years of TOPEX/POSEIDON data which they filtered to cut out short-period activity unrelated to Rossby waves. The filtered data were presented as time-longitude sections for the extratropical pacific, showing definite westward propagation at a number of latitudes. These results were representative of other extratropical regions of the

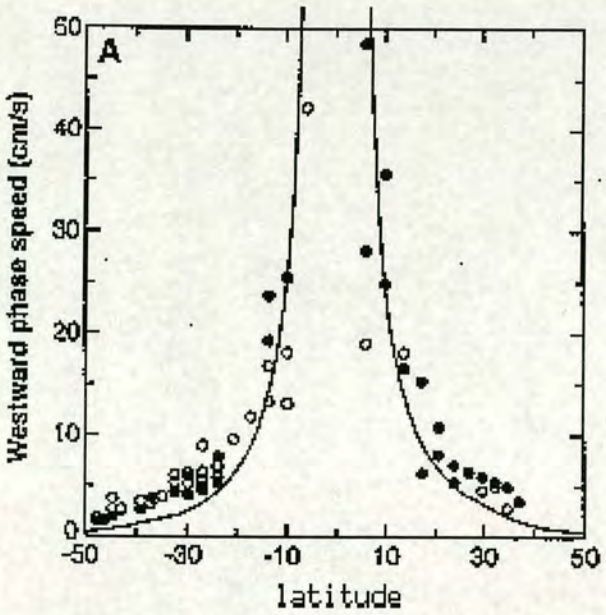

Figure 2.5: Results from Chelton and Schlax (1996) of observed (dots) and theoretical (line) phase speeds against latitude.

world ocean. Phase speeds of westward propagating signals were estimated from time-longitude sections constructed throughout the world ocean, and these were compared to phase speeds predicted by the standard linear theory of freely propagating Rossby waves. The results are shown in figure 2.5 which shows theoretical westward phase speeds (continuous line) and measured phase speeds (dots) for the latitude range of 50°S to 50°N. Solid dots are measurements from the Pacific and open dots are measurements from the Atlantic and Indian oceans. These results are consistent with other measurements of phase speeds, and provide a good summary of observed phase speeds in the world ocean. Pole-wards of 20°, the observed phase speeds are consistently faster than the theoretical values. This comparison is discussed further in section 2.4.

Variability over the World Ocean was studied by Stammer (1997) who used three years of TOPEX/POSEIDON data to calculate frequency and wavenumber spectra. These were compared across the globe and seen to show universal characteristics relating to the eddy field. In particular, the variation of eddy scale with latitude in the extratropical ocean was significantly correlated with the variation of the first Rossby deformation radius. Eddy timescales and length-scales were quantified, and the results supported the hypothesis that baroclinic instability is

the major mechanism for eddy generation.

2.3.5 Observations from ERS1

The ERS1 satellite was launched in 1992 and had instrumentation which included an altimeter and an along-track scanning radiometer for the purpose of sea surface temperature (SST) measurements. Its spatial resolution is about four times better than that of TOPEX/POSEIDON, at the expense of a longer repeat cycle of 35 days.

SST and altimetry data measured by ERS1 instruments were used by Hughes et al (1998) to study propagation of mesoscale features in the Southern Ocean. The SST and SSH data were converted to zonal gradients and cross spectral analysis was used to estimate zonal wavenumbers. These were presented for the typical wave periods of 4.8 and 4.6 months for the SST and altimetry data respectively, and compared with the same quantities derived from FRAM output. An example of the results from the SST data is shown in figure 2.6. This shows the zonal wavenumber for the along-track gradient of SST, at a period of 4.8 months. Eastward propagation is associated with the ACC (red regions) and westward propagation outside. The eastward wavenumber is less than 0.02 km^{-1}, corresponding to a wavelengths greater than about 300km. Smaller wavelengths (down to about 200km) are found if the SST derived v is used instead of along-track gradient. The propagation directions derived from the two different data sources (SST and altimetry) are consistent, showing a well defined region of eastward propagation within the ACC. The accuracy of the wavelength estimates, however, were limited by the coarse spectral resolution, and results were found to be sensitive to the processing method. This work highlighted some of the difficulties of using spectral information to understand the mean circulation.

2.4 Revisions to standard linear theory

In many of the observations discussed in section 2.3, the observed phase speeds were found to differ from results predicted by the standard linear theory, presented

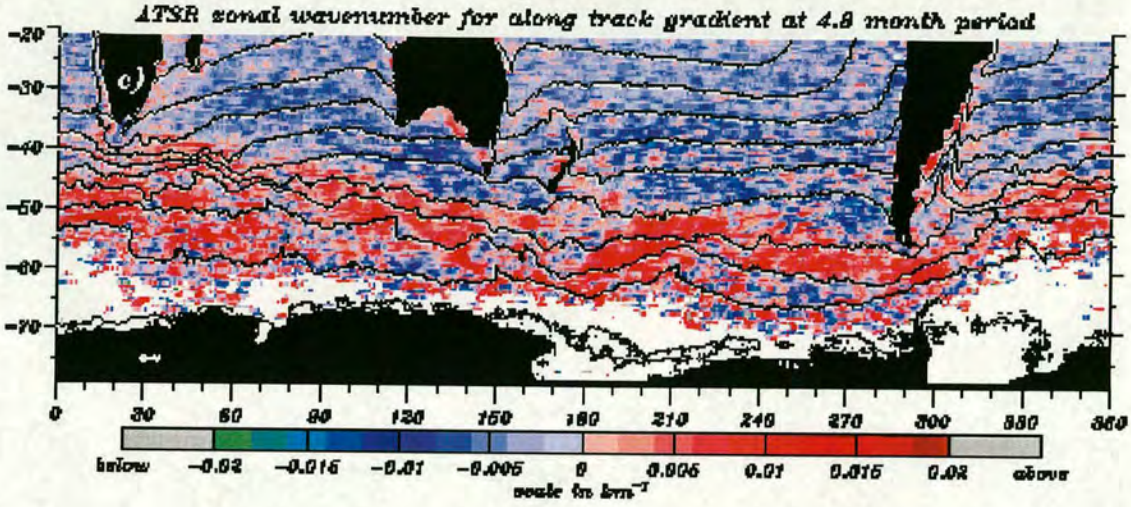

Figure 2.6: Figure from Hughes et al (1998) showing the zonal wavenumber at a period of 4.8 months, calculated from SST measurements from the ERS1 satellite. Contours of mean SST are superimposed with a contour interval of 3°C.

in section 2.1 (Chelton and Schlax, 1996). Particularly outside the tropics, observed phase speeds were found to be two or three times the theoretical values. This can be seen by taking the ratio of the observed and theoretical phase speeds from figure 2.5, and this is shown in the top part of figure 2.7. Killworth et al (1997, hereafter KCDS) has addressed this issue and presented arguments to explain these discrepancies. This section reviews the results of KCDS' work.

First the assumptions of linear theory were scrutinised to identify which might have broken down. Four possible discrepancies were identified, these being

1. the flow is not free but forced by wind and/or buoyancy;
2. the ocean has a varying depth;
3. the wave activity is nonlinear;
4. the background state of the ocean is not at rest.

The first of these was dismissed on grounds that the effect on wave propagation would not be consistent enough to result in a uniform overestimate of phase

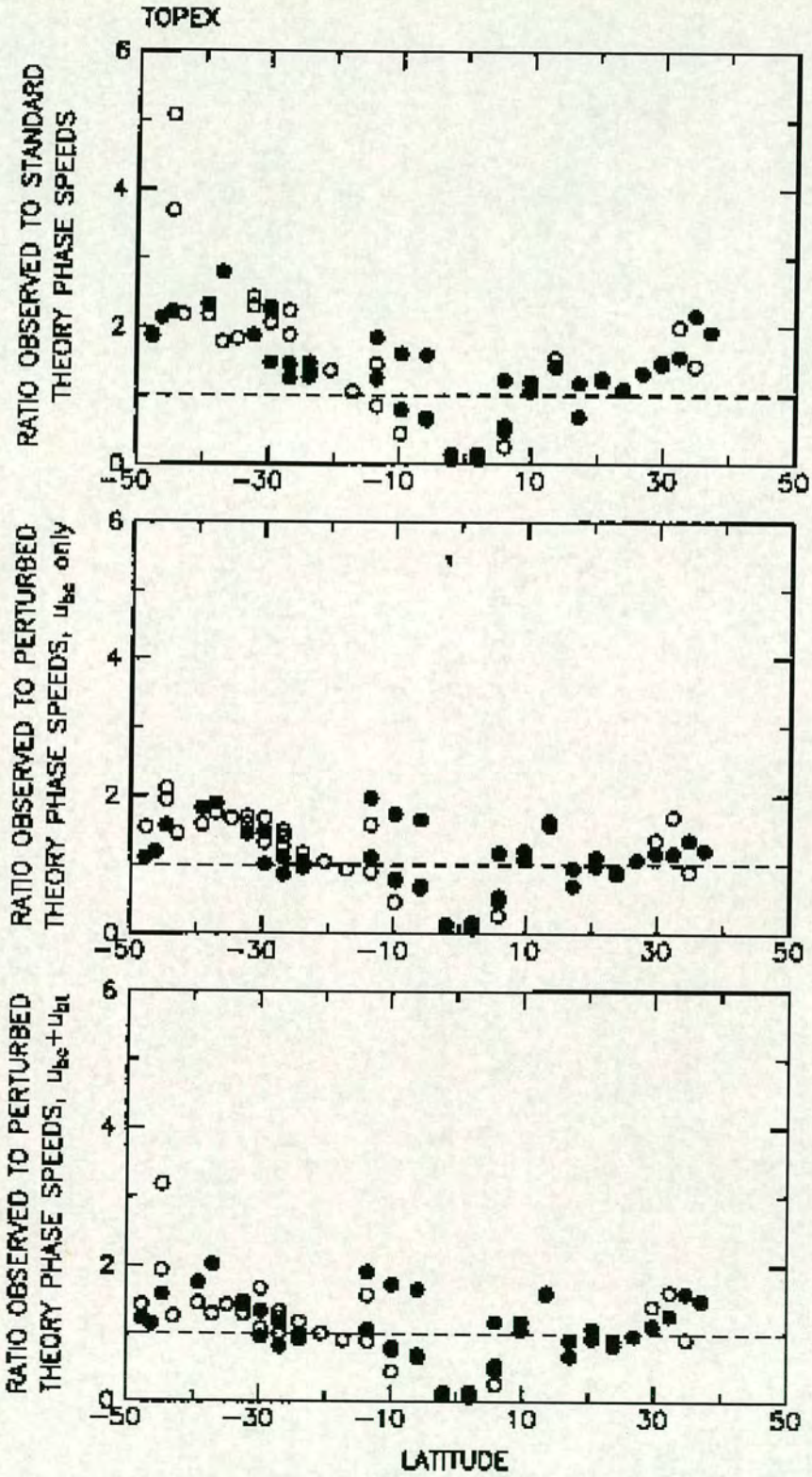

Figure 2.7: Figure from Killworth (1997) showing ratios of observed and theoretical Rossby wave phase speeds against latitude, as referred to in the text. Solid dots are from the Pacific and open dots are from the Atlantic and Indian oceans.

speeds. The effect of option 2 was thought unlikely to be systematic, but this is addressed in a separate study (Killworth, personal communication). This study will show that the effect of topography explains little of the discrepancy. It is possible that nonlinearity might have an effect, and this has been studied by Anderson and Killworth (1979) and, specifically for the ACC, by Clarke (1982). The nonlinearity was found to alter the local stratification, resulting in vertical structures that are not observed in the real ocean (Chelton et al, 1998). This left option 4 as a mechanism to be studied in greater detail. Since phase speeds are of the same order as mean flows, they could well be altered by them.

Propagation through generally orientated mean flows is very difficult to analyse and so the analysis was restricted to east-west baroclinic flows. In order to simplify the situation, only the long-wave problem was considered. Long waves are also less affected by critical layers (Killworth, 1979). KCDS set up the eigenvalue problem for waves in the presence of an east-west mean flow with vertical shear and a corresponding north-south density gradient. Approximate analytical solutions were obtained for the cases of small u, u of the same order as c, and u much larger than c. In the first case, the mode 1 phase speed was adjusted (either way) by an amount proportional to the mean flow. With the mean flow comparable to the mode 1 phase speed, adjustments were at least as large as the mode 1 speed, with the possibility (depending on signs and vertical structure) of increasing the westward phase speed or inducing a critical layer. In the final case, if the maximum westward mean flow is in the ocean interior, there is a mode whose phase velocity is approximately equal to the minimum value of the applied mean u field, increased westward by an additional amount depending on the strength of the mean flow.

The approximate results were tested numerically for cases of uniform stratification, exponential stratification and exponential $u(z)$ field. It was found that values of u_{min} several times c_1 were required before the westward phase speed doubled. This implied that the interaction with the baroclinic mean flow could account for some but not all of the observed increases in phase speeds.

The real ocean was studied for evidence of the wave-mean flow interaction mech-

anism by analysing temperature-salinity data of Levitus and Boyer (1994) and Levitus et al. (1994). Values of $N^2(z)$ and $u(z)$ were produced on a 1° grid at standard depths and east-west velocity deduced from in situ densities by the thermal wind relation, $fu_z = g\rho_y/\rho_0$. The baroclinic u field was then obtained by subtracting the vertical average of u.

The linear wave problem (with the background ocean at rest) and the problem with the calculated $u(z)$ field were solved in the same way, using a vertical finite-difference scheme for the eigenvalue problem. Results of the Rossby wave-speed were presented for the unperturbed case and the case with applied baroclinic u field. With a baroclinic u field there is more structure than in the unperturbed case, where lines of constant c are largely zonal. Also, in the sub-tropics c is 10 to 30% larger in the baroclinic case. These results confirmed the numerical results, showing that the presence of a baroclinic flow field can account for much of the difference between observed and theoretical Rossby wave speeds. The ratio of observed phase speeds and those from the theory modified by baroclinic flow are shown in the middle part of figure 2.7. This shows a definite improvement to the original ratios (top part of the figure), but the observed values are still too large outside the tropics by up to a factor of two.

A final section looked at the inclusion of a barotropic as well as baroclinic flow. The barotropic flow field was taken from the OCCAM model (Gwilliam et al., 1997) output as the barotropic flow is not well known from observations. The results show that barotropic flow generally has a small and mixed effect on Rossby wave speeds, with a slight improvement in the South Atlantic and Indian oceans between 30° and 40°S. These results can be seen in the ratios of observed to theoretical phase speeds for this case, given in the bottom part of figure 2.7.

The conclusion of this work was that observed phase speeds are faster than theory suggests mostly due to the mode 2 east-west velocity (eastward at the surface and changing sign twice in the vertical, i.e. eastward-westward-eastward). The mode 1 velocity (eastward over westward) was found to have very little effect. It was considered this to be an essential mechanism in the theory of Rossby wave propagation, though not the only additional mechanism to be involved. The

results were obtained for zonal propagation and were found to change very little for propagation at angles $\pm 10°$ north or south. A three dimensional study would be necessary to confirm these results for general propagation.

2.5 Summary

This chapter has looked at a selection of previous work relating to the theory and observations of Rossby waves, particularly in the ocean. Section 2.1 gave an introduction to the theory of Rossby waves and showed the derivation of the Rossby wave dispersion relation. Section 2.2 described some numerical studies of Rossby waves propagating in the presence of mean flows. This included a section on Rossby wave critical layers, and a section on the idea of waveguides for Rossby waves. Section 2.3 summarised previous observational studies of Rossby waves in the ocean, focusing on observations from satellite altimeters. The phase speeds of the observed Rossby waves were shown to differ from values predicted by linear theory. A final section (2.4) reviewed some recent theory which begins to explain this discrepancy between theory and reality. The work reviewed in the chapter forms a basis for, and a means of comparison with, the research undertaken in this thesis. This is especially the case with the previous observational studies described in section 2.3.

Chapter 3

Analysis of FRAM output

This chapter describes the use of FRAM output to study Rossby wave and eddy activity in the model Southern Ocean. The benefit of model output is that wave activity can be compared with the true surface currents fields. It is also free from the errors and sparsity of observations in the real ocean. The disadvantage is the difference from reality due to simplification of the system. The aim of the chapter is to develop techniques which can subsequently be applied to the altimeter data, where true surface current fields are not known. If relationships between wave activity and mean currents can be established in the model output, for example, then it is likely they will also apply to the real ocean. The purpose of the analysis is not to fully investigate the dynamics of FRAM, but to study relevant quantities in the model to set a foundation for analysis of the real ocean.

The chapter contains a description of the FRAM model in section 3.1 and then three sections of output analysis. Section 3.2 describes a study of the frequency of wave activity in FRAM. Section 3.3 looks at the phase speeds of Rossby wave propagation and section 3.4 studies the total eddy activity. A final section summarises the results and draws conclusions.

3.1 Description of FRAM

The Fine Resolution Antarctic Model (FRAM) is a model of the ocean south of 24°S, developed for an NERC Community Research Project as part of the UK

contribution to the World Ocean Circulation Experiment (WOCE). FRAM is eddy resolving and has a resolution of 1/4° in latitude by 1/2° in longitude, giving equal spatial resolution at 60°S. There are 32 levels in the vertical. The code is based on the Bryan/Cox/Semtner code (Cox, 1984) for solving the primitive equations of oceanography.

FRAM was run for an equivalent of 16 years. Initially in a uniform state, the model was spun up by relaxing the temperature and salinity to climatological data from Levitus (1982) and imposing annual mean fields of surface wind stress from Hellerman and Rosenstein (1983). After six model years the relaxation to Levitus was stopped in all but the surface layer, and the winds were changed to climatological monthly values, also from Hellerman and Rosenstein (1983).

FRAM employs the rigid lid approximation. This means that the barotropic mode is solved using a vorticity representation which allows the model to be integrated without the need to calculate absolute pressures. The surface pressure fields must therefore be calculated diagnostically, after the model run. This was done by Simon Thompson of the former Institute of Oceanographic Sciences, Deacon Laboratory, Surrey, UK, who kindly provided 72 months of sea surface pressure fields from the last six years of model output. The mean geostrophic zonal flow at the surface for these last 72 months of FRAM output is shown in figure 3.1. This is included here for reference and gives a good impression of the ACC with its structure of eastward jets and regions of reverse flow.

Although FRAM output has many differences from the real ocean (Stevens and Killworth, 1992) it provides a dynamically consistent data set which enables wave information to be compared directly with the surface current fields.

3.2 Spatial correlations in frequency

This section describes a study of the frequency distribution in FRAM output in order to identify regions associated with specific periods of Rossby wave activity. This is to establish areas of the domain suitable for the more detailed analysis presented in subsequent sections. The study is split into two sections. First, the

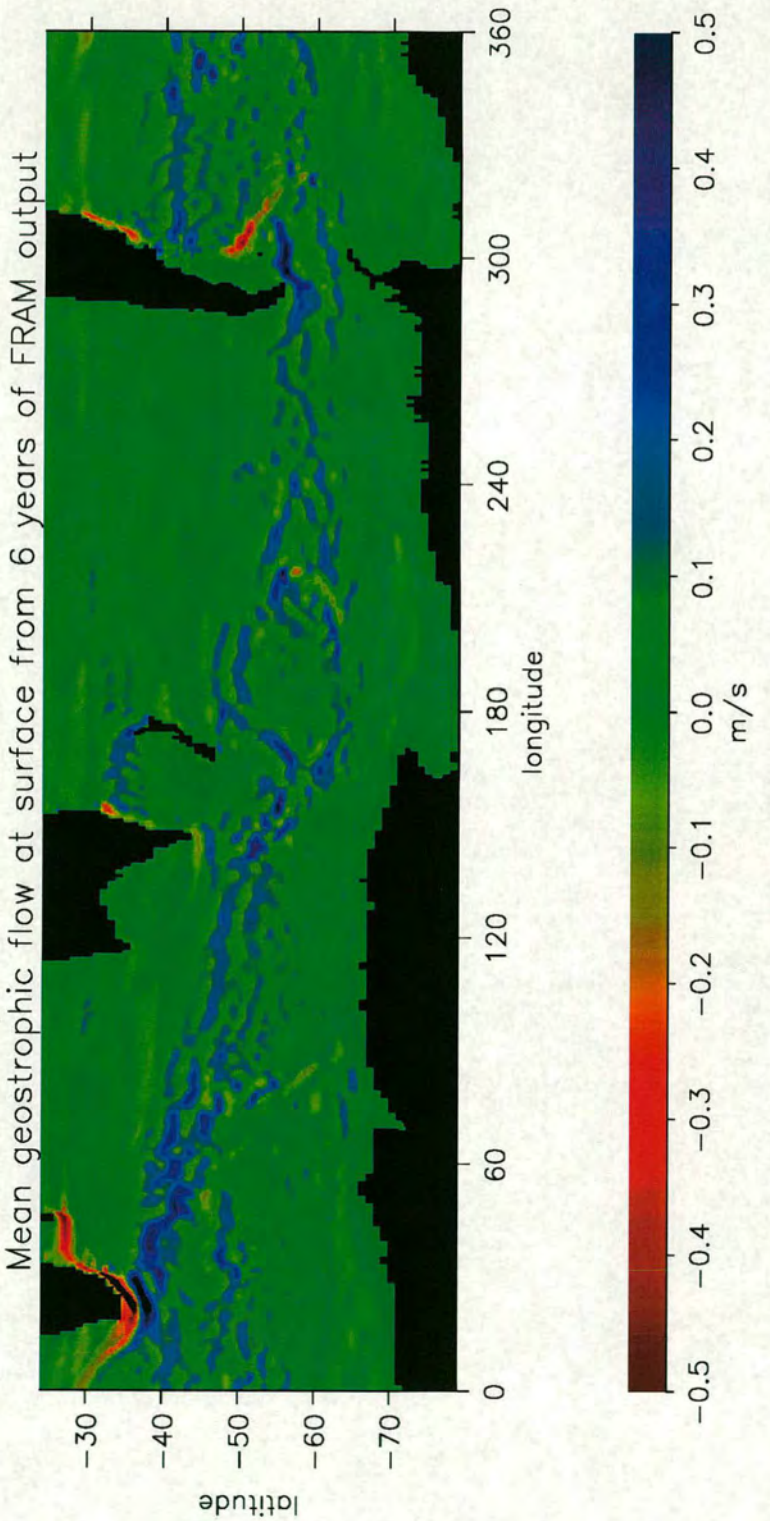

Figure 3.1: Mean geostrophic zonal current at the surface, from the last six years of FRAM output

power spectrum for the wave activity is calculated. After looking the total power, spatial fields of normalised power are presented. Then, principal components analysis is introduced in order to study the spatial structure of the wave activity in more detail. The specific aim of this latter work is to identify waveguides of Rossby waves.

3.2.1 Power spectrum analysis

Output processing

The 72 months of FRAM surface pressure fields were converted to separate datasets of zonal and meridional gradients of SSH (dh/dx and dh/dy respectively). The mean of the data was subtracted to give the monthly anomalies of SSH gradient. The zonal gradient of SSH (dh/dx) was used in this analysis as the best representative of the wave activity independent of the predominantly zonal flow. The time series of dh/dx at each gridpoint was converted by fast fourier transform (FFT) to give a periodogram containing 35 frequency components (and a steady state component of zero). These components and the associated frequencies and periods are given for reference in table 3.1. Each periodogram was smoothed over three frequency components to improve discretisation errors and so give an estimate of the power spectrum.

Total wave power

The total power due to fluctuations of dh/dx is shown in figure 3.2. This is equivalent to the sum of the power spectrum at each gridpoint. The first thing to note is the very large amplitude just South of Africa, in the Agulhas region. Here the maximum amplitude is about 18 (off scale), which is several times greater than other high power regions such as downstream from the Agulhas, east and southeast of Australia, and east of South America. Despite the small area of the Agulhas compared to the whole Southern Ocean, it has a major influence on the mean power spectrum. This is shown in figure 3.3 (left), which shows the total proportion of power at each period from the variability of dh/dx. The

Component	0	1	2	3	4	5	6	7	8
Frequency	-	0.01	0.03	0.04	0.06	0.07	0.09	0.10	0.11
Period	-	70.0	35.0	23.3	17.5	14.0	11.7	10.0	8.8
Component	9	10	11	12	13	14	15	16	17
Frequency	0.13	0.14	0.16	0.17	0.19	0.20	0.21	0.23	0.24
Period	7.8	7.0	6.4	5.8	5.4	5.0	4.7	4.4	4.1
Component	18	19	20	21	22	23	24	25	26
Frequency	0.26	0.27	0.29	0.30	0.31	0.33	0.34	0.36	0.37
Period	3.9	3.7	3.5	3.3	3.2	3.0	2.9	2.8	2.7
Component	27	28	29	30	31	32	33	34	35
Frequency	0.39	0.40	0.41	0.43	0.44	0.46	0.47	0.49	0.50
Period	2.6	2.5	2.4	2.3	2.3	2.2	2.1	2.1	2.0

Table 3.1: Frequency in months^{-1} and period in months for components of the FRAM power spectrum

major peak at a period of 4.1 months is due to the Agulhas region. The extra power here amounts to about 10% of the power from the variability of dh/dx in FRAM. A smaller peak centred at a period of 11.7 months is due to the annually repeating wind forcing in FRAM. The overall shape of the mean power spectrum shows decreasing power as the period decreases. This is known as a "red" spectrum, which is typical of the oceans. The standard deviation associated with the mean spectrum is shown with the mean in the right hand graph of figure 3.3. This is larger than the mean by a factor of at least three, indicating the vast spatial variability of the power spectra. At the Agulhas period, 4.1 months, the standard deviation is about 13 times the mean. Though this region is small, the power values there are typically over 1000 times the mean, giving rise to such a large standard deviation. It is clear there would be problems in studying the spatial structure of wave activity using these spectra. In order to eliminate problems of the domination of the Agulhas region, the spectrum at each gridpoint will be normalised to show the fraction of power at each period. This will simplify the problem to a spatial study of waves of different periods, independent of amplitudes.

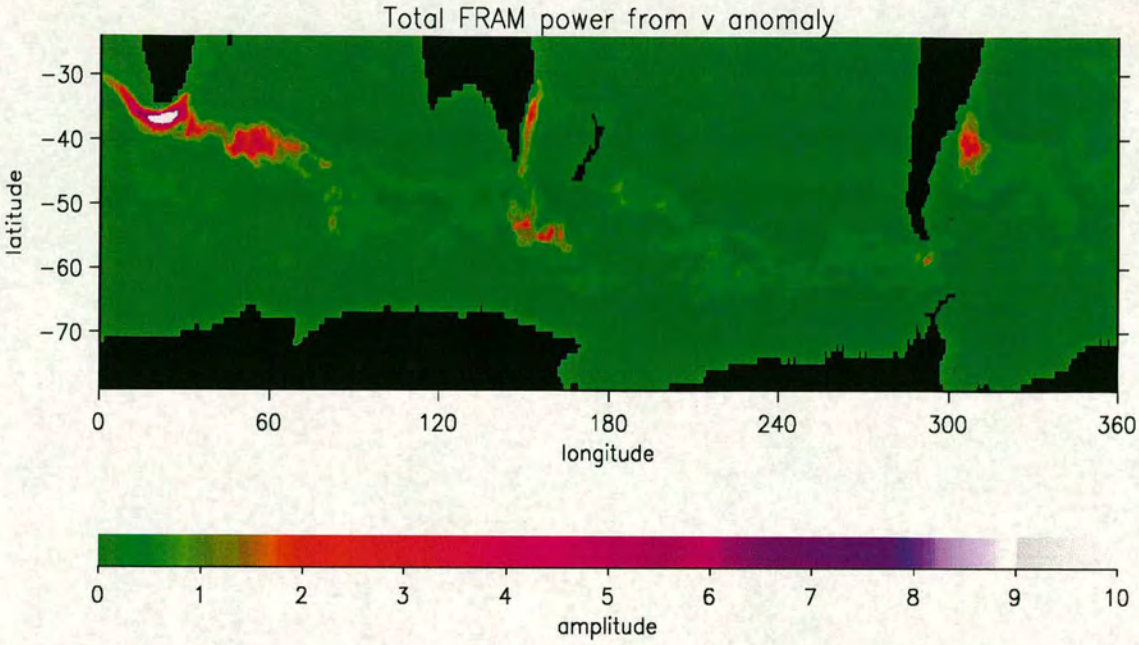

Figure 3.2: Total power from the variation of dh/dx in the last six years of FRAM output.

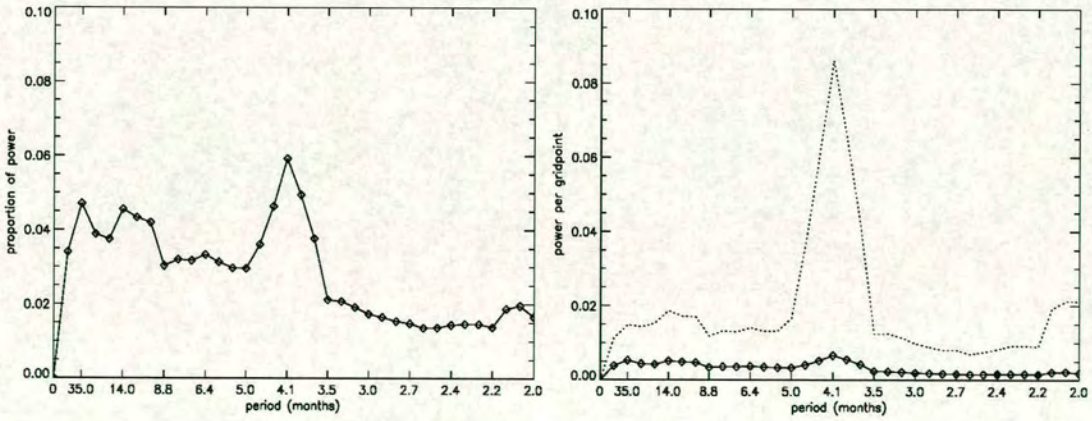

Figure 3.3: Average proportion of total power at each period from the variability of dh/dx (left), and the same average power spectrum and associated standard deviation with units equivalent to figure 3.2 (right).

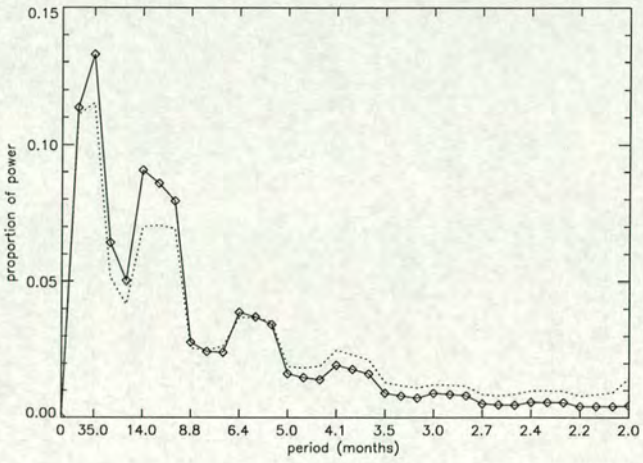

Figure 3.4: Mean normalised spectrum from FRAM

Normalised wave power

The spectrum at each gridpoint was normalised by dividing by its total, such that the sum of the normalised power over all frequency components became unity at all locations. The normalised power spectra, which show the fraction of power at each period, were then averaged over the field to give a field-mean, normalised power spectrum. This mean power spectrum is shown in figure 3.4 (solid line) and represents the mean shape of the power spectrum. The standard deviation (dotted line) has an amplitude varying from a similar magnitude to the mean at long periods, to over twice the mean at the shortest periods. This shows there is very large spatial variability in the spectrum shape, and this mean spectrum will not be representative of the spectrum at any particular place. The overall shape of this mean spectrum is consistent with the expected red spectrum, but there are definite peaks at regular intervals, with amplitudes increasing with wave period. The reason for the regularity of this wave-like superposition on a smooth red spectrum is not clear, but it will be seen that different peaks result from the contributions of different regions in the ocean.

Figures 3.5 and 3.6 show spatial fields for individual components of the normalised power spectra, corresponding to wave activity at specific periods. The results are presented for the 70 month period, approximate annual period (11.7 months) and

at two Rossby wave periods (4.4, and 3.0 months). These periods are chosen as a representative sample of the results and for comparison with results presented in later sections. The figures are presented using the same amplitude range for spatial comparison within a period. The relative amplitude of different periods is indicated by figure 3.4. The figures contain only frequency information, and further analysis is required to establish whether this corresponds to Rossby wave propagation. However, it is anticipated that regions of strong propagation will show a higher fraction of power at Rossby wave periods compared to elsewhere.

The field for the period of 70 months shows that the fractional power at the longest period is greatest to the south of the domain, mainly south of the expected path of the ACC. These regions are low power (cf figure 3.2). This period is not interesting in terms of Rossby waves, but the result will be used for comparison in the next section. At a period of 11.7 months a very different spatial structure is observed. The transition in spatial structure between periods of 70 and 11.7 months is not smooth. There is a sharp change to the spatial structure whenever there is a step in the mean normalised spectrum (figure 3.4), such as between periods of 35 months and 23.3 months, and between periods of 17.5 and 14 months. This shows that different peaks in the mean normalised spectrum are due to regional differences in the spectrum shape.

For the period of 11.7 months the fractional power is greatest to the north of the domain, particularly in the Pacific sector, and in some regions very close to Antarctica. These are also regions of low total power, and relate to the annual cycle in the monthly winds and Levitus data used to force the FRAM model. There will be some regions associated with long period Rossby wave propagation, but this is difficult to distinguish from the annual cycle. The FRAM model does not include ice, so the region of low fractional power to the South is due to the lack of annual variability in winds and climatology at those latitudes. The other main area of low fractional power at this annual period is the Agulhas region. Agulhas eddies are very large and their annual variation is insignificant compared to variation at the eddy periods. There is strong anti-correlation between the fields for the period of 11.7 months and the period of 70 months. Individual normalised spectra from low power regions tend either have a strong peak at the

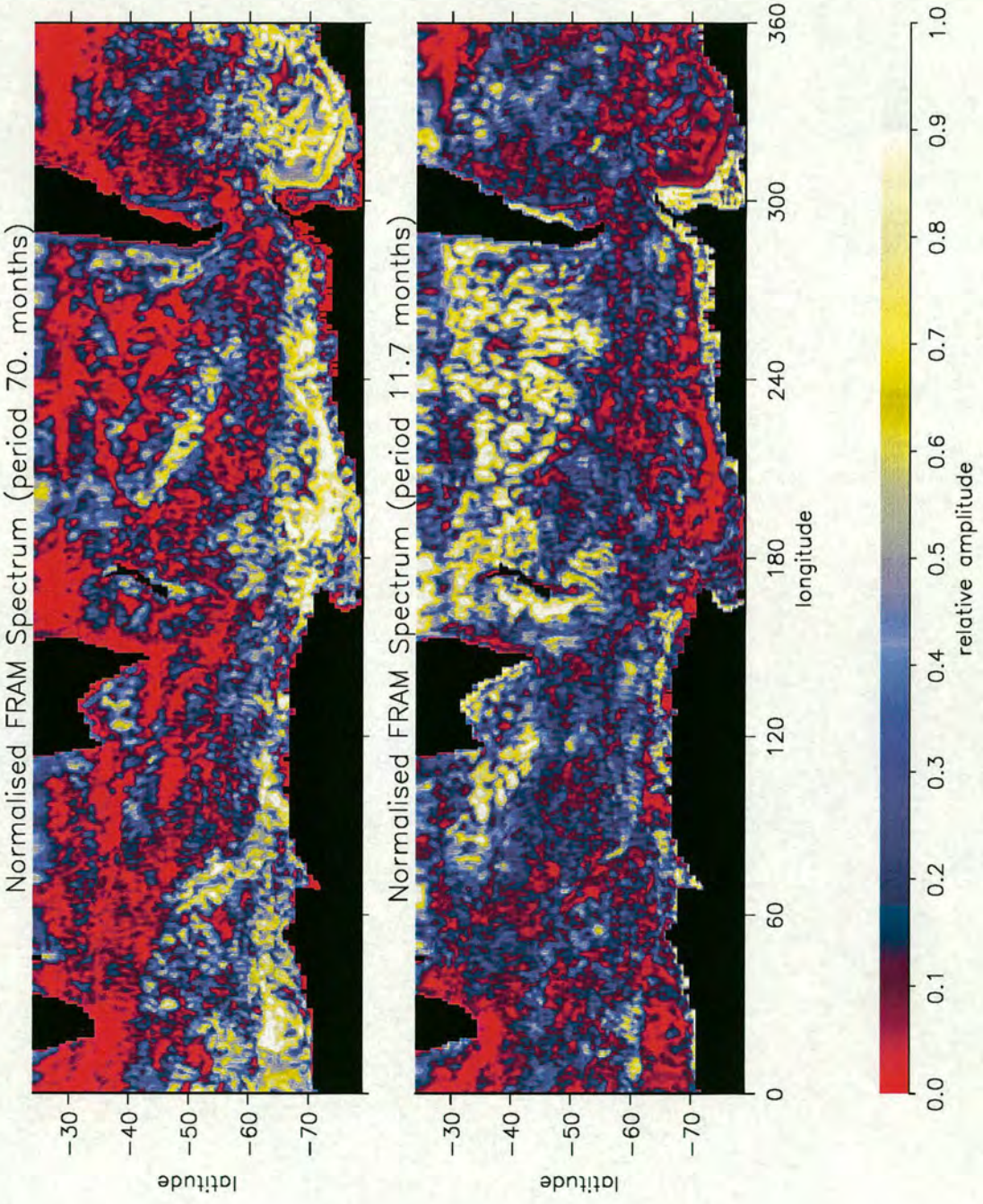

Figure 3.5: Spatial fields of the spectral power for periods of 70 months (top) and 11.7 months (bottom).

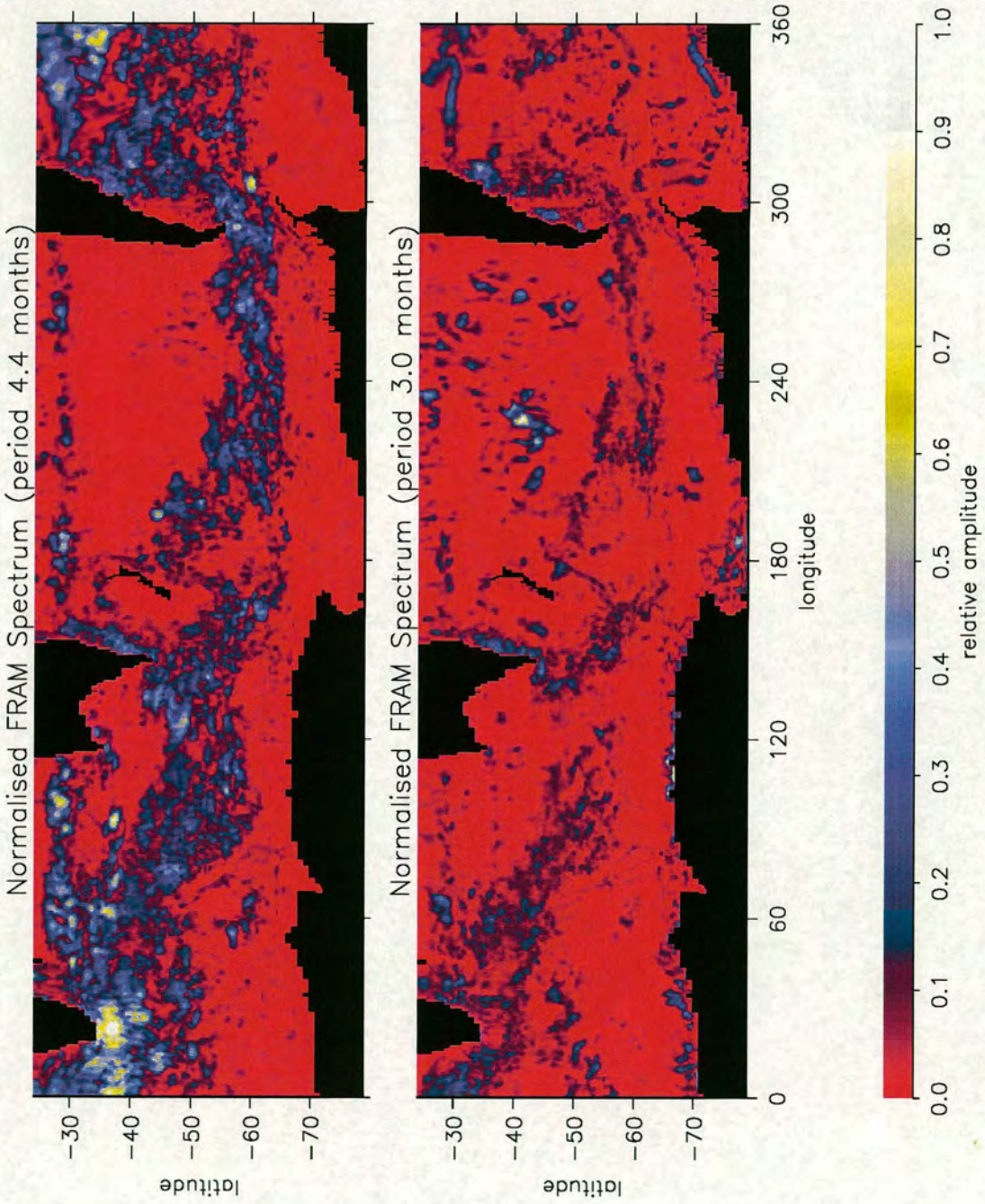

Figure 3.6: Spatial fields of the spectral power for periods of 4.4 months (top) and 3.0 months (bottom).

longest periods or at the annual period, but not both.

The periods of 4.4 and 3.0 months are typical Rossby wave periods. At a period of 4.4 months (top of figure 3.6), the highest fractional power is generally confined to regions associated with the ACC (see figure 3.1), where the strong eastward currents are likely to be advecting westward propagating Rossby waves eastwards. There are some high amplitude regions outside the band of the ACC, particularly to the north of the domain, and these could indicate regions of westward propagation. This period is close to the prominent period of Agulhas eddies (4.1 months), and the Agulhas region stands out in the spatial field. At a period of 3.0 months (bottom of figure 3.6), the highest fractional power is associated with the ACC and in regions elsewhere, generally on small scales. Again, the spatial structure is likely to be due to a combination of eastward advection of Rossby waves in the ACC and westward propagation outside. The reduced amount of high amplitude regions as the period gets lower is a reflection of the relative power, shown in the mean power spectrum (figure 3.4).

The fields comparing fractional power highlight areas associated with activity at different wave periods, and these areas would be suitable for more detailed analysis of Rossby wave propagation. In general, however, the fields are messy, and the existence of specific waveguides at Rossby wave periods is not obvious. A major reason for looking at the normalised power is to provide a foundation for the principal components analysis described below.

3.2.2 Principal components analysis

A sophisticated approach to studying the information associated with spatial variations in the normalised power is to use principal components analysis, also known as empirical orthogonal function (EOF) analysis. This will break down the total spectral variation into a set of spectral patterns, known as principal components, each with a certain significance to the total variation. Each of these spectral patterns has an associated spatial field which shows the contribution of different regions to that pattern. It will be seen that the number of spectral patterns equals the number of frequency components, and only the most significant

few patterns are required to describe the majority of the total variation in the normalised power. The analysis is quite involved, but it will provide a clearer indication of the wave activity at different periods than was seen in figure 3.6, and some useful results on the way.

Motivation for analysis

The main aim of this work is to identify waveguides of Rossby waves, which will hopefully relate to jets in the mean flow. The reasoning behind this begins with the basic Rossby wave dispersion relation (equation 2.11) but without zonal flow ($\overline{u} = 0$). The associated relationship between frequency, ω, and zonal wavenumber, k, was shown in figure 2.2. The relationship has a maximum frequency which depends on β, and hence depends on latitude. Near the equator the majority of Rossby wave frequencies are able to propagate, whereas near the pole only lower frequencies will propagate. If there is a broad band forcing such that waves of all frequencies are expected to be found, the normalised spectrum at a point would show a drop in amplitude at a cutoff frequency which depends on latitude. The expected normalised spectrum might look like this:

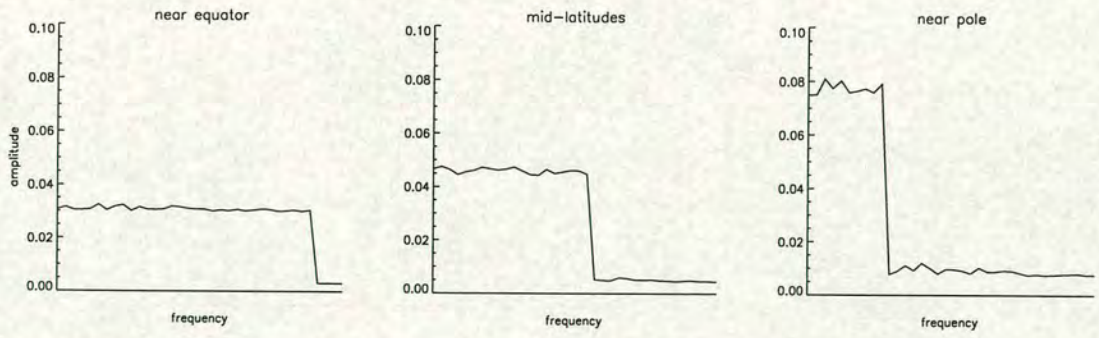

The nature of the EOF analysis is such that the first EOF would identify this spatial variation, and show a pattern of less energy at high frequencies and more energy at low frequencies. The amplitude of this EOF would depend on latitude. This represents a kind of equatorial waveguide with high frequency waves trapped near the equator.

Similarly, on a smaller scale, if eastward jets in the ACC are acting as waveguides,

then it is expected that high frequency waves would be trapped at the centre of jets, because of the modification of the dispersion relation to include effective β ($\beta_e = \beta - \overline{u}_{yy}$). This should result in a similar EOF structure to that for the equatorial waveguide, but with an amplitude depending on distance from the centre of the jet. With the ACC having such an influence in the Southern Ocean, and with the mean normalised spectrum (figure 3.4) suggesting a very different structure to the ideal broadband response illustrated above, this is a certainly simplification. Nonetheless, the idea provides motivation for the EOF analysis described below.

The EOF procedure

EOF calculations are usually performed in the time or space domain. This method applies the same technique in the frequency domain. The starting point for an EOF calculation is a covariance matrix. For a field of N gridpoints and a time series of P fields, the temporal covariance matrix is defined by

$$C^T_{k,l} = \frac{1}{N}\sum_{i=1}^{N}(H_k H_l)_i \tag{3.1}$$

where C^T is the matrix of size $P \times P$, i is the gridpoint number, k and l are different times and H is the anomaly of the quantity being analysed. At each gridpoint, the mean of the time-series of H must be zero.

In the frequency domain, the power spectrum of the time series is taken, as calculated for section 3.2.1, and the time indices, k and l, are substituted for frequency indices, f and g. The anomaly H is substituted for the anomaly of the normalised power spectrum, A. The covariance matrix becomes

$$C^F_{f,g} = \frac{1}{N}\sum_{i=1}^{N}(A_f A_g)_i \tag{3.2}$$

where C^F is now of size $(P/2 \times P/2)$. For each gridpoint, the anomaly spectrum, A_i, was calculated by subtracting the field-mean, normalised power spectrum (figure 3.4) from the normalised spectrum at that gridpoint. For a particular

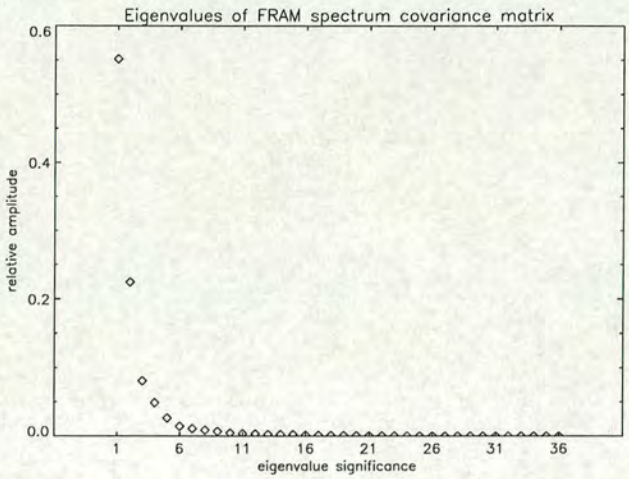

Figure 3.7: Eigenvalues of the covariance matrix of the FRAM spectrum field.

gridpoint, this emphasises frequencies which have more (positive anomaly) or less (negative anomaly) fractional power than the mean.

The covariance matrix, C^F, was calculated at a gridpoint by multiplying each component of A_i by every other component. This matrix (which is of size 36×36) was summed for the whole field, and divided by the number of gridpoints to give a field-mean covariance matrix of the amplitude anomalies of the normalised power spectrum. The largest values of this symmetrical matrix lie along the diagonal which represents the products of anomalies at a frequency with themselves (i.e. the variance).

The eigenvalues and corresponding eigenvectors of this matrix were found. Each eigenvector represents an EOF and looks like a power spectrum, having values at each frequency component which indicate spatial variation of the fractional power at that component. The relative magnitude of the corresponding eigenvalues indicates the hierarchy of the EOFs and their proportion of relevance to the total spatial variation of the fractional power. These eigenvalues are shown in figure 3.7. This shows that most of the spatial variation is accounted for by the first few EOFs, for example the first six EOFs represent almost 95% of the total variation.

EOF results

Figure 3.8 shows the most significant six EOFs, corresponding to the first six eigenvalues. The eigenvector calculation results in EOFs with a value at each frequency component and a mean of zero. The overall sign of the EOFs is arbitrary and it is the deviation from zero which is important. The relative sign, both within an EOF and between EOFs, is important for the spatial fields presented in the next two subsections.

The dominant EOF, EOF 1, represents 55% of the total variation (see eigenvalue 1 in figure 3.7). The main peaks in the EOF show that the principal pattern of spatial variation is due to regions with more fractional power at the longest periods and less fractional power at the annual periods (and shorter periods to a lesser extent), and other regions with less fractional power at the longest periods and more fractional power at the annual periods. This will become clearer when the spatial patterns associated with the individual EOFs are presented in the next subsection. EOF2 accounts for about 22% of the total variation and is the dominant EOF for the remaining 45% of variation not accounted for by EOF 1. EOF 2 represents a spatial pattern where there are regions of more (or less) fractional power at the annual and longest periods, and less (or more) fractional power at periods of 8.8 months and below. EOF3 accounts 8% of the total variation. EOF 3 has a more complicated structure than the first two EOFs, but mainly shows regional differences in variations at the approximately biennial period which are balanced by variations at periods around 5.8 months. EOF 4 represents 5% of the total activity and shows regional differences due to the fractional power at periods 5.3 to 6.4 months and 23.3 months, balanced by variation at periods less than 5.0 months. The significance of individual EOFs 5 and more is becoming small (less than 3% of the total variation). EOFs 5 and 6 are shown here, however, as they are included in results showing the spatial field for a sum of EOFs (figure 3.12).

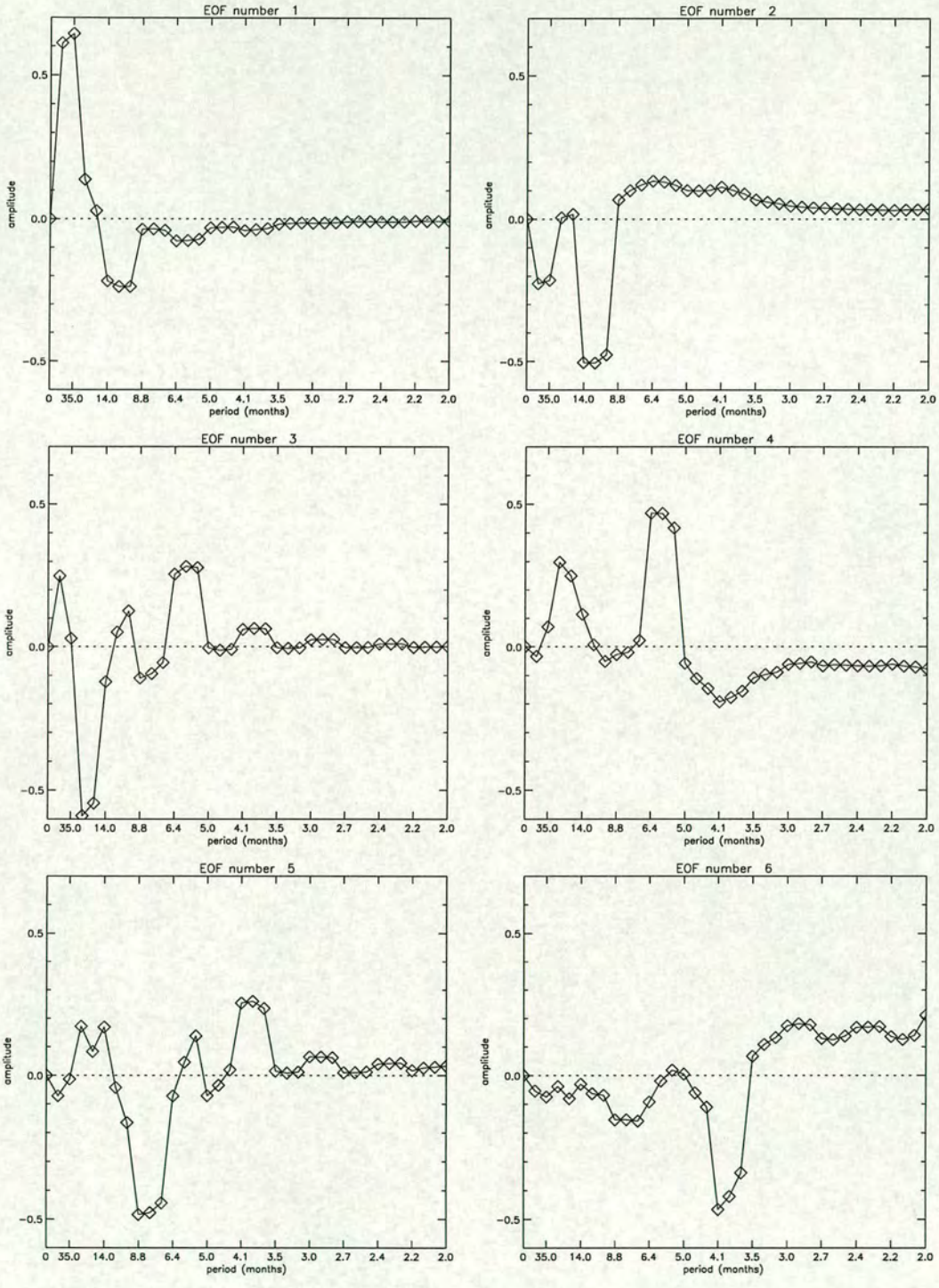

Figure 3.8: The dominant EOFs of the FRAM spectrum field. The proportion of relevance to the total is approximately (top left to bottom right) 55%, 22%, 8%, 5%, 2% and 1%.

Spatial fields - individual EOFs

Spatial fields for each EOF are calculated by summing the product of the EOF spectrum (eigenvector) and the fractional power anomaly (as used to calculate C^F) at each gridpoint, i.e. a vector dot product. This has the effect of emphasising points (either as positive or negative) where the fractional power anomaly has a similar shape to the EOF (particularly in terms of the major peaks). The spatial field for an EOF is projected for a single frequency by multiplying the field by the value of the EOF spectrum at that frequency. The resulting field shows the spatial structure associated with the variation captured by the EOF, and will just vary in amplitude according to the frequency used for projection. The total of the values over the whole field for an EOF is zero. The sum of individual spatial fields for the most significant EOFs can also be projected for a particular frequency to give a filtered field of deviation from the mean, normalised power spectrum. For example, high value regions at the annual frequency in such a field show places where the annual cycle is more significant than elsewhere in the field. These cumulative EOF results are presented in the next subsection.

Figures 3.9 and 3.10 show the individual spatial fields for the first four EOFs. Positive and negative regions depend on the shape of the fractional power anomaly at a gridpoint compared to the EOF. A sign convention is used such that a hypothetical gridpoint where the fractional power anomaly has the same shape as the EOF (as shown in figure 3.8) is positive. The spatial field for EOF 1 shows the structure of the principal spatial variation in fractional power (which is due to activity at the longest and annual periods - see EOF 1). Positive regions indicate high fractional power at the longest periods (compared to the rest of the field), and negative regions indicate high fractional power at the annual periods (compared to the rest of the field). This is best illustrated by taking an example of the fractional power at two separate gridpoints from strong positive and negative regions.

The lefthand graph of figure 3.11 shows the fractional power (dashed line) and fractional power anomaly (solid line) at 74°S, 195°E, where the field for EOF 1 is strongly positive (blue). The difference between these two curves is the mean,

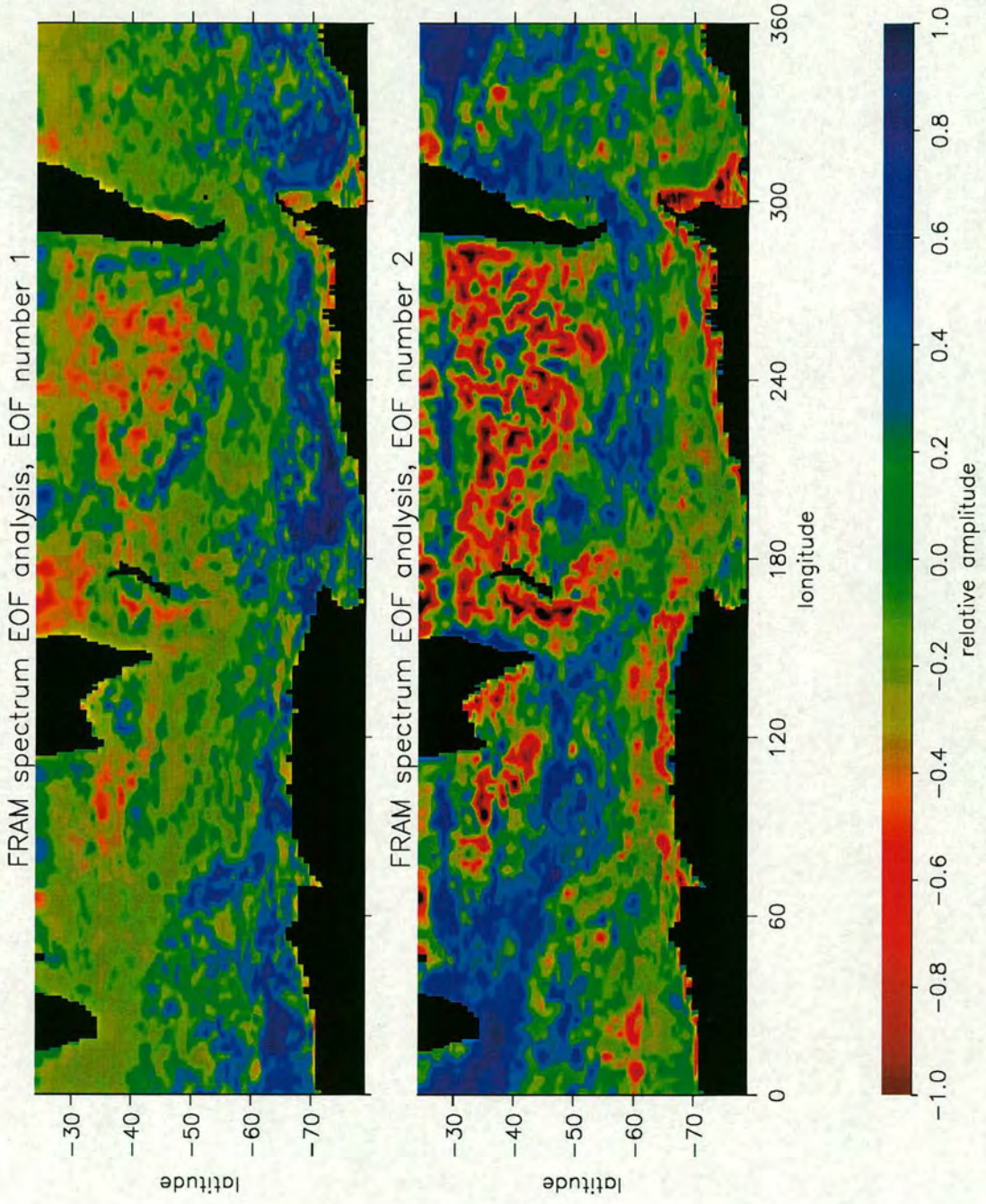

Figure 3.9: Spatial fields for individual EOFs 1 and 2

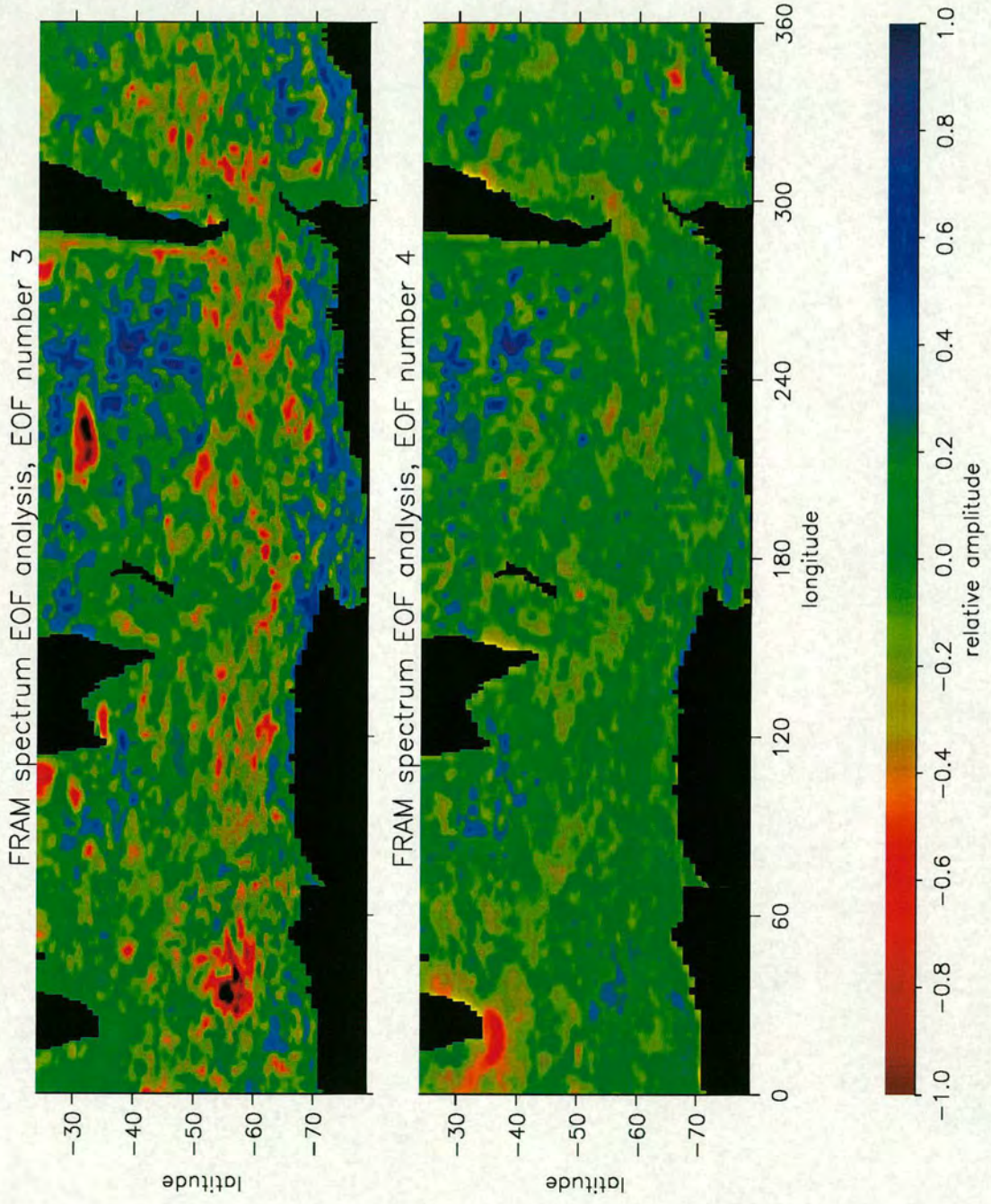

Figure 3.10: Spatial fields for individual EOFs 3 and 4

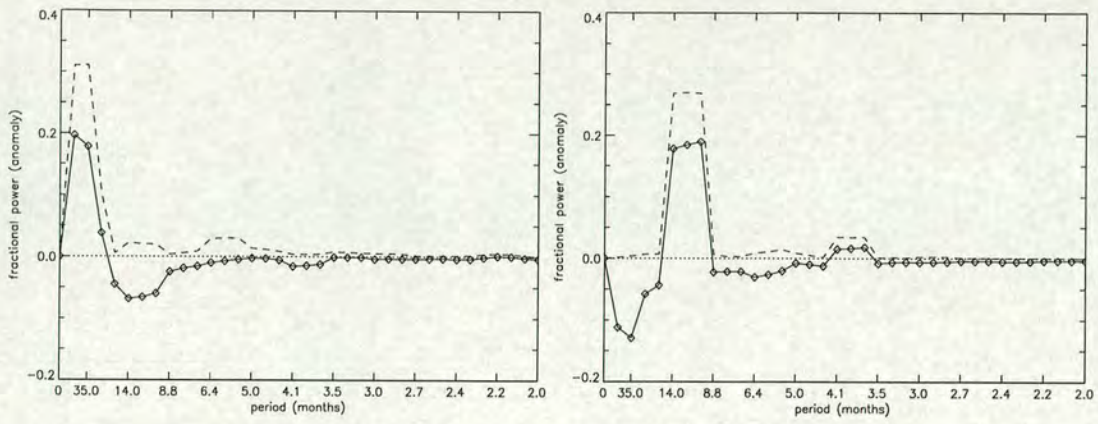

Figure 3.11: Samples of normalised spectra (dashed line) and normalised spectra anomaly (solid line) at 74°S, 195°E (lefthand graph), and at 26°S, 165°E (righthand graph).

normalised power spectrum (figure 3.4). At this location, over 60% of the power is at the longest periods of 35 and 70 months. There is a large positive fractional power anomaly at these periods and a corresponding negative fractional power anomaly at the annual periods. Because this is also the form of EOF 1, this region of the spatial field is strongly positive. At 26°S, 165°E (righthand graph), about 80% of the power is at the annual periods. This gives positive fractional power anomaly at those periods and a corresponding negative fractional power anomaly at longest periods. This is opposite in sign to the form of EOF 1 and so this region is negative (red). Because the positive and negative regions relate to the longest and annual periods respectively, they compare well to the respective fields of fractional power at those periods (figure 3.5). The longest periods are dominant to the South and the annual periods stand out to the North, particularly in the Pacific region.

In EOF 2, the strongest peak is negative and at the annual periods. There is a secondary negative peak at the longest periods, and all periods of 8.8 months and below are positive. This means that negative regions of the spatial field show where there is positive fractional power anomaly at the annual and longest periods. More importantly (since these longer periods featured strongly in EOF 1), positive regions show positive fractional power at periods which are expected

to represent Rossby waves. These regions lie mainly within the ACC (comparing with figure 3.1), and also in other small regions, particularly in a band at 30°S. The Rossby wave activity could be eastward or westward propagating, and is likely to be the former when waves are advected eastwards by the strong flows of the ACC. Periods of 8.8 months and below hardly featured in EOF 1. This shows that Rossby wave activity accounts for less than half of the spatial variation in fractional power. In terms of the total power, however, we have already seen that the Rossby waves and the Agulhas eddy activity are the largest contributors (figures 3.2 and 3.3).

The field for EOF 3 is determined mainly by the negative peak in the EOF at periods 17.5 and 23.3 months, and the positive peak at periods 5.3 to 6.4 months. Of major note in this spatial field is the two strong negative regions at 55°S, 30°E and at 32°S, 220°E. These regions represent high fractional power anomaly at periods 17.5 and 23.3 months, and were not prominent in the spatial field for the first two EOFs. Both regions are outside the ACC (figure 3.1) and could therefore represent long period Rossby waves propagating westwards. For the south Pacific region, there is no obvious association with topography (figure 1.3), but the region South of Africa coincides with a deep part surrounded by shallower water to the West, North and East. The surface temperature contours also dip to the South around this deep feature, suggesting some topography related dynamics here. Further analysis of these two regions is beyond the scope of this thesis, except to say that activity at these periods is not related to wind forcing, which repeats annually.

In the field for EOF 4, positive regions are dominated by the period of 5.8 months (positive peak in the EOF), with a secondary peak at a period of 17.5 months with the same sign. The Agulhas region is negative due both to its lack of fractional power at long periods and the negative values in EOF 4 at Agulhas periods (around 4.1 months). Other negative regions are likely to be related to periods of 5.0 months and below. EOF 4 only represents 5% of the total activity and so fields for subsequent EOFs start to become insignificant. There is notably less spatial variation in the fields for EOFs 3 and 4 than in the fields for EOFs 1 and 2. To summarise this subsection, the spatial fields for individual

EOFs have demonstrated the structure of spatial variation in the fractional power. The majority of this spatial variation is due to annual and long period activity, which dominate EOF 1. The Rossby wave activity, which is of most interest to this study, appears mainly in EOF 2, which represents 22% of the variation in fractional power. Rossby waves also have significant influence in higher EOFs, but these contribute less to the total variation. The next subsection uses the individual spatial fields to reconstruct fields relating to activity at a single period.

Spatial fields - cumulative EOFs

The smoothed EOF reconstruction of the power spectrum anomaly field is shown for periods of 4.4 and 3.0 months in figure 3.12. These are generated by adding the spatial fields at a particular period for the dominant six EOFs. The result is a field highlighting significant fractional power at a period, indicated as positive (blue). Yellow and red regions show where fractional power at that period is significantly less than average for the field. The fields can be related to the equivalent fields of fractional power (figure 3.6) but are less noisy, and have fewer, but more prominent, features. If all EOFs were used in these reconstructions, the fields would be equivalent to subtracting the average fractional power at the relevant period from the spatial field of fractional power (figure 3.6). Using just six EOFs gives the most important information relating to spatial variation at a period, so acts as a sort of filter. The first six EOFs capture 95% of the total spatial variation in fractional power (from the eigenvalues in figure 3.7). Note that 95% of the spatial variation is captured by the field as a whole, and this may not necessarily apply to a smaller region.

At the period of 4.4 months (top of figure 3.12) the Agulhas region is very prominent. Other positive features highlight activity at that period, both within and outside the ACC. Some of these may represent waveguides, particularly where features are aligned with the direction of mean flow. One such region is at 48°S 120°E, within the eastward flow of the ACC. At the period of 3.0 months (bottom of figure 3.12), there are many positive features within the ACC. One prominent region is at 55°S, 230°E and this was less obvious in the raw spectrum field (figure

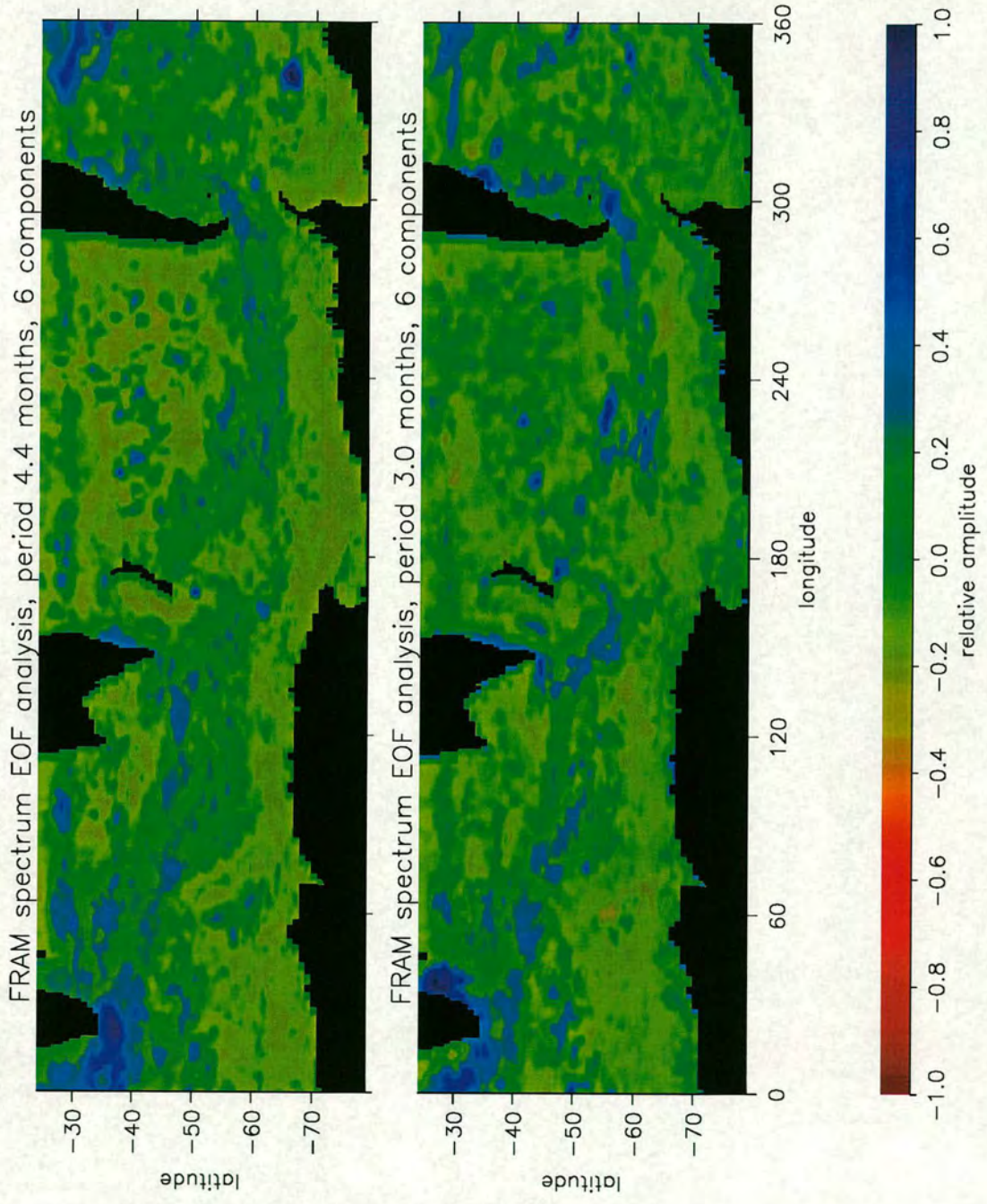

Figure 3.12: Spatial fields for the sum of six EOFs for periods of 4.4 months (top) and 3.0 months (bottom).

3.6).

The EOF reconstruction at a period enables regions with unusual spectral characteristics to be identified. These regions may indicate waveguiding at particular periods, and hence they provide a focus for the phase speed analysis presented in the next section. The EOF analysis has improved on the information provided by the raw normalised spectrum fields by presenting anomalies relative to the mean spectrum, and filtering out unwanted information. This section has demonstrated a novel approach to the spatial study of wave activity which can be applied directly to altimeter data.

3.3 Phase speed calculations

This section looks at the calculation of Rossby wave phase speeds, using the time series of dh/dx from FRAM. Wave propagation is observed in longitude-time diagrams, and the phase information from FFT output is used to calculate phase speeds at different wave periods. This is performed for the whole domain, and then more locally for a jet in the FRAM mean flow.

3.3.1 Longitude-time diagrams

Focusing on regions identified using the EOF results of section 3.2.2, longitude-time diagrams were generated to show propagation of anomalies along a zonal slice of the domain. Longitude-time diagrams for single periods were generated by inverting single spectral components of the fourier transform in time. Figure 3.13 shows an example of the raw and single-period (4.4 months) longitude-time diagrams. The latitude is 46°S and the longitude spans 100° to 120°E. Eastward propagation is very evident in both diagrams, with the single period diagram (on the right) being inherently periodic in time. It is the single period results that will used to calculate phase speeds at different frequencies.

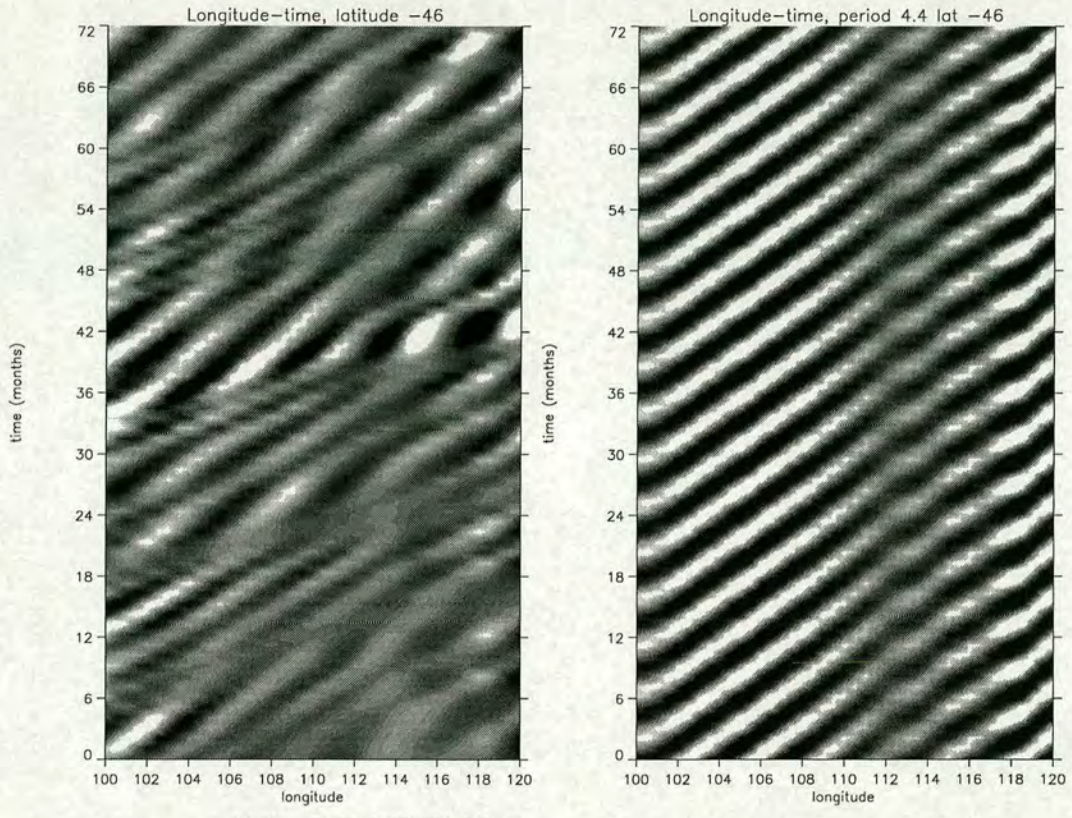

Figure 3.13: Longitude - time diagrams of FRAM dh/dx data, for all data (left) and a spectral component at a period of 4.4 months (right). The latitude is 46°S and the longitude range is 100° to 120°E.

3.3.2 Analytical phase speeds

The simplest way to calculate phase speeds is by using the phase information from the FFT. The difference in phase between adjacent gridpoints is divided by 2π and multiplied by the wave period to give the time difference between gridpoints. The distance between gridpoints is divided by this time difference to give the phase speed. This is equivalent to taking the local gradient of longitude-time diagrams at a single period, such as the right diagram of figure 3.13.

Phase speeds were calculated in this way for the whole domain. A sample result for waves of period 4.4 months is given in figure 3.14. The image has been zonally smoothed over 5 gridpoints. The colour scale has been chosen to highlight eastward propagation, which appears as yellow. Though there is a lot of noise, coherent regions of eastward propagation are evident around the band of the

ACC, but away from the Agulhas region (comparing with figure 3.1). Values of eastward propagation are typically a few cm/s. This field can be compared with the field of fractional power, and the field of EOF reconstruction at that period (figures 3.6 and 3.12 respectively). Eastward phase speed is associated with high fractional power in the Pacific, west Atlantic and east Indian sectors of the ACC. In the west atlantic sector there is high fractional power to the north of the domain which is associated with westward propagation. Eastward propagation in the south Pacific and south of Australia has a greater meridional extent than the high fractional power at that period, showing that the phase speed results are independent of wave amplitude. The EOF reconstruction at this period (figure 3.12) is scaled to highlight the most prominent regions of high fractional power. The feature at 48°S, 120°E corresponds to zonally coherent eastward propagation in figure 3.14, and also corresponds to an eastward jet in the FRAM mean flow (figure 3.1). The major feature in figure 3.12 is associated with strong westward propagation in the Agulhas region (off the southern tip of Africa and extending into the south Atlantic). Other features in the EOF reconstruction are associated with eastward propagation within the ACC or westward propagation outside.

This kind of figure provides a good indication of phase speeds at a single period and over the whole domain, enabling distinction between eastward and westward propagation. To look in more detail at propagation along possible waveguides, and at the variation of phase speed with frequency, phase speeds will be analysed more locally, along eastward jets in the FRAM mean flow.

3.3.3 Analysis along a jet

Figure 3.15 shows jets in the FRAM mean flow which are greater than 15cm/s eastwards. A selection of the longest jets were selected for further analysis. Local phase speeds (c_x) were calculated as described in 3.3.2. The calculation was performed for different periods and at positions along the jet axes (meridional position of maximum time-mean zonal velocity (U)), and up to 2° N and S of the centre of each jet. The results were mixed, with several of the jets having inconsistent phase speeds from one gridpoint to the next. For one jet in partic-

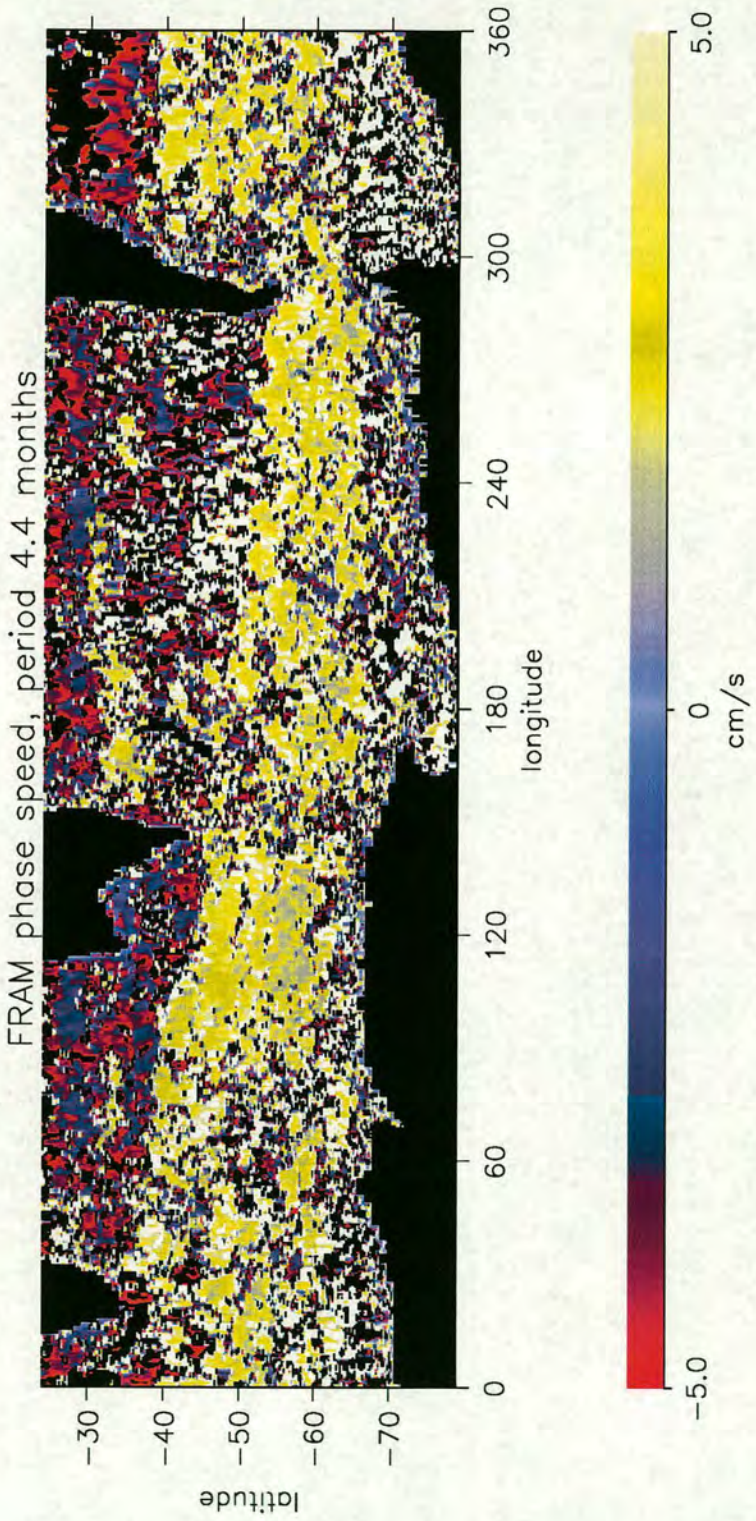

Figure 3.14: Smoothed phase speed from FRAM fourier transform at period 4.4 months. Black is land and off scale (negative) and white is off scale positive.

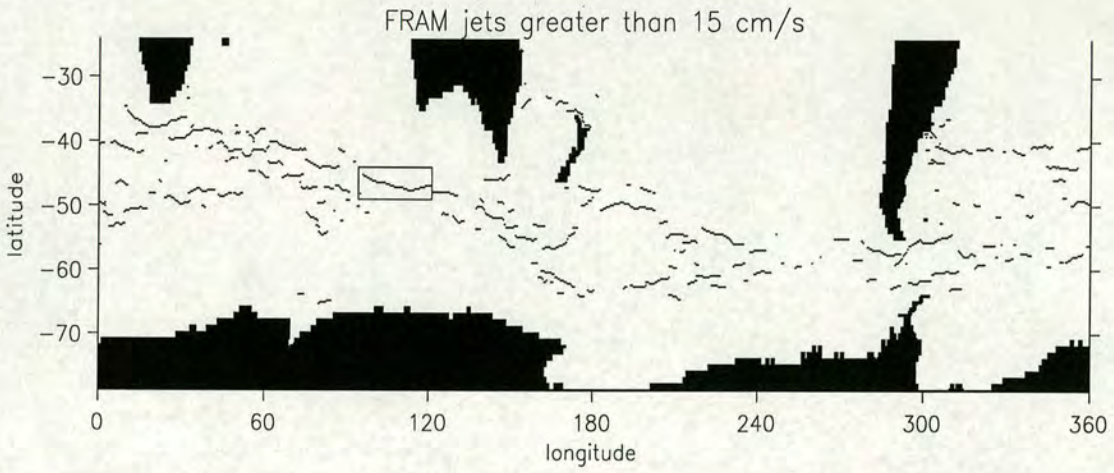

Figure 3.15: FRAM jet axes where U is greater than 15 cm/s eastwards

ular, however, the results were especially good. This jet is at 45°S 95°E, and is identified by the box on figure 3.15. This jet, which was also mentioned in the previous subsection, is suitable for more detailed analysis of phase speeds at different frequencies.

Figure 3.16 (top graph) shows U along the axis of the jet (top curve) and in the jet flanks (average of values 2° N and S of the jet centre), together with the meridionally averaged phase speed (in m/s) and related quantities at three different wave periods (lower three graphs). The jet was selected to start at 95°E, and covers 25° of longitude. The latitude of the jet axis changes from 45°S to 47°S over this longitude range. U at the jet axis varies between 15 and 23cm/s and is close to the absolute mean velocity, as the jet is approximately zonal. The jet width (where the velocity falls to a meridional minimum) is between 3 and 4° of latitude (350-450km).

The mean phase speed ($\bar{c}_x$) is an average of five values of c_x, taken at the jet axis and at 1° and 2° N and S of the axis (in the shear flow and at the flank of the jet). A positive phase speed is eastward. The dashed line shows the standard deviation of these five values, which indicates the relative accuracy of the value of $\bar{c}_x$. This is because $\bar{c}_x$ is found not to vary with U across the jet for a quality measurement, as demonstrated below. The dotted line shows the magnitude of the FFT component used in the calculation of c_x at the jet centre (scale as $\bar{c}_x$,

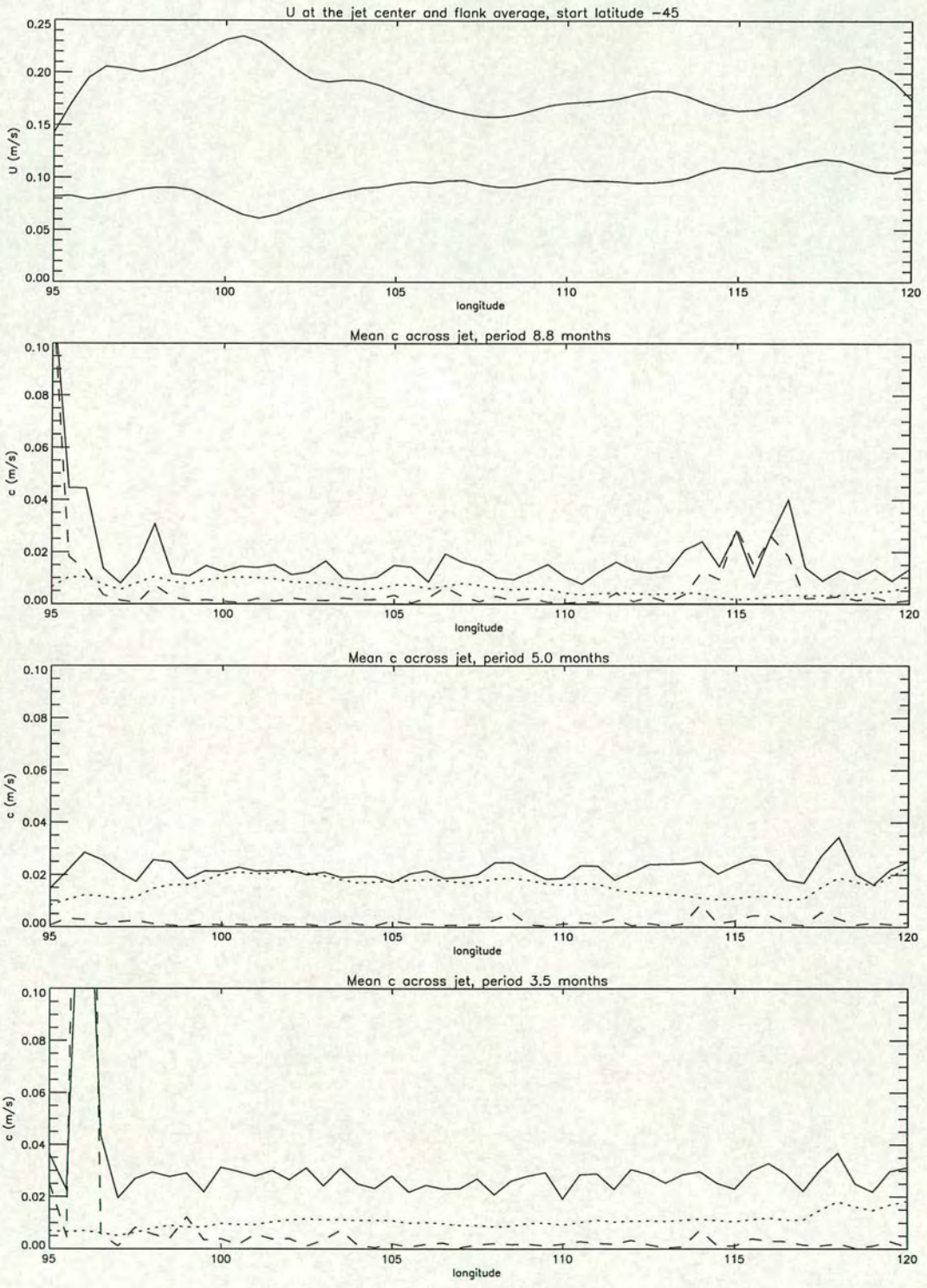

Figure 3.16: Mean zonal velocity (top graph) at jet centre (upper curve) and in jet flanks (average of values 2° N and S), and phase speeds along a FRAM jet for periods 8.8, 5.0 and 3.5 months (second, third and fourth graphs), with standard deviation (dashed line) and FFT magnitude (dotted line).

but no units). This gives an idea of the amplitude of the wave activity. The FFT magnitude is greatest for the period of 5.0 months and this period also gives the smoothest results. For all three periods the FFT magnitude varies along the jet, but not in the same way for each period and not in a way that relates clearly to U.

Common to all three periods is a lack of variation in $\bar{c}_x$ (solid line in lower three graphs) compared to U (top graph). Ignoring values where the standard deviation is greater than 1cm/s, $\bar{c}_x$ varies by about 1cm/s compared to the 8cm/s variation in U. Variation in $\bar{c}_x$ is not related to variation of mean U, but is on small scales in longitude. The low standard deviation (dashed line) shows that $\bar{c}_x$ also varies little across the jet, though the velocity in the jet flanks drops to between one third and two thirds of the maximum value (top graph). This is a surprising result; the eastward phase speed seems unrelated to the mean eastward velocity. In other words, the eastward flow does not appear to advect the waves in proportion to its strength. Rossby wave propagation in eastward flows has not been widely studied, and studies which do exist (such as Killworth (1979) - see section 2.2) are based on idealised circumstances with small, linear mean flows. There is currently no theory available to support this model observation, so it will be interesting to see if a similar result is found in the real ocean. This is addressed in chapter 5. The relationship between $\bar{c}_x$ and U in FRAM is studied further in the next chapter.

From the results at these three periods, $\bar{c}_x$ appears to increase as period decreases (frequency increases). Figure 3.17 shows how the phase speed, averaged over the whole jet, varies with frequency. These phase speeds were calculated by performing a linear fit to the along-jet $\bar{c}_x$ where the standard deviation was less than 1cm/s. For each frequency, the linear fit was near constant with longitude and so a jet-average $\bar{c}_x$ was taken from the linear fit at the start of the jet.

Average phase speeds are shown for frequency numbers (fn) 5 to 25, equivalent to periods between 14.0 and 2.8 months (see table 3.1). Over this range, the phase speed increases linearly with frequency number (which is proportional to frequency). The linear fit is particularly good between fn 6 and 14 and these are

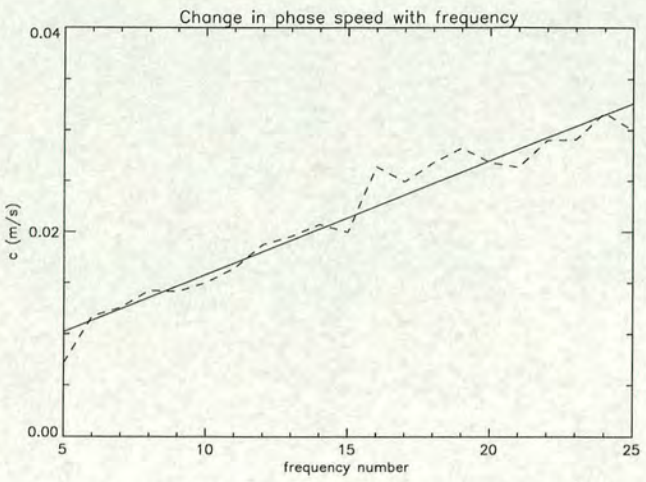

Figure 3.17: Mean phase speed against frequency number for a jet in FRAM (dotted) with linear fit (solid). The periods associated with frequency numbers are given in table 3.1.

the most prominent frequencies for wave activity associated with this jet (from the work in section 3.2). The average phase speed increases from 1.0cm/s at fn 5 (period of 14.0 months) to 3.2 cm/s at fn 25 (period of 2.8 months). The linear increase of phase speed with frequency is expected for fixed zonal wavelength, from the simple relationship $c = \omega/k$ (angular frequency, $\omega = 2\pi/T$ (period T) and zonal wavenumber k). The wavelengths from figure 3.17, however, is 368km at fn 5 and 236km at frequency number 25, decreasing in proportion to 1/fn in between. $\bar{c}_x$ therefore increases more slowly with frequency than is expected for a fixed wavelength. A relationship between phase speed and wavelength is given by the dispersion relation (equation 2.11). For first-mode baroclinic Rossby waves with no flow, this is given by

$$c_x = \frac{\omega}{k} = \frac{-\beta}{k^2 + l^2 + R_0^2}, \tag{3.3}$$

Where R_0 is the first Rossby deformation radius. The relationship between angular frequency, ω, and wavenumber, k, was shown for this dispersion relation in figure 2.2. It will be seen in the next chapter that a typical first Rossby deformation radius in the Southern Ocean is 20km. The turning point in the ω-k relationship occurs at a zonal wavenumber of $1/R_0$, which for an R_0 of 20km

gives a zonal wavelength of about 126km. The waves identified here have longer wavelengths than this, so smaller k than $1/R_0$. This means that ω is expected to be proportional to k and so wavelength is inversely proportional to frequency as shown by the results of figure 3.17. This offers a qualitative explanation for the observed relationship between phase speed and wavelength, though the argument has neglected the effects of mean flow and is based on westward propagation.

This section has demonstrated some interesting results relating to the propagation of eastward Rossby waves in the FRAM model. Though the dispersion relation is based on very simplified dynamics and may not necessarily hold in FRAM, it may be crucial to the understanding of these results. Also, the dispersion in its full form relates phase speeds to zonal flow. If all the terms in the full dispersion relation (equation 2.18) apart from U were known for a FRAM jet, it would be possible to solve for a U in the jet and compare the result with the actual U. The next chapter addresses this, and other issues raised here, by studying the dispersion relation in more detail.

3.4 Eddy quantities

Eddy quantities in this study are quantities derivable from the eddy velocities which are the fluctuating part of the velocity field. It is these velocities that are measured most accurately by the satellite altimeter and so a study of the eddy quantities in FRAM can be directly applied to real data. The eddy quantities include the zonal Rossby wave activity studied in the previous two sections (which was due to fluctuations in dh/dx), and all other variability as well. This section shows how the eddy quantities are calculated and represented for convenient interpretation. Spatial fields calculated from the FRAM output are presented and discussed. The aim of the work is to relate the time-average eddy activity to the mean flow in FRAM. Any relationships might then apply to the real ocean.

3.4.1 Velocity variances and covariance

For two-dimensional flow, the instantaneous velocities u and v can be split into time-mean and fluctuating parts to give

$$u = \overline{u} + u', \quad v = \overline{v} + v' \tag{3.4}$$

The velocity variance terms, p and q, and the covariance term, r, are then given by

$$p = \overline{u'u'}, \quad q = \overline{v'v'}, \quad r = \overline{u'v'}. \tag{3.5}$$

These quantities are conveniently combined in a symmetric tensor,

$$T = \begin{pmatrix} p & r \\ r & q \end{pmatrix}, \tag{3.6}$$

which can be represented graphically as a velocity variance ellipse.

3.4.2 Velocity variance ellipses

Following Hughes (1997), the tensor, T, can be diagonalised by a plane rotation through an angle θ, where θ is given by

$$p - q + r\left(\tan\theta - \frac{1}{\tan\theta}\right) = 0. \tag{3.7}$$

Noting that $\tan\theta - 1/\tan\theta = -2/\tan 2\theta$, and defining $s = (p-q)/2$ results in

$$\tan 2\theta = \frac{r}{s} \tag{3.8}$$

.

This gives more than one value for θ, but for the purpose of the variance ellipse, the value between $\pm\pi/2$ is chosen. The rotated tensor is now given by

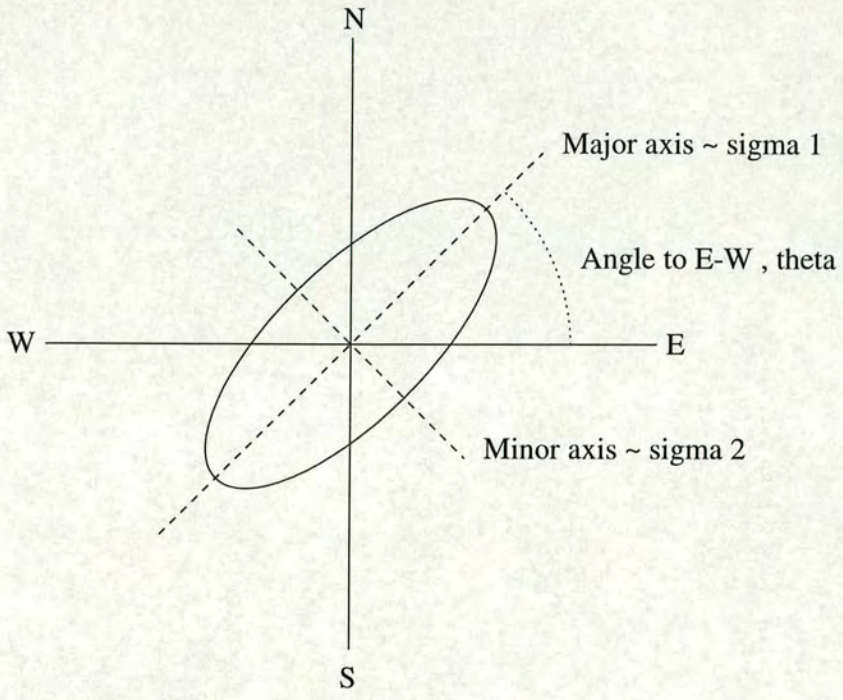

Figure 3.18: Schematic of a velocity variance ellipse. Sigma 1, sigma 2 and theta represent the symbols σ_1, σ_2 and θ respectively.

$$T_r = \begin{pmatrix} \sigma_1 & 0 \\ 0 & \sigma_2 \end{pmatrix}, \tag{3.9}$$

where σ_1 and σ_2 are given by

$$\sigma_1, \sigma_2 = (p+q)/2 \pm \sqrt{s^2 + r^2}. \tag{3.10}$$

The velocity variance ellipse is drawn with its major axis proportional to σ_1, at an angle θ anticlockwise from the x axis, and with its minor axis proportional to σ_2. A schematic of the velocity variance ellipse is shown in figure 3.18. The ellipse is representative of the actual eddy shape and shows how the eddies interact with the mean flow over the timescale used for the calculation of the eddy quantities. This is discussed below.

3.4.3 Total variance and anisotropy

The total eddy variance is given by the size of the ellipse,

$$\sigma_1 + \sigma_2 = p + q. \tag{3.11}$$

This is twice the eddy kinetic energy and gives the magnitude of eddy activity, independent of the mean flow.

The eddy anisotropy is given by the eccentricity of the ellipse,

$$\sigma_1 - \sigma_2 = 2\sqrt{s^2 + r^2}, \tag{3.12}$$

and, for two-dimensional incompressible flow, this represents the amount of interaction with the mean flow (apart from simple forces associated with horizontal gradients of kinetic energy). The larger the anisotropy, the greater the transfer of momentum between the eddies and mean flow. The nature of this momentum transfer is given by the orientation of the ellipse, θ. The sign of θ depends on the signs of r and s. In the case of a zonal eastward flow (such as in the ACC), positive θ indicates the transfer of eastward momentum northwards, and negative θ indicates the transfer of eastward momentum southwards. The expected eddy ellipse arrangement for a stable eastward jet is shown schematically in figure 3.19. This has been observed in studies with quasi-geostrophic models (e.g. McWilliams et al (1978), McWilliams and Chow (1981)).

To the north of the jet axis, θ is negative and eastward momentum is transferred southwards into the jet. South of the jet axis, θ is positive, again feeding eastward momentum into the jet, which is therefore sustained by the eddy forcing (assuming this is barotropic). At the jet centre θ is 90° and there is no eddy momentum input to the mean flow. The velocity variance ellipse provides invaluable information about the eddy activity, which is primarily due to Rossby wave propagation. Representing the variance ellipses over the FRAM domain is difficult, however, as each gridpoint is associated with a different ellipse. The same information can

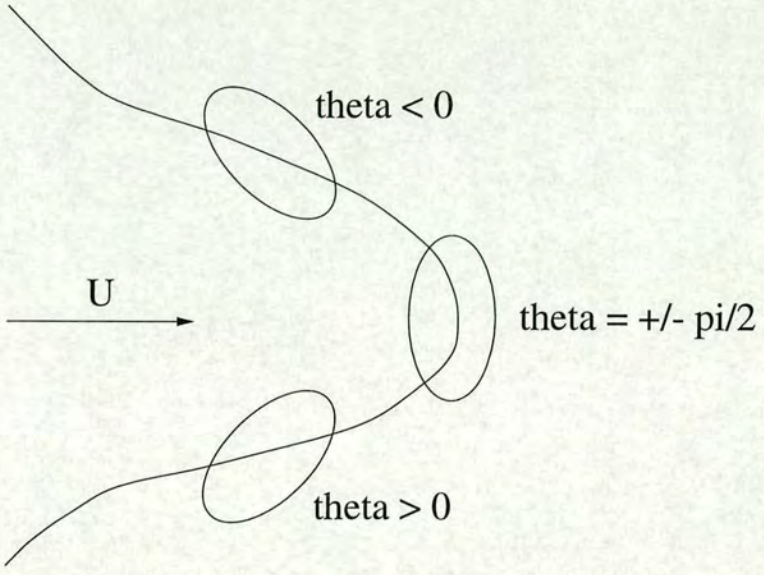

Figure 3.19: Schematic of an eastward jet and associated eddies

be conveniently displayed as three separate fields of the total eddy variance, eddy anisotropy and angle theta.

The velocity variance and covariance terms, p, q and r, were calculated from the 72 months of FRAM velocity anomalies and used to produce spatial fields of the three eddy quantities. Box averaging over 5 zonal by 2 meridional gridpoints (2.5° longitude ×0.5° latitude) was used to obtain smooth fields.

Total variance field

The total variance field calculated from the FRAM velocity anomalies is shown in figure 3.20. This shows the relative amount of eddy activity over the domain. This result does not contain information about the mean flow, though regions of high eddy activity are likely to be associated with regions of strong mean flow. In particular, the pattern of eddy variance appears to relate closely to the path of the ACC (see figure 3.1), with strong activity in the Agulhas region and in the western ocean boundaries by Australia and Argentina.

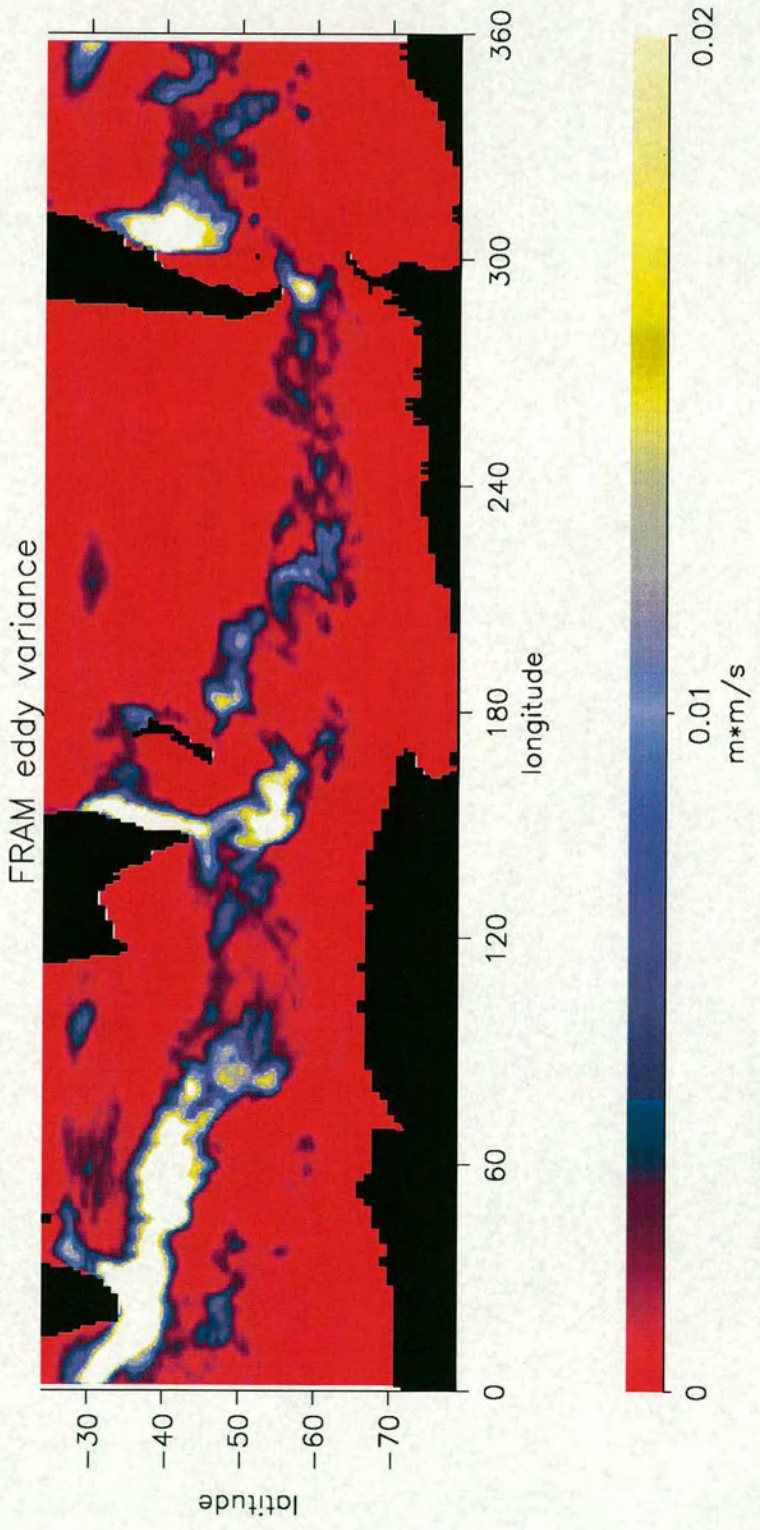

Figure 3.20: Smoothed eddy variance field from FRAM

Anisotropy field

Figure 3.21 shows the field of eddy anisotropy. The spatial structure is very similar to the variance field, with values approximately 60% of the variance. This shows the ellipses to have a large eccentricity, with the length of major axis typically four times that of the minor axis. The similar structure implies the eddy activity interacts with the mean flow by an amount proportional to the variance, with the variance ellipses varying more in size than in shape.

Differences between eddy variance and anisotropy are only evident on small scales, where the anisotropy has a finer structure. Because the anisotropy represents interaction with the mean flow, it is plausible that these small-scale differences are related to features of the mean flow which are not discernible in the variance field. This is studied further in chapter 6.

Theta field

The field of orientation of the velocity variance ellipses (θ) is shown in figure 3.22. The superimposed white lines show the axes of jets in the mean flow, where the mean flow is greater than 15cm/s (as shown in figure 3.15). Notably, the jet axes in the mean flow are often exactly coincident with lines of $\theta = \pm\frac{\pi}{2}$ axes in the mean flow. This is consistent with the expected relationship between eddies and stable jets in the mean flow, illustrated in figure 3.19. The eddy orientation angle, θ, was derived from time varying velocity components and yet it provides an excellent indication of the position of jets in the mean flow. This is an important result that can be applied to altimetry data. Note that meanders in a jet will also appear as eddies in this analysis, though their timescale is likely to be larger than that for rotating eddies or propagating Rossby waves.

3.5 Trend in u

The results presented so far have been obtained for the full six year time series of FRAM output, and so represent an average over that period. Quantities have

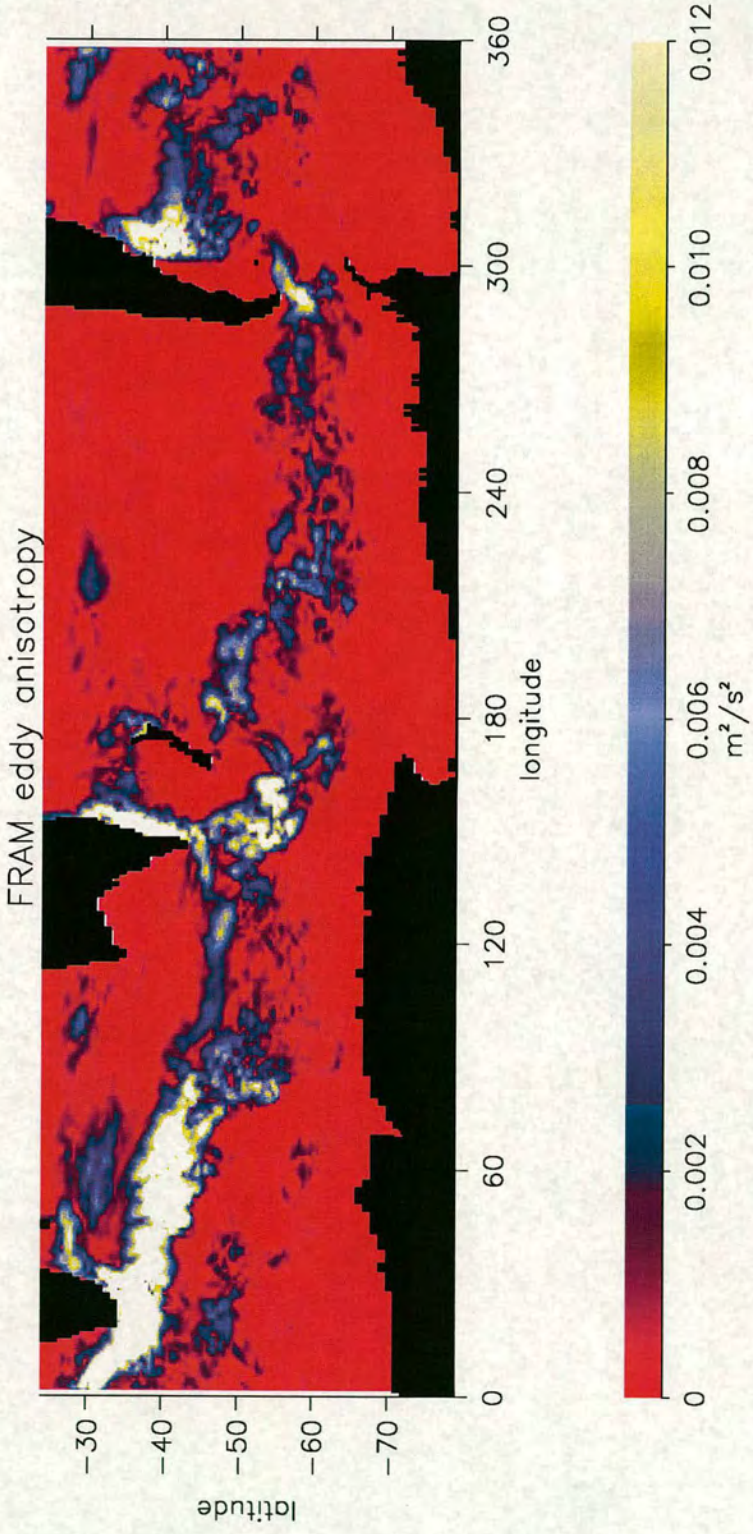

Figure 3.21: Smoothed eddy anisotropy from FRAM

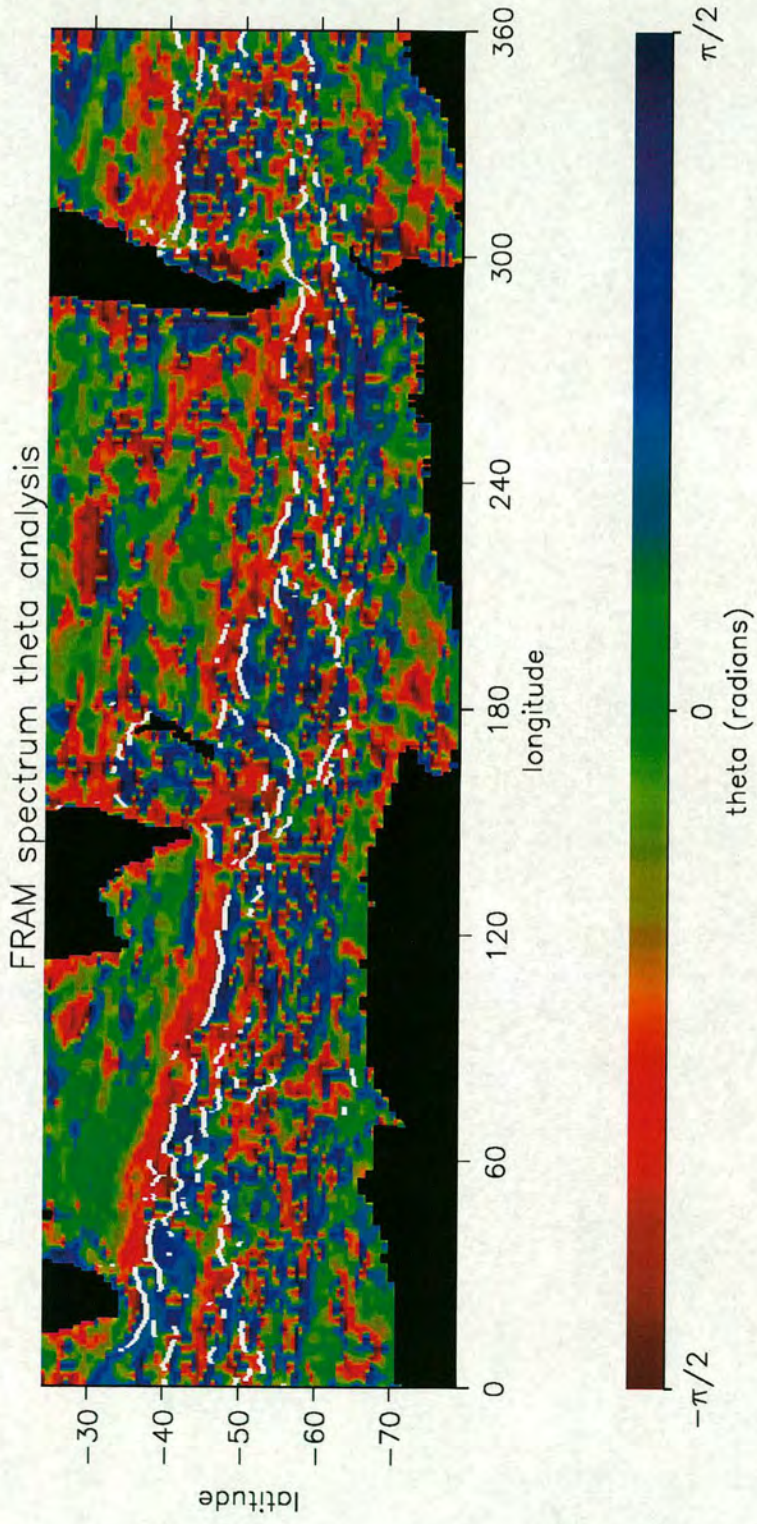

Figure 3.22: The angle the major axis of the velocity variance ellipse subtends to the zonal direction. White lines show the position of jet centres in the mean flow, where U is greater than 15 cm/s.

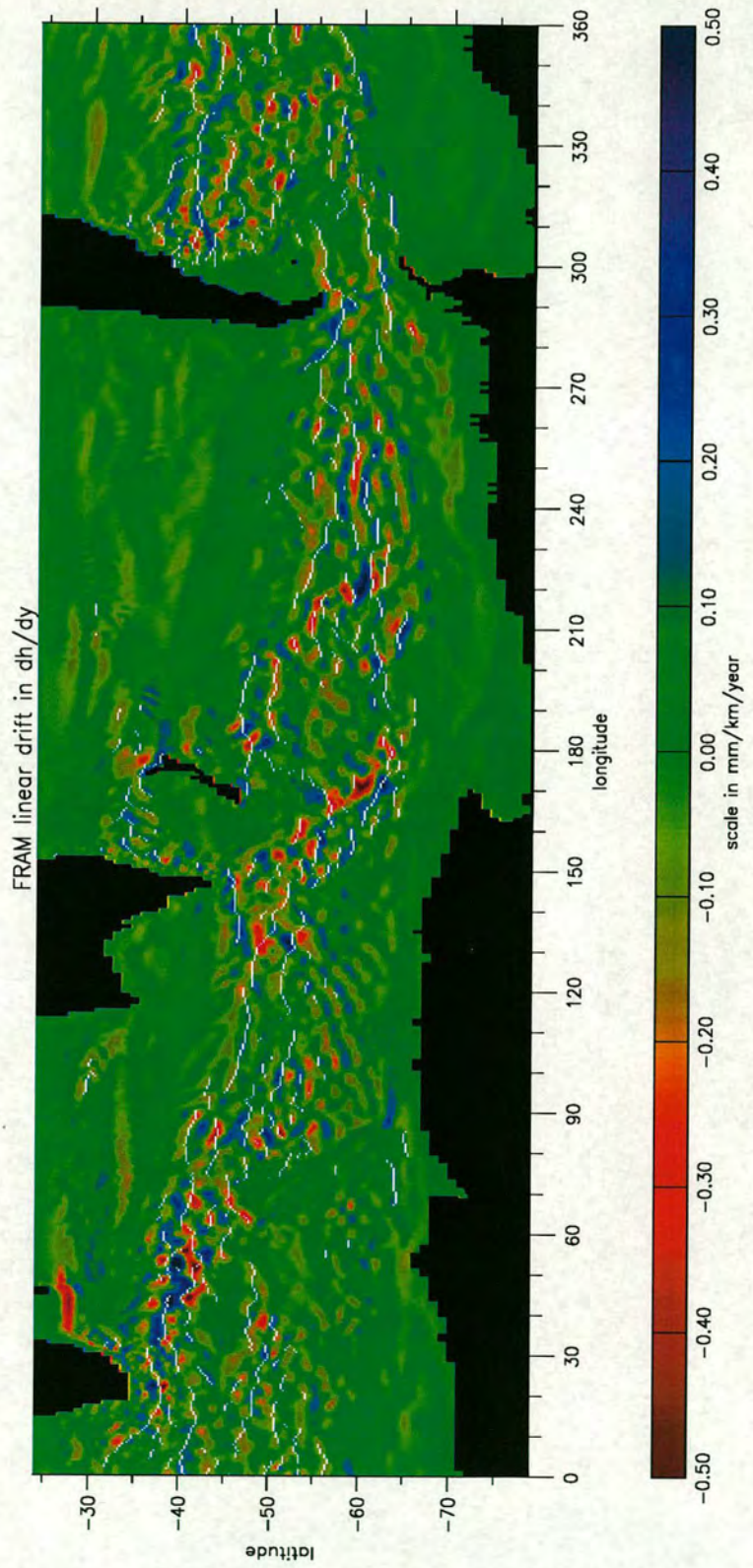

Figure 3.23: Linear trend in dh/dy over the six years of FRAM output

been derived from current anomalies because absolute currents will not be available in the altimetry data. The change in the absolute currents over the time period can be obtained from just the current anomalies, however, and this might be a useful quantity to compare with the mean flow. This section looks briefly at the linear change in u over the six years of FRAM output, and compares this with jets in the mean flow.

Figure 3.23 shows the linear trend in dh/dy anomaly over the six years of FRAM output. Positive parts (blue) show an increase in u according to the formula $u = -g/f \times dh/dy$, such that at 60°S a change in dh/dy of 0.5 mm/km/year is equivalent to a change of 8 cm/s/year. The axes of jets in the mean flow greater than 15cm/s (as shown in figure 3.15) are superimposed in white.

The linear trend has a clear meridional scale of between one and two degrees of latitude, and this compares very well to the scale of jets in the mean flow (see figure 3.1). There is not a consistent relationship between the position of jets in the mean flow and the linear trend in u. Some jets are aligned with features of the linear trend and others lie between features. The jet at 47°S, 95° to 120°E, for example, has accelerated in the central longitudes and has decelerated at either end. The jet at 51°S, 180° to 200°E is aligned with a deceleration feature. Where the jet is aligned with features in the linear trend, such as in these two examples, the jet is likely to have changed in strength over the six years but maintained it's position. Where the jet in the mean flow lies between features of the linear trend, such as 57°S, 240°E, the jet is likely to have moved meridionally over the six years (in this case, the jet lies between a positive feature to the south and negative feature to the north, so has moved southwards).

Without knowledge of the field of mean U, the linear trend in u may at least indicate the meridional scale of jets in the mean zonal flow, as it seems to in many parts of FRAM (by comparison with figure 3.1). This section has just introduced the quantity as an additional diagnostic. The linear trend will be considered for the real Southern Ocean in chapter 6.

3.6 Summary

This chapter has set out to analyse FRAM output in a way that could be applied to altimetry data, and with a focus on relating quantities derivable from velocity anomaly measurements of the mean flow at the surface.

Section 3.2 described a study of the frequency of wave activity in the FRAM output, using EOF analysis to identify the most significant information. This highlighted particular regions as being associated with certain frequencies, and which were therefore possible waveguides.

Section 3.3 then used a simple Fourier transform technique to measure the phase speed of Rossby wave propagation at different frequencies. Focusing on one particular jet in the mean flow, it was found that the eastward phase speed remained fairly constant along the jet, for a particular frequency. The insensitivity of phase speed to jet velocity is a surprising result. It is not explained by theory and therefore remains an empirical observation in the model output. The phase speed was found to increase regularly with frequency. This was shown to be consistent with the dispersion relation, but could not be understood quantitatively.

Section 3.4 described the calculation of eddy quantities using time varying velocity components. The associated spatial fields were presented and discussed in terms of relationships with the mean flow. In parts of the ACC, the orientation of velocity variance ellipses enabled the position of jet axes to be located.

Finally, in section 3.5, the linear trend in u was introduced as a diagnostic which could be calculated from the anomalies of dh/dy. This was compared with jets in the mean flow and was seen to indicate the meridional scales of those jets but not the meridional position.

The FRAM output has provided a time series with adequate temporal and good spatial resolution for the work described above. Furthermore, the output is free from noise and includes the velocity field. The spatial resolution of altimetry data is significantly worse than FRAM (though the temporal resolution better). Noise in the data will also have to be accounted for, so the techniques described in

this chapter will have to be applied with caution. These issues will be addressed in chapter 5. Work described in this chapter has formed a useful basis for the analysis of real data. If similar results were obtained for the real ocean, it would provide at least a greater understanding of Rossby wave activity in the ACC.

At this stage it is necessary to point out that there will be differences between a model (such as FRAM) and the real ocean, and these will have implications when applying the techniques developed here to real data. Eddy kinetic energy observations have been compared with results from FRAM by Stevens and Killworth (1992), who describe differences between FRAM and reality. One of the main regions where FRAM fails to reproduce realistic behaviour is downstream of Drake Passage. In FRAM the highest variability here is located in a single oval-shaped region between about 35° and 45°S, 300° to 320°E (see figure 3.20). In the real ocean, however, there is a characteristic 'c' shape to the variance here, with a distinct filament of high variability at 50°S. This comparison will become possible when results of satellite-derived eddy variance are presented later in this thesis. Another significant difference relates to the Agulhas eddy region southwest of Africa. Here the eddies are larger in FRAM than is expected in the real ocean (Webb et al, 1991). Other differences are noted in regions where topography is likely to have an influence. Topography will be discussed further in the next chapter, and will be found to have important implications when seeking to apply some of the results from this chapter to the real ocean. Though the results may differ in the real ocean , the techniques used in this chapter are likely to be a useful means of analysis.

Chapter 4

Rossby waves and the mean flow

One of the aims of this thesis is to relate time varying currents to the mean flow. This chapter looks at the relationship between Rossby waves and the mean flow, and discusses whether Rossby wave observations might be used to estimate mean flows. The first and main section looks at the use of the Rossby wave dispersion relation for calculating mean flows from wave information in the FRAM model. A second section discusses the use of simplified models for relating waves to the mean flow and a final section discusses the relevance of topography to the work presented in this thesis.

4.1 Dispersion relation in FRAM

A dispersion relation for Rossby waves in a zonal, stratified flow with constant shear was derived in section 2.1. This is based on linear theory which was found not to hold well in the real ocean (see section 2.4). If, however, the discrepancy between theory and reality is regular and predictable, the dispersion relation may still provide a means of relating changes in Rossby wave parameters to changes in the mean flow. This section uses FRAM output to look at the possibility of using the dispersion relation for this purpose. Results in the previous chapter showed that phase speed did not vary with mean flow for a particular frequency of Rossby wave, so other quantities must vary in order to balance the dispersion relation. The analysis will seek to explain this observed relationship between phase speed

and mean flow in FRAM. The study will focus on a waveguide jet in the mean flow, where the insight is expected to be greatest. The dispersion relation was derived for linear flow and so its application to a jet, which has mean flow scales comparable to a wavelength, must be treated with caution. Nevertheless, in the absence of a non-linear version, the dispersion relation provides a useful starting point for this analysis.

The Rossby wave dispersion relation is given by equation 2.18 as follows:

$$c_x = \frac{\omega}{k} = U - \frac{\beta_e}{k^2 + l^2 + \frac{f_0^2 m^2}{N^2}}. \tag{4.1}$$

Re-arranging for the zonal mean flow, U, gives,

$$U = c_x + \frac{\beta_e}{k^2 + l^2 + \frac{f_0^2 m^2}{N^2}}. \tag{4.2}$$

If all the terms on the right hand side are known at a location then an independent value of U can be obtained. The zonal phase speed, c_x, was measured successfully in FRAM and presented in chapter 3. This was done at set frequencies (ω) and thus fixes the zonal wavenumber, k, according to $k = \omega/c$. The measurements were made from Fourier components of the time series for six years and so represent the average values over that time. The vertical wavenumber term, $\frac{f_0^2 m^2}{N^2}$ is fixed by the Rossby deformation radius, R_0 (it is equivalent to $1/R_0^2$ - see chapter 2). The first baroclinic mode Rossby radius of deformation has been computed globally by Chelton et al. (1998) whose results are shown in figure 4.1. This shows, for the first internal mode (mode 1), that R_0 is between 10km and 30km for most of the Southern Ocean. In FRAM, however, the variability over the depth is observed to be more like equivalent barotropic than mode 1 (Killworth, 1992). This means that R_0 is expected to be larger than its first-mode value, between the values for mode 1 (10-30km) and the barotropic mode (around 12000km), though much closer to the mode 1 value. A suitable value will be chosen in section 4.1.2.

Now the effective beta, β_e, and meridional wavenumber, l, are the remaining

unknowns. The effective beta, β_e, is equivalent to $\beta - U_{yy}$ where β is the known meridional gradient of Coriolis force. The term U_{yy}, the curvature of the profile of U, is dependent on U itself and could be incorporated in the left hand side to form a differential equation in U. With FRAM, however, U_{yy} can be measured to provide a semi-independent value for U. This leaves the meridional wavenumber, l, as the final unknown. Means of determining l are discussed in 4.1.1, below.

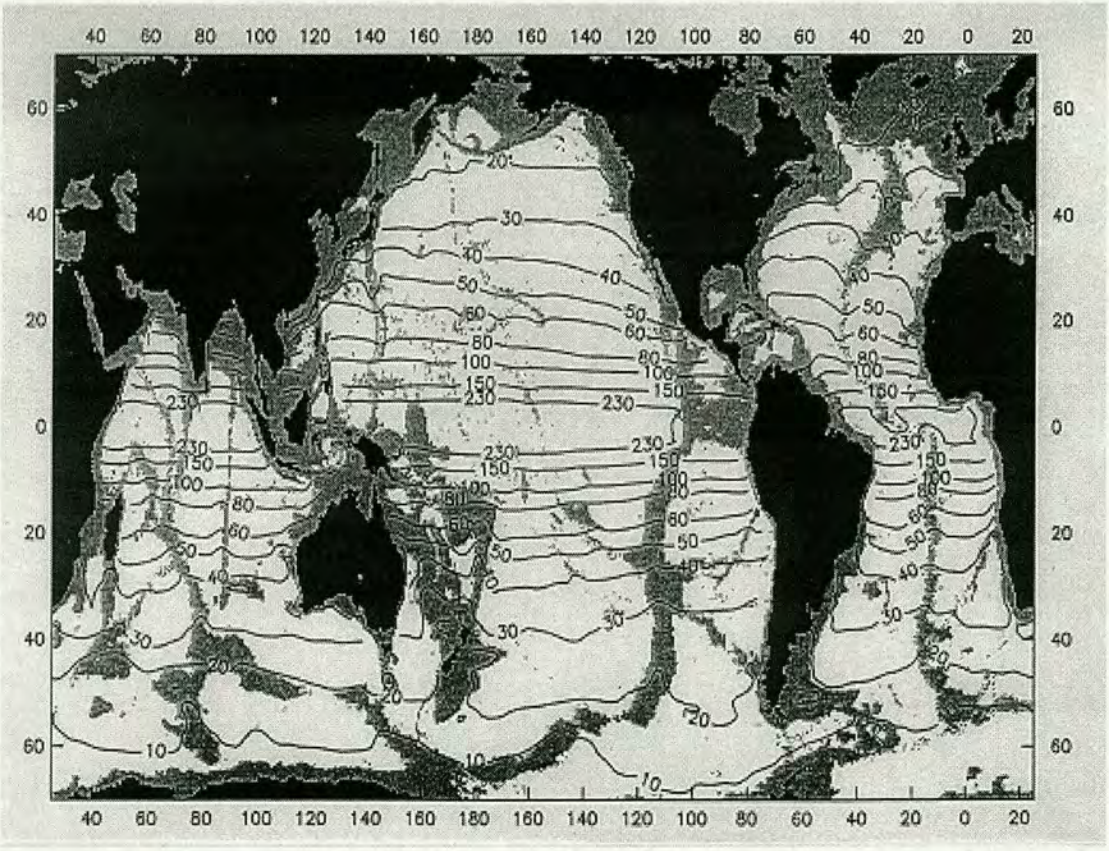

Figure 4.1: Global contour map of the $1° \times 1°$ first baroclinic Rossby radius of deformation in km, from Chelton et al (1998). Shaded parts are where the depth is less than 3500m.

The analysis presented in this section builds upon results from section 3.3 of phase speed against frequency in FRAM. The same jet will be used to assess the balance of terms in the dispersion relation. Figure 4.2 shows the position and the mean zonal velocity of this jet, which lies to the south of Australia. The zonal extent of 25° is equivalent to 1896km at the central latitude (47°S). The meridional distance for 8° of latitude is 889km.

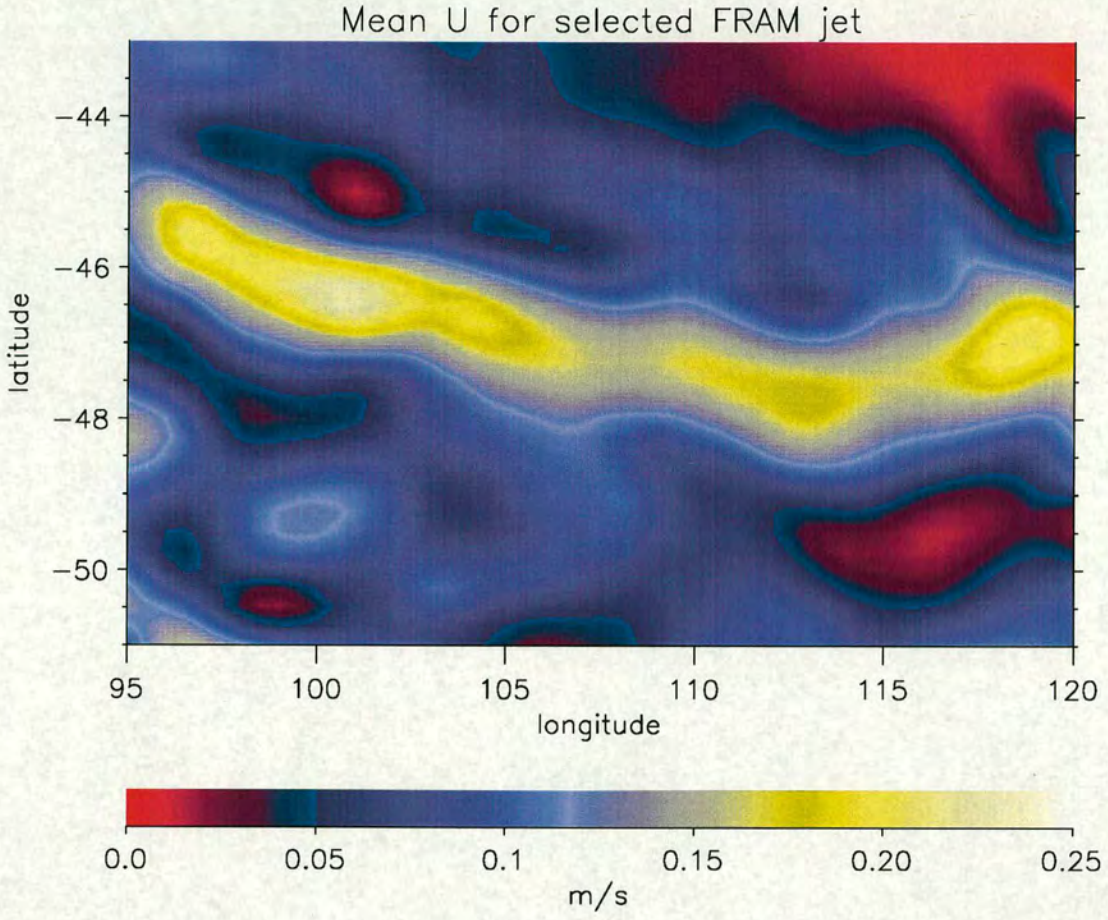

Figure 4.2: Mean geostrophic zonal current at the surface, for a region of FRAM south of Australia.

4.1.1 Meridional wavenumber

One method of estimating l is by examining the scales of v anomalies. The v anomalies were used in the analysis of Rossby wave phase speeds because most of the anomalies in v are due to Rossby wave activity rather than fluctuations in the near-zonal mean flow. A near-zonal mean flow gives rise to very small anomalies in v because the mean meridional velocity is very small.

A snapshot of the v anomaly field for the jet is shown in figure 4.3. Comparing this with the mean zonal velocity, the anomalies have a meridional scale which is slightly larger than the jet width. For this snapshot, half a meridional wavelength spans 3° of latitude. The meridional wavelength, λ_y, is therefore 667km and l is then given by $2\pi/\lambda_y$. The zonal wavelength is also clear in this snapshot. There are 7 zonal wavelengths in 1896km giving λ_x =271km. To obtain a mean value

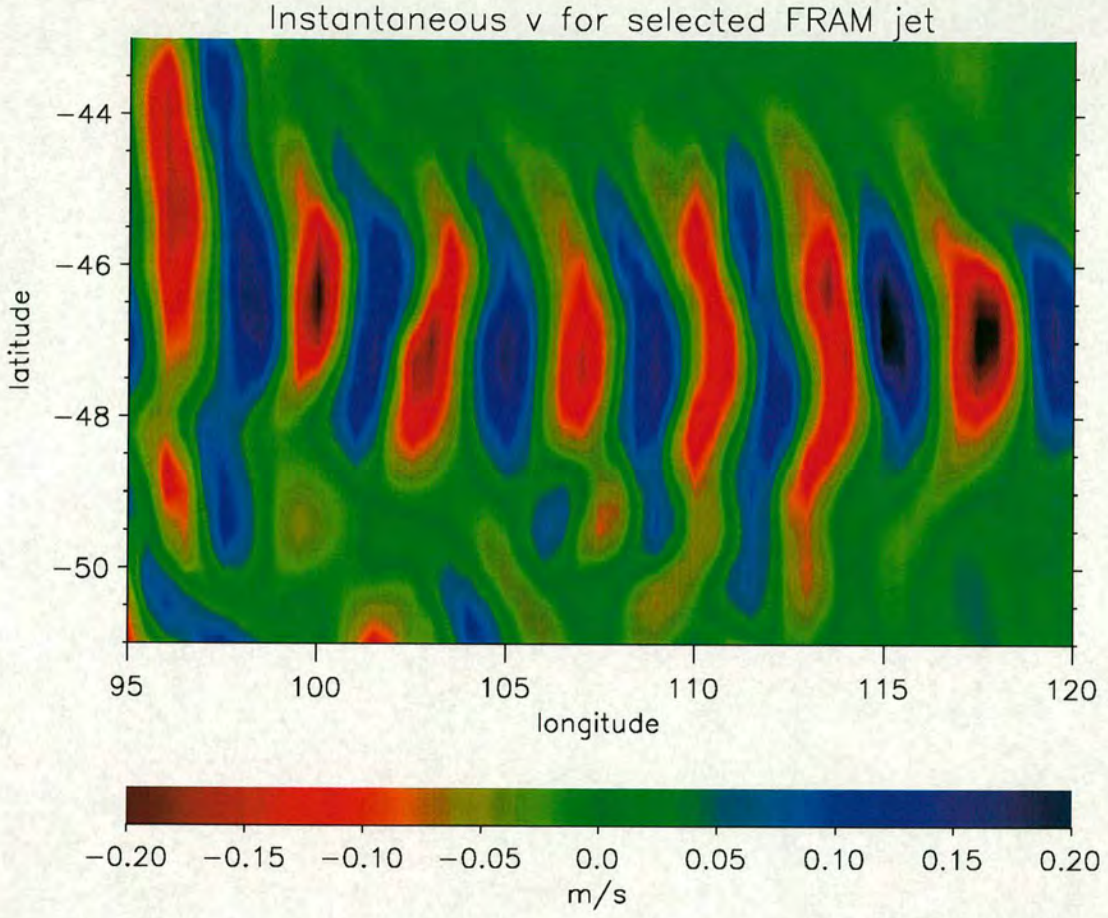

Figure 4.3: Instantaneous field of v anomaly at the surface, for a region of FRAM south of Australia.

of λ_y by this method, it would be necessary to average the values obtained from each monthly snapshot. This would require a consistent criterion for measuring the meridional extent of the eddies which is not a straightforward task.

A mean value of l is more easily obtained by studying the background vorticity gradient, β_e. If β_e becomes negative (for example in troughs either side of a jet in U) then Rossby waves cannot propagate due to a change in sign of the North-South gradient in potential vorticity (see section 2.2.2). A meridional scale for the waves is then fixed between these regions of negative β_e, as critical lines are expected to exist where $\beta_e = 0$ (see section 2.2.2). Identifying critical lines relies on knowledge of the U field, which is available from the FRAM output for the purpose of the analysis presented in this section. If only wave parameters and velocity anomaly fields were known, however, then l would need to be inferred

from the v field as discussed above.

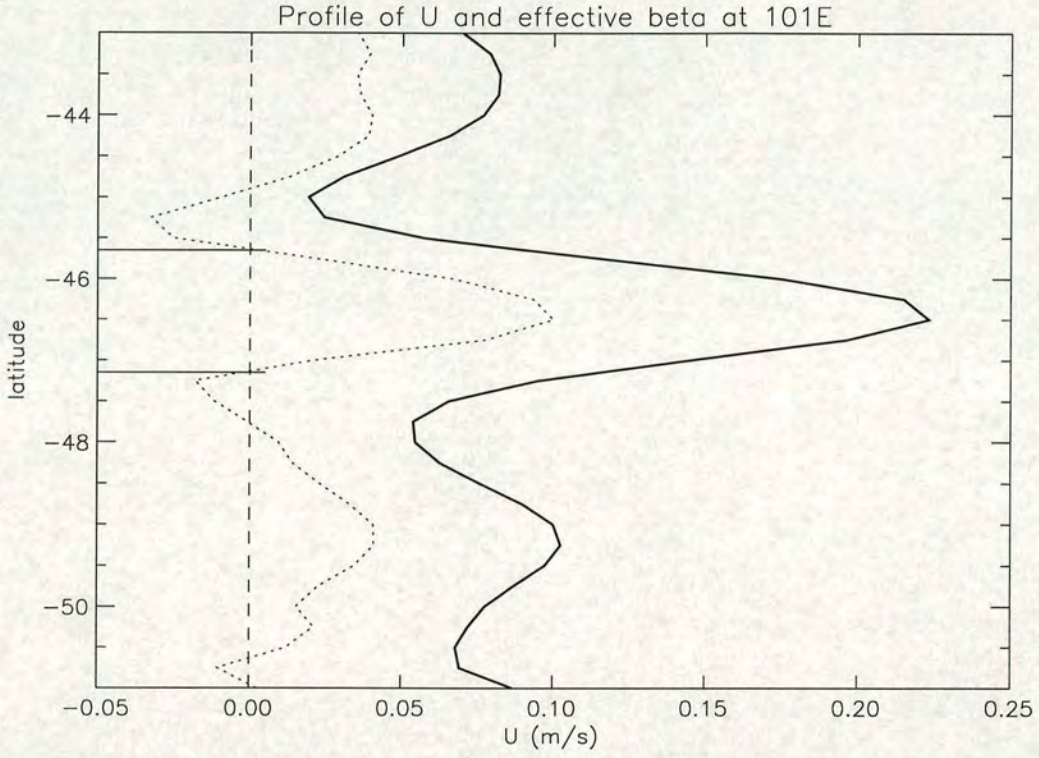

Figure 4.4: Profile of U (solid line) and effective beta, β_e, (dotted line) from FRAM at 101°E. The scale of β_e is not given, but the maximum value is 6.13e-11 $(\text{ms})^{-1}$ at 46.5°S.

Figure 4.4 shows a meridional profile of the jet in mean U at 101°E, together with β_e. β_e has been scaled for comparison, but has a very similar form to the U profile. The points where β_e becomes negative either side of the jet centre are marked by horizontal lines. Immediately outside these bounds the background vorticity gradient at the surface is negative. Although the potential vorticity (PV) gradient will also depend on the stratification and relative vorticity, these bounds are an indication of where the PV gradient will become zero or negative such that Rossby waves cannot propagate (see section 2.1.2). The distance between the bounds therefore represents an estimate of the meridional length-scale for waves associated with the jet. This distance is between latitudes of 45.65° and 47.15°S which is 1.5° of latitude or 167km. This meridional scale will be taken as half a wavelength, as suggested from the snapshot, figure 4.3. The mean meridional wavelength from the profile of β_e is therefore 334km. This is half of the wavelength indicated in figure 4.3 which was an instantaneous estimate rather

than an average value over the six years.

With the meridional wavenumber now established, there are estimates from FRAM output for all the terms in the dispersion relation. U can now be calculated and compared with the actual model value. The calculation will be based on the surface geostrophic U, rather than a depth average, because it is only surface quantities which can be measured by satellite, and the phase speeds measurements were made at the surface.

4.1.2 Balance of terms

At a point

First, U is calculated at 101°E using the maximum value of β_e. This is done using the results of phase speed against frequency shown in figure 3.17, and equation 4.2. Table 4.1 shows the terms from the dispersion relation and the value of U obtained for the selected frequency numbers of 5, 15 and 25 (periods 14.0, 4.7 and 2.8 months respectively - see table 3.1). The results for all frequency numbers from 5 to 25 are shown in figure 4.5 for different values of R_0. The calculated U is not the same for different frequencies, but has a curving profile which varies with R_0. This implies that l or R_0, or both, must vary with frequency if the calculated U in figure 4.5 is to be constant (as it should be). If l varies, a sensible possibility is that it would vary with k (such that the waves maintain their overall shape), but this would increase the gradient of the calculated U-frequency relationship. A fixed l is therefore more suitable than one which, say, varies with k. R_0 depends on the vertical wavenumber, and the variation of this with frequency is hard to establish. In figure 4.5, U is most uniform over the frequency range for R_0=70km, for which the variation is about 10%. This is good enough to proceed with the use of the dispersion relation for calculating an independent value of U, and indicates that a constant Rossby deformation radius of 70km is a suitable value to use (see discussion earlier in the chapter). This variation with frequency, however, should be noted.

The calculated value of U of 8 cm/s is about one third of the maximum U

from figure 4.4 of about 23 cm/s. The minimum value for the jet between the critical lines is about 9 cm/s, which is still above the calculated value. There is therefore a clear discrepancy between the calculated and model U, but this was anticipated in the light of the comparisons between theory and reality laid out in Killworth (1997), and the lack of suitability of the dispersion relation for a non-linear jet. The differences here are discussed further in 4.1.3, below. As stated in the opening paragraph, the discrepancy between the calculated and model U is not so important if the relative change in model U along the jet is matched by the relative change in calculated U.

Variable	Fn=5	Fn=15	Fn=25
c_x (m/s)	0.010	0.022	0.032
λ_x (km)	368	270	236
k (m^{-1})	1.71×10^{-5}	2.33×10^{-5}	2.66×10^{-5}
λ_y (km)	334		
l (m^{-1})	1.88×10^{-5}		
R_0 (km)	70		
$k^2+l^2+R_0^{-2}$	8.50×10^{-10}	1.10×10^{-9}	1.27×10^{-9}
β_e	6.13×10^{-11}		
U (m/s)	0.082	0.078	0.080

Table 4.1: Calculation of U from the dispersion relation for frequency numbers 5, 15 and 25 at 101°E

Along the jet

The results presented in figure 3.16 showed that the zonal phase speed at a given frequency was approximately constant along the jet. If c_x does not change, the dispersion relation must be balanced by change in some other parameter. For a given frequency, the zonal wavenumber, k, is also constant along the jet, and the deformation radius, R_0 will not change significantly on the scales of the jet (see figure 4.1). The focus is therefore on the terms β_e and l.

Figure 4.6 shows meridional profiles of U and β_e downstream of the previous profile, at 108°E and 120°E. Assuming that l is constrained by the critical lines as before, values of U at these locations can also be calculated using the dispersion

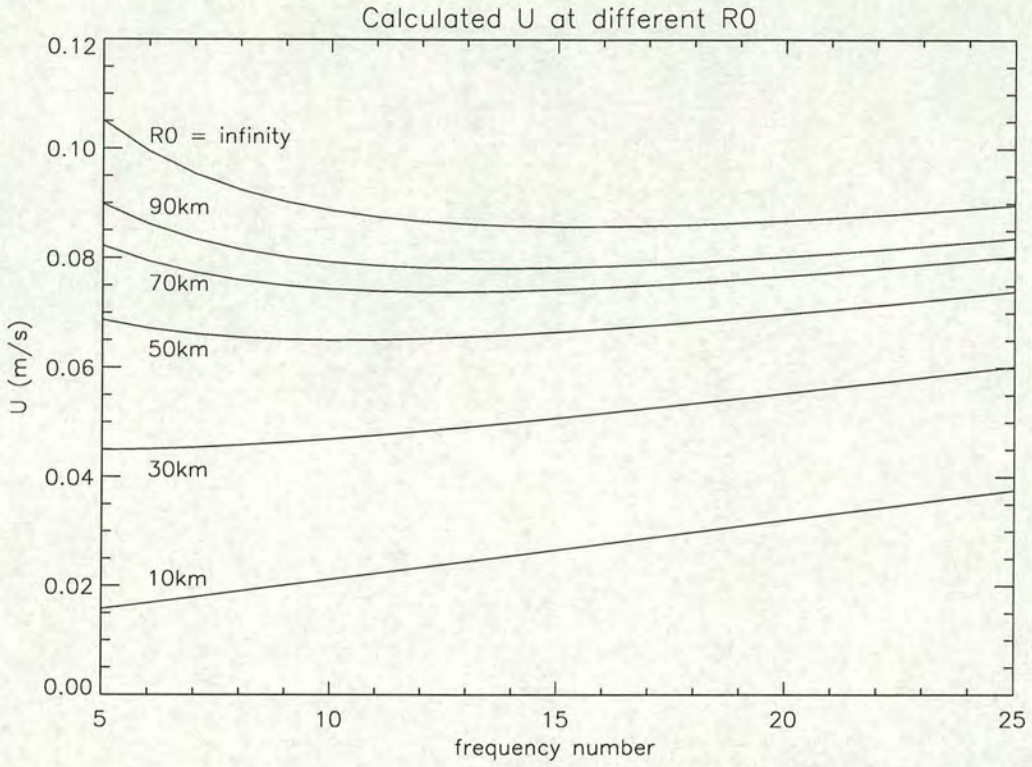

Figure 4.5: Calculated U against frequency number for different Rossby deformation radii (which are marked next to the appropriate curve). As R_0 increases, the curves converge to a maximum, when R_0 = infinity. This is appropriate for the barotropic mode R_0.

relation. The results are given in table 4.2 for the frequency number of 25, and using both the maximum and average value of β_e (where the average is taken between the critical lines). The only difference in the calculation at different locations is a change in l and β_e. Two columns are given for the profile at 120°E. The first is based on the same criteria as the other two profiles (with the jet width constrained by the critical lines). The final column uses a different jet width taken between the critical line to the North (46°S), and the point south of the jet maximum where β_e first becomes minimum (47.5°S). This is for comparison purposes. The profile of β_e at many longitudes in the jet does not become negative either side of the jet maximum. In these cases it is necessary to define the jet width between the points where β_e is a minimum. The profile at 120°E enables a comparison between the two definitions of jet width.

The change in calculated U (U_{calc}) at the different locations is compared with the actual change in U (U_{fram}) in table 4.3. The values presented in this table are an

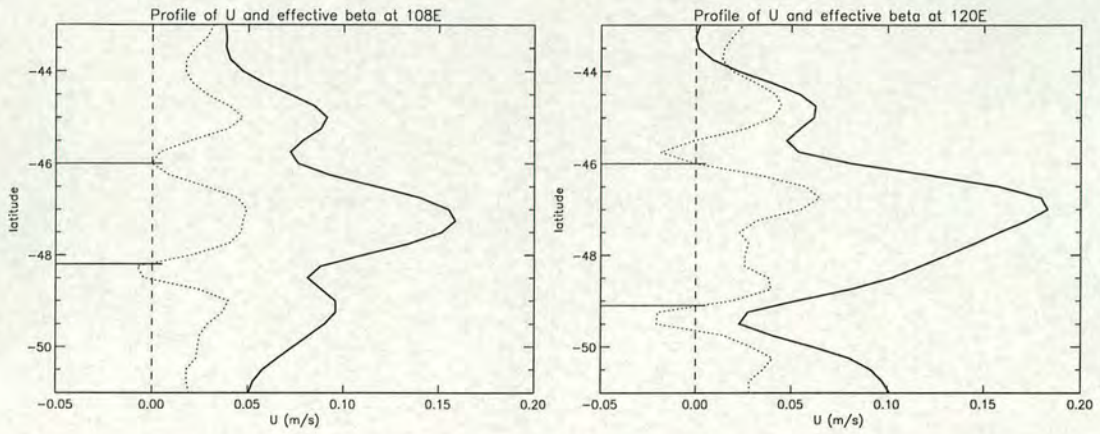

Figure 4.6: Profile of U (solid line) and effective beta, β_e, (dotted line) from FRAM at 108°E (left) and 120°E (right). The scale of β_e is not given, but the maximum value at 108°E is 3.02×10^{-11} at 47°S and the maximum value at 120°E is 3.95×10^{-11} at 46.75°S.

average over the frequency range. For the maximum case (calculation performed with maximum β_e and compared with maximum U_{fram}), the ratio U_{calc}/U_{fram} is the same for the first two locations, at 0.34. For the third location, this ratio is 0.38 in the first case and 0.31 when the smaller jet width is used. For the average case (calculation performed with average β_e and compared with average U_{fram}, where averages are over the jet width), the ratio is 0.32 and 0.34 for the first locations. At 120°E the ratio is 0.36 in the first case and 0.28 with the smaller width. From these results, U_{calc}/U_{fram} for both the maximum and average values agree well at the first two locations. At 120°E best agreement would be obtained for a jet width somewhere between the two values. The indication is that the smaller jet width is equally suitable for defining l as the full width between critical lines, and could be used at a longitude where critical lines do not exist. With such a small sample of locations, however, it is not possible to say much about the balance of the dispersion relation along the whole jet. These selected results have been included to show a breakdown of the calculation and raise the issue of the definition of jet width. To look at the balance of terms along the whole jet, U is calculated at each longitude, using the second definition of jet width where the profile of β_e does not become negative.

Variable	101°E	108°E	120°E (1)	120°E (2)
c_x (m/s)	0.032			
k (m^{-1})	2.66×10^{-5}			
λ_y (km)	334	489	689	334
l (m^{-1})	1.88×10^{-5}	1.28×10^{-5}	9.12×10^{-6}	1.88×10^{-5}
R_0 (km)	70			
$k^2+l^2+R_0^{-2}$	1.27×10^{-9}	1.08×10^{-9}	9.95×10^{-10}	1.27×10^{-9}
β_e (max)	6.13×10^{-11}	3.02×10^{-11}	3.95×10^{-11}	
β_e (ave)	3.89×10^{-11}	1.94×10^{-11}	2.07×10^{-11}	2.31×10^{-11}
U (m/s) (β_e max)	0.080	0.060	0.072	0.063
U (m/s) (β_e ave)	0.063	0.050	0.053	0.050

Table 4.2: Calculation of U from the dispersion relation for frequency number 25 at 101°E, 108°E and 120°E.

Quantity	101°E	108°E	120°E (1)	120°E (2)
Calculated U (β_e max)	0.077	0.054	0.069	0.057
Maximum U	0.223	0.159	0.183	
Ratio	0.34	0.34	0.38	0.031
Calculated U (β_e ave)	0.056	0.042	0.046	0.042
Average U	0.178	0.126	0.129	0.150
Ratio	0.32	0.34	0.36	0.028

Table 4.3: Comparison of calculated U and actual U, both maximum and average, as an average over the frequency range at 101°E, 108°E and 120°E.

Quantities relevant to the calculation and comparison of U along the whole jet are shown for reference in figure 4.7. The top left graph shows meridional maximum U_{fram} (solid line) and the meridional average U_{fram} over both variable width (dashed line) and fixed width (dotted line). The variable width is defined by critical lines, or by the first meridional minimum in β_e where critical lines do not exist. These variable widths, used for the meridional average, are given in the bottom left graph. The top right graph shows the maximum (solid line) and average (dashed and dotted line for variable and fixed width respectively) β_e, and the bottom right graph shows the meridional wavenumber, l, calculated on the basis that half a wavelength equals the jet width.

The curves in the top two graphs of figure 4.7 explain why the zonal phase speed,

c_x, varies little with mean zonal velocity, U, along the jet. β_e (the variation of which is governed by U_{yy}) varies with U, both for the maximum values and as an average over the jet width. There is therefore a balance between the variation of U and the variation of the β_e term in the dispersion relation. This is confirmed by the ratio of U_{calc}/U_{fram}. The ratio U_{calc}/U_{fram} for the whole jet and as an average over the frequency range is given in figure 4.8. The left-hand graph shows this ratio for the maximum value of U_{calc} (calculated from the maximum of β_e) and maximum U_{fram}. The right-hand graph shows this ratio for an average value of U_{calc} and U_{fram}, where the average is taken over the jet width used to define l. The solid line is calculated using a varying jet width and the dotted line is calculated using a fixed jet width, which is equal to the average of the varying jet width. Slight differences from values in table 4.3 are due to jet widths for the purpose of these graphs being rounded to the nearest 0.5° in latitude.

For the maximum case, U_{calc}/U_{fram} falls steadily along the jet, from just below 0.4 at 95°E to just above 0.3 at 120°E. If the dispersion relation is to be used to calculate U then this ratio must be constant along the jet. The decrease in this ratio results from a proportionally greater decrease in maximum β_e compared to maximum U_{fram} along the jet. This is due to the broadening of the jet to the East. This should be compensated for by the increase in jet width (which is observed in the meridional profiles). The criteria used for measuring the jet width therefore results in an increasing error (under-estimation) to the East. This was anticipated by the results in table 4.3. The results for a fixed jet width (dotted line) are inferior between 100 and 105°E, but otherwise compare well. This suggests the criteria used to measure jet width is not satisfactory. The conclusion is that the dispersion relation is sensitive to the jet width (the value selected to define l) when used to calculate a maximum jet velocity. Since the appropriate jet width is hard to measure even with the benefit of the velocity field (U_{fram}), this maximum jet velocity will not be measurable to useful accuracy using Rossby wave parameters. This is not surprising, however, because the Rossby waves span the whole jet width such that most propagation occurs away from the jet axis (line of meridional maximum jet velocity).

Results of U_{calc}/U_{fram} for the average jet velocity are better. The ratio remains

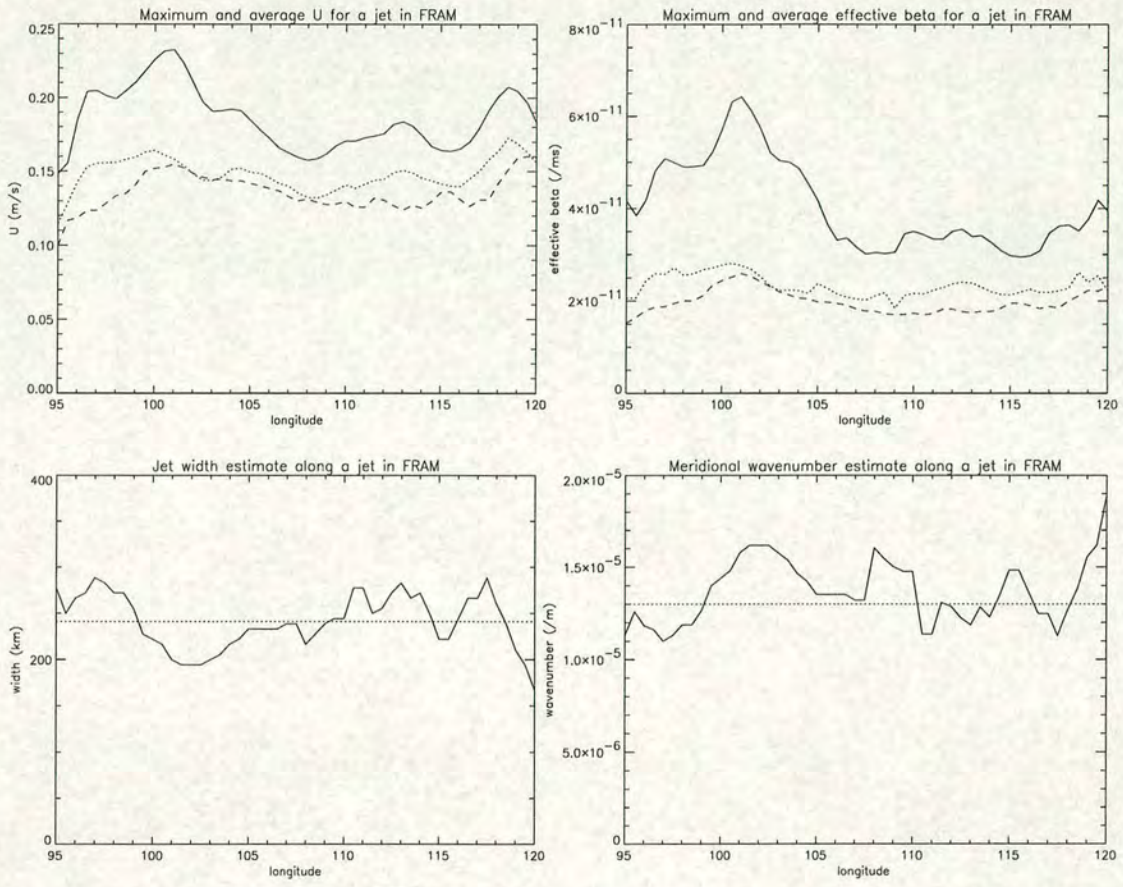

Figure 4.7: Quantities used in the calculation and comparison of U along a jet in FRAM. Top left: Meridional maximum U (solid line) and meridional average U (over variable width - dashed line, and fixed width - dotted line). Top right: Meridional maximum β_e (solid line) and meridional average β_e (over variable width - dashed line, and fixed width - dotted line). Bottom left: Estimated jet width and average used for fixed width. Bottom right: Meridional wavenumber corresponding to variable jet width and fixed jet width.

steady along most of the jet at just over 0.3, with significant differences only at either end of the jet. In this case the results for a fixed jet width are slightly steadier than with the varying width. This shows that over the fixed width, the average value of β_e changes in proportion to the average value of U as discussed above. This is consistent with a jet which is some combination of strong and narrow; weaker, broader and more rounded in profile; or strong, broader and less rounded in profile. This is observed in the three jet profiles at 101, 108 and 120°E.

The change in average U_{calc} therefore depends on changes in β_e. This was established from the FRAM U field and so it is not possible to say anything indepen-

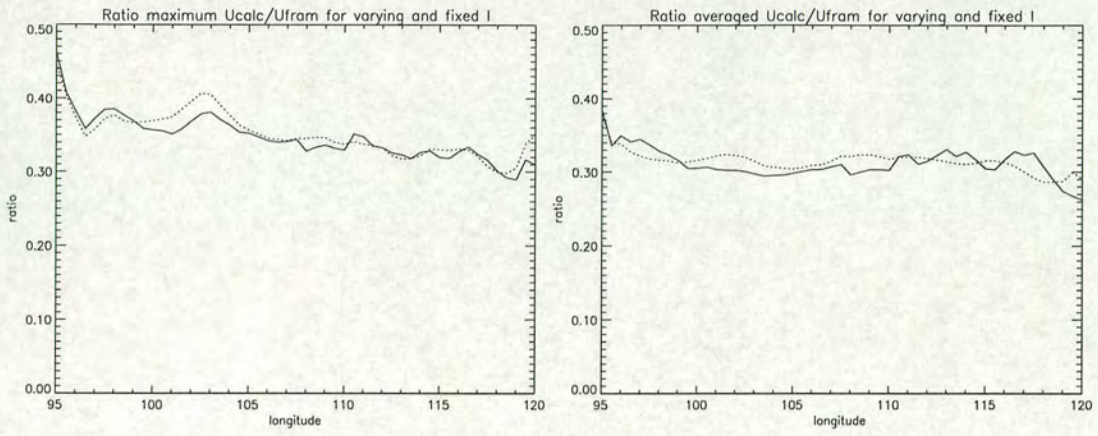

Figure 4.8: Ratio of calculated to actual U along jet

dent about the average U. An independent calculation of U might be possible if the dispersion relation is solved as a differential equation. This is achieved by rewriting β_e to $\beta - U_{yy}$, where β is a known constant:

$$U = c_x + \frac{\beta - U_{yy}}{k^2 + l^2 + R_0^{-2}} \tag{4.3}$$

Re-arranging gives,

$$U_{yy} + K_t^2 U - (\beta + c_x K_t^2) = 0 \tag{4.4}$$

where K_t^2 is the total wavenumber term $k^2 + l^2 + R_0^{-2}$. This is a Sturm-Louiville type equation with numerous solutions which are dependent on boundary conditions. A suitable solution is:

$$U = A\cos K_t y + \frac{\beta + c_x K_t^2}{K_t^2} \tag{4.5}$$

where A is a constant to be determined. This gives a sinusoidal jet structure which varies along the jet length according to the variation in meridional wavenumber, l (part of the term K_t^2), and the constant A. If l is fixed, as is reasonable from the results of figure 4.8, then this will have a fixed profile which varies in amplitude

according to A. Determination of A relies on boundary conditions which are hard to specify for a fixed width. The solution would be more appropriate for a varying jet width, in which case the profile and amplitude could vary along the jet in a more realistic way. Boundary conditions such as $U_{yy} = \beta$ could be applied at the side of the jet to determine A. This brings us back to the need for an independent and accurate measurement of the jet width, which is hard to obtain.

4.1.3 Discussion

The analysis presented above has focused on an individual jet in the FRAM mean flow. An attempt was made to relate the mean U (U_{fram}) to a value of U calculated using the dispersion relation (U_{calc}). Results for a single longitude showed that the maximum U_{calc} was less than the minimum U_{fram} over the latitude range of calculation. Typically, U_{calc} was one third of the actual value. This could be for three reasons. The first is that the dispersion relation, developed from simplified linear equations, does not hold in the real ocean. There is known to be problems with applying linear theory to reality (Killworth, 1997) and this could account for much of the discrepancy observed here. The second reason is potential differences between the FRAM model and the real ocean. Numerical models, and in particular finite difference models, are known to have problems with the realistic propagation of waves if the resolution falls to about five gridpoints per half wavelength (Hughes, personal communication). FRAM was designed to resolve Rossby waves but some waves are close to that limit (which represents a wavelength of about 250km). The final reason is that this comparison of velocities is based on surface values of U_{fram}. The mean velocity decreases with depth so the difference between U_{calc} and U_{fram} would be less if a depth-average value of U_{fram} was used in the comparison. The Rossby waves are not constrained to the surface, but have a depth influence dependent on R_0. R_0 in FRAM is larger than the mode 1 value because the flow is observed to be equivalent barotropic (Killworth, 1992), whereby flow at one depth is parallel and proportional to flow at another. The flow structure cannot be produced by a linear combination of barotropic and mode 1 baroclinic flows because in the top 1000m the velocity profile tails off more sharply with depth than it would for mode 1 baroclinic

behaviour. This gives rise to a lower depth average flow compared to mode 1. The effect of the equivalent barotropic mode compared to mode 1 is therefore a further reduction of the difference between U_{calc} and U_{fram} if a depth average is used. This supports the use of a depth-average U_{fram}, but surface quantities were used for comparison here because it is only those that can be measured by satellite. It is likely the discrepancy between calculated and model U arises from a combination of the factors discussed above.

The maximum U_{calc} and maximum U_{fram} were found not to vary in proportion along the jet. This was partly due to the problems with establishing a correct meridional wavelength, l. There are also problems with using the dispersion relation for such a specific purpose. The dispersion relation was developed for the case of uniform zonal flow, modified by a large-scale variation in zonal shear. Here it has been applied to a specific jet and there is no reason for the balance along the jet to hold for a quantity such as the maximum jet velocity. The variation in U_{calc} was shown to match the variation in U_{fram} along the jet in an average sense. This relationship held for a fixed jet width and so demonstrated that the mean profile of β_e varied in the same way as the mean profile of U_{fram} over a fixed width. This is an interesting result in itself. However, no information about the variation of one or other of these terms along the jet could be established in the absence of an accurate determination of the meridional wavenumber, l.

This section has demonstrated that there are problems with using the dispersion relation for relating wave information to the mean flow in the FRAM model. Though numerical models are known to have deficiencies in the accurate simulation of wave activity, the issues raised here suggest that it is not possible, without a greater understanding of the theory involved, to obtain mean flows in the real ocean from the measurement of Rossby waves. Even if the theory was fully understood, it is possible that the characteristics of Rossby waves do not uniquely specify the mean flow.

4.2 Simplified modelling

Another way of studying the relationship between Rossby waves and the mean flow is by using simplified ocean models. One such simplified model is the quasi-geostrophic (q-g) model, which has been used extensively in the past for studying Rossby wave behaviour (see section 2.2). A q-g model can be used to look at wave propagation under constrained conditions and so reveal mechanisms which might be applied in a more complex situation.

In the early stages of the project, a q-g model was developed and used to investigate the propagation of Rossby waves along an eastward zonal jet with a sinusoidal profile. One simple experiment illustrated some of the waveguide and stability properties of jets in the mean flow, although the overall insight gained from this work was limited. This experiment looks at the effect of the jet velocity on wave propagation and will be briefly described as an example.

Using the linearised q-g equations, the model solves for barotropic vorticity and streamfunction on a grid of 256 points in the x-direction by 100 points in the y-direction. The latitude range is 900km (9km gridpoint spacing) and β is taken at 50°S. The zonal resolution is the same, giving a longitude range of about 2300km. The background mean flow is re-circulating and consists of three sinusoidal zonal jets, travelling eastward with a minimum flow of 0cm/s at the troughs (at latitudes y=1, 34, 67 and 100). The maximum flow was varied for different cases in the experiment. Waves were forced into the model using a wavemaker positioned in the region y=40-60 and x=0-60. The wave period was 100 days and the wavelength (zonal and meridional) was 360km. A sponge extracted wave vorticity from the last 50 zonal gridpoints of the domain.

Snapshots of vorticity anomaly after a period of model run are shown in figure 4.9 for three different maximum jet velocities of 5cm/s, 10cm/s and 40cm/s. In each case, the model was run for an equivalent advection time (of 1000, 250 and 125 days for the flow of 5cm/s, 10cm/s and 40cm/s respectively) and did not reach steady state. The amplitudes of the anomalies are not given but it is the scales and position of the anomalies which are important. With a maximum flow

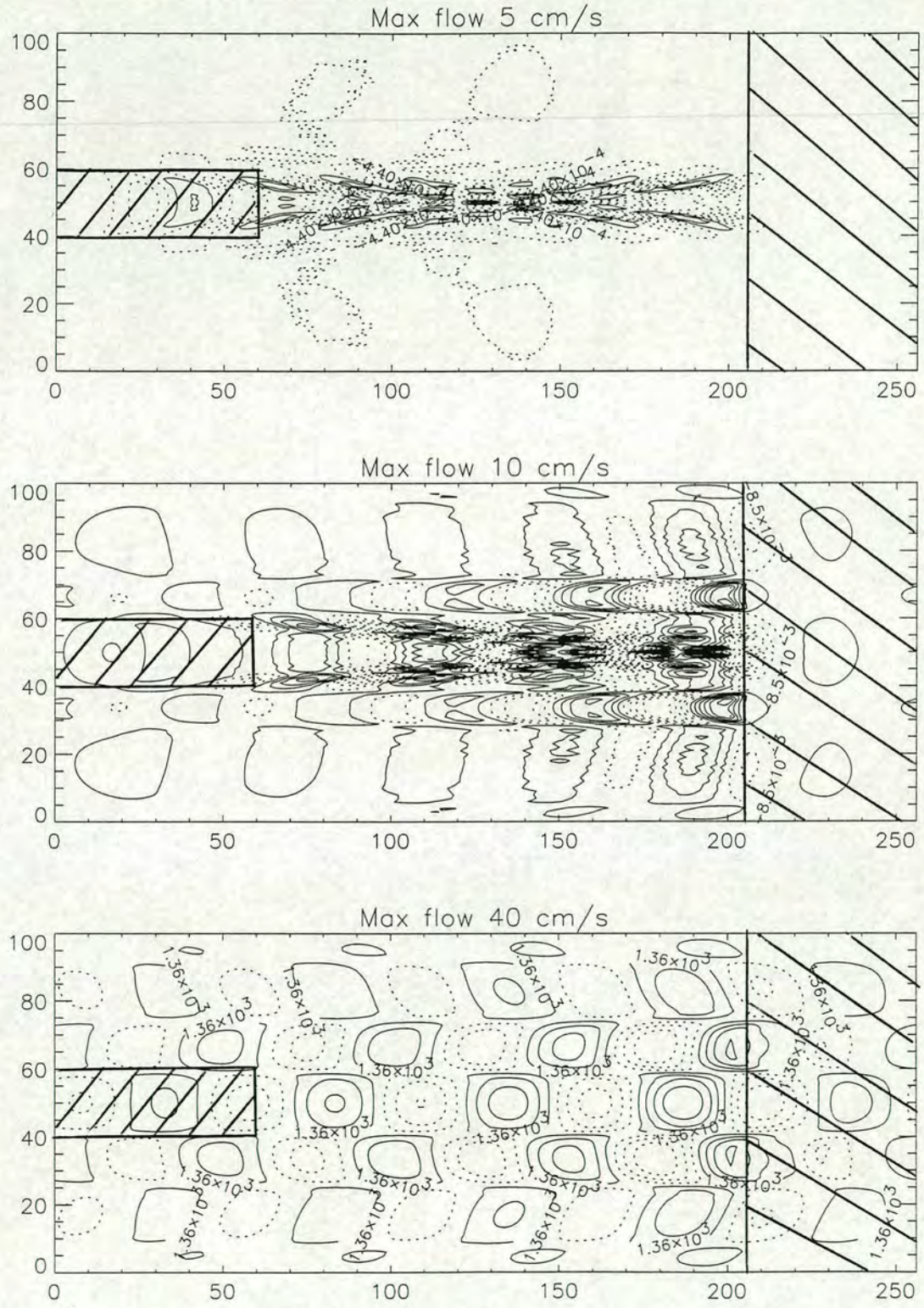

Figure 4.9: Vorticity anomaly snapshots for ideal jet model runs. In each case there are three sinusoidal, eastward jets. These are centred on y=17, 50 and 83 where the velocities are 5cm/s, 10cm/s and 40cm/s for the top, middle and bottom cases respectively. The minimum flow between jets is 0cm/s. The wavemaker is in the region y=40-60, x=0-60, and the sponge covers the last 50 gridpoints (see cross-hatched regions).

of 5cm/s, waves are trapped within the central jet and the meridional scales of anomalies have become much smaller than the meridional scale of the wavemaker. With a maximum flow of 10cm/s, the majority of activity is concentrated in the central jet, and has reduced in meridional scale as in the 5cm/s case. In addition, some wave activity has reached the jet minimum, and an even smaller amount into the side jets. In the trough, the zonal wavelength remains the same as the wavemaker scale but the meridional wavelength is approximately halved. The final case, with a maximum flow of 40cm/s, illustrates a case of barotropic instability. The wave activity has spread across all the jets and has approximately retained the wavemaker wavelengths. The amplitude of anomalies is much larger than the previous two cases (where the amplitudes were comparable) as the waves are growing exponentially.

Some understanding of these results is obtained by examining an equation for the total derivative of meridional wavenumber following a wave packet. This can be derived from the dispersion relation (Badger, 1997) and is given as follows:

$$\frac{D_g l}{Dt} = \frac{k}{K_T^2}\frac{\partial \beta_e}{\partial y} - k\frac{\partial U}{\partial y} \tag{4.6}$$

This equation states that the change in meridional wavenumber along a waveguide depends on the balance between the meridional gradients of β_e and mean U. If the first (β_e) term is larger than the second (U) term, l will increase along the waveguide and so the meridional wavelength will decrease and waves will be concentrated into the centre of the guide. If the U term is largest, the opposite happens and waves spread out as they move along the guide. In the results for a maximum flow of 5cm/s, the meridional velocity shear is relatively small and $D_g l/Dt$ is positive. The meridional scale decreases and the waves are trapped within the central jet. As the maximum velocity increase, the meridional velocity shear increases faster than the shear in β_e. With a maximum velocity of 10cm/s, the β_e term still dominates in the centre of the jet, where the meridional scale decrease. In the flanks, however, the velocity shear has become dominant and the waves spread meridionally from the central jet. As the maximum velocity is increased further, the extent to which waves spread out should increase. This is

happening when the maximum flow is 40 cm/s, but now instability has occurred and become dominant. This is due to β_e becoming negative in the jet flanks leading to exponential growth over the whole domain. In the real ocean, this situation would quickly lead to wave breaking and hence mixing of momentum in the jets and a change in the profile of mean flow.

The example given above is an illustration of the use of simplified modelling for studying waves in ideal propagation scenarios. Simple models are useful for studying specific aspects of Rossby wave characteristics. They are not, however, a suitable means of relating Rossby wave parameters to mean flows in a way which can be applied to the real Southern Ocean.

4.3 Topographic effects

Bottom topography was mentioned in the introduction as being an important influence on the circulation of the ACC. It is also known to be important for the dynamics of Rossby waves in regions where the flow interacts with topography. For example, barotropic eastward flow over a meridional, planetary ridge results in a standing Rossby wave downstream of the ridge. This is forced by the conservation of potential vorticity (f/H, where f is the coriolis parameter and H the depth) which results in a change in latitude (giving smaller f) in compensation for the reduction of H at the ridge. This section discusses the relevance of topography to the work presented in this thesis.

The theory of barotropic, topographic Rossby waves in the ocean was discussed in depth by Hughes (1992). A description of ocean flow in terms of topographic normal modes was presented, and these modes were calculated for the Southern Ocean. This work showed the modes to be very localised and therefore unsuitable for the description of flow on the large scale. Inclusion of the effects of both topography and stratification are required for an accurate dynamical description of dynamics in the Southern Ocean. Neglecting topography results in transport estimates for the ACC an order of magnitude too great (Munk and Palmén, 1951). Conversely, models which include topography, but not stratification, have

predicted transports almost an order of magnitude too small (Schulman, 1970; Bryan and Cox, 1972).

Recent studies of the influence of topography on the circulation of the Southern Ocean have not directly considered the effect of Rossby waves. Hughes and Killworth (1995) studied stratified flow on an f-plane (constant coriolis parameter), which does not support Rossby waves. It was shown that this flow regime is an approximation to first order of the large-scale circulation in this region. The topography was found to be a major constraint to this first-order flow. The resulting bottom pressure field also provided information on second order processes, such as Reynold's stresses, bottom friction and β, which become important in local areas which are associated with specific topographic features. Marshall (1995) makes the assumption that potential vorticity is uniform on surfaces of constant density. The stratification results in flow along contours which lie between those of constant f, which would result in too large a transport, and constant f/H, for which the transport is too small. The strength of currents at depth was found to depend on balances in both momentum and buoyancy, and eddies were shown to be important in the maintenance of the general mean flow.

Hughes et al. (1998) do consider the effect of Rossby waves in a study of dynamics in the Southern Ocean. They suggest that the interaction of the ACC with topography is influenced by the fact that the flow is supercritical with respect to first baroclinic mode Rossby waves. They also consider the representation of topography in FRAM to be a major cause of differences between FRAM and the real ocean. The discretised bottom leads to large values of topographic beta which heavily upsets the representation of the true topographic effects.

Such studies have improved our understanding of the interaction of topography and the large-scale, mean circulation. A comprehensive theory of topography and Rossby waves, however, is still not available. It is very possible that problems raised in section 4.1 may be blamed partially on this lack of knowledge. The analysis presented in this thesis relates to currents, eddies and Rossby waves at the surface and not depth-integrated transports. The circulation at the surface will be the least influenced of the whole water column as it is furthest from the

bottom. One area of the Southern Ocean where topography is unlikely to be important at the surface is the Southeast Pacific. From about 250°E to Drakes passage the Ocean is deep (>4km) and without major topographic features in the vicinity of the ACC (see figure 1.3). Elsewhere, however, shallower features like the Kerguelen Plateau, Campbell plateau, Southeast and Southwest Indian Ridges, and Pacific-Antarctic Ridge are certainly important to flow at the surface (see figure 1.3, taken from Hughes et al. (1998)).

While the topography may dictate the path of currents at the surface, the results presented in chapter 3, and those to be presented in subsequent chapters, are concerned with the behaviour of time varying current components within the mean flow. In studying this, it is not so important to explain the position of the mean flows and so topography may be less important. Results shown in figure 3.22, for example, show a relationship between eddy activity and mean flows in the FRAM output which was established without knowledge of topographic effects. This, and the fact that satellites only observe the surface, provides justification for the analysis of quantities at the surface in a self-contained way. The influence of topography must be a consideration, however, when interpreting results from the Southern Ocean.

4.4 Summary

Using FRAM output, this chapter has investigated the possibility of using Rossby wave measurements to infer mean flows. The main section (4.1) looked at the calculation of mean U from the linear Rossby wave dispersion relation, and compared this with the actual U. The analysis was performed for a jet south of Australia, which was associated with particularly good Rossby wave propagation and for which phase speeds were calculated in chapter 3. The calculated U was found to be significantly less than the actual U and reasons for this were suggested. Problems were identified with establishing the meridional wavenumber in the real ocean, but this could be estimated in FRAM from the knowledge of the effective beta field. The insensitivity of zonal phase speed to U was shown to result from a balance between U and effective beta (which depends on d^2U/dy^2).

The calculated U was shown to vary in proportion to actual U along the jet, in a meridional average sense, but this association did not deteriorate when a fixed meridional wavelength was used. The calculation relied on knowledge of the effective beta field, and this was determined from the actual FRAM U field. The conclusion is that Rossby wave parameters cannot be used to calculate eastward mean flows in FRAM, and therefore the real ocean, given our current understanding of Rossby wave theory.

Section 4.2 discussed briefly, with an example, the use of simplified modelling for relating Rossby wave propagation to mean flows. Although such models are useful for bridging the gap between theory and reality, their simplicity means it is not possible to use the results for a detailed description of active parts of the real ocean, such as the ACC. The final section, 4.3, raised the issue of topography and its effect on Rossby wave dynamics. Although topography is known to be important to Southern Ocean dynamics, its role is less relevant to the association between time varying and time mean currents at the surface. While the influence of topography need not be studied directly, it should be a consideration for results presented in the remainder of the thesis.

Chapter 5

Analysis of TOPEX/POSEIDON data

This chapter is the first of two major chapters which present results from the real Southern Ocean. It describes the analysis of sea surface height (SSH) data obtained by the TOPEX/POSEIDON satellite altimeters at ground-track crossover points in the Southern Ocean. Following a description of TOPEX/POSEIDON and of the data that is used, the analysis is presented in three sections. These sections describe similar methods to those used for analysis of FRAM output (chapter 3). Section 5.3 contains a study of the frequency of wave activity. Section 5.4 describes the measurement of Rossby wave phase speeds and section 5.5 presents the eddy quantities and the errors involved in their calculation.

5.1 Description of TOPEX/POSEIDON

The TOPEX/POSEIDON satellite was launched in August 1992 as a joint project between the United States' National Aeronautics and Space Administration (NASA) and the French Space Agency, Centre National d'Etudes Spatiales (CNES). The satellite's main instrument is a dual-frequency radar altimeter. This provides measurements of the height of the satellite above the sea surface, the wind speed, the wave height and the ionospheric correction. Once processed, the data gives the height of the sea surface above a reference ellipsoid to an accuracy of better than 5cm (Shum et al, 1995).

The satellite orbits at a height of 1336km and with an inclination of 66.04°. It operates on a repeat cycle of 9.9156 days during which time it makes 127 revolutions. The resulting ground track is a periodic pattern between about −66°S and 66°N which shifts by 2.835° in longitude every cycle. Individual data points are an average of 10 or 20 measurements (for the TOPEX and POSEIDON altimeters respectively) and are recorded every second, at a spacing of 5.8km along the ground-track.

5.2 TOPEX/POSEIDON data

This section describes the data used for analysis in this chapter. In chapter 3, zonal gradients of SSH were used in the analysis of wave activity. This gradient can be resolved from the along-track gradients at crossover points (see 5.2.2, below). Both the zonal and meridional gradients of SSH at crossover points will be used in this chapter, in preference to pure height data. The advantage of using slopes instead of heights is the reduction of errors from long-wave sources such as orbit, tides and bias due to sea state and electromagnetic interference. The disadvantage is the poor spatial resolution of crossover points (see below), and for this reason height data will be used in chapter 6 as a comparison.

5.2.1 Corrections to raw data

TOPEX/POSEIDON SSH data were obtained from the AVISO merged GDRs (AVISO, 1992). A single measurement of SSH is subject to several corrections for processes that affect the signal and the SSH, independent of dynamics. Path length corrections were applied for dry atmospheric pressure (from modelling), atmospheric water vapour (from radiometer measurements), and ionospheric effects (from the dual frequency altimeter). The SSH was also corrected for tides using a tidal model (Le Provost et al., 1994), the inverse barometer and sea state bias (Gaspar et al., 1994). These corrections were applied by Chris Hughes of the Proudman Oceanographic Laboratory, Merseyside.

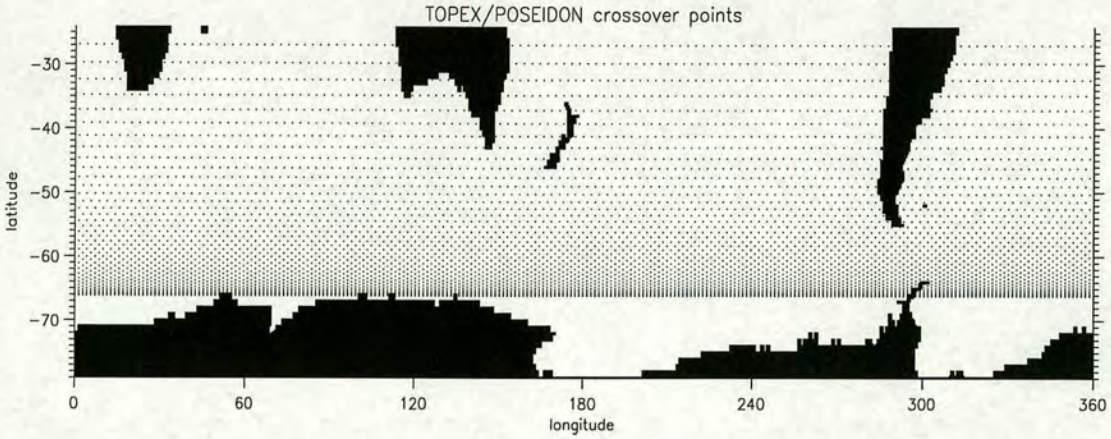

Figure 5.1: Distribution of TOPEX/POSEIDON crossover points

5.2.2 Crossover points

The ascending and descending passes of different revolutions in a cycle coincide at ground-track crossover points. The positions of the ground-track crossover points in the Southern Ocean are given in figure 5.1. While the zonal spacing is always 2.835° of longitude, the meridional spacing increases in a non-linear way when moving from 66°S towards the equator. At 66°S this is a fraction of a degree, and at 25°S this is about 3° of latitude. Ignoring land, 50% of the crossover points in figure 5.1 lie south of 60.5°S. At crossover points, the along track gradient of SSH from ascending and descending passes can be resolved into zonal and meridional gradients of SSH for convenient calculation of v and u. The accuracy of these quantities is influenced by the crossover angle which varies non-linearly with latitude. At 66°S the ground tracks subtend an angle of 1.4° to the zonal direction, giving good accuracy in v but poor accuracy in u. At 24°S this angle is 67.6°. Accuracy is discussed in 5.2.4, below.

5.2.3 Zonal and meridional gradients

177 cycles (cycles 10 to 187) of TOPEX/POSEIDON data were used in the analysis. This gave a time series of 4.8 years from December 1992 to October 1997. Data were obtained from Chris Hughes in the form of along track gradient of

SSH for ascending and descending passes at ground-track crossover points. The ascending and descending passes were less then five days apart. The corrected SSH measurements had been linearly interpolated onto a set of latitudes with an along-track spacing of 7km. The along-track slope was then taken as a linear fit to 15 consecutive height measurements (spanning 100km) centred on the crossover point. The zonal (H_x) and meridional (H_y) gradients of SSH were calculated according to the formulas $H_x = \frac{1}{2}(H_a + H_d)/cos\theta$ and $H_y = \frac{1}{2}(H_a - H_d)/sin\theta$ respectively, where H_a and H_d are the along-track slopes of the ascending and descending passes respectively and θ is the angle between the altimeter track and the zonal direction. The mean was subtracted to give the gradient anomalies over the 4.8 year period.

5.2.4 Accuracies

The accuracy of a single SSH measurement is less than 5cm rms (Shum et al., 1995). The accuracy of the along track slope is estimated to be 1 cm per 100 km, which compares well to the typical signal for moderate activity of 20 cm per 100 km. The accuracies of the zonal and meridional gradients in SSH depend on the crossover angle which varies with latitude. This has been computed assuming an along-track error of 1 cm per 100 km and assuming errors are Gaussian and uncorrelated. The errors are shown against latitude in figure 5.2. The error in zonal gradient is least to the South and increases from 0.7 cm per 100 km to 1.85 cm per 100 km across the Southern Ocean. The error in meridional gradient is least in the North (less than 0.8 cm per 100 km) and increases rapidly south of 60°S to reach over 2 cm per 100 km at 65°S. Equal accuracy for zonal and meridional gradients is when the ground tracks are orthogonal at 56.5°S. Here the accuracy is the same as the along-track slope, at 1 cm per 100 km.

The errors shown in figure 5.2 are only the result of the combination of the error in the along track slopes when calculating zonal and meridional slopes. In addition, there are temporal errors due to ascending and descending passes not being coincident. These errors will vary between crossover points and will not depend on latitude. They can be considered as a random distributed error which

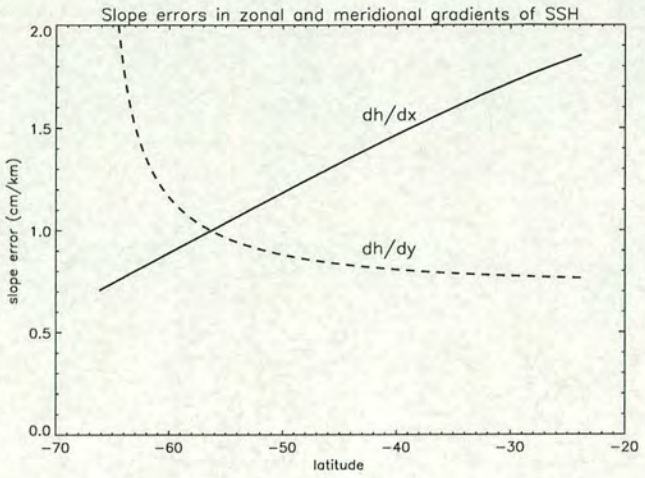

Figure 5.2: Error in zonal gradient (solid line) and meridional gradient (dashed line) of SSH for different latitudes, when calculated from along-track slopes with an error of 1 cm per 100 km

is not expected to interfere with any analysis.

5.2.5 Representation of crossover data on a grid

For clear representation of crossover data on a cylindrical equidistant grid (equal spacing for latitude and longitude), data was averaged within 3° E-W by 1° N-S boxes at a resolution of 1° in longitude by 0.5° in latitude. The resolution of the data then depends on latitude according to the meridional spacing of crossover points (see figure 5.1). This is illustrated in figure 5.3 which shows the eddy variance from data at crossover points. South of 65°S, poor results are obtained due to lack of measurements and acute crossover angles. North of 52°S there are white zonal bands where there is insufficient proximity to crossover points for the presentation of data. All the TOPEX/POSEIDON results presented in this chapter are represented in this way for comparison with FRAM results. The eddy variance illustrates the path of the ACC and is a useful reference for results in subsequent sections. It will be discussed more fully in section 5.5.

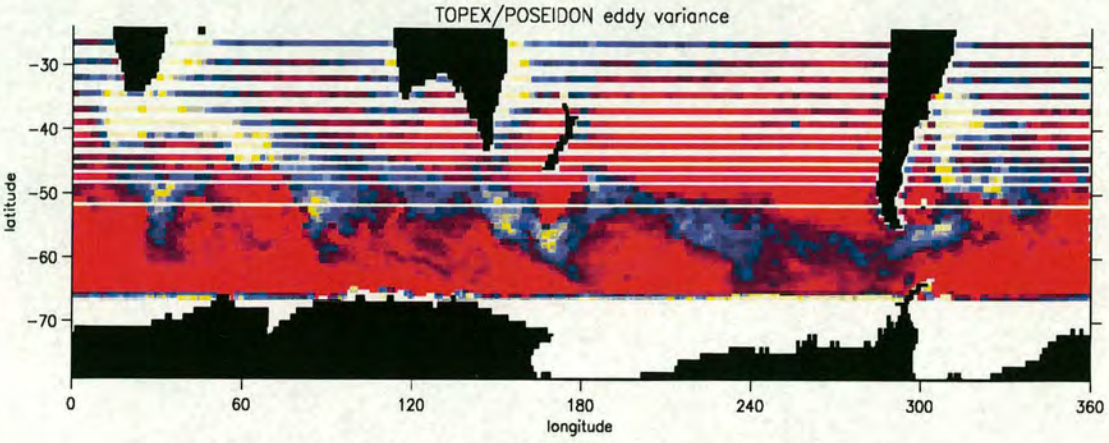

Figure 5.3: Grid representation of TOPEX/POSEIDON variance

5.3 Spatial correlations in frequency

This section applies the fractional power and EOF analysis described in section 3.2 to the TOPEX/POSEIDON crossover data. The aim is to look for waveguide jets in the ACC, which are expected to trap higher frequency waves at their centre (see section 3.2.2). It will be seen that the mean normalised spectrum shows a much smoother response than was found with FRAM. High spectral accuracy is achieved at crossover points, though at the expense of spatial resolution.

5.3.1 Power spectrum analysis

The mean, normalised, power spectrum was calculated for dh/dx data at TOPEX/POSEIDON crossover points, using the same method applied to the FRAM output (see section 3.2). Missing data in a time series at a point was filled by linear interpolation where there were no more than two consecutive missing values. Otherwise the time series was rejected. Unfortunately, this results in significant loss of data to the South, where ice coverage affects measurement for parts of the year. Some other missing data are due to bad satellite tracks and the odd spurious point. The available spectral data, and the density of crossover points in the gridded representation are illustrated in figure 5.4. Despite the missing data,

comparison with figure 5.3 shows that the majority of high variability regions are visible.

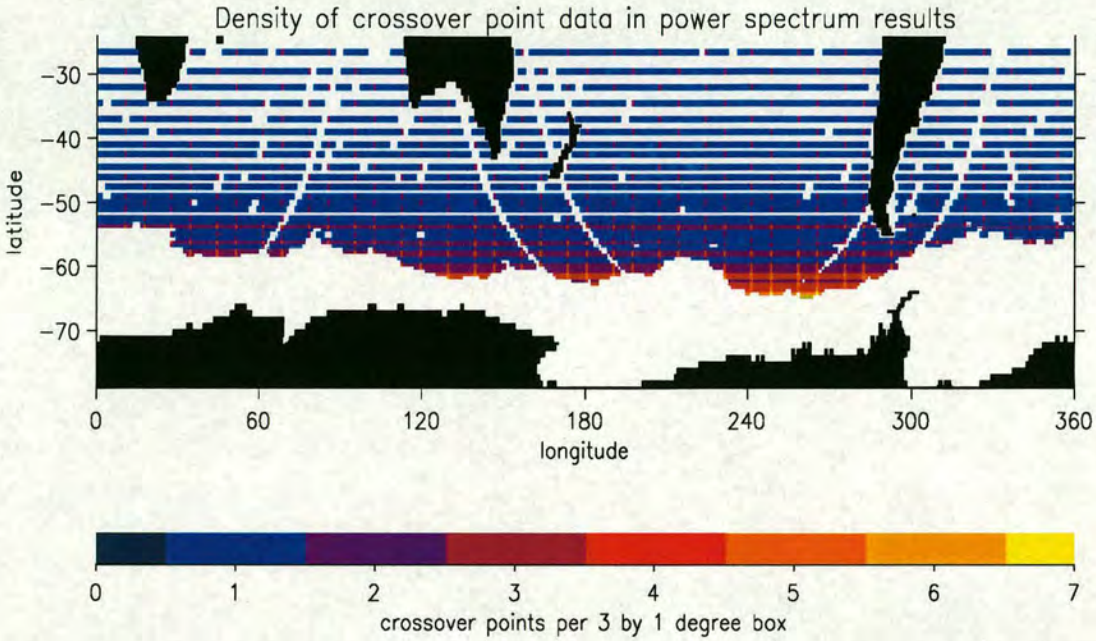

Figure 5.4: Availability and density of crossover point data in the power spectrum results.

The frequency components from FFT, and associated periods, are given in table 5.1 for periods of 45 days and more (40 out of the total of 88 components). Lower periods exist down to 20 days, but are not relevant to this study of Rossby wave propagation. The mean, normalised power spectrum for these periods is shown in figure 5.5 (solid line) together with the standard deviation (dotted line). Compared to FRAM (figure 3.4), this mean spectrum is much smoother. The standard deviation is less than the mean showing less spatial variability of the normalised spectra. The availability of data means that higher variability regions are more represented than they were in FRAM. There is no data for the quiet regions to the South, and only limited data for the quiet regions to the North. The highest availability of data is in the regions of most interest, especially between 120 and 300°E. The more even distribution of normalised power is an improved foundation for the EOF analysis compared to FRAM, which suffered from the weighting of normalised power spectra in quiet regions. Of final note in the mean spectrum is a peak centred at period 62 days, and this corresponds to the M2 tidal

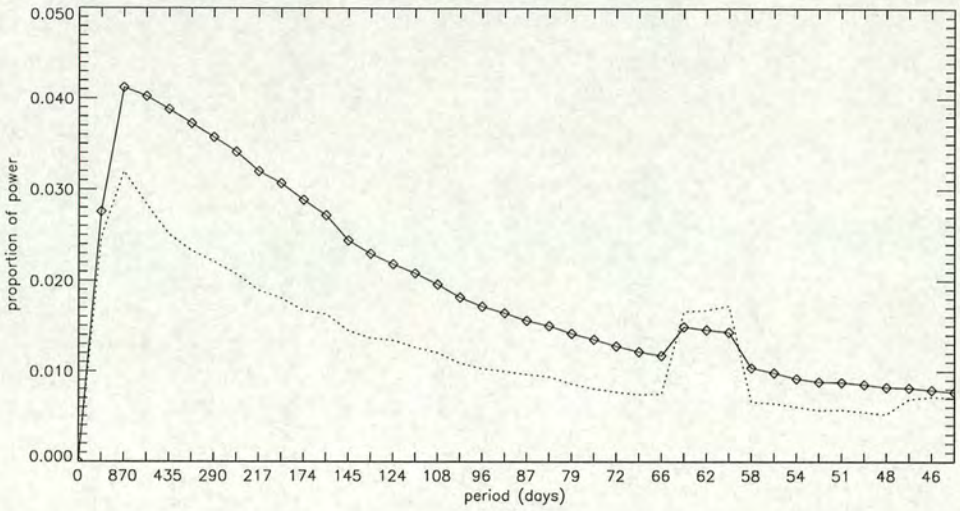

Figure 5.5: Mean, normalised power spectrum in the Southern Ocean from TOPEX/POSEIDON.

alias frequency (Hughes, 1995), which arises due to errors in the tidal correction procedure. This period is fixed by the satellite orbit and is below the period of Rossby wave activity. It will not, therefore, interfere with any analysis.

Component	0	1	2	3	4	5	6	7	8	9
Period	-	1740	870	580	435	348	290	249	217	193
Component	10	11	12	13	14	15	16	17	18	19
Period	174	158	145	134	124	116	108	102	96	92
Component	20	21	22	23	24	25	26	27	28	29
Period	87	83	79	76	73	70	67	64	62	60
Component	30	31	32	33	34	35	36	37	38	39
Period	58	56	54	53	51	50	48	47	46	45

Table 5.1: Period in days for 40 components of the TOPEX/POSEIDON normalised power spectrum.

Figures 5.6 and 5.7 shows the spatial field for the normalised power spectrum (i.e. fractional power) at selected periods of 870, 348, 174 and 87 days. The scale is presented as a relative amplitude for easy comparison. Actual amplitudes are given by this relative scale multiplied by 5 times the value at the respective period from the mean normalised spectrum in figure 5.5 (e.g. at the period of 870 days, 1.0 represents an amplitude of $1.0 \times 5 \times 0.0419$). These periods are chosen

as a representative, and for comparison with the EOF results presented later. At the long period of 870 days, some latitude dependence is observed with generally less fractional power to the North and more to the South. Within this pattern there are some regions to the south with low fractional power, such as at 80°E, 170°E and 220°E. At the near-annual period of 348 days, the pattern is similar to 870 days but with higher amplitudes further North in the pacific. Compared to FRAM, these fractional power fields change much more smoothly from one period to the next.

Spatial fields for periods of 174 and 87 days show that the fractional power is more evenly distributed compared to FRAM, where high fractional power at similar periods was confined to regions associated with the ACC (see figure 3.6). This is likely to be due to the influence of the quiet regions in FRAM which are less represented in the crossover results. At the period of 174 days, the quiet regions to the South observed in the spatial fields for periods 870 and 348 days are still evident, but at the period of 87 days there are quiet regions elsewhere. While there is significant fractional power to the South at all of these periods, the fractional power to the North increases as the period decreases (with the exception of the South Pacific, which showed high fractional power at annual periods). This is consistent with the model suggested in the motivation for the EOF analysis (section 3.2.2). Specific features of high fractional power at a period, which might relate to jets in the mean flow, are not obvious from these fields. Results of the EOF analysis presented in the next section will prove to be more useful.

5.3.2 EOF analysis

EOF analysis was performed with the TOPEX/POSEIDON spectral data in the same way as with the FRAM data (section 3.2.2), using gridpoints where the data exists. The most significant eigenvalues of the spectral covariance matrix, corresponding to the most significant EOFs, are shown in figure 5.8. As with FRAM, the relative magnitude of the eigenvalues indicates the hierarchy of the EOFs and their proportion of relevance to the total spatial variation of the spectrum anomalies. EOF number 1 represents 28% of the total variation. This is

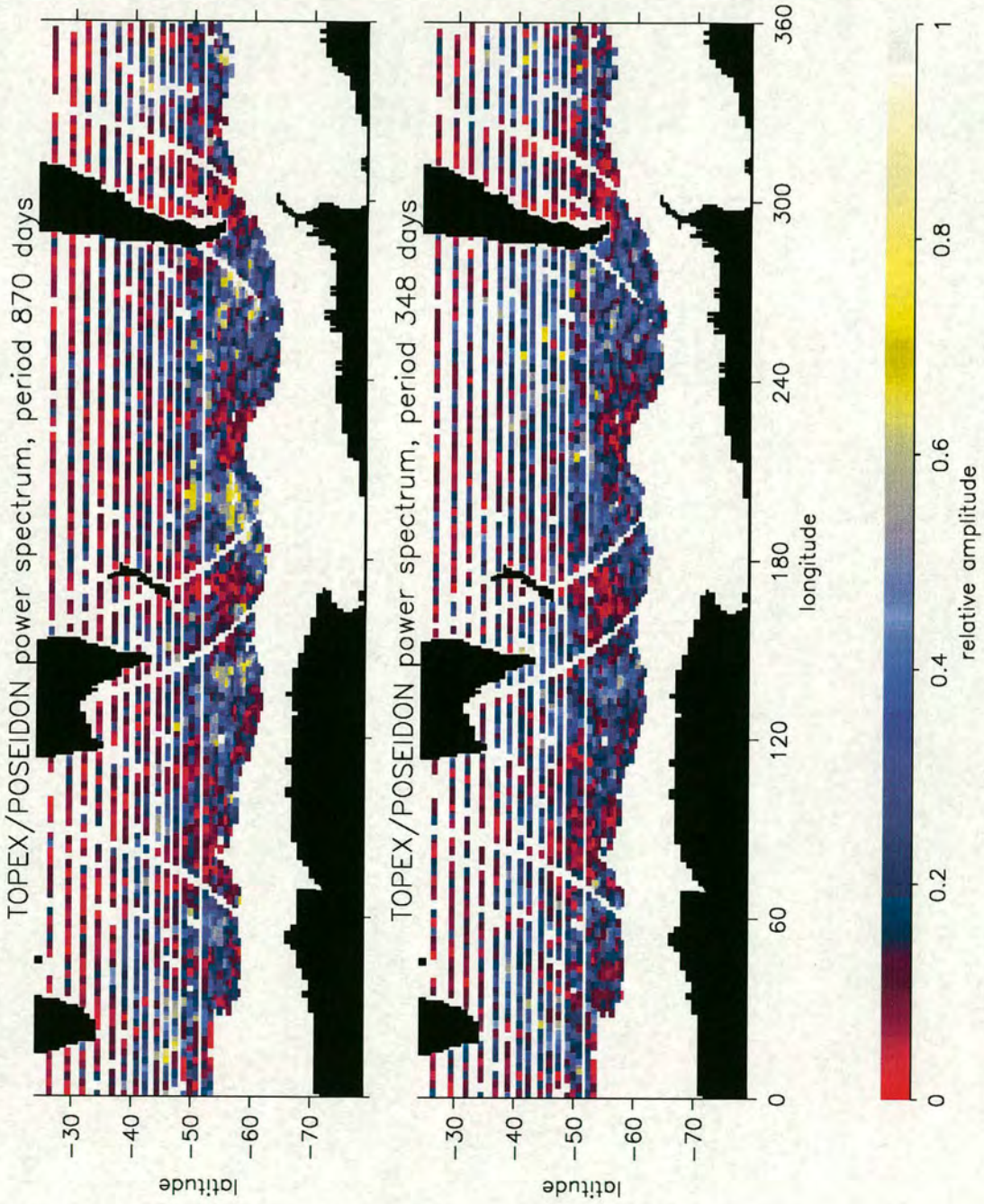

Figure 5.6: Field of the normalised power spectrum for periods 870 days (top) and 348 days.

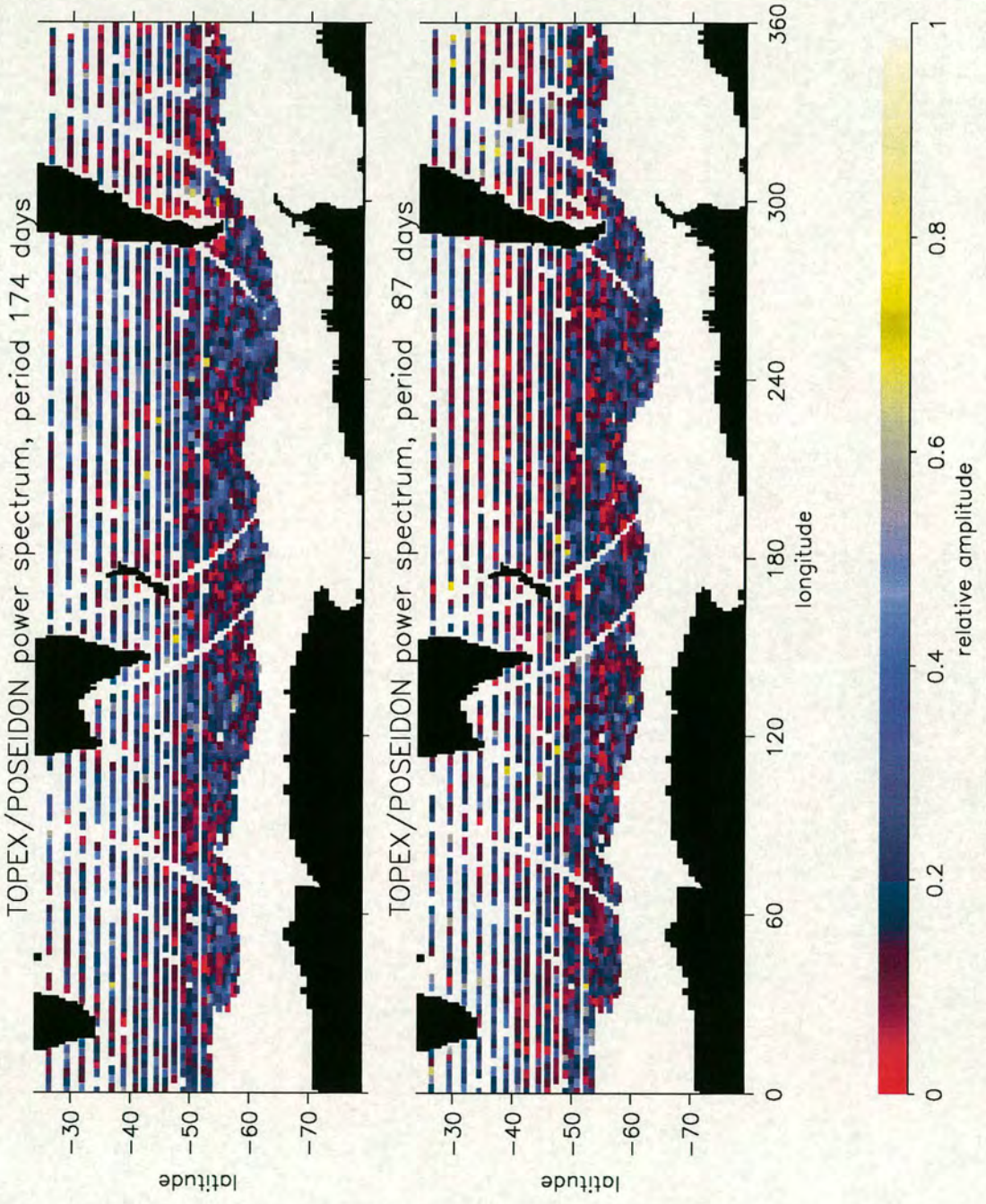

Figure 5.7: Field of the normalised power spectrum for periods 174 days (top) and 87 days.

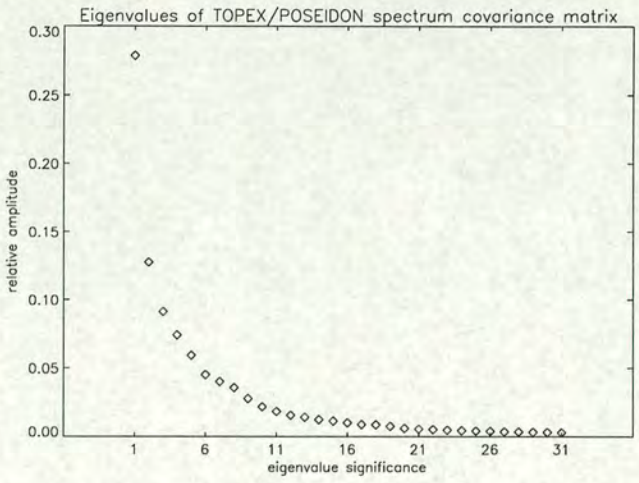

Figure 5.8: Most significant eigenvalues of the covariance matrix of the TOPEX/POSEIDON spectrum field

about half of the FRAM equivalent (where EOF 1 represented 55% of the total) therefore less dominant. EOF number 2 represents 13% of the variation compared to 22% with FRAM. The proportion represented by subsequent EOFs decreases less rapidly with TOPEX/POSEIDON than it did with FRAM, such that EOF 3 and upwards represent more of the total here than the equivalent in FRAM (e.g. EOF 3 accounts for 9% of the variation compared to 8% with FRAM). The most significant six eigenvalues represent 67% of the total. With FRAM, the first six eigenvalues represented 95% of the total and the same proportion here represents 87% of the total. This lower percentage, and the less rapid decrease in eigenvalue significance compared to FRAM, are due to the real world being more variable than the model.

Figure 5.9 shows the most significant six EOFs plotted down to periods of 60 days. EOF 1 represents 28% of the total. It shows that the principal pattern of spatial variation is due to regional differences in fractional power at the longest periods (greater than 174 days, and maximum at 870 days) balanced by fractional power at all shorter periods. There will be regions with higher fractional power at the longer periods balanced by lower fractional power at the shorter periods, and vice-versa. This is consistent with a variation in fractional power with latitude (as discussed in the motivation for the EOF analysis in section 3.2.2), and the extent

of this will be seen in the spatial fields presented below. EOF 2 represents 13% of the total. This shows a balance between regional differences in fractional power at periods between 134 days and 435 days ('middle' periods) and all other periods, especially periods longer than 435 days which have a larger amplitude than the short periods. The peak at the middle periods is not centred on the annual period but on the period of 248 days. It is likely to be influenced by annual variations and Rossby wave activity. EOF 3 (9% of the total) does have a peak at the annual period (348 days), with this and very short periods balanced mainly by periods between 79 and 248 days. As this is the first EOF in which the annual cycle features strongly, the annual cycle is fairly weak in this frequency analysis (it featured in both EOF 1 and 2 with FRAM). This is a plausible result, as ice affected regions are excluded from the analysis, and the best coverage of data coincides with much of the ACC, which is highly variable and will be dominated by shorter period activity. EOFs 4, 5 and 5 are of less significance (7.5%, 6% and 5% of the total respectively). They are shown here as they are included in the EOF reconstructions presented in 5.3.2. They also show, along with the first three EOFs, that the number of changes in sign in an EOF correspond to the number of the EOF. This was not observed in the FRAM EOFs, possibly due to the stepped nature of the FRAM mean normalised spectrum.

Spatial fields - individual EOFs

The spatial fields for the first four individual EOFs are shown in figure 5.10 (EOF 1 and 2) and figure 5.11 (EOF 3 and 4). The fields were generated as described for the FRAM analysis in section 3.2.2, with a sign convention such that a point with a fractional power anomaly similar to the shape of the EOF will be positive. The spatial fields have an equivalent scaling which is presented as a relative amplitude for easy comparison.

The field for EOF 1 is overlaid with mean surface temperature contours from ATSR measurements (from figure 1.3). This is useful to introduce at this stage, as it provides an independent indication of features in the mean flow and a means of comparison with bottom topography using figure 1.3. Positive and negative

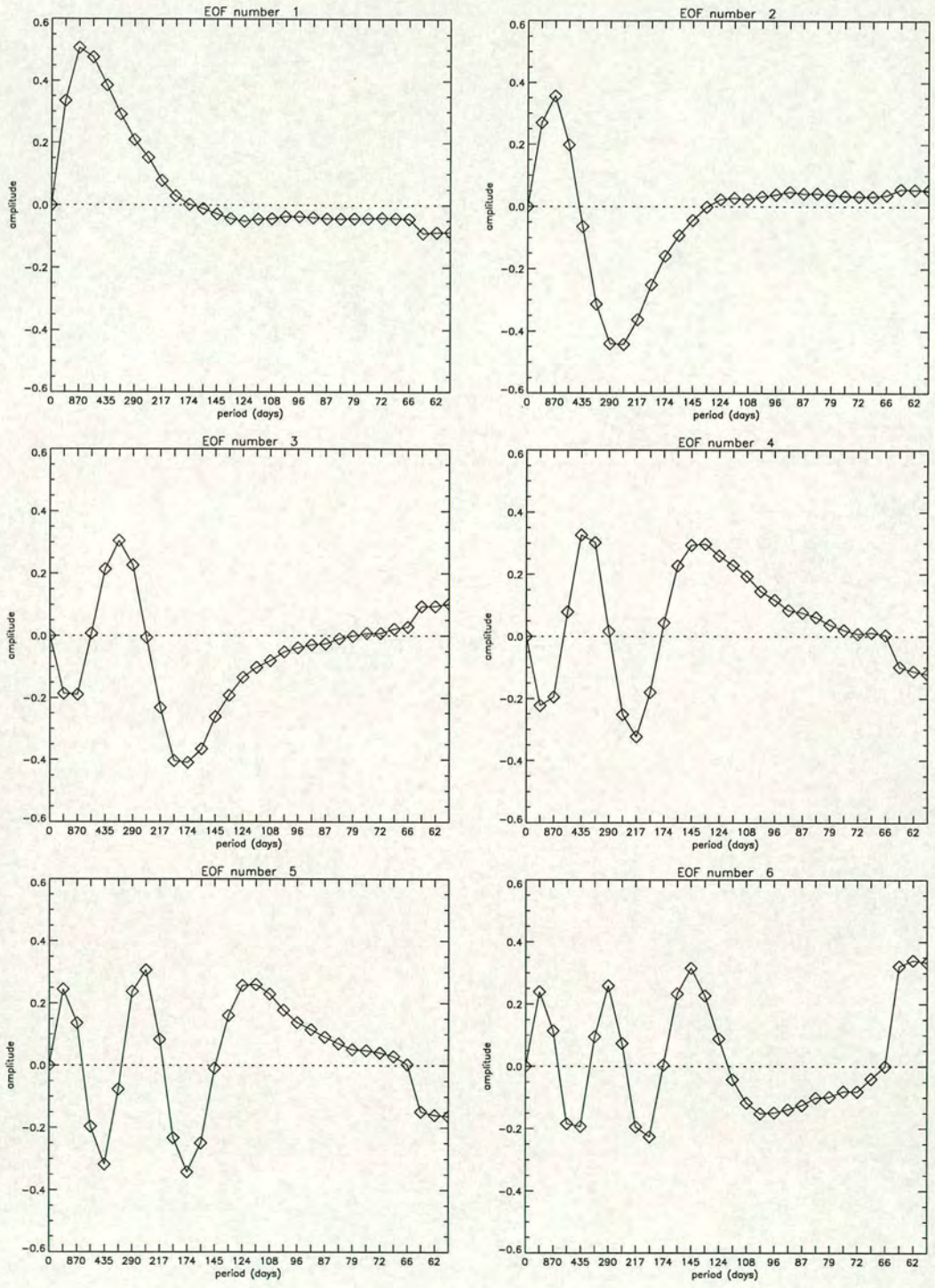

Figure 5.9: The dominant EOFs of the TOPEX/POSEIDON spectrum field. The proportion of variation accounted for by each EOF is as follows (top left to bottom right): EOF1 - 27.6%, EOF2 - 12.6%, EOF3 - 9.0%, EOF4 - 7.5%, EOF5 - 5.9% and EOF6 - 4.7%.

regions in the field are on large scales, with negative regions dominating to the North and positive regions more prominent in the South. Positive regions show high fractional power at long periods (greater than 174 days) and low fractional power at shorter periods because of the shape of the EOF spectrum (figure 5.9). This principal variation in fractional power shows overall consistency with the idea of an equatorial waveguide, with shorter periods being trapped closer to the equator (where negative regions show a higher proportion of power at shorter periods). There are notable exceptions to this, with some prominent negative regions to the south of the field. Some of these can be associated with probable jets in the mean flow (where temperature contours are close together), such as at (48°S, 110°E), two jets around (56°S, 210°E), and at (60°S, 310°E). These features are likely to be due to Rossby wave propagation and may indicate waveguiding. Other negative regions to the south, at (50°S, 80°E), (55°S, 170°E) and (42°S, 320°E), are associated with highly active regions (by comparison with the eddy variance, figure 5.3), and so relate to eddy generation. These are east of shallow topography (by comparison with figure 1.3), where eddy generation is well known about (Gille, 1997).

Another definite negative feature is to the east of South Argentina. Inspection of the field of normalised power for the tidal alias period (62 days) demonstrates it is this region that is responsible for the small peak at the alias period in the mean power spectrum (figure 5.5). The sign of this region in the spatial fields for individual EOFs is therefore determined by the sign at the period of 62 days in the associated EOF spectrum (negative in EOF 1 and 4, positive in EOF 2 and 3). Strong positive features are located to the west of shallow topography (by comparison with figure 1.3). These features correspond to regions of high fractional power in the field of fractional power at a period of 870 days (figure 5.6) and this is expected from the structure of the EOF spectrum. Negative features correspond to low fractional power at this period, showing the influence of long periods in EOF 1.

The spatial field for EOF 2 has smaller scale features than the field for EOF 1. Positive regions show low fractional power at periods between 134 and 435 days and high fractional power at shorter periods. High fractional power at periods

longer than 435 days will also contribute to positive regions. Negative regions show high fractional power at periods between 134 and 435 days. Rossby wave activity, which will have periods both longer and shorter than 134 days, will appear as positive and negative features. In a couple of locations within the expected path of the ACC (58°S, 270°E; and 55°S, 250°E), zonal features are positive to the West and negative to the East. These may indicate a waveguide within the eastward flow, with longer periods propagating further downstream. The resolution it not sufficient to capture a meridional variation within these features. The negative features which related to the mean flow in the spatial field for EOF 1 are not evident in this spatial field, so their influence was fully captured by EOF 1. Much of the South Pacific is negative, and this corresponds with high fractional power at a period of 348 days (figure 5.6), indicating annual variation as it did with EOF 2 in FRAM (figure 3.9).

The spatial fields for EOFs 3 and 4 are less relevant and harder to interpret than the fields for EOF 1 and 2. The tidal alias region east of Argentina stands out strongly in each, and there are many small scale positive and negative features which depend on the local fractional power anomaly and EOF spectra. Features in the spatial fields for these first four individual EOFs may indicate waveguide regions associated with frequency bands, depending on peaks in the corresponding EOF spectrum. The details associated with particular frequencies, however, are hard to distinguish. The EOF reconstruction of spatial fields at individual frequencies should clarify waveguide features observed in these fields.

Spatial fields - cumulative EOFs

Figure 5.12 to 5.15 show a sequence of EOF reconstructions of the power spectrum anomaly field for frequency numbers 5 (period 348 days) to 20 (period 87 days), a range of periods expected to cover the majority of Rossby wave activity. These fields are obtained by the summation of the spatial fields (projected at the required period) for the dominant 6 EOFs, which represent 87% of the total variation. As with the FRAM results, positive values (blue) show areas with more than average fractional power at a period. Coherent positive regions are an

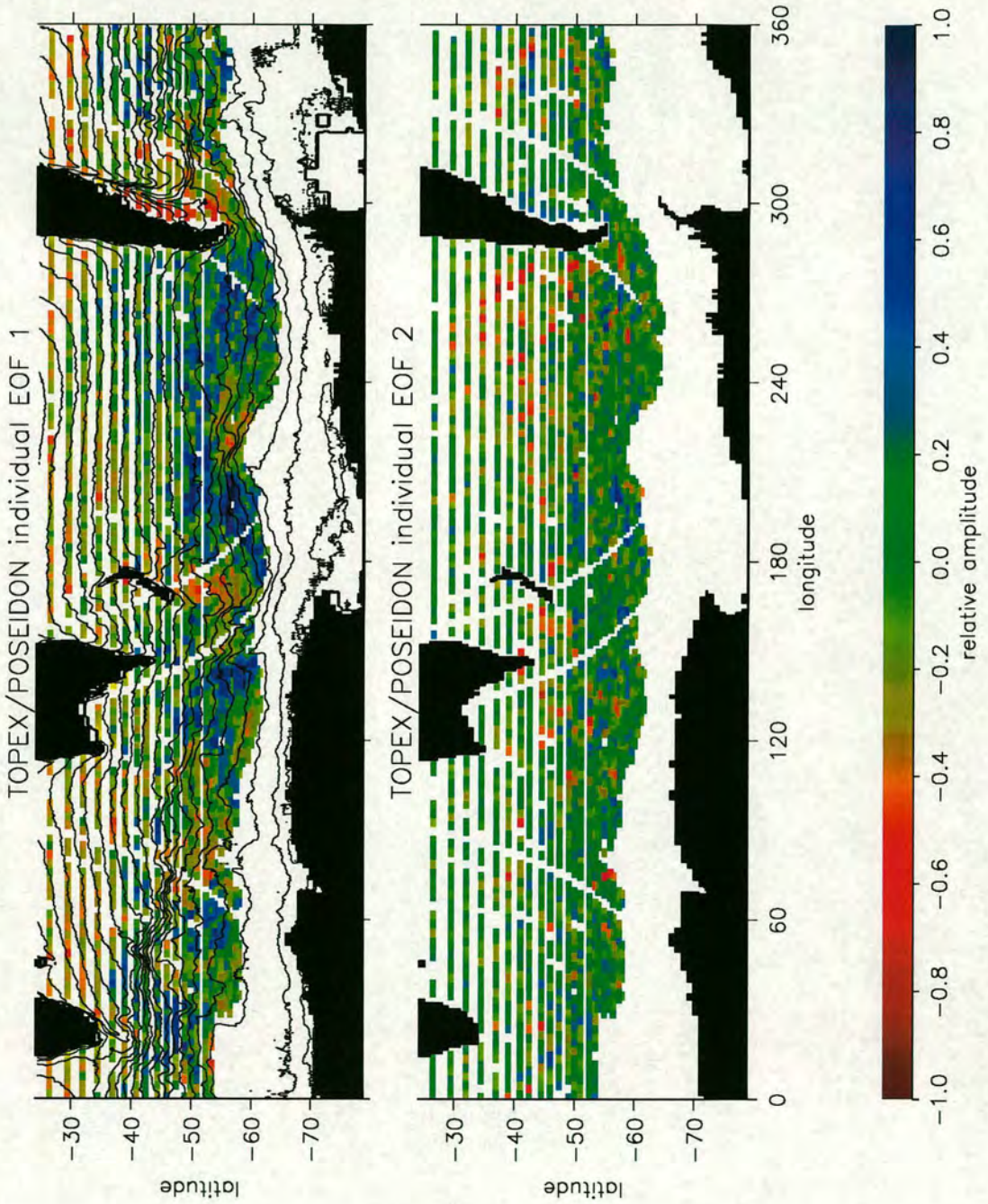

Figure 5.10: Spatial fields for individual EOFs 1 and 2

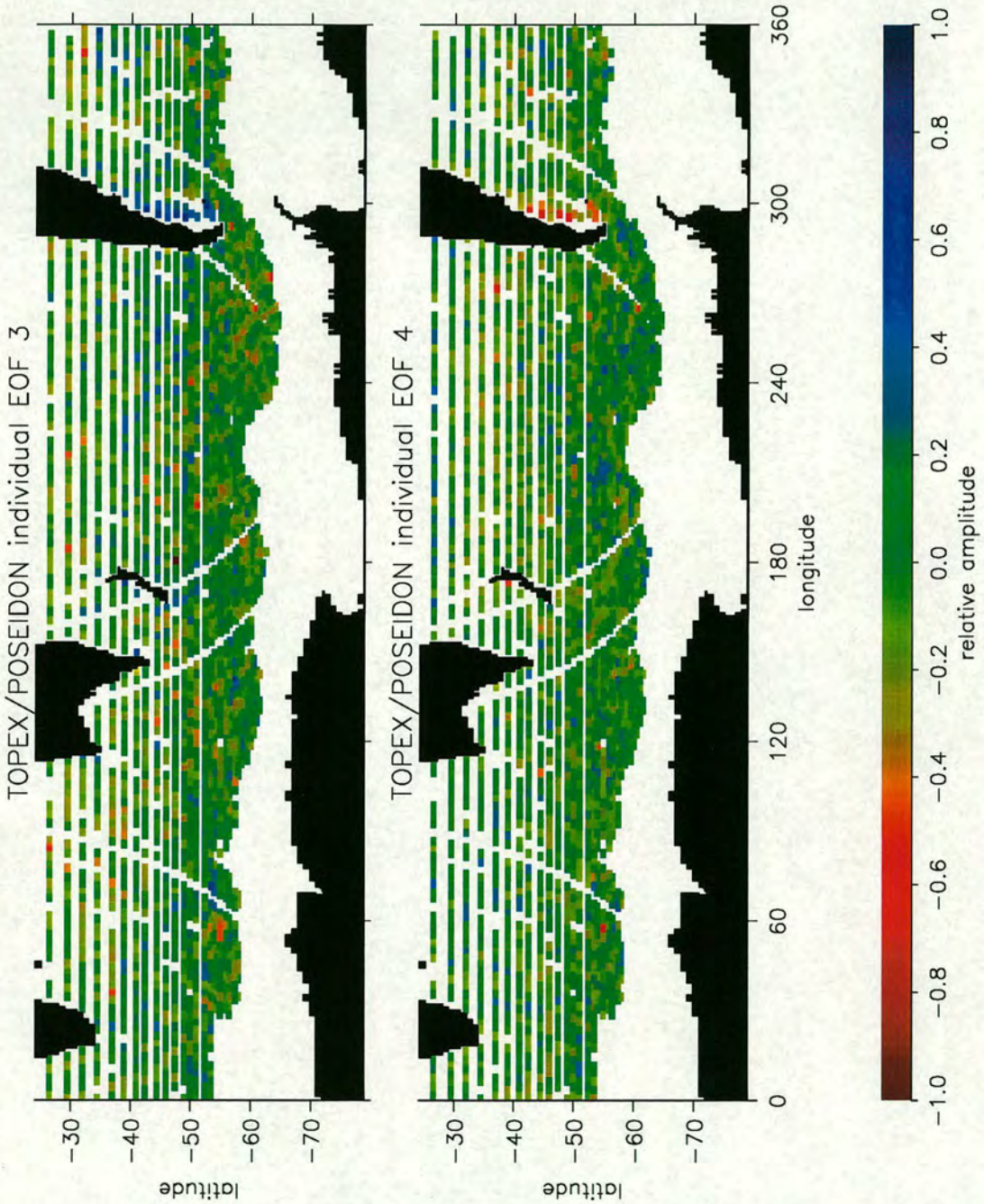

Figure 5.11: Spatial fields for individual EOFs 3 and 4

important indication of wave activity. Negative values show areas with less than average fractional power at the given period, indicating regions of relatively low wave activity at that period. The scale is presented as a relative amplitude for easy comparison. Actual amplitudes are given by this relative scale multiplied by 0.02 times the value at the respective period from the mean normalised spectrum in figure 5.5 (e.g. at the period of 348 days, 1.0 represents an amplitude of $1.0 \times 0.02 \times 0.0371$).

The first thing to note is that these figures offer much improved visualisation of activity at single wave periods compared to the fields of fractional power shown in figures 5.6 and 5.7. Though this is partly due to the choice of colour scale, it is mainly because these fields present anomalies relative to the mean normalised power spectrum. This could have been presented without performing the EOF analysis, but these reconstructions use only the largest six EOFs and so provide a filtered version of the fractional power anomaly fields (containing only the most significant information). In addition, the spatial fields for individual EOFs contained valuable information on regions associated with ranges of wave periods.

To study these fields, which have a lot of spatial structure, notable positive features will be identified and discussed. The selected features are listed in table 5.2. The approximate position of each feature is given in the second column. The third column gives the frequency number and period of the field (days) on which the feature is identified by a black box. This is also the the approximate frequency number and period of maximum prominence. The fourth column show the range of frequency numbers and periods over which the feature is evident, and the final column indicates whether the feature is within the ACC according to the field of eddy variance. Features in the ACC are expected to indicate eastward advected Rossby waves and features outside are expected to indicate westward propagation. A question mark indicates that a feature is on the edge of a high variability region.

Features 1, 2, and 8 lie within the ACC, so it is these which may represent waveguides for eastward advected Rossby waves. If this is the case then the meridional extent of a feature is expected to decrease with decreasing period, as described in

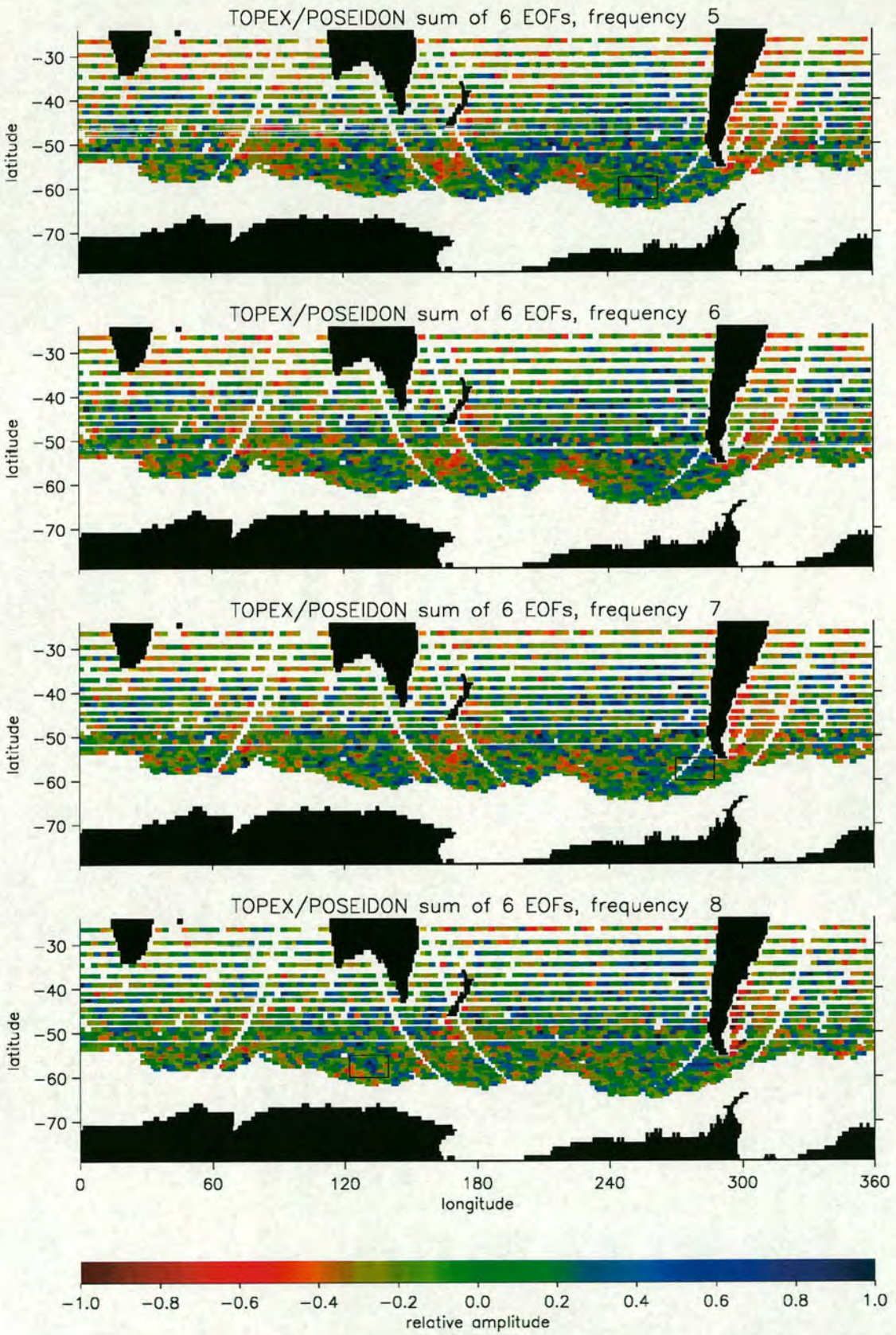

Figure 5.12: Fields of EOF reconstructions at periods 348 (top), 290, 249 and 217 days.

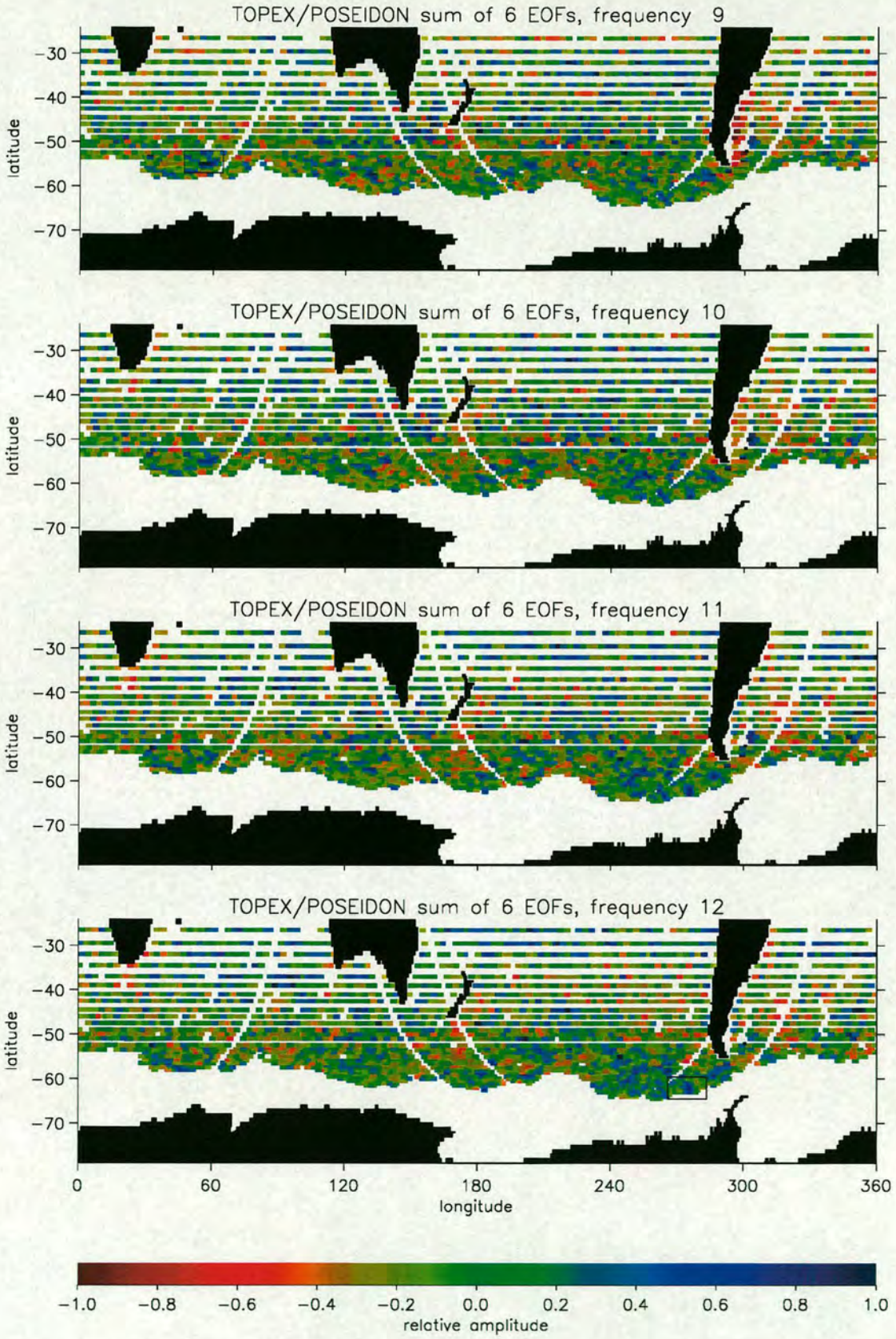

Figure 5.13: Fields of EOF reconstructions at periods 193 (top), 174, 158 and 145 days.

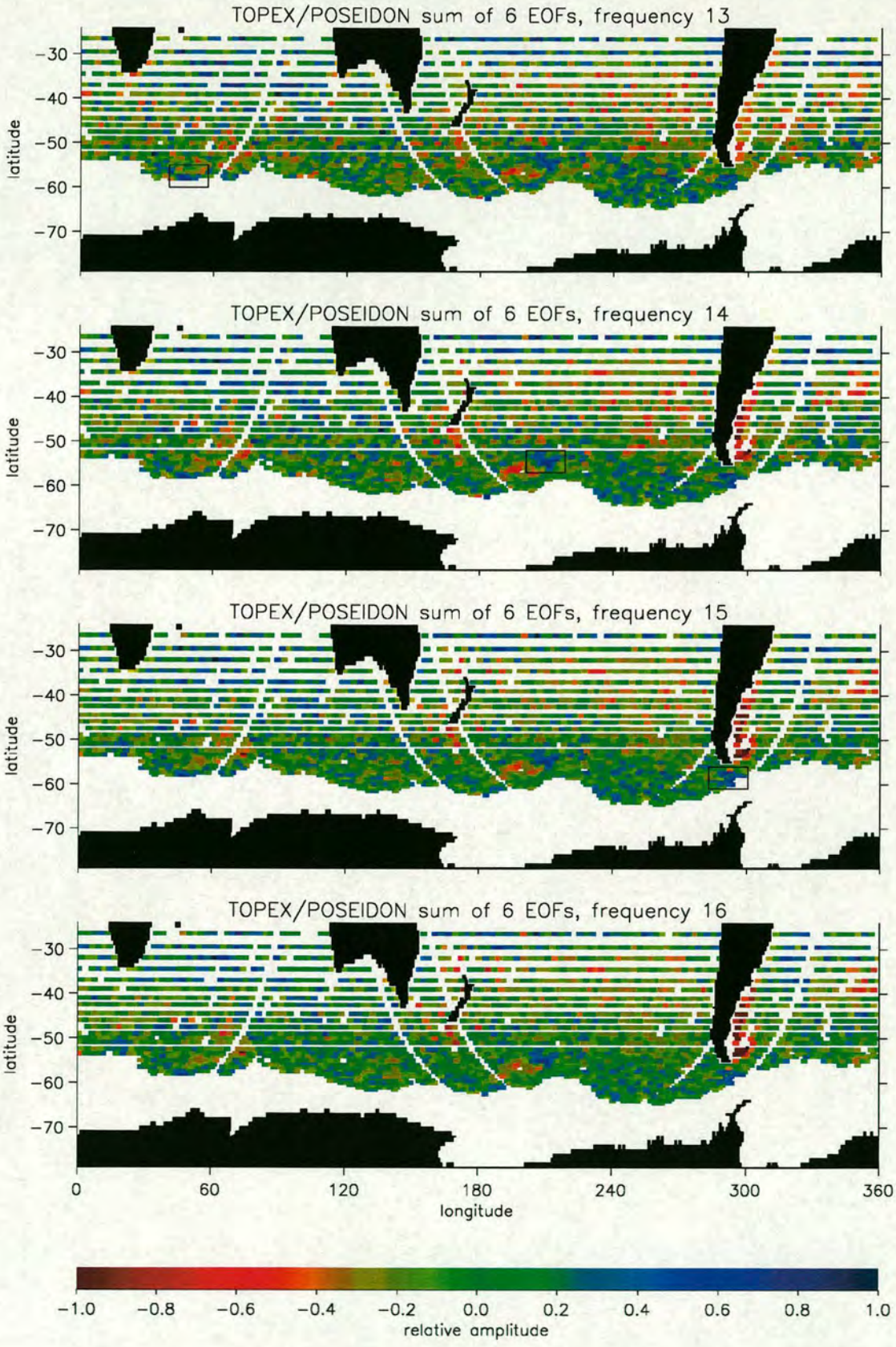

Figure 5.14: Fields of EOF reconstructions at periods 134 (top), 124, 116 and 108 days.

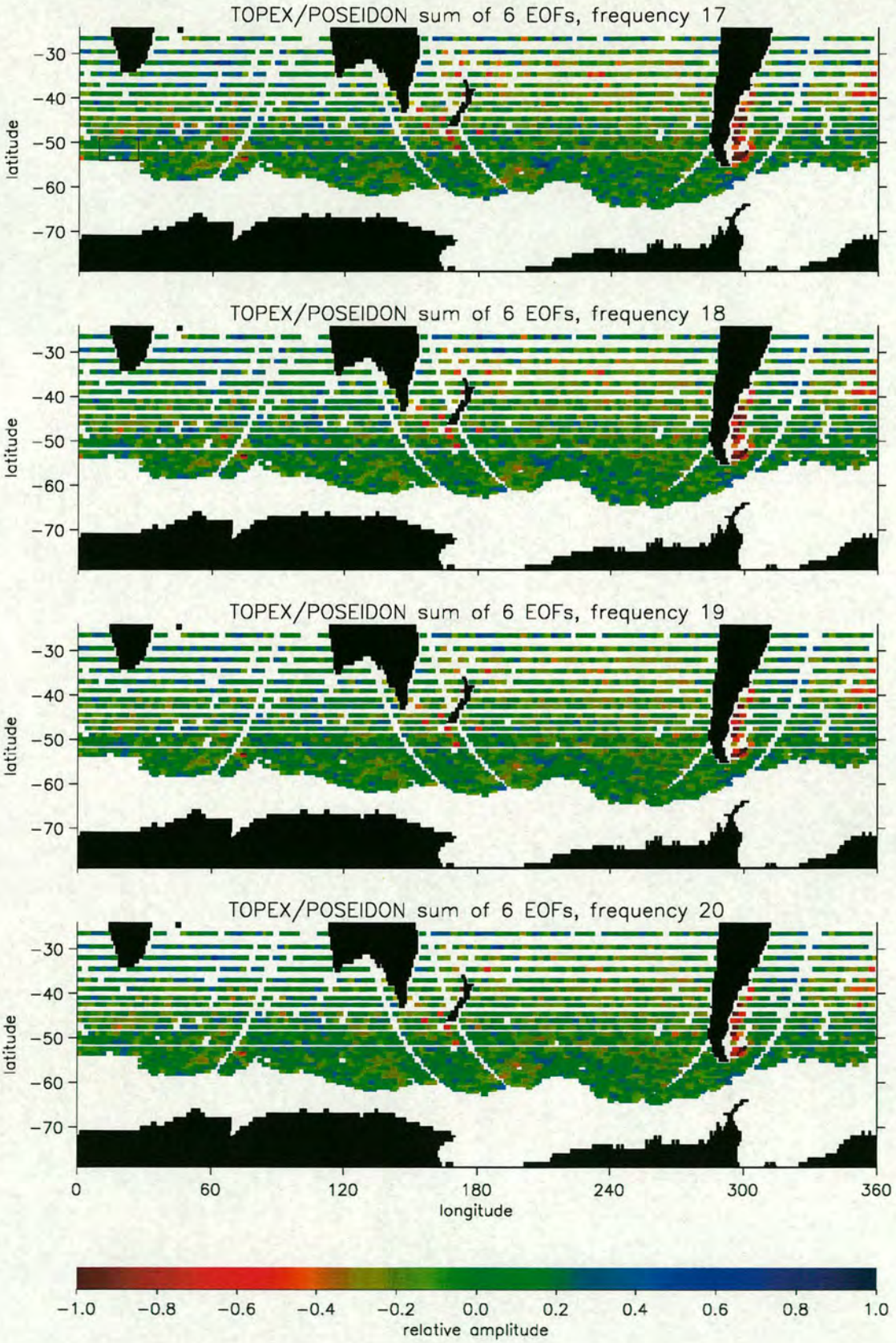

Figure 5.15: Fields of EOF reconstruction at periods 102 (top), 96, 92 and 87 days.

Feature	Position	Fn (period)	Fn range (period range)	In ACC?
1	60°S 254°E	5 (348)	5-12 (145-348)	Yes
2	58°S 279°E	7 (249)	5-10 (174-348)	Yes
3	58°S 131°E	8 (217)	5-12 (145-348)	No
4	55°S 56°E	9 (193)	6-12 (145-290)	No
5	62°S 275°E	12 (145)	8-16 (108-217)	?
6	58°S 49°E	13 (134)	10-18 (96-174)	No
7	55°S 210°E	14 (124)	8-20 (87-217)	?
8	59°S 292°E	15 (116)	12-20 (87-145)	Yes
9	52°S 18°E	17 (102)	15-20 (87-116)	No

Table 5.2: Positive features of the EOF reconstructions

the motivation for the EOF analysis (see section 3.2.2). Lower frequency waves should penetrate further into the wings of a jet, where the effective beta will limit the propagation of higher frequencies. The features should also be elongated in the direction of flow if they are related to eastward jets. Feature 1 is highlighted in the field for period 348 days. At this period it is aligned at about 120° to North and extends for about 15° of longitude. Down to a period of 193 days, the feature decreases in downstream extent. This is consistent with higher frequencies being more attenuated downstream due to being trapped within the centre of the jet, but there is not a noticeable change in the meridional extent of the feature. From period 193 days down to 145 days the feature is more aligned at about 60° to North, and extends upstream from a minimum size at period 193 days. This is not an expected characteristic of an eastward waveguide. At lower periods there are several smaller scale positive features in this region but it is hard to say if they are related. Feature 1 may therefore represent a waveguide for waves of periods 193 to 348 days (and possibly longer, but longer periods are not given here).

Feature 2 is highlighted in the field for period 249 days. It is aligned zonally and increases in downstream extent from period 348 days down to about period 217 days, where it covers about 15° of longitude. The maximum meridional extent is also at period 217 days. At periods less than this, the zonal extent reduces from the west until period 145 days. Down from this period, the feature increases in size to the east and becomes categorised as feature 8, being in a different position

to the original feature 2. Feature 2 may represent a zonal waveguide with a maximum efficiency at period 217 days. The downstream end at this point may be a source of waves with lower periods, which then propagate along a waveguide related to feature 8. In this case, unlike feature 1, lower period waves between periods 348 and 217 propagate further downstream. This may be related to a source of waves which have a dominant period of 217 days, and does not follow the expected result for a broadband waveguide. Feature 8 (highlighted in the field for period 116 days) seems to take over from feature 2 as mentioned above. It expands meridionally from a period of 158 days down to a period of 145 days, then persists at that size until decreasing in presence down from a period of 108 days. Lack of data in this area prevents knowledge of the downstream zonal extent of this feature, which is likely to represent a waveguide at periods from periods 145 days down to 87 days or lower.

Feature 5 is on the edge of a high variability region, upstream of Drake Passage, and is highlighted in the field for period 145 days. The feature emerges at a period of 217 days and expands meridionally northwards, but not zonally, as the period decreases to 158 days. It then contracts from the South as the period decreases to 108 days. The short zonal extent implies only a short waveguide, if at all, but the decrease in width from period 158 days down to 108 days is characteristic of waveguiding at those periods. Waves at this location could be either eastward of westward. The nature of the feature at longer periods suggests a limited source of longer period waves. Feature 7 is also on the edge of a high variability region, and is identified in the field for period 124 days. This is the most persistent feature of all, evident from a period of 217 days down to 87 days or lower. It is small from period 217 down to period 158 days, then expands meridionally and to the East down to a period of about 124 days. Here it spans about 15° of longitude and 4° of latitude. It then decreases in size meridionally as the period decreases. This feature therefore demonstrates waveguide characteristics for periods of about 124 days and below. Though it is on the edge of a high variability region, comparison with the spatial field for EOF 1 (figure 5.10) indicates that this feature is just upstream of the jet implied by the SST measurements. It is therefore likely to be due to eastward propagation. From a period of about 145 days and lower

there is a large negative feature to the southwest of this feature. This region is west of a topographic ridge, and is coincident with a strong positive feature in the spatial field for EOF 1, and a smaller positive feature in the spatial field for EOF 2 (figure 5.10). The region is just south of the ACC and so Rossby wave propagation should be westward. It seems something is happening to inhibit wave activity at typical Rossby wave periods in this region, and this is almost certainly topography related.

Some other negative features are also worth a mention. At the period of 348 days, there are prominent negative features which were identified in the spatial field for EOF 1 as being coincident with jets observed in the SST data (figure 5.10). These are at (48°S, 110°E), (56°S, 210°E) and (60°S, 310°E). These features are negative at the longer periods, and become gradually less negative as the period decreases. Only the second of these features is slightly positive at a period of 87 days, with the others close to neutral. This shows that these regions are associated mainly with periods less than 87 days. This is likely to be due to high frequency eddy activity rather than Rossby waves, so these negative features do not relate to waveguides. The other main negative feature, appearing in many of these EOF reconstructions, is the tidal alias region east of Argentina. The positive features outside the ACC (features 3, 4, 6 and 9) show similar characteristics to the positive features already discussed in terms of waveguide behaviour, but will relate to westward propagation and not jets in the ACC.

Problems with the interpretation of the features of table 5.2 arise from various factors. The first is resolution which gives the coarse structure of the various features. This makes it hard to see smooth changes in meridional extent with period, which are an important indication of waveguiding. Another major factor is lack of knowledge about wave sources. Smaller features may just show a source of wave activity and not waveguiding. Waveguides may not show the characteristic response discussed in section 3.2.2 if the associated source of waves is specific to a certain range of periods and not broadband. Finally, some of the features are on the edge of the available data so may not be fully visible. The features identified here, however, are a useful start to the analysis of Rossby wave activity in the Southern Ocean, and have been obtained from data with high spectral accuracy.

Rossby wave propagation associated with these features will be studied further in the next section, which looks at the measurement of phase speeds from the data at crossover points.

5.4 Phase speed analysis

Previous studies of satellite measurements of Rossby wave phase speeds were discussed in section 2.3. Studies carried out in the North Atlantic have used SSH anomaly data mapped onto a regular grid. This section looks at phase speed measurements from the zonal gradient of SSH measured at ground-track crossover points. The aim is to evaluate the usefulness of this form of data for phase speed measurement in the Southern Ocean, and then obtain results of phase speeds over the 4.8 year time period. Initially phase information from FFT is used (as in section 3.3), then the Radon transform is introduced and applied to longitude-time diagrams. Attention is focused on regions identified by the EOF analysis as being active at Rossby wave frequencies.

5.4.1 Resolution issues

Time-longitude diagrams for the zonal gradient of SSH at crossover points are shown in figure 5.16 for longitudes of 240° to 300°E and near 58°S. This zonal slice lies upstream of Drake Passage and incorporates feature 2 of table 5.2. The left hand diagram includes data from a single row of crossover points, at 58.3°S. This appears to show regions of westward propagation and only limited eastward propagation. The zonal spacing of crossover points at this latitude, however, is 165km. By the Nyquist criterion, only waves with a wavelength greater than twice this spacing (330km) can be resolved. As many Rossby waves are expected to have wavelengths less than this, this diagram is not a useful indication of Rossby wave propagation.

The right-hand diagram includes crossover points from the adjacent latitude row to the North (at 57.7°S), which lie at longitudes between the longitudes of points on the original row. The meridional spacing of the two rows of crossover points is

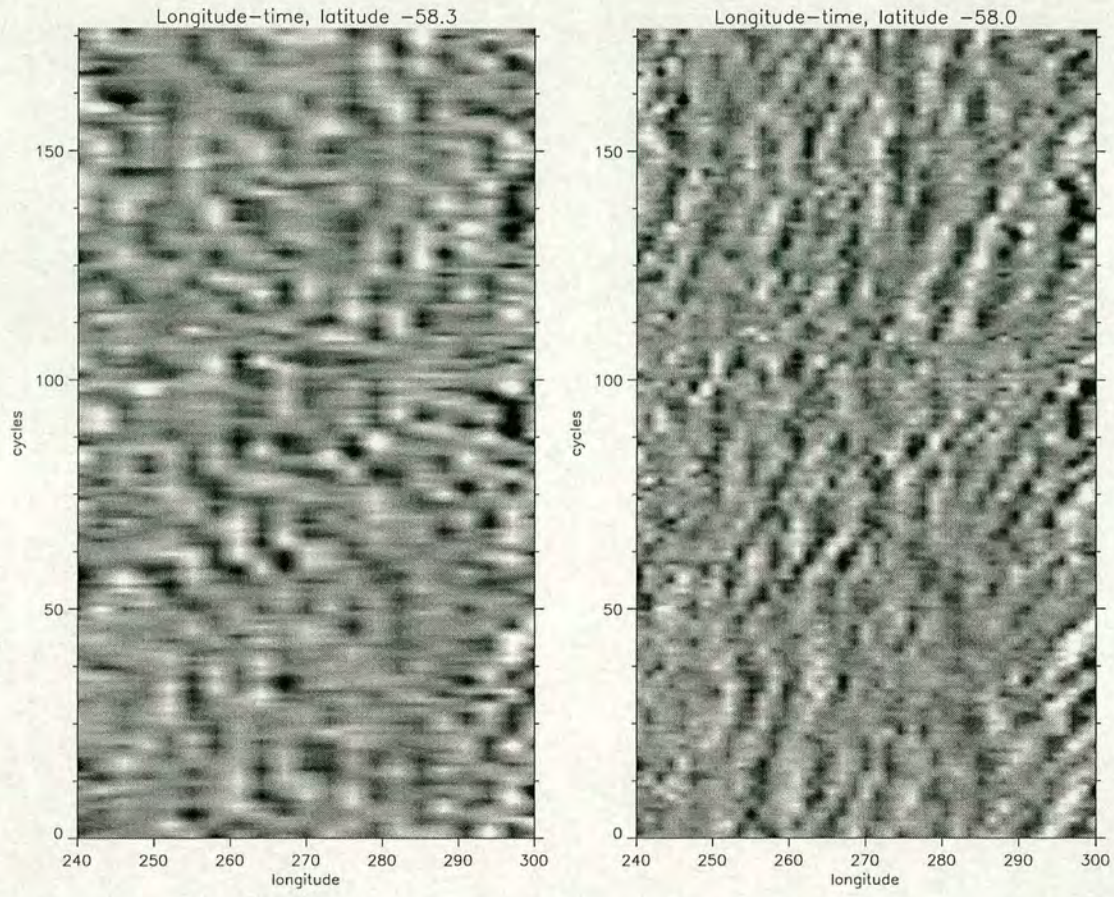

Figure 5.16: Longitude - time diagrams of TOPEX/POSEIDON dh/dx data at crossover points, for a single row at 58.3°S (left), and including the row above giving an average latitude of 58.0°S (right). The longitude range is 240° to 300°E and the time scale is 9.9 days per cycle.

0.67° (75 km) giving an average latitude of 58.0°S. Provided that waves are coherent over this latitude range, the combined time-longitude diagram will represent zonal propagation of waves with wavelengths greater than 165km. This can then be used to analyse phase speeds. Coherent eastward propagation is evident in the combined time-longitude diagram. Examples of clear eastward propagation are at 290° to 300°E, cycles 0-50, for faster waves, and at 280° to 290°E, cycles 110-140, for slower waves. A mixture of propagation speeds can be observed at different times and longitudes for this zonal slice. Phase speeds from this diagram will be calculated and discussed further in section 5.4.4.

Figure 5.17 shows the limitations of the crossover distribution for the resolution of waves at different latitudes. The solid line shows the minimum wavelength of

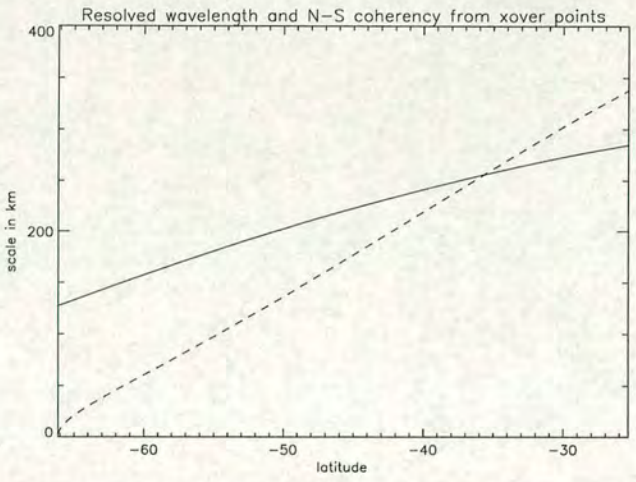

Figure 5.17: Latitude dependence of minimum resolved wavelength (solid line) and minimum north-south coherency (dashed line) of waves measured from pairs of rows of TOPEX/POSEIDON crossover data (distances in km).

resolved waves, which increases from 130km at 66°S to 290km at 24°S. Typical minimum wavelengths in FRAM were 230km at high Rossby wave frequencies. This suggests the crossover data will only be useful south of 40°S where waves with this wavelength can be resolved. The dashed line shows the meridional distance over which waves must be coherent if they are to be captured by a pair of adjacent crossover rows. At 40°S waves must be coherent over 200km. This is a typical meridional scale for jets in the FRAM mean flow and so represents a maximum range of coherency for Rossby waves. The coherency requirement relaxes almost linearly to the South to become negligible at 66°S. The implication of these resolution criteria are that crossover data should only be used for phase speed measurements south of 40°S. In practise, adjacent rows of crossover points may not capture the same propagation if they are north of about 50°S.

5.4.2 Phase speeds from Fourier components

The phase information from FFT components was used in chapter 3 to analyse phase speeds at different frequencies. The same technique was applied to pairs of rows of crossover data. Results of zonal phase speeds for periods of 116, 158, 217 and 348 days are shown in figure 5.18. The calculation was performed south of

38°S using only complete time series (as was used for the EOF analysis). North of this latitude there are resolution problems. Zonal banding to the north reflects the separation of crossover rows and indicates the latitude range of coherency required for sensible results.

On first acquaintance it is clear there are limitations with applying this method to the crossover data. Much of each field contains values which are off-scale (black and white) and not consistent with surrounding values, giving a general lack of smoothness. It is possible to identify coherent features, however, and the fields show some useful qualitative results. Focusing on the southeast Pacific, it is evident from the coherent regions that phase speeds increase with frequency, as expected. These fields can be compared with the EOF reconstructions at the same periods (figures 5.12 to 5.15). Regions of coherent eastward phase speed are found on similar scales to positive features in the corresponding EOF fields. Some positive features of the EOF reconstructions are certainly coincident with coherent propagation (such as off the Southwest tip of Chile at a period of 217 days and 158 days), but a general comparison is hard to make.

Figure 3.14 showed phase speeds from FRAM, calculated using the same method, for the period of 4.4 months, which lies between periods of 116 and 158 days. The FRAM results showed coherent propagation on scales larger than features in the equivalent EOF reconstruction (top of figure 3.12), unlike the comparable scales are observed here. The eastward phase speeds in the FRAM results were very consistent at about 3.0cm/s, and this was seen not to vary with the strength of mean flow. In the TOPEX/POSEIDON results, the coherent regions of eastward phase speed cover a wider range of speeds, but there are cases of steady values (for example at 58°S, 250°E in the field for 116 days). The values of a few cm/s compare well to the FRAM results. The reduced clarity and spatial extent of the coherent regions in the TOPEX/POSEIDON results compared to FRAM is likely to be due to the resolution of the data at crossover points, and the higher variability in the real ocean compared to the model. From these results it is not possible to confirm the observation in FRAM that phase speeds do not vary with the strength of mean flow, largely because in the TOPEX/POSEIDON results the position of jets is not known. The phase speeds would only be seen to be

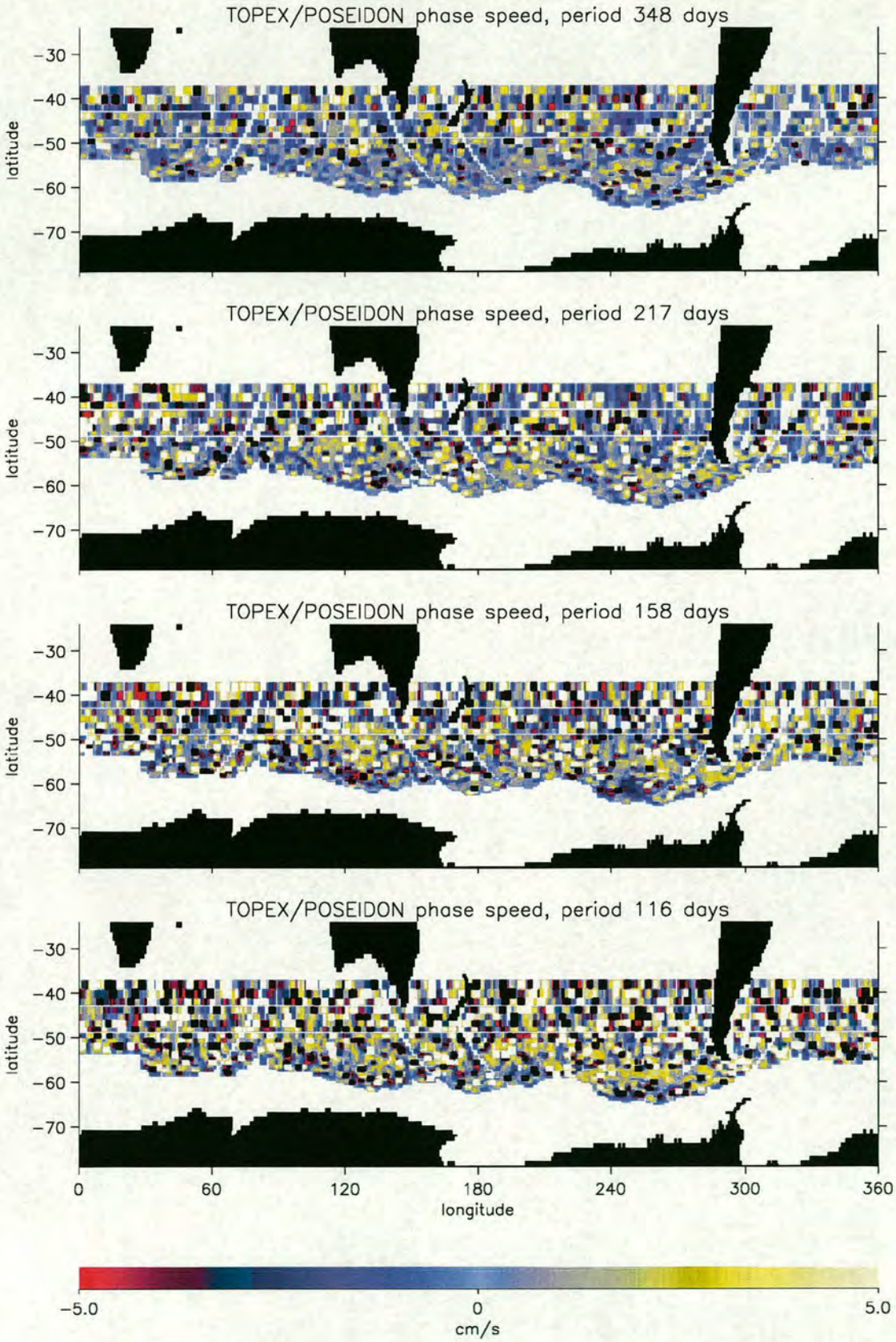

Figure 5.18: Phase speeds from Fourier components of data at TOPEX/POSEIDON crossover points. Periods are 348 days (top), 217 days, 158 days and 116 days.

invariant with the mean flow if large areas of uniform phase speed were observed in the results, and this is not the case. Phase speeds, and their variation with frequency, can be studied further by making local measurements using time-longitude diagrams and a combination of FFT and the Radon transform.

5.4.3 Time-longitude diagrams

Figure 5.16 showed a time-longitude (t-l) diagram from a region upstream of Drake Passage. This contains clear eastward propagation and is associated with feature 2 from the results of EOF reconstructions (see table 5.2). This section examines t-l diagrams associated with this and other features of the EOF reconstructions, as a basis for the local calculation of phase speeds.

Figure 5.19 shows the t-l diagrams associated with features 1 to 6 of table 5.2 (top left to bottom right respectively). Feature 1 is within the ACC. Eastward propagation is evident in the associated t-l diagram (top left) but only at certain times, and over a limited range of longitudes (e.g. at 140 cycles, 250°E; 50 cycles, 265°E). More definite eastward propagation is evident in the t-l diagram associated with feature 2 (top middle), which is also within the ACC. Consistent propagation can be seen between cycles 0 and 100, 285° to 295°E, and this shows definite wave-guiding over this time (almost 3 years). Longer period propagation is evident from cycle 110, 275° to 295°E. Feature 3 is outside the ACC, and the associated t-l diagram (top right) shows coherent westward propagation, especially from cycle 50 to 175 and between 115° and 135°E. This shows feature 3 represents a waveguide for westward propagating Rossby waves. The t-l diagram associated with feature 4, which is outside the ACC, shows little propagation (bottom left). If anything there are some standing waves between 50° and 60°E. At this latitude (55°S) the meridional separation is 0.88° (98km), so it is possible that propagation here is not effectively captured by the crossover data. Feature 5 is on the edge of a high variability region, but it is clear from the t-l diagram (bottom middle) that westward propagation dominates, particularly for the first 140 cycles. Feature 6 is outside the ACC. Coherent westward propagation in the t-l diagram (bottom right) is not as evident as it was for features 3 and 5, but

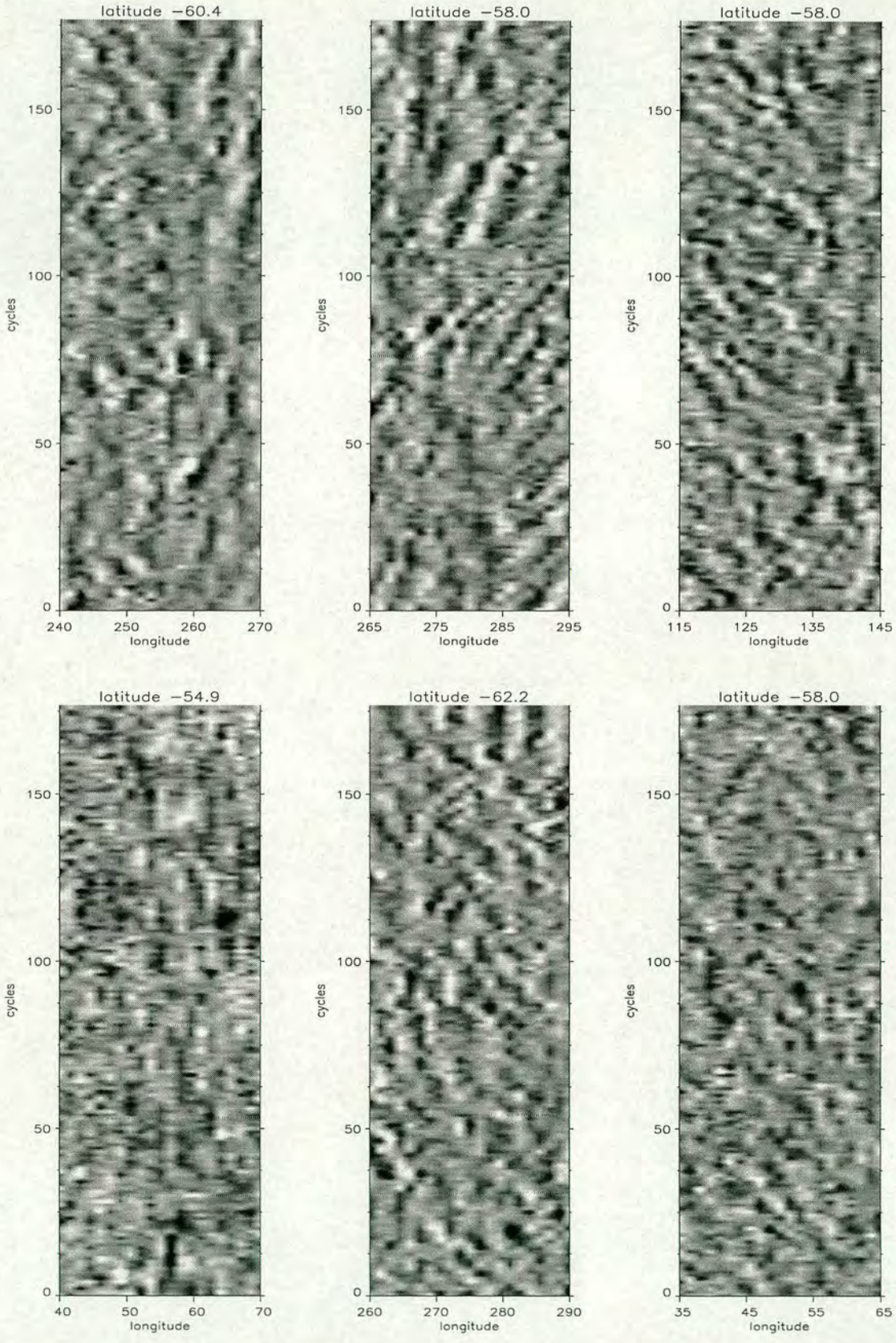

Figure 5.19: Longitude - time diagrams of TOPEX/POSEIDON dh/dx data at crossover points, for features 1 to 6 of table 5.2 (top left to bottom right).

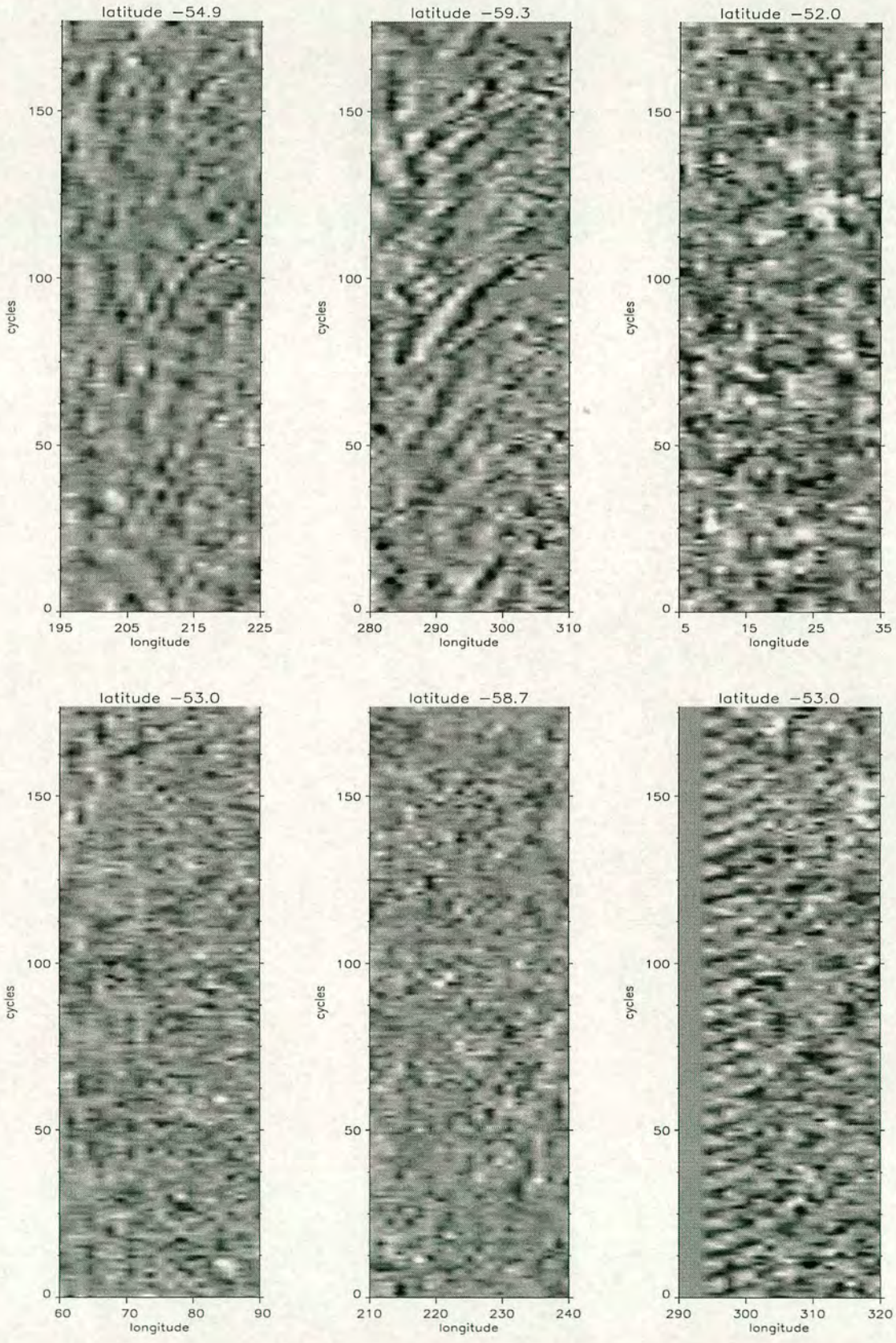

Figure 5.20: Longitude - time diagrams of TOPEX/POSEIDON dh/dx data at crossover points, for features 7 to 9 of table 5.2 (top row), and three other locations.

can be found over the first 100 cycles between 45° and 55°E. This shows a weak westward waveguide over this time.

The top row of figure 5.20 shows the t-l diagrams associated with features 7 to 9 of table 5.2 (left to right respectively). Feature 7 is on the edge of a high variability region. The t-l diagram (top left) shows some eastward propagation in its eastern half, but the propagation is not coherent over long periods. At this latitude there may be resolution problems, so it is difficult to confirm the existence of a waveguide relating to this feature. Eastward propagation is much clearer in the t-l diagram associated with feature 8 (top middle), and can be seen between 280° and 300°E at most times. This feature is in the ACC and the t-l diagram indicates an eastward waveguide. The t-l diagram associated with feature 9 (top right) shows little in the way of propagation. The latitude is 52°S so there is likely to be resolution problems using the crossover data in this way. The bottom row of figure 5.20 shows the t-l diagrams at three locations associated with negative features of the EOF reconstructions (figures 5.12 to 5.15). Each of these locations were associated with high frequency eddy activity. This is confirmed in the bottom left and middle t-l diagrams by a lack of coherent propagation and the small timescale of variability. The bottom right t-l diagram shows coherent and steady eastward propagation between 294° and 300°. This is the region east of Argentina, and this apparent propagation is due to the tidal alias problem and does not represent wave activity. The remainder of this diagram shows features on small timescales and a lack of propagation, indicating eddy activity.

For these t-l diagrams to successfully indicate waveguides of Rossby waves, the propagation must be near zonal and captured by the meridional resolution of the crossover data. The diagrams have successfully provided evidence of waveguides associated with several of the features of table 5.2, especially features 1, 2, 3, 5, 7 and 8. T-l diagrams for these features will be used as a basis for the measurements of Rossby wave phase speeds at the respective locations.

5.4.4 The Radon transform

This section introduces the Radon Transform (RT) as a means of measuring phase speeds from time-longitude (t-l) diagrams. The RT was used successfully by Cipollini et al (1997) to measure phase speeds in the North Atlantic. They applied the RT to t-l diagrams of mapped data. Here it will be applied to some of the t-l diagrams shown in figures 5.19 and 5.20, as well as t-l diagrams for individual frequencies. The RT is performed on a two-dimensional image and is the projection of the sum of the image at a given angle ψ, along the direction normal to that angle. For a square t-l image with a single phase speed (diagonal lines), the sum of the squares of the RT are maximum when ψ is the angle of propagation. Images are analysed initially by computing the sum of the squares of the RT over a range of angles. The amplitude of these results is normalised to be 1.0 at an angle of zero. Then the same procedure is performed on a uniform image of the same size, and the result is subtracted from the image results to give a plot of amplitude against angle. This has peaks at dominant angles of propagation in the Longitude-time plot.

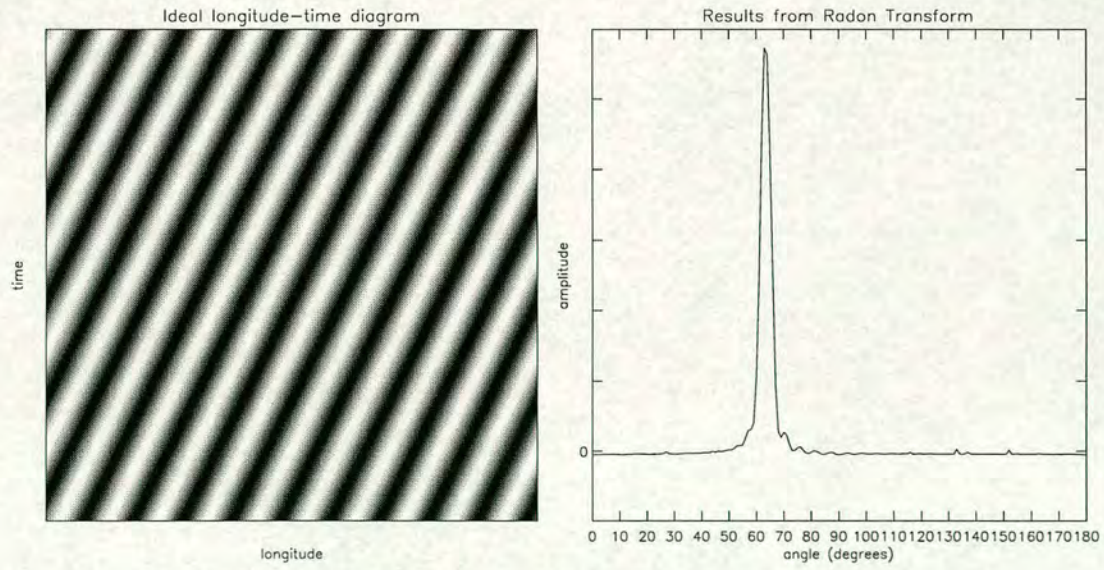

Figure 5.21: Idealised longitude-time diagram and results obtained using the Radon Transform to find the angle of propagation.

To illustrate this, an example of an ideal image and the results from the RT are shown in figure 5.21. A more general image of propagation will have peaks at

different angles enabling different phase speeds to be measured. The RT was performed on images covering 30° in longitude and 50 cycles in time, though any size image could be used. The phase speed, c, (in m/s) is then calculated from the propagation angle ψ as follows:

$$c = \frac{1.11 \times 10^5 \times cos(\phi)}{tan(\psi) \times 9.92 \times 86400} \times \frac{3}{5}, \tag{5.1}$$

where 1.11×10^5 is the separation of 1° of latitude in m, ϕ is the latitude, 9.92 is the number of days in a cycle, 86400 is the number of seconds in a day and 3/5 is the chosen size ratio of the image (30° by 50 cycles).

5.4.5 Phase speeds from the Radon transform

This section presents results of phase speeds measured using the Radon transform (RT). First, the RT is applied to time-longitude diagrams at single frequency components to investigate the relationship between phase speed and frequency. Then the RT is used on the complete time-longitude diagrams to establish dominant phase speeds.

Phase speed and frequency

To measure phase speeds at particular frequencies, t-l diagrams were generated at individual frequencies by inverting single spectral components of the FFT in time. An example such a diagram was shown for FRAM in the right half of figure 3.13. The process was performed for features 1, 2, 3, 5, 7 and 8 of table 5.2, and over a frequency range of frequency number 5 (period 348 days) to 20 (period 87 days). Figure 5.22 shows examples of the resulting t-l diagrams for feature 2, at frequency numbers 5, 8, 11, 14, 17 and 20 (periods 348, 217, 158, 124, 102 and 87 days). Coherent eastward propagation is evident, particularly in the first 5 diagrams. The RT is a convenient method of determining the average phase speed from each of these diagrams. A choice of 50 cycles for the RT image represents the complete diagram, as the pattern is repeating in time. The results of performing

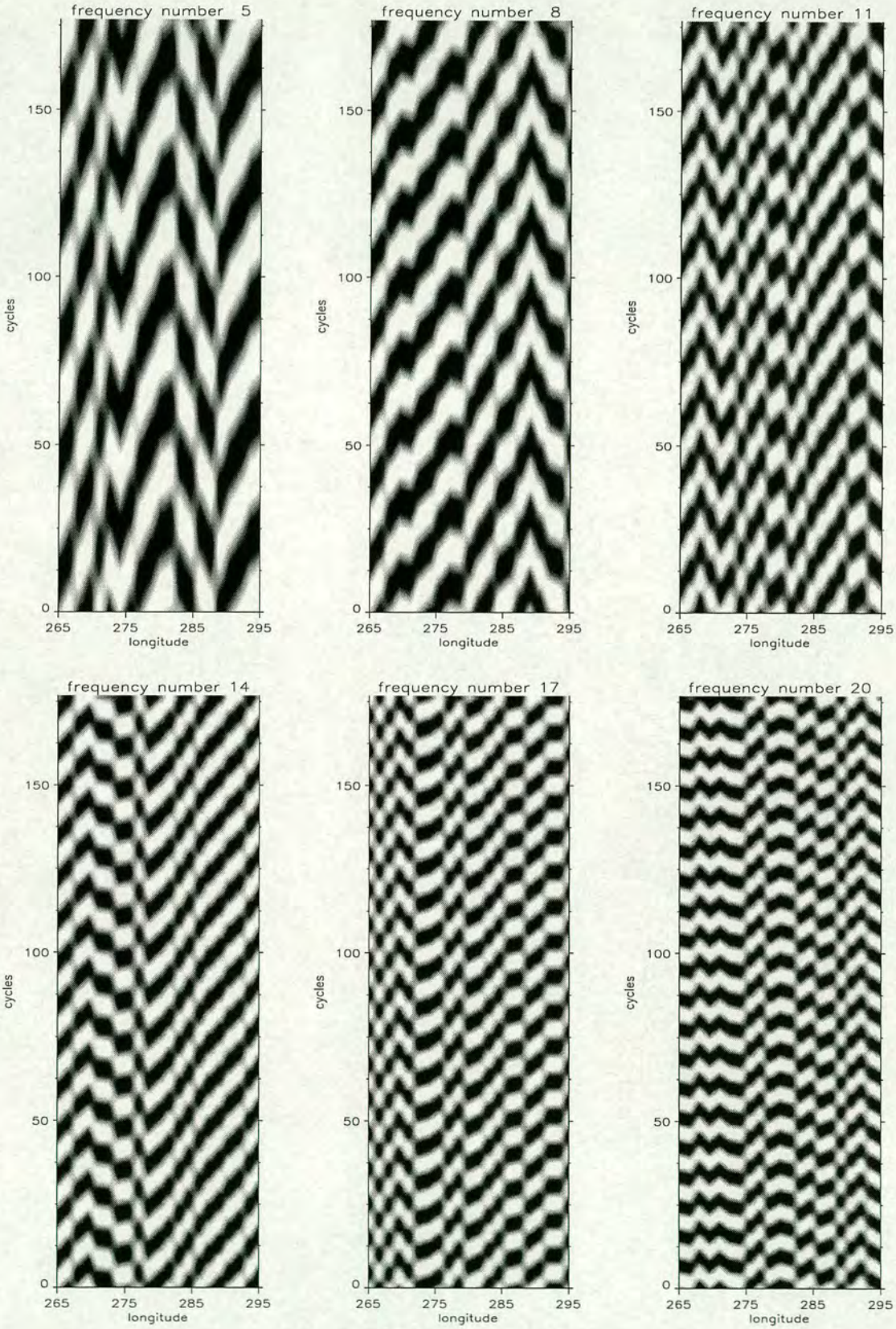

Figure 5.22: Longitude - time diagrams of TOPEX/POSEIDON dh/dx data at single frequencies for feature 2 of table 5.2. Periods in days are 348, 217, 158, 124, 102 and 87 (top left to bottom right).

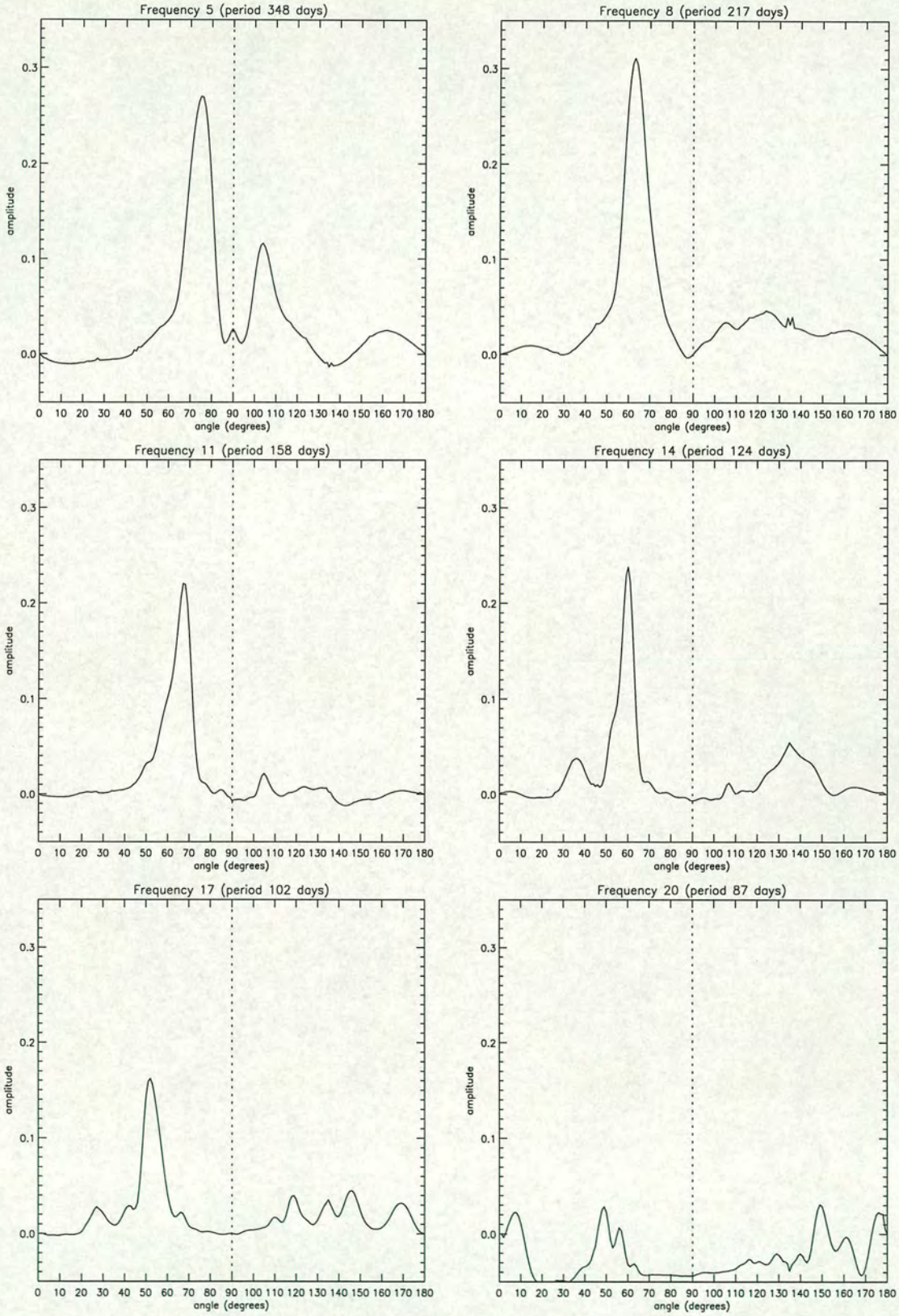

Figure 5.23: RT results at different frequencies.

the RT on these diagrams is shown in figure 5.23, which shows magnitude of RT against angle of propagation for the six sample periods. Strong peaks are seen in the first five graphs, and the magnitude bears relation to the prominence of feature 2 in the EOF reconstructions (figures 5.12 to 5.15). At a period of 87 days, the RT results are largely negative due to relatively high values at angle 0. There are peaks, but their amplitude is small and so phase speed measurements at this frequency will be unreliable. Phase speeds are measured from these results by taking the propagation angle, and using equation 5.1. This was done for all frequency numbers between 5 and 20 to give results of phase speed against frequency.

Figure 5.24 shows the results of phase speed against frequency number for features 1, 2, 3, 5, 7 and 8 (top left to bottom right), which were generated as described above for feature 2. The phase speeds are given by the dashed line, with the solid line giving a least-squares linear fit. The magnitude of the RT used in each phase speed calculation is shown by the dotted line (which scales as phase speed$\times$20), and this gives an idea of the reliability individual phase speed measurements. A linear relationship between frequency and phase speed was established for a jet in FRAM (section 3.3). An approximate linear relationship is evident in the results shown here, though some results contain large deviations from a linear fit. Features 1, 2, 7 and 8 were associated with eastward propagation from the time-longitude diagrams (figures 5.19 and 5.20), and an eastward phase speed-frequency relationship is shown here. Phase speeds rise from between 1.0 and 1.5cm/s at a period of 348 days (11.4 months, frequency number 5), to between 3 and 4 cm/s at a period of 87 days (2.9 months, frequency number 20). This compares very well with the equivalent FRAM results (figure 3.17), which range from 1.3 cm/s at a period of 11.7 months to 3.3 cm/s at a period of 2.9 months. The best relationship can be seen for features 2 and 8, and it is these which showed clearest eastward propagation in the associated t-l diagrams. It should be noted, however, the RMS deviation from the linear fit for features 2 and 8 is about 1.0 cm/s. Features 3 and 5 are associated with westward propagation. The results of phase speed against frequency for these features have a lot of scatter, but the linear fit is still appropriate and shows an increase in westward phase speed with

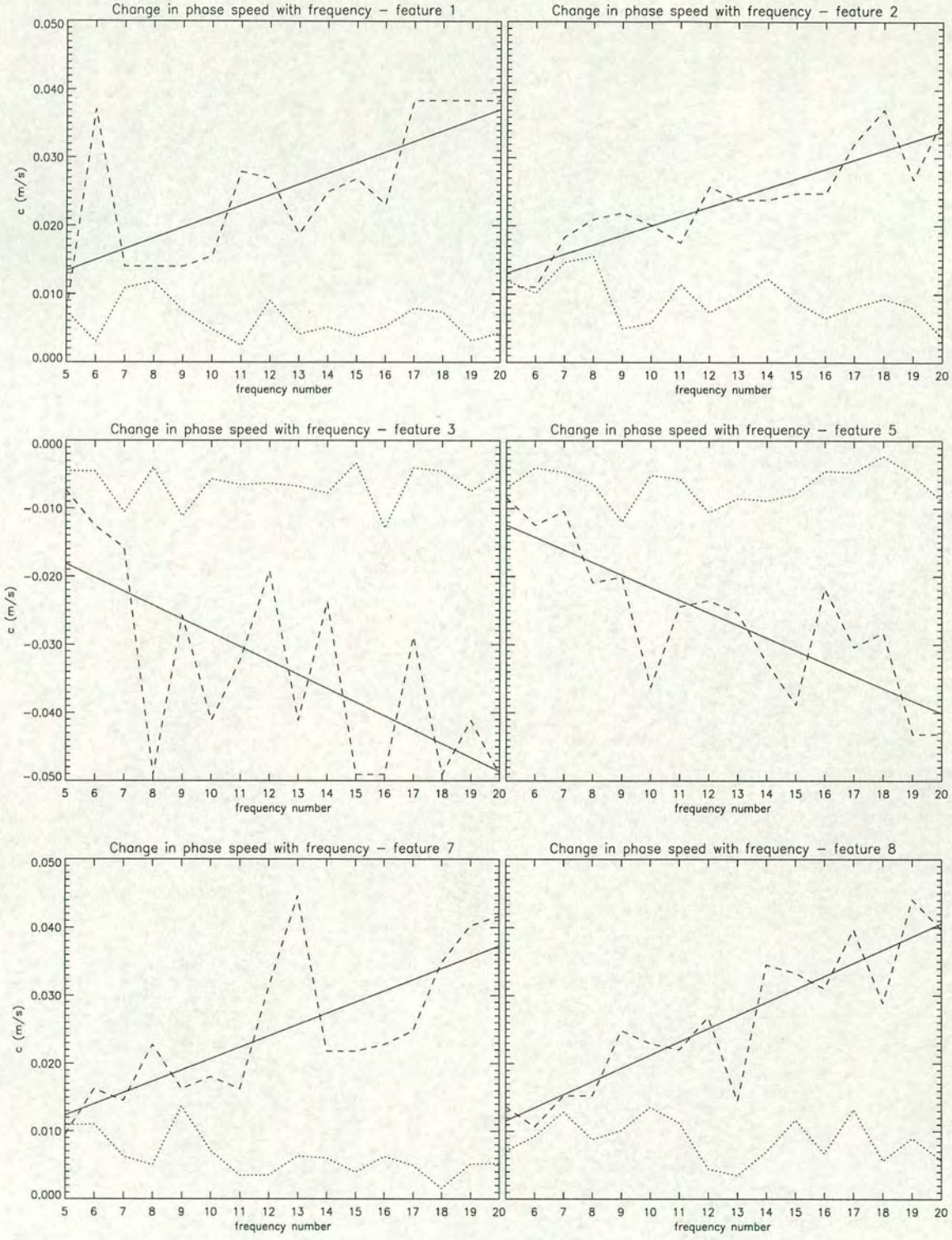

Figure 5.24: Phase speeds against frequency number (dashed line) for features 1, 2, 3, 5, 7 and 8 from table 5.2. The solid line is the linear fit, and the magnitude of the dotted line is a measure of the amplitude of the associated Radon transform, with a scaling of 20× phase speed.

frequency. On the evidence of these two features, phase speeds are slightly faster westward than they are eastward for the same frequency number (westward phase speeds are between 4 and 5 cm/s at frequency number 20 compared to eastward phase speeds between 3 and 4cm/s). The Radon Transform has provided a suitable means of studying the relationship between phase speed and frequency from time-longitude diagrams for single frequency components. The results obtained here will be discussed further in section 5.4.6, below.

Dominant phase speeds

For completeness of results, this sub-section presents results of dominant phase speeds in the complete time-longitude diagrams (figure 5.19 and 5.20), calculated using the Radon Transform. The RT was applied to the t-l diagrams associated with features 1, 2, 3, 5, 7 and 8 of table 5.2. The calculation was performed over three consecutive time periods of 50 cycles (496 days) each. This time period was chosen to give a suitable size image for the RT and to study how phase speeds might vary over the total time period under study. The phase speed results are shown in table 5.3.

The third, fourth and fifth columns show phase speeds for cycles 1-50, 51-100 and 101-150 respectively. There are three rows of results for each column and feature, and these represent the three most dominant peaks in the RT results, with the largest at the top. If only two values are given then there is no obvious third peak in the RT results. The value in brackets is the magnitude of the peak in the RT results.

There is often a change in sign of the phase speed from the dominant three peaks of the RT for a particular time sample. This can either mean there is opposite propagation at different longitudes or different times within the 30° by 50 cycle sample, or that an opposite direction falsely appears in the results due to the resolution of the data. Caution must therefore be used when interpreting these results, and reference must be made to the relevant t-l diagram (figures 5.19 and 5.20). For example, the t-l diagram for feature 2 shows eastward propagation at all times, but in the first 50 cycles it is confined to the eastern 10° of longitude.

Feature	Position	C_x (RT value) Cycles 1-50	C_x (RT value) Cycles 51-100	C_x (RT value) Cycles 101-150
1	60°S 254°E	-2.0 (0.013) 0.0 (0.012) 2.7 (0.008)	-1.0 (0.013) -6.7 (0.009) 3.2 (0.006)	0.7 (0.028) -0.5 (0.023)
2	58°S 279°E	0.0 (0.007) 1.6 (0.003)	2.6 (0.016) -2.6 (0.014) -0.1 (0.009)	1.5 (0.06) -1.1 (0.028) -1.1 (0.03)
3	58°S 131°E	-0.5 (0.014) -4.7 (0.013) -2.2 (0.012)	4.1 (0.018) 2.8 (0.018)	-5.1 (0.016) -7.4 (0.011) -4.9 (0.015)
5	62°S 275°E	-1.9 (0.009) 3.6 (0.007) 0.8 (0.007)	4.8 (0.006) 1.6 (0.004) -1.6 (0.003)	-0.8 (0.006) -1.6 (0.004) -0.6 (0.006)
7	55°S 210°E	4.5 (0.013) 1.8 (0.012) 5.3 (0.010)	-4.5 (0.016) -0.9 (0.009) 0.5 (0.004)	-2.3 (0.011) -4.5 (0.009) 0.5 (0.007)
8	59°S 292°E	2.2 (0.006) -2.0 (0.005) 0.8 (0.002)	-0.6 (0.007) 1.2 (0.007) 2.1 (0.006)	4.3 (0.003) -4.9 (0.003) 0.21 (0.002)

Table 5.3: Phase speeds from time-longitude diagrams

For cycles 51-100 and 101-150, the dominant peaks in the RT results represents the obvious propagation, with eastward phase speeds of 2.6 and 1.5 cm/s respectively, but neither the results from the first 50 cycles (0 and 1.6 cm/s eastwards) represent the obvious propagation to the east, which has a phase speed close to that for cycles 51-100 (2.6 cm/s). These results are not of good enough quality to warrant a full analysis, but they can be used to quantify some of the obvious propagation in the time-longitude diagrams. The previous results of phase speed against frequency are more suitable for further discussion.

5.4.6 Discussion of results

The phase speed measurements in the previous subsection can now be compared to previous results and values predicted by linear theory. Previous observations of phase speeds are conveniently presented for the world ocean by Chelton and

Schlax (1996). Their summary of observed phase speeds against latitude was shown in figure 2.5. The observations are given between 50°S and 50°N, and presented as circles. In the Southern Ocean, phase speeds are seen to decrease with latitude in an approximately linear fashion, from 5 cm/s at 30°S to 2 cm/s at 50°S. These are westward phase speeds, measured outside the ACC, and this linear decrease with latitude is in accordance with the dependence of Rossby waves on β and the stratification. Westward phase speeds in the Southern Ocean were calculated in this section and presented in figure 5.24 for features 3 and 5 of table 5.2. The results from Chelton and Schlax are for long Rossby waves, so it is appropriate to make comparison with the longest period waves in figure 5.24. For both features 3 and 5 the westward phase speed for the period of 348 days (frequency number 5) is close to 1 cm/s (though the linear fit suggest a slightly higher value). These features are at 58°S and 62°S respectively, so 1 cm/s is higher than would be expected from linear extrapolation from figure 2.5. However, given that the extrapolation should not be strictly linear and that phase speeds for periods longer than 348 days are expected to be lower, the results for features 3 and 5 are consistent with previous observations of westward phase speeds. Linear theory is known to predict lower values of westward phase speeds than are observed in the real ocean. This, and the latest improvements to the linear theory, were discussed in section 2.4. The linear increase in phase speed with frequency was explained in section 3.3.3. The phase speeds increase slower with frequency than expected for a fixed wavelength due to the wavelengths being inversely proportional to frequency. This is because of a low first Rossby deformation radius at these latitudes (20 to 30km), which means all the waves observed here have long-wave characteristics with respect to the dispersion relation.

Eastward propagating Rossby waves in the Southern Ocean have most recently been studied by Hughes et al (1998), who present results from the ERS1 altimeter of zonal wavenumber at a single period of 4.6 months. This period is about 140 days, which lies between the periods for frequency numbers 12 and 13 (145 and 134 days respectively). The range of eastward phase speeds for this period from figure 5.24 is 2.0 to 2.5 cm/s. This is consistent with the results in Hughes et al of zonal wavelengths between 200 and 600km for the region of the ACC, which

equates to an eastward phase speed range of 1.7 to 5.0 cm/s at this period. There is currently little theory of eastward propagating Rossby waves in the ACC with which to make further comparisons.

This section has shown that phase speeds can be measured from the crossover data, provided resolution criteria are met and provided that regions are previously identified as being associated with zonal propagation of Rossby waves. A linear relationship between phase speed and frequency was identified in FRAM, and results presented in this section confirm this to be the case in the real ocean. The relationship has been shown for Rossby waves propagating both eastward (in regions associated with strong eastward flows) and westward. For westward propagation this can be explained in terms of the long-wave characteristics of the dispersion relation. The linear relationship for eastward propagation might follow the same argument, but this does not explain why eastward phase speeds are typically much slower than the mean flow in which the waves are propagating. Phase speeds in FRAM were found to be very uniform for a particular frequency (see figure 3.14), and this is also evident in results from FRAM at a 4.8 month period presented by Hughes et al (1998). It has not been possible to confirm this result in the altimetry results, so the uniformity of phase speeds for a particular frequency in FRAM remains a model observation.

A limitation to this work may have been the poor spatial resolution of the data. Figure 5.25 compares the time-longitude diagram from the right of figure 5.16 with an equivalent time-longitude diagram derived from data as mapped anomalies. Though the mapped data (right) provides a much smoother diagram, the propagation is well resolved in the diagram based on data at crossover points. An obvious suggestion for further work is to repeat analysis presented here using the mapped data, which was not available in a suitable length time-series at the time of research. This chapter set out to analyse data at crossover points, however, and this has provided useful results in this section, as well as highlighting the limitations associated with this form of data. Also, crossover data was especially suitable for the work presented in section 5.3 due to the associated high spectral accuracy. Data as mapped anomalies will be introduced for the work presented in the next chapter.

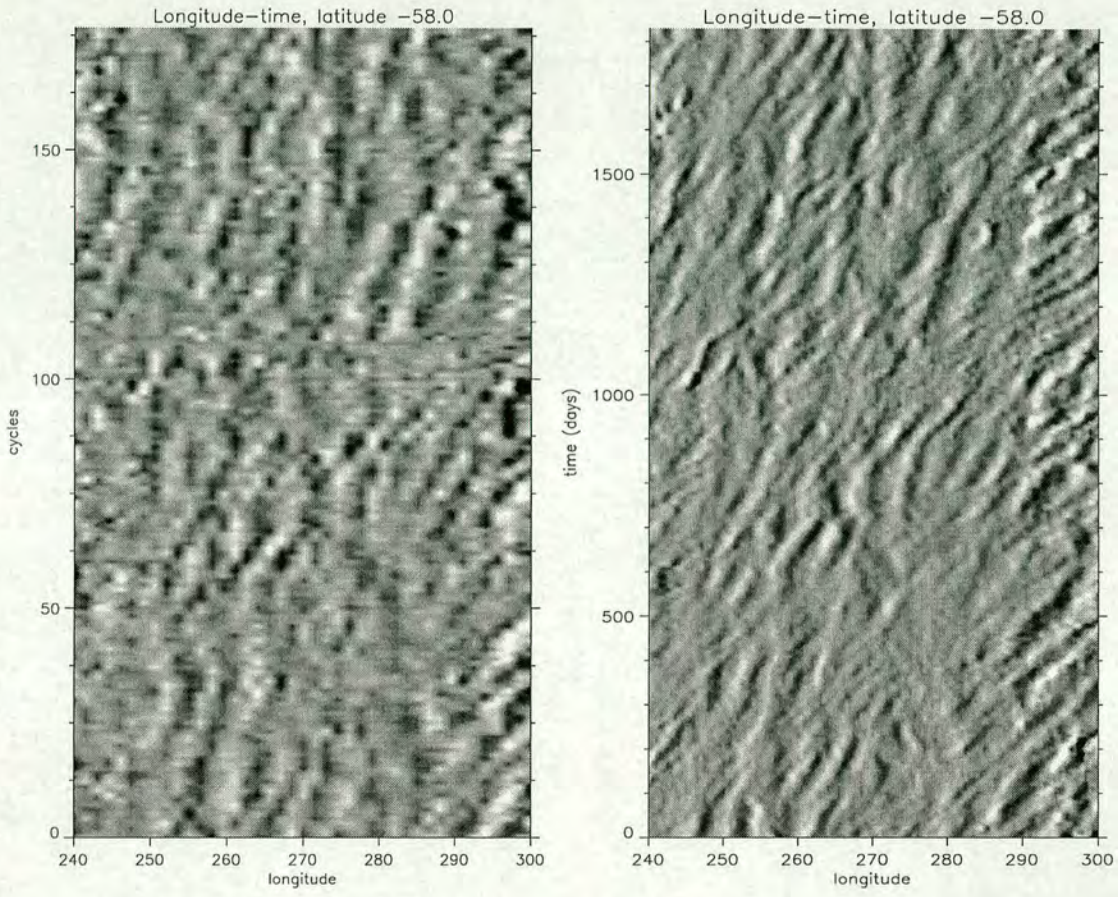

Figure 5.25: Longitude - time diagrams of TOPEX/POSEIDON dh/dx data at crossover points (left), and from mapped anomaly data (right). The longitude range is 240° to 300°E and the latitude is 58°S.

5.5 Eddy quantities

A description of eddy quantities was given in section 3.4. This section describes the calculation of eddy quantities from the TOPEX/POSEIDON crossover data. Results are displayed on a FRAM grid, as discussed in section 5.2.5. All good data values were used for the calculation. Where data at a point was missing for no more than two consecutive cycles, this was filled by linear interpolation.

5.5.1 Accuracy of p, q and r

Recapping from chapter 3, the variance quantities p, q and r are given by $p = \overline{u'u'}$, $q = \overline{v'v'}$ and $r = \overline{u'v'}$. Figure 5.26 shows the errors in u and v against latitude,

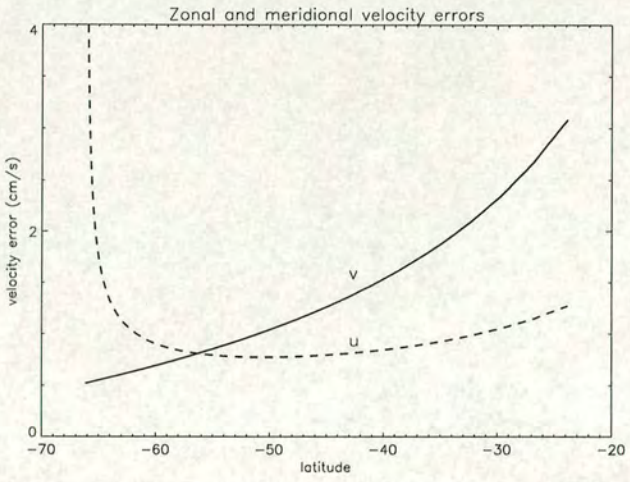

Figure 5.26: Error in v (solid line) and u (dashed line) for different latitudes, when calculated from along-track slopes with an error of 1 cm per 100 km.

when calculated at crossover points. This is equivalent to the slope errors shown in figure 5.2 modified by the coriolis parameter. For errors in u and v of δu and δv respectively, the errors in the variance quantities are calculated as follows:

The error in uu, $\delta(uu)$ is given by,

$$\delta(uu) = 2\, u\, \delta u, \tag{5.2}$$

and similarly for vv. The error in uv is given by,

$$\delta(uv) = \sqrt{v^2(\delta u)^2 + u^2(\delta v)^2}. \tag{5.3}$$

Assuming errors for different cycles are uncorrelated, the errors in p, q and r are,

$$\delta p = \frac{\delta(uu)}{\sqrt{n}}, \quad \delta q = \frac{\delta(vv)}{\sqrt{n}}, \quad \delta r = \frac{\delta(uv)}{\sqrt{n}}, \tag{5.4}$$

where n is the number of measurements in the time series.

The resulting errors in the variance quantities are shown as a percentage in the left-hand graph of figure 5.27 for a typical velocity anomaly (u' and v') of 10cm/s

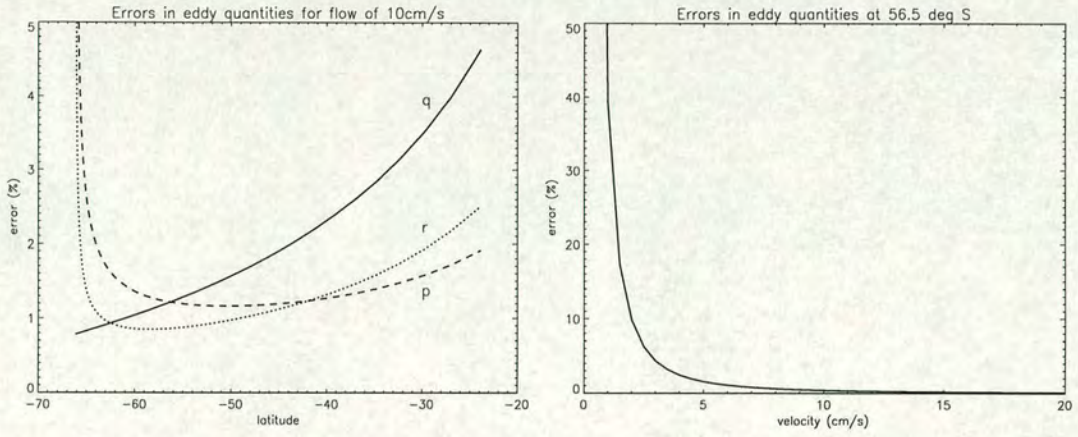

Figure 5.27: Error in variance quantities against latitude (left) and against velocity anomaly at 56.5°S (right), when calculated from along-track slopes with an error of 1 cm per 100 km.

and for the time series of 177 cycles. Errors for p, q and r are all less than 2% for latitudes between 45° and 64°S. The velocity anomaly of 10cm/s is chosen as a typical value to give a scaling. The percentage errors will be modified for different velocity anomalies by an amount shown in the right-hand graph of figure 5.27. This shows a large increase at velocities below a few cm/s. The smaller signals at low velocities, however, mean the higher percentage errors are less important.

Additional loss of accuracy will occur where data is missing from the time series. The percentage of missing data is shown in figure 5.28 which shows high values to the South corresponding to sea ice coverage. The calculated variance quantities can be considered accurate between 45° and 64°S and where this field is green. The quantities p and r can be considered accurate further North, the error in figure 5.27 being less than 5% up to 33°S.

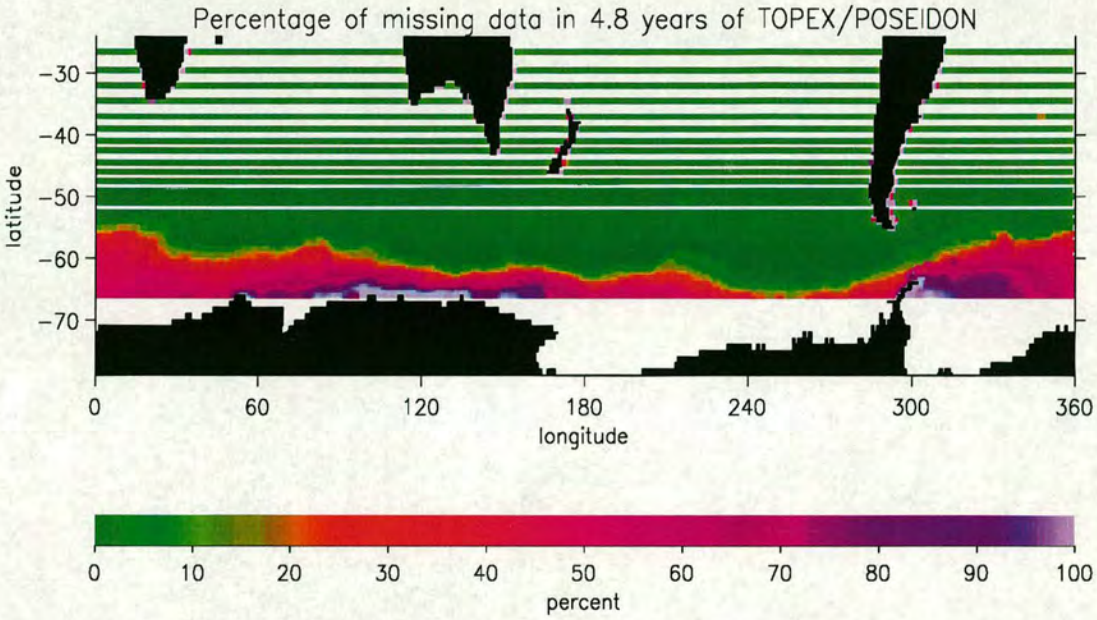

Figure 5.28: Percentage of missing data at TOPEX/POSEIDON crossover points for the measurement period of 4.8 years

5.5.2 Total variance and anisotropy

Recapping from chapter 3, the eddy variance and anisotropy are given by the sum and difference respectively of the major and minor axes of the velocity variance ellipse. In terms of the variance quantities, p, q and r, these are given by,

$$\text{variance} = \sigma_1 + \sigma_2 = p + q; \tag{5.5}$$

$$\text{anisotropy} = \sigma_1 - \sigma_2 = 2\sqrt{s^2 + r^2}, \tag{5.6}$$

where $s = (p - q)/2$.

Variance

Figure 5.29 shows the eddy variance calculated from the 4.8 years of u' and v' data at TOPEX/ POSEIDON crossover points. This is equivalent to twice the eddy kinetic energy. This quantity relates to surface height variability, which has been presented for the Southern Ocean using Geosat observations (Morrow et

al, 1994) and shorter time series of TOPEX/POSEIDON data (Hughes, 1995). These results, however, benefit from the longer time series and the accuracy of the velocity anomaly measurements at crossover points. Despite the spatial resolution problems to the north, the nature of variability in the ACC is clearly visible. Accuracy is only a problem south of 64°S.

The amplitude of the variance field is about four times that of the variance results from FRAM (figure 3.20), and this discrepancy is a known deficiency of ocean models. Despite this, the structure of the variance field compares well to the FRAM equivalent, with high amplitude features in the same locations and with similar spatial scales. The variance field provides a good indication of the position and strength of the ACC. It has already provided a useful reference for the phase speed work in section 5.4.

Anisotropy

Figure 5.30 shows the eddy anisotropy calculated according to 5.6. As with the FRAM results, the variation in amplitude of anisotropy closely corresponds to the variation in amplitude of the variance. The amplitude is about 40% of the variance, compared to 60% in the FRAM results. The real eddies are therefore more isotropic, but still interact significantly with the mean flow. Again there are differences on smaller scales and this is particularly evident in the SE Pacific, where the ACC passes further South and the spatial resolution is better. The anisotropy here has a jet structure on the scales that would be expected in the mean flow. If these are real features then it seems plausible that the anisotropy is closely related to the mean flow. This is investigated further in the next chapter.

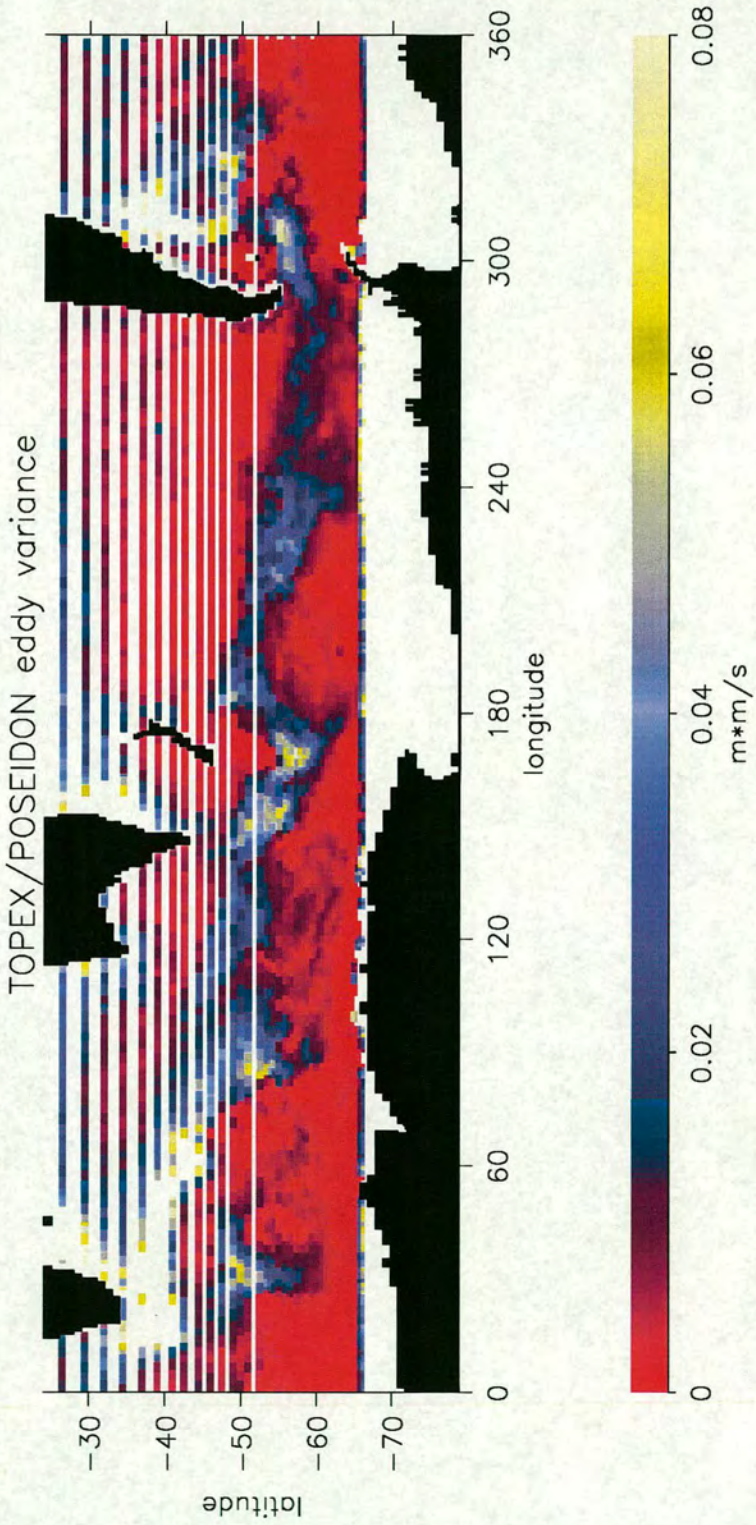

Figure 5.29: Gridded eddy velocity variance from TOPEX/POSEIDON crossover data.

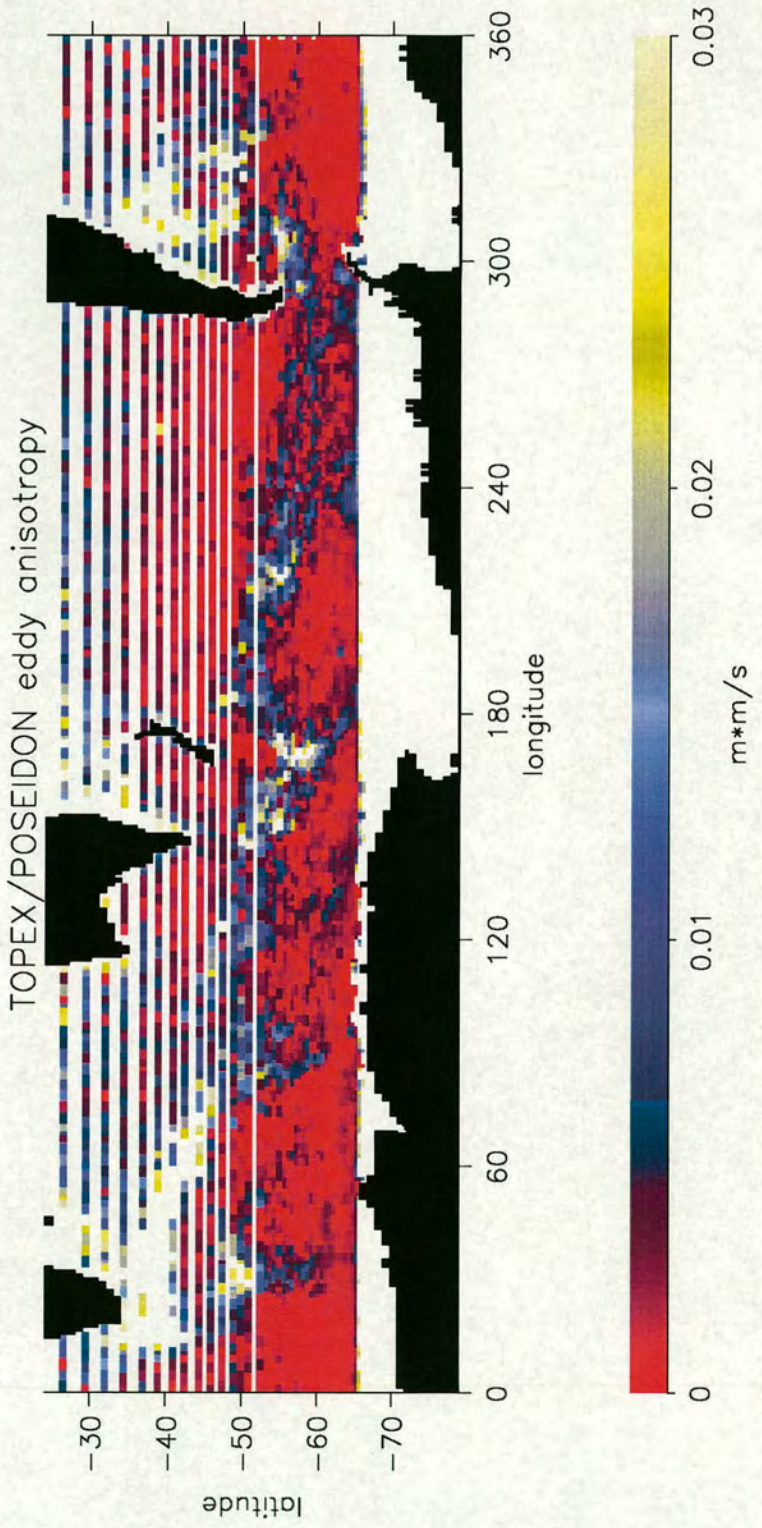

Figure 5.30: Gridded eddy anisotropy from TOPEX/POSEIDON crossover data.

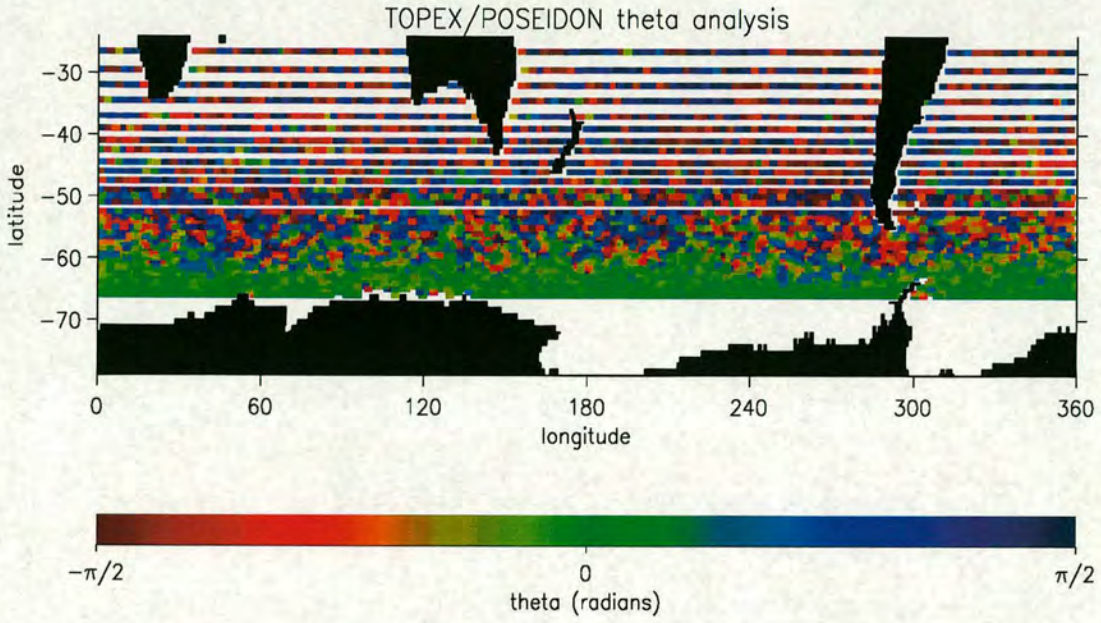

Figure 5.31: Gridded eddy orientation angle from data at TOPEX/POSEIDON crossover points.

5.5.3 Theta

Results for the eddy orientation angle, θ (given by $\tan 2\theta = r/s$, where $s = (p-q)/2$), are shown in figure 5.31. North of about 60°S (the latitude for orthogonal crossovers) θ tends toward $\pi/2$ and south of this latitude θ tends towards zero. This is not a satisfactory result, due to the sensitivity of the calculation to crossover angle. This is confirmed by repeating the calculation on data as noise, generated by randomly shuffling all data values in time. A definite transition from zero to $\pi/2$ is then evident at 56.5°S. This is related to the errors in p and q (figure 5.27), which intersect at this latitude. It is hard to present the errors for θ graphically, however, due to the tan2θ function. The fractional error in $\tan 2\theta$ is given by,

$$\frac{\delta(\tan 2\theta)}{\tan 2\theta} = \sqrt{\left(\frac{\delta r}{r}\right)^2 + \left(\frac{\delta s}{s}\right)^2}, \tag{5.7}$$

which depends on the errors in r and s. Because $s = (p-q)/2$ the error in s will be much larger than the error in r, so the relative errors in p and q have a strong

influence in the result.

The θ results from FRAM were found to relate closely to axes of jets in the mean flow. It would be very useful to reproduce such a result in the real data. The next chapter looks at the calculation of θ from data in the form of mapped anomalies, which includes measurements away from crossover points.

5.6 Summary

This chapter has used data from the TOPEX/POSEIDON satellite altimeters to study the Southern Ocean in various ways. Zonal and meridional gradients of SSH were resolved at ground-track crossover points and this subset of the altimeter measurements was used throughout the chapter. This provided data of high accuracy at the expense of spatial resolution. Techniques that were developed in chapter 3 were applied to this 177 cycle (4.8 years) time-series of data.

Section 5.3 described a study of spatial correlations in the frequency of wave activity. Principal components (EOF) analysis was used in the frequency domain to identify regions which were associated with particular frequencies, and which could therefore represent waveguides. These regions were found to be small, but they provided a focus for the analysis of phase speeds, presented in section 5.4. Longitude time diagrams from these regions, which incorporated pairs of crossover rows, enabled wave propagation to be observed, and provided the basis for phase speed measurement. These diagrams were shown to have resolution restrictions, but are a suitable indication of Rossby wave propagation South of 50°S. Fast Fourier Transform (FFT) components were found to have limitations in the calculation of phase speeds, but were adequate when combined with the Radon Transform (RT) in certain locations. The combination of FFT and RT enabled the relationship between frequency and phase speed to be presented, and this compared very well to results from FRAM. Phase speeds increase linearly with frequency, but slower than expected for a fixed wavelength. Theory shows that wavelengths are inversely proportional to frequency for the long Rossby waves observed here, and this offers an explanation for this relationship between phase

speed and frequency. Phase speed measurements were also compared favourably to previous results.

Section 5.5 presented eddy quantities calculated from the TOPEX/POSEIDON crossover data. The field of eddy variance clearly showed the nature of variability in the Southern Ocean over the measurement time period, despite resolution problems to the North. The field of eddy anisotropy corresponded to the eddy variance, but contained features on smaller scales. The eddy orientation angle could not be calculated accurately from the crossover data due to its sensitivity to crossover angle.

This chapter has dealt successfully with data at ground-track crossover points, which has provided useful information relating to Rossby wave activity in the Southern Ocean. A limitation has been the poor spatial resolution of the data. Improved results might be obtained by repeating the analysis using mapped anomaly data (introduced in the next chapter), but this was not available in a sufficient length of time-series at the time of research. Another aim of the thesis is to investigate relationships between velocity anomaly measurements and the mean flow. Chapter 4 looked at the relationship between Rossby waves and the mean flow. The next chapter expands on sections 3.4 and 5.5 by further investigating relationships between eddy quantities and the mean flow.

Chapter 6

Eddy quantities and the mean flow

Diagnostics of eddy quantities were presented for FRAM in chapter 3 and for TOPEX/POSEIDON in chapter 5. In FRAM, the eddy orientation angle was found to be a good indicator of the axes of jets in the mean flow. In addition, the scales of features in the field of eddy anisotropy were similar to that expected for jets in the mean flow. In the TOPEX/POSEIDON results (figure 5.30), structures which could relate to the mean flow were particularly evident in the southeast Pacific, where the improved resolution to the south coincides with the path of the ACC. This chapter compares the eddy quantities and currents in greater detail, initially in FRAM and then in the altimetry data, with the help of current measurements from ship cruises. Unfortunately the eddy orientation angle, θ, could not be obtained accurately from data at TOPEX/POSEIDON crossover points, and therefore altimetry data in the form of mapped anomalies is introduced in order to improve resolution and try and overcome this problem.

6.1 Eddy quantities and mean flow in FRAM

The mean zonal velocity in FRAM, U, was given in figure 3.1. The fields of eddy variance and anisotropy from FRAM were presented in figures 3.20 and 3.21. These fields were discussed in the corresponding sections but no formal comparison with the mean flow was made. This section compares meridional

profiles of the mean flow and eddy quantities, and then looks at correlations between the mean flow and various eddy quantities in the FRAM output.

6.1.1 Meridional profiles

Figure 6.1 shows three pairs of meridional profiles of U from FRAM (figure 3.1) (solid line), at 270°E (top), 240°E and 210°E (bottom), in the South Pacific. Superimposed (dotted lined) is the eddy anisotropy (left column) and eddy variance (right column) for the same profile, taken from figures 3.21 and 3.20 respectively. The velocity and eddy quantities have been smoothed in the same way and the scaling of the eddy quantities is the same for each profile. This scaling is chosen as $U/55$ for the anisotropy, and $U/63$ for the variance.

At 270°E there is a remarkable agreement between the mean U and anisotropy (top left) in the region of the ACC, between 53° and 63°S. Over this latitude range, the size, amplitude and position of jets in the mean flow are reflected very closely by the structure of the anisotropy. The variance (top right) agrees well for the jet at 55°S but has a larger scale structure than the mean flow to the South. At 240°E (middle profiles), jets between 55° and 65°S are reflected in both the anisotropy and variance, with the relative amplitude of the variance closer to the amplitude of U in this case. At 210°E (bottom profiles), the reflection of U is similar in the anisotropy and variance, with a jet in the eddy quantities at about 62°S which represents a westward jet in U. This sample of profiles suggests that the eddy quantities might be used to infer the position of jets in the mean flow, at least in this part of the Southern Ocean. There is also indication that the magnitude of U can be estimated from the eddy quantities in certain circumstances. This provides motivation for attempting a similar comparison in the TOPEX/POSEIDON data, particularly as jet-like structures were observed in the anisotropy field in this region. The real mean flow is not known, however, and finding out about this is the objective. Nevertheless, it is possible to use current measurements from ship cruises to estimate the mean flow along specific profiles. This is addressed in section 6.3.

The latitude dependence of the agreement shown in figure 6.1 is interesting. The

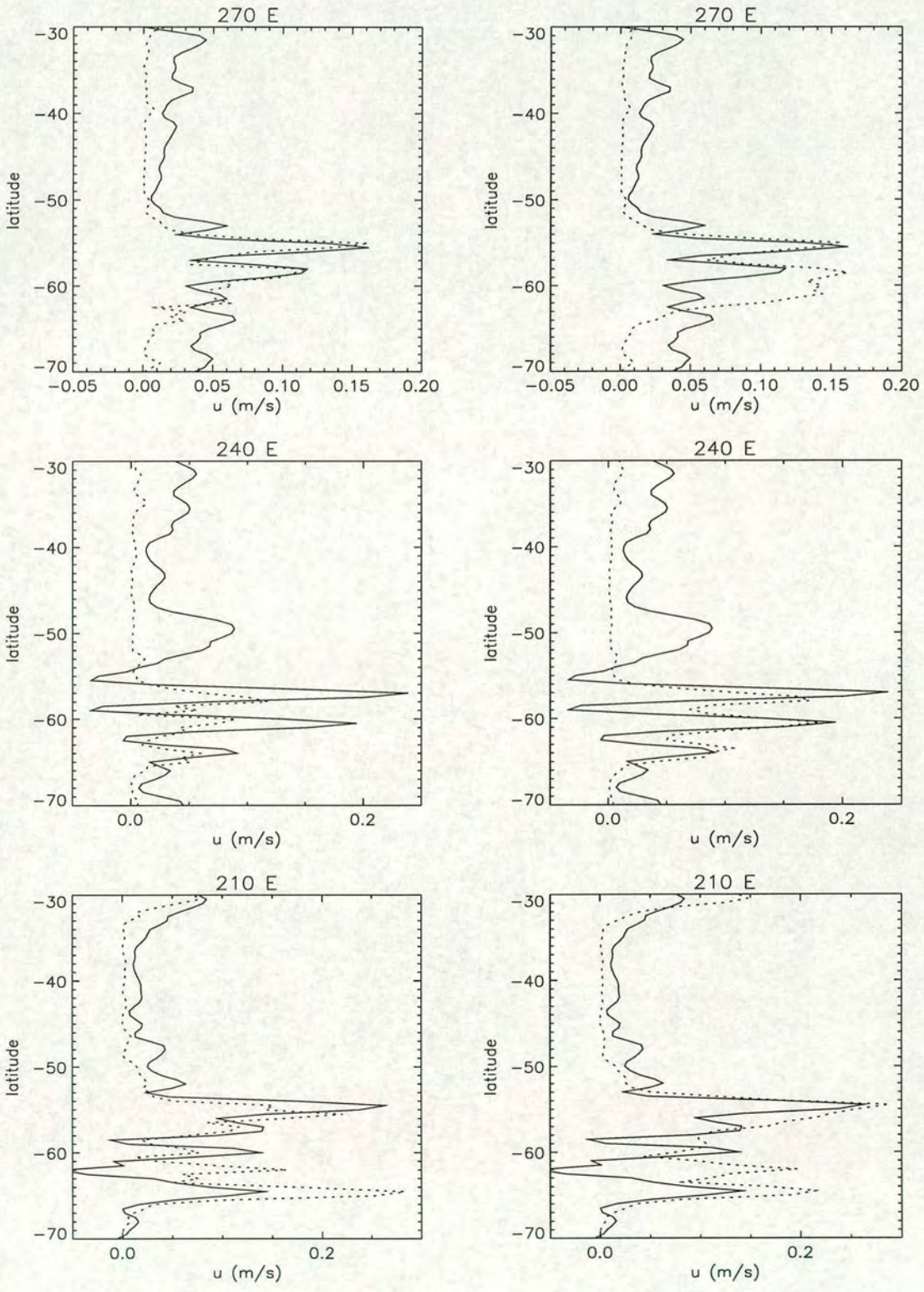

Figure 6.1: Meridional sections of mean U (solid line) and anisotropy (dotted line - left), and U and variance (dotted line - right), for 270°E (top), 240°E and 210°E (bottom). The anisotropy and variance are scaled, and equal to $U/55$ and $U/63$ respectively.

jet in U at 50°S, 240°E, for example, is not reflected at all in the eddy quantities. At other longitudes, a similar latitude dependence is observed, with the eddy activity high in the ACC and very low outside, even if the mean flow away from the ACC is relatively large. A reason for this could be that the amount of eddy activity at the surface depends heavily on the wind forcing. This has been suggested by Wunsch (1998) who used TOPEX/POSEIDON data to calculate estimates of the work done by the wind on the ocean. This is dominated by the Southern Ocean, where the forcing is confined to the band of the ACC. Outside this, the flow is more baroclinic and so more driven by buoyancy forcing. For the baroclinically stable situation this gives rise to mean flows with low eddy activity. From these profiles it seems as though FRAM, which is forced by climatological monthly winds, is displaying this behaviour.

6.1.2 Correlations

To study the relationship between the eddy quantities and mean U in FRAM in more detail, correlation coefficients can be calculated. Figure 6.2 shows the correlation coefficients between U and eddy quantities, for U greater than different values, and for the whole FRAM domain. The correlation calculates how one field varies with the other and is not changed by the addition of a constant to, or taking a factor of, the whole of either field. The solid curve is the correlation with the square root of eddy anisotropy (hereafter sqrt(sd)), and the dashed curve is the correlation with the square root of eddy variance (hereafter sqrt(ss)). The reason for using the square root will become clear. The dash-dotted line is the correlation with the eddy anisotropy (sd) and the dotted line is the correlation with the eddy variance (ss). The number of points in the correlation decreases approximately exponentially, from 26000 for U greater than 0cm/s, to 400 for U greater than 30cm/s.

The highest correlation is with the square root of variance for U greater than 0cm/s, at 0.65. The equivalent correlation coefficient with the square root of anisotropy is slightly less, at 0.63. For U greater than 5cm/s to 12cm/s, the best correlation is with the square root of anisotropy. This represents the velocity

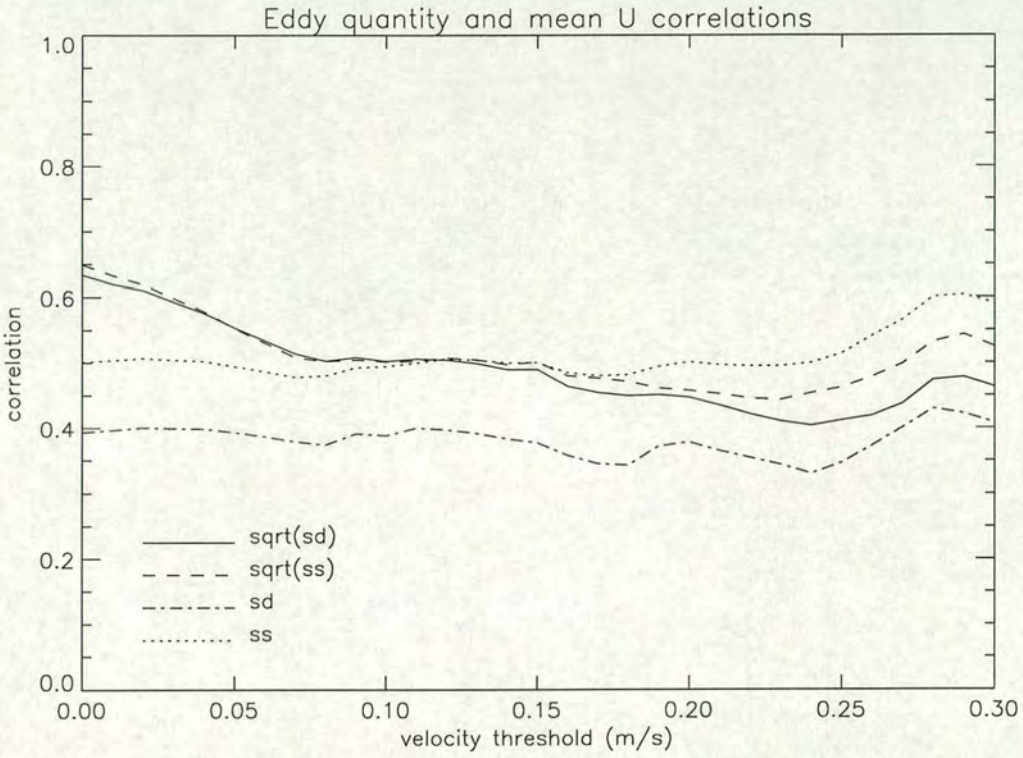

Figure 6.2: Correlation coefficients for various eddy quantities correlated with U, when U is above the value given on the x-axis. The dotted line is for the eddy variance, the dash-dot line is for the eddy anisotropy and the dashed and solid lines are for the square root of the respective eddy quantities.

range of most interest when comparing the two quantities, as U lies in this range in the majority of the field. Correlations when U is high (greater than 20cm/s) are best with the straight eddy variance. The correlations shown in Figure 6.2 represent eastward velocities over the entire Southern Ocean. The same curves were calculated for just the ACC region, as defined in FRAM by Wells and De Cuevas (1995) (between the 10 and 180 Sverdrup contours of streamfunction, shown for reference in figure 6.3). The results are shown in the left hand graph of figure 6.4. In this case the number of points in the correlation decreases nonlinearly from about 11000 for U greater than 0cm/s, to about 100 for U greater than 30cm/s. There are clear differences from figure 6.2. For the ACC region the correlations for different quantities vary by less for a given velocity threshold. The values, however, drop rapidly with increasing threshold, particularly above 0.15 m/s, until becoming negative above 0.27 m/s. The correlations are therefore very poor at high velocity thresholds and this is a disappointing result. The

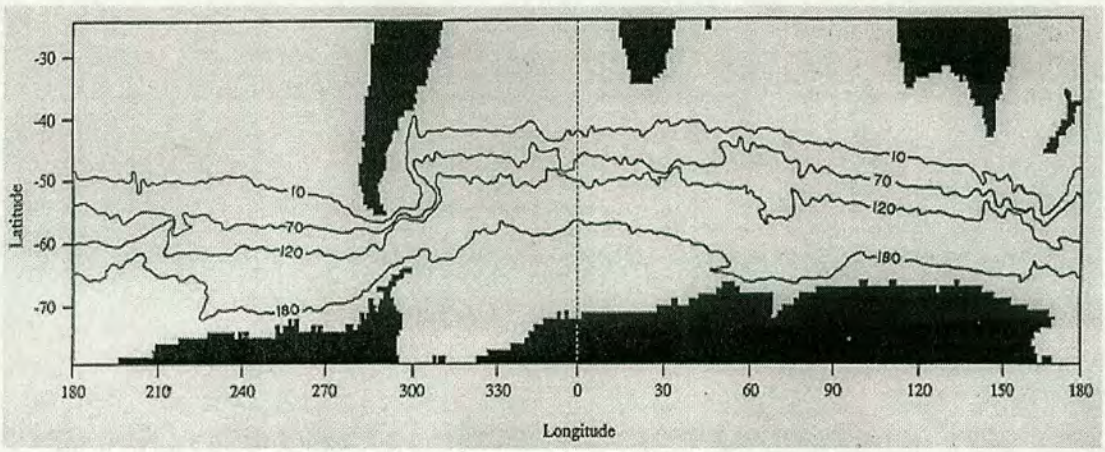

Figure 6.3: Boundaries of the ACC region in FRAM (10 and 180 Sverdrup contours), from Wells and De Cuevas (1995).

right hand graph of figure 6.4 shows the correlations for all points North of this ACC region. The number of points in these correlations is similar to that for the ACC region (falling from about 12000 to 100). These correlations are much better, particularly for sqrt(ss) and sqrt(sd) which remain above 0.6 for most of the velocity thresholds. Inspection of the mean U field associated with the Wells and De Cuevas ACC region shows that this region does not capture many of the northernmost jets associated with the high variance region. This, and the results of figure 6.4, demonstrate that it is inappropriate to restrict the analysis to the Wells and De Cuevas ACC region. Some final correlations will be presented for different regions of the Southern Ocean.

Correlation curves for different regions of the Southern Ocean are shown in figure 6.5. Each graph represents 60° of longitude such that region 1 covers 0°E to 60°E and region 6 covers 300°E to 0°E. All latitudes in FRAM are included. The range of threshold U for these curves is 0 to 10 cm/s. Correlations are highest in regions 1, 2 and 5. In region 1, the highest correlation is with sqrt(sd), with a coefficient between 0.62 and 0.74. In region 2, the highest correlation is with sqrt(sd) for most values of the U threshold, with the coefficient between 0.51 and 0.70. The best correlations are found in region 5, the Southeast Pacific. This is again with sqrt(sd), with a coefficient between 0.64 and 0.77. For a velocity threshold between about 4 and 8cm/s, the correlation is best with sd and this ties in with the comparisons shown in figure 6.1. As well as giving the best

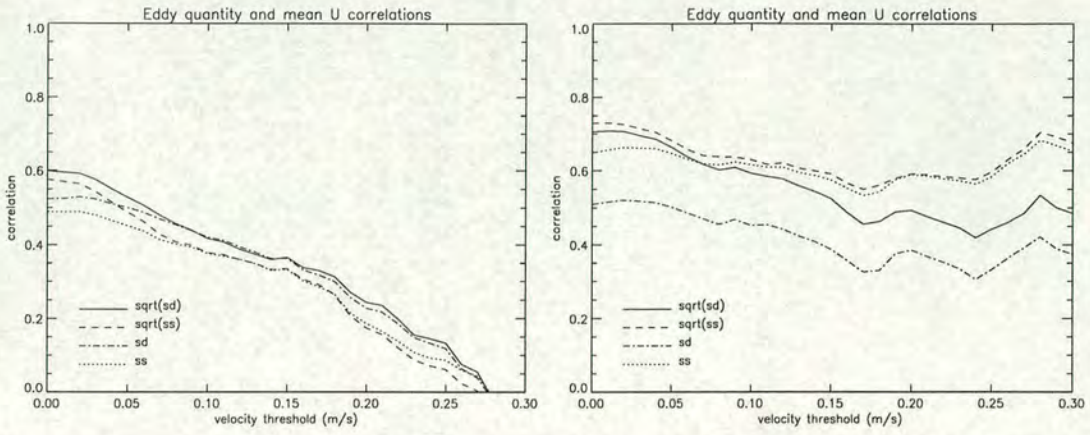

Figure 6.4: As for figure 6.2 but for the ACC region as defined by Wells and De Cuevas (1995) (left), and for the region North of this (right).

coefficients, region 5 also has the lowest U on average over the region. This implies the relationship between the eddy quantities and U is better for weaker stretches of the ACC. Indeed the highest regional average U is found in regions 3 and 6 where the correlations were least good. In addition, the regions upstream of Drake Passage in the Southeast Pacific was noted to be relatively free from the effects of topography (section 4.3), and this may also be an important factor.

The correlations are least good in regions 3 and 6. These regions include the western boundaries of Australia and South America respectively. Here the mean flow is less zonal than many parts of the Southern Ocean, and this is likely to be affecting the relationship. This might also be expected of the Agulhas region (region 1), but here the mean flow which is non-zonal is westward, and so not included in the correlation calculation. Finally, region 4 has good correlation coefficients for when U is positive (0.66), but this drops to 0.24 for U greater than 10cm/s. This implies that the correlation is good for low eastward values of U and these lower values dominate this region. The poor correlations for high values of U could be related to the topographic influence just upstream of this region, where the ACC passes South of New Zealand. It is possible that the relationship between eddy quantities and U in this part of the ACC is disrupted by the propagation of topographic Rossby waves into this region.

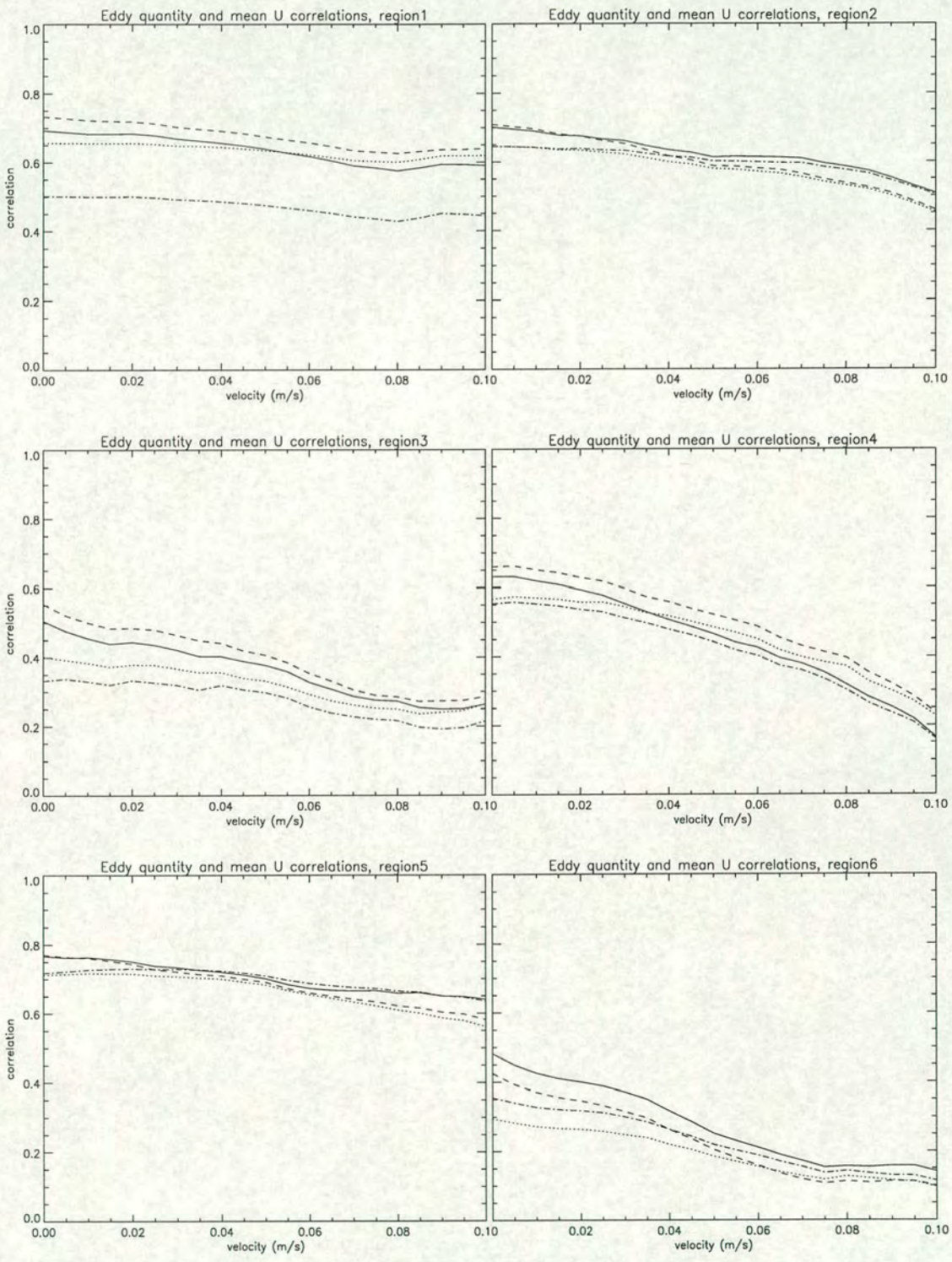

Figure 6.5: Correlation coefficients as 6.2 but for different regions of the Southern Ocean. The top left (region 1) is for the longitude range 0° to 60°E and subsequent regions (moving left to right) are for subsequent 60° slices of longitude.

Almost without exception, it is the square root of one of the eddy quantities which correlates best with U. In half the regions (1, 3 and 4) the correlation is best with sqrt(ss) and in the other half the correlation is best with sqrt(sd). This is an attractive result, as the square root of the eddy quantities has the same units as U. The quality of some of these regional correlations shows that the eddy quantities are a good indication of the magnitude of U in certain regions such as the southeast Pacific. This is a useful result which might be applied to the real ocean. In order to study the real observed eddy quantities in more detail, maps of sea surface height (ssh) anomaly which combine data from the TOPEX/POSEIDON and ERS1/2 satellite altimeters will be used.

6.2 Data as mapped anomalies

Two datasets of mapped SSH anomalies were obtained, one for TOPEX/POSEIDON anomalies (which will be referred to as TOPEX), and one combining data from TOPEX/POSEIDON and ERS-1 and ERS-2 altimeters (which will be referred to as TPERS). These altimeter products have been produced by the CLS Space Oceanography Division as part of the European Union' Environment and Climate projects AGORA (ENV4-CT9560113) and DUACS (ENV4-CT96-0357). Both maps are at a resolution of 0.25° in longitude by 0.25° in latitude. TOPEX maps span the period of 12/10/92 to 5/11/97 with one map every 10 days. TPERS maps span the period of 12/10/92 to 26/10/97 but with a gap from January 1994 to March 1995, when ERS data was not available (ERS-1 was in a 'geodetic' phase, when it's orbit was unsuitable for SSH measurement). From June 1996, data from ERS-2 were used. An individual map shows the SSH anomalies relative to a 3-year mean (January 1993 to January 1996). The mapping procedure is documented in Le Traon et al. (1998).

A dataset for the Southern Ocean was taken from the TOPEX and TPERS maps. This was based on the TPERS maps but included TOPEX maps to fill the gap between January 1994 to March 1995. The anomalies were adjusted to be relative to the full 5-year mean.

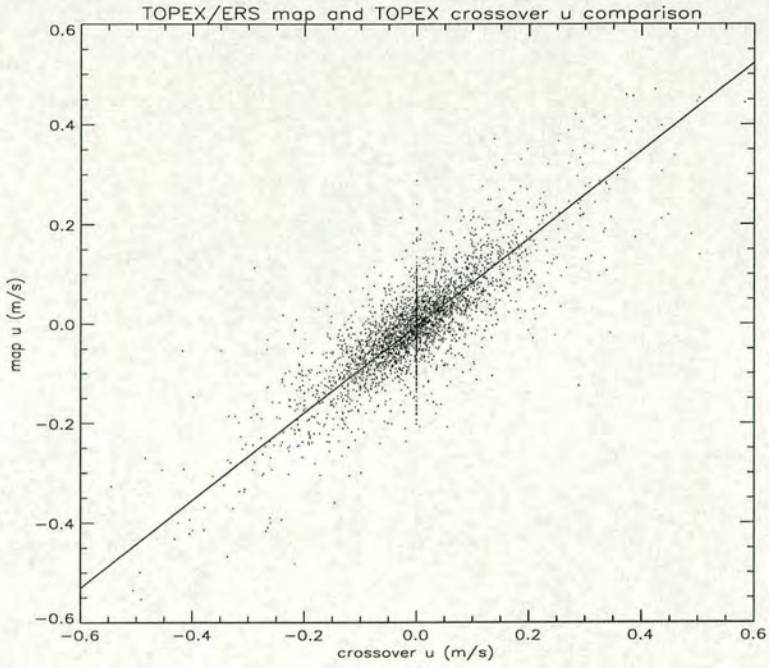

Figure 6.6: Scatter-plot of u anomaly comparison between map u (y axis) and crossover u (x axis) for crossover points north of 64°S. The solid line is a least-squares linear fit.

6.2.1 Velocities

Velocities are obtained from the mapped anomalies by differentiating to obtain zonal and meridional gradients of SSH. The disadvantage of this compared to data at crossover points is loss of accuracy when differentiating smoothed data. However, there are vast resolution benefits compared to calculating velocities at crossover points as the maps make use of data at all points along the ground track. For an individual map, the velocity anomaly field can be calculated and compared with the equivalent crossover velocities.

A typical comparison between zonal velocity anomaly calculated at crossover points and from an anomaly map is shown in figure 6.6. All crossover points north of 64°S have been included (South of this the error in crossover u becomes large - see figure 5.26). The values obtained from the map have been interpolated meridionally onto crossover latitudes. Zonal interpolation was deemed unnecessary as the crossover longitudes differed from map longitudes by less than 10km. Despite some scatter, the gradient of the least-squares linear fit shows that a

correction factor should be applied when obtaining velocities from maps of SSH anomalies, because the crossover velocities are most accurate. The correction for map velocities is equal to 1/0.9 as (map u)=0.9×(xover u). This correction will be applied when using zonal velocities calculated from the TPERS maps, but it will not be applied when calculating eddy quantities as the absolute magnitude of those results is not important.

6.2.2 Eddy quantities

Eddy quantities, described in 3.4, were calculated using velocities obtained from the mapped anomalies. The results of eddy velocity variance and eddy anisotropy are shown in Figure 6.7. These can be compared with the equivalent results from the data at TOPEX/POSEIDON crossover points, figures 5.29 and 5.30. The increased resolution of the mapped anomalies gives a much clearer field, especially towards the north of the domain. Data from the maps also extends further South due to the orbit of the ERS satellites, which made measurements over the whole domain shown here. It must be noted, however, that south of 66°S the results rely only on the ERS altimeters, so there is less data and poorer temporal resolution (due to the 35-day repeat period of the ERS satellites compared to 10 days for TOPEX/POSEIDON). Patches of missing data around Antarctica reflect ice coverage. The quality of these fields compared to the equivalent from crossover data makes them more suitable for the further analysis presented in this chapter.

Small-scale features in the anisotropy in the southeast Pacific are much clearer and there are many other features with a more detailed structure than could be seen before. A plot of the relative anisotropy (anisotropy divided by the variance) is shown in figure 6.8. This highlights regions where the eddies are most anisotropic (bright parts) and shows where the mean eddy field is virtually isotropic (red parts). Figure 6.7 shows the amplitude of anisotropy corresponds to the amplitude of velocity variance. The relative anisotropy, however, is generally greatest where the anisotropy is large. In other words, regions of high variance are generally associated with proportionally higher anisotropy. Highly isotropic regions occur over much of the field but on fairly small scales. These regions are

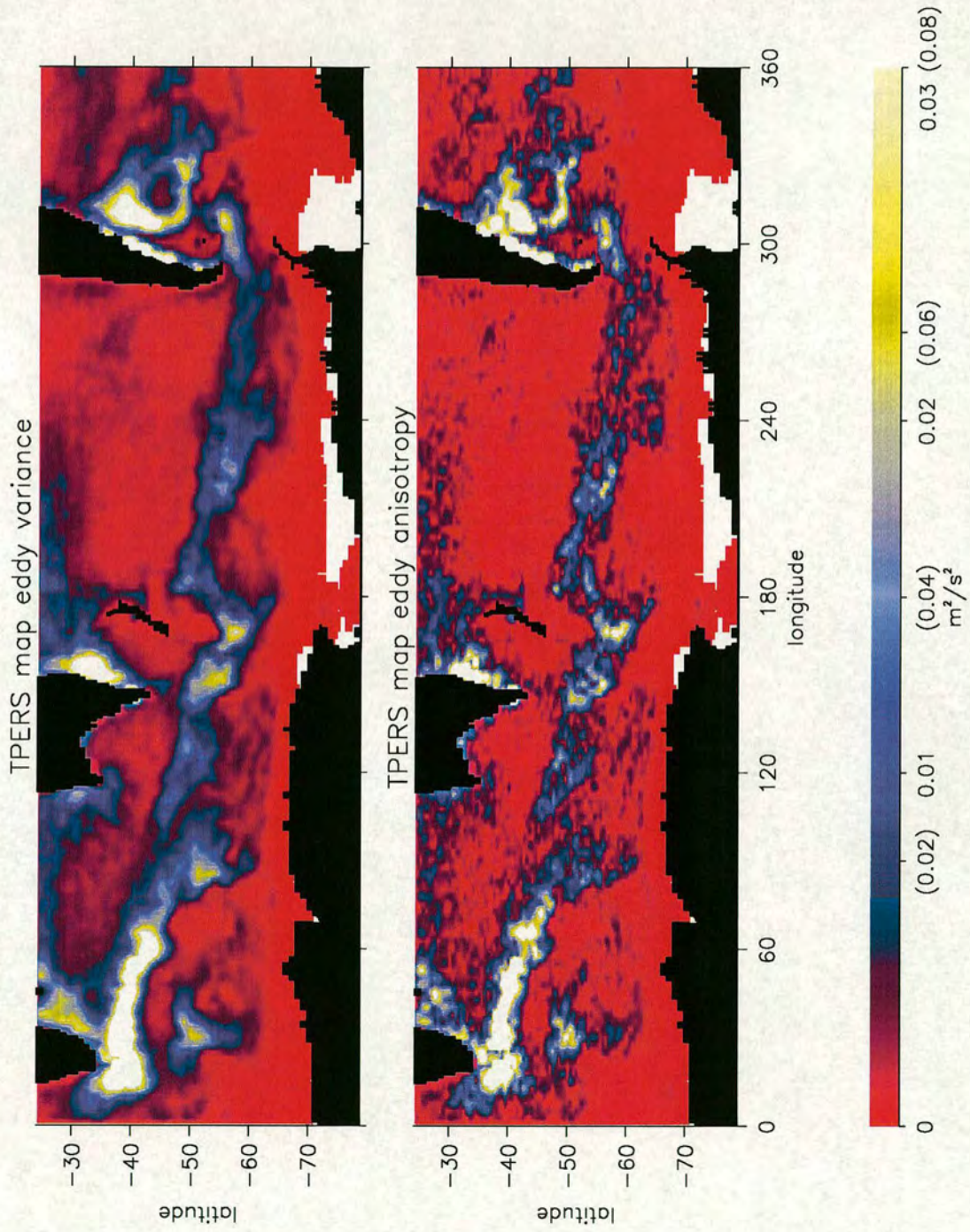

Figure 6.7: Eddy velocity variance (left) and anisotropy calculated from TOPEX/ERS combined maps of SSH anomaly. Values in brackets on the colour bar refer to the velocity variance field.

evenly distributed and mostly outside the ACC, where eddies will be weak.

A field for the eddy orientation angle, θ, can also be calculated from the mapped data. This is shown in figure 6.9, where as before θ is the angle to the zonal direction (positive for a positive gradient). The field is free from the large errors affecting the calculation of θ at crossover points, though there will be errors arising from the mapping procedure which are hard to define. Although the field is not as clear as the FRAM equivalent (figure 3.22), there are many interesting features. Variations are on a smaller scale than with FRAM. Despite this, there are several places where θ is $\pm\pi/2$ along a direction which is near zonal. In the FRAM results, this was where axes of jets in the mean flow were aligned (see figure 3.22). Large regions to the North where θ is close to zero in FRAM do not appear in the observed field. In the active regions on the western boundaries, the two fields compare well. On the East coast of South Africa, θ is positive in both cases, with a definite band in the observed field. Just East of Australia θ is negative and off Argentina θ is positive, apart from a thin negative strip along the coast in the observed field.

This field of θ is a very important result as it shows that more information can be obtained from the eddies than just the variance and anisotropy. The eddy orientation angle, θ, has only previously been calculated in the Southern Ocean from Geosat data, at a resolution coarser than 1° in latitude and longitude (Morrow et al, 1994). Here it is presented at a resolution of 0.25° by 0.25° and should be able to resolve features associated with individual jets of the ACC. It would be particularly valuable to obtain an estimate for the mean flow along a meridional profile, to test whether the relationship observed in the FRAM θ field holds in the real ocean, in addition to making comparisons with the anisotropy field. This might be possible with the use of current measurements from ship cruises, and this is discussed in section 6.3. The fields of eddy quantities from the TPERS maps provide an important basis for analysis in the remainder of the thesis, where they will be used and discussed further.

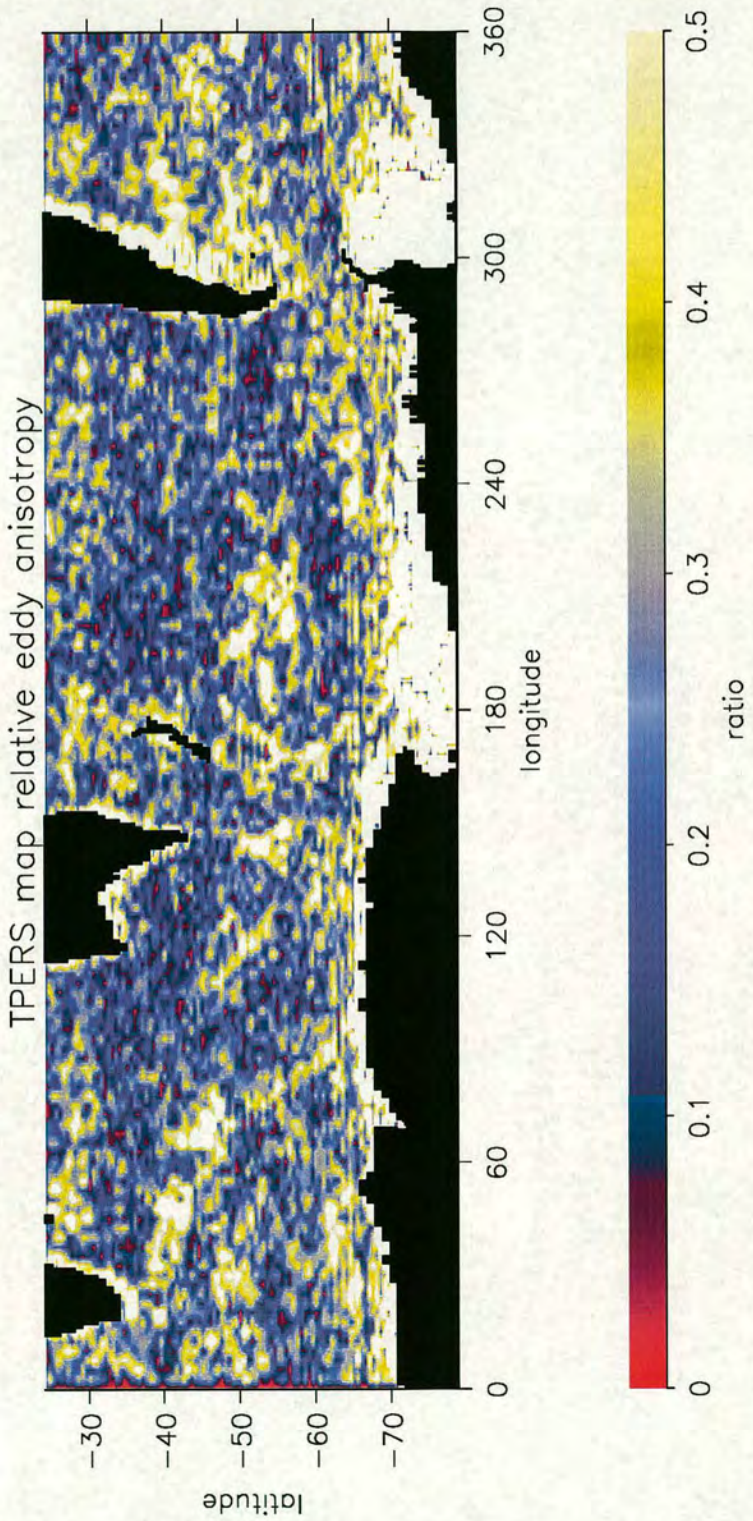

Figure 6.8: Eddy anisotropy divided by velocity variance from TPERS mapped anomalies

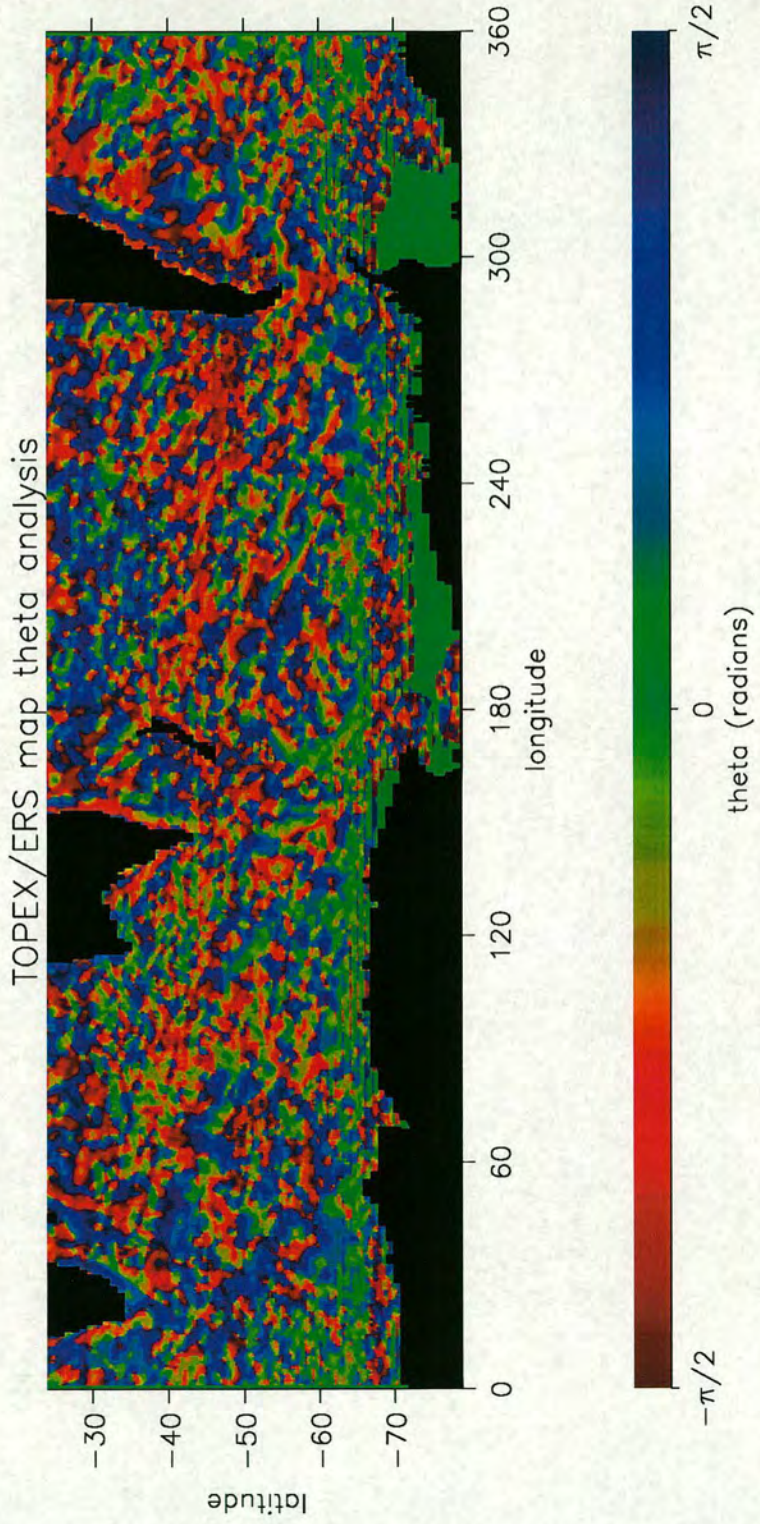

Figure 6.9: Eddy orientation angle from TPERS mapped anomalies

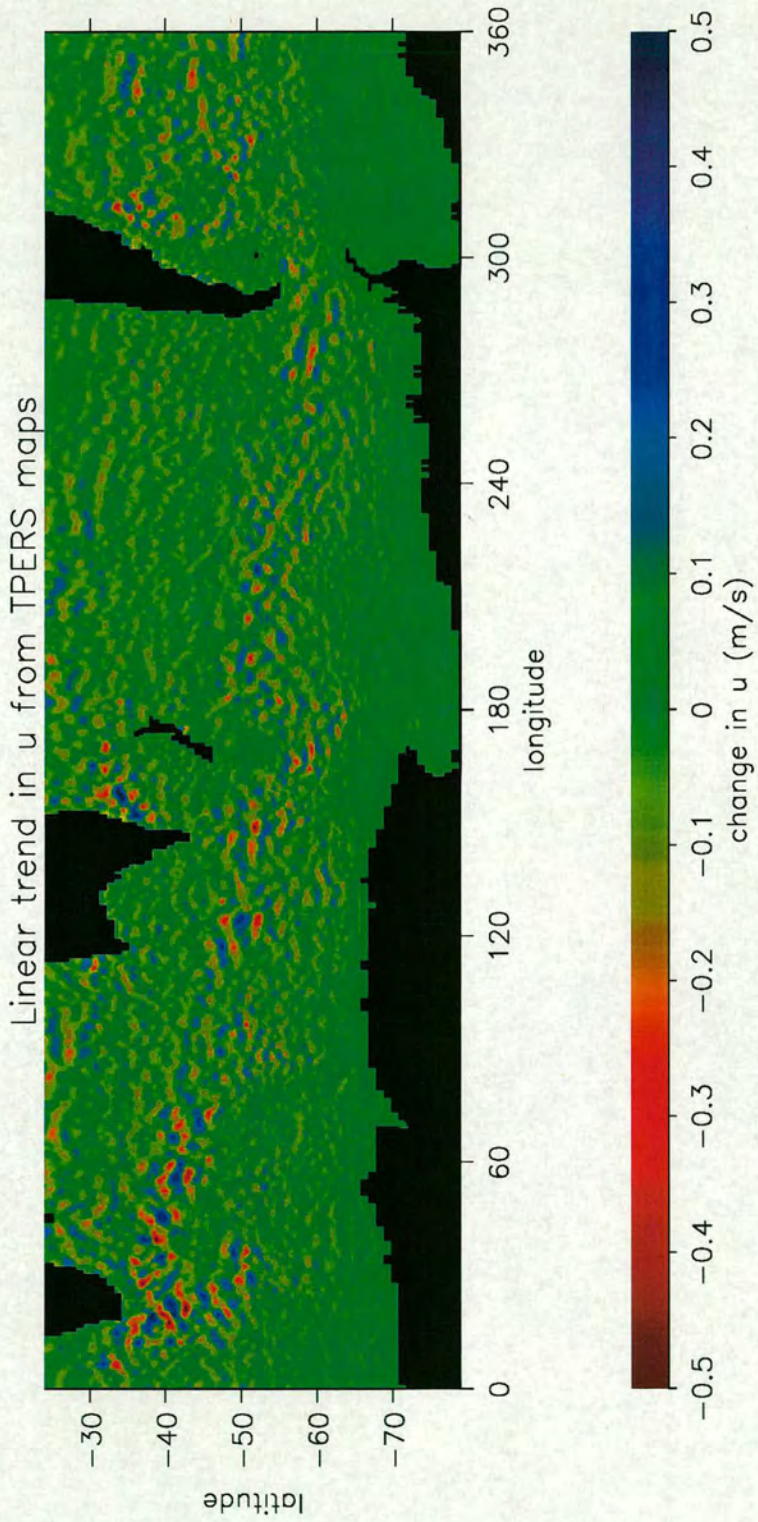

Figure 6.10: Linear trend in u from TPERS maps, calculated by taking the difference between the first and last value of a least-squares linear fit to the time series of u at each gridpoint.

6.2.3 Trend in u

A final quantity that will be derived from the TPERS maps is the linear trend in zonal velocity over the 5 year time period. This was presented for FRAM in section 3.5 as a potentially useful diagnostic when making comparisons with the mean flow. The superposition of axes of jets in the mean flow showed how the trend in u resulted from a mixture of accelerating jets and jets shifting meridionally. The linear trend in u from the TPERS maps is shown in figure 6.10. This was calculated by taking the difference between the first and last value of a least-squares linear fit to the time series of u at each gridpoint. Here it is not possible to make comparisons with the mean flow, but a similar structure to the FRAM results is evident, with a distinct meridional scale. The trend is greatest in the most active regions of the Southern Ocean, as expected. The linear trend has been calculated as a linear trend, but it is important to realise it is the linear trend over the time period of study (i.e. about 5 years). It is not necessarily a trend which will continue after, or which existed before the period of study. It is more likely to represent low frequency variability with a period of many years, caused by gradual cyclical changes in the positions and strengths of jets in the mean flow. The linear trend presented here will be discussed further in section 6.4.

6.3 Ship measurements in the Southern Ocean

As part of the World Ocean Circulation Experiment (WOCE), Acoustic Doppler Current Profiler (ADCP) measurements have been taken on cruises throughout the world ocean. Some of the cruises ventured into the Southern Ocean and can provide current data for comparison with altimetry measurements and derived quantities. This section looks at ADCP data from the WOCE Global Data, Version 1.0 (WOCE Data Products Committee, 1998) and derives an estimate of the mean flow along the relevant cruise tracks.

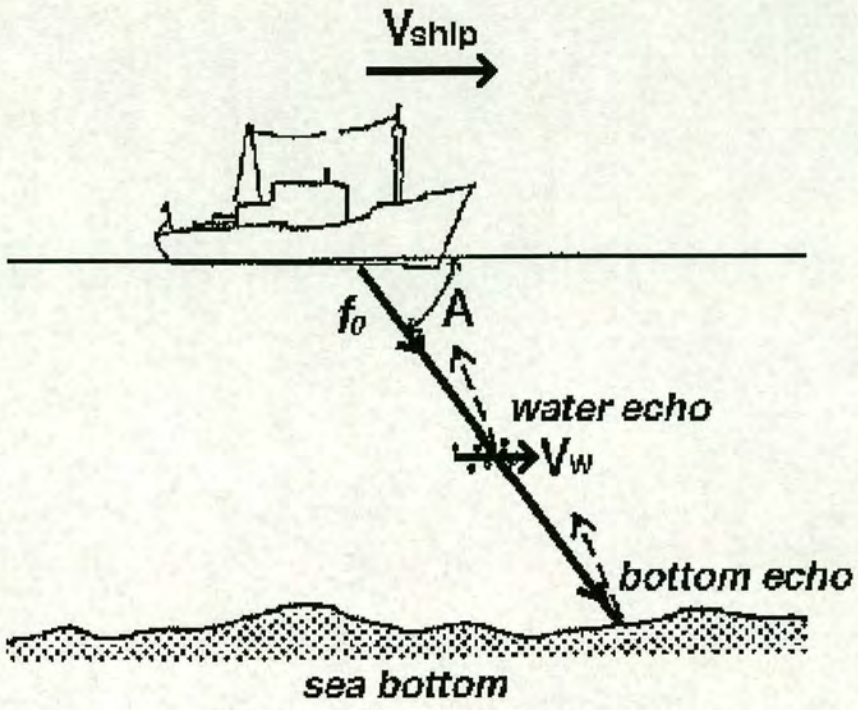

Figure 6.11: Schematic of an ADCP measurement beam. The acoustic beam is represented by f_0, A is the angle of the beam to the horizontal and V_w is the water velocity relative to the ship velocity (V_{ship}).

6.3.1 ADCP data

The ADCP uses sound to measure the horizontal and vertical components of current as a function of depth, relative to the ship velocity. The Doppler effect enables measurement of the relative velocity between the instrument and scatterers in the ocean. Three acoustic beams are required for the three velocity measurements and a fourth beam is used to provide an error estimate. A schematic of an ADCP beam is shown in figure 6.11. Beams are transmitted about once a second and the resulting current measurements are averaged over a few minutes to reduce the effect of noise. A data acquisition system records the currents and calibration parameters, as well as ship navigation data. Absolute currents are obtained from the calibrated ADCP currents relative to the ship, and the absolute ship velocity which is derived from the navigation data.

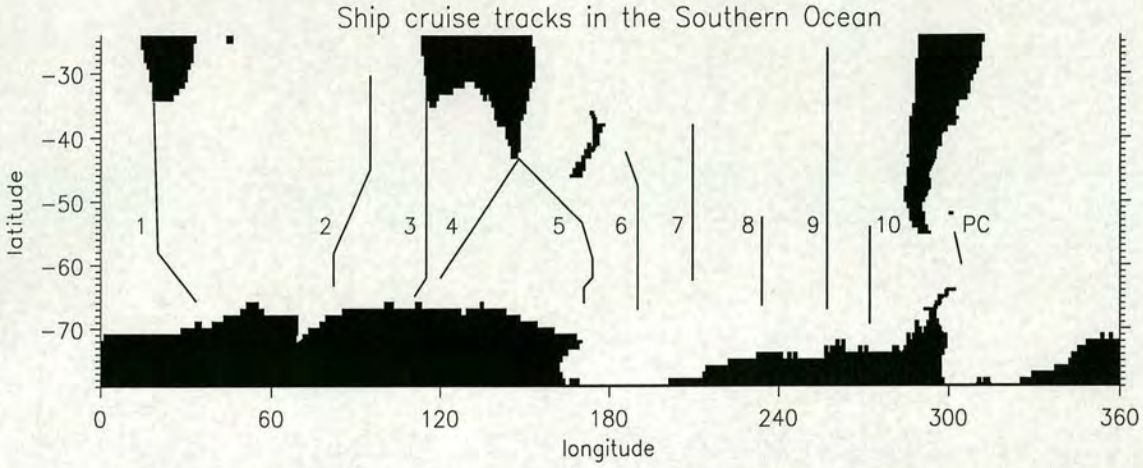

Figure 6.12: Selected WOCE cruise tracks in the Southern Ocean. Information about each track (1-10) is given in table 6.1. Track 'PC' is an additional cruise used for work by Challenor et al (1996).

6.3.2 Cruises

Figure 6.12 shows selected tracks of cruises in the Southern Ocean for which there are ADCP current measurements. Information about the ten cruise transects is summarised in table 6.1.

Absolute currents are available for these transects at depth intervals of 10m from depths of about 30m to 300-400m, depending on the cruise. The absolute currents include a geostrophic and an ageostrophic part. The ageostrophic current corresponds to wind driven circulation in the mixed layer, which extends from the surface to depths of about 100m, depending on geographical position. Below the mixed layer, the ageostrophic current can be considered negligible. The SSH differences measured by the altimeter only depend on the geostrophic current at the surface. To obtain the geostrophic part of the total surface current from the ADCP measurements, it would be necessary to use the deeper geostrophic current and adjust this according to the geostrophic shear. The geostrophic shear for the current perpendicular to the ship track can be measured from Conductivity - Temperature - Depth (CTD) data which is taken on the same cruises as ADCP data (although CTD measurements are made less frequently than ADCP measurements). The geostrophic surface currents were calculated in this way by

Transect	Project ID	Position range	Date range	P.I.
1	00205	34S 018E to 66S 034E	10/05/96 to 21/05	J.S.
2	00179	30S 095E to 63S 082E	05/12/94 to 28/12	E.F.,P.H.
3	00179	65S 111E to 25S 115E	01/01/94 to 17/01	E.F.,P.H.
4	00205	62S 120E to 44S 148E	27/06/96 to 02/07	J.S.
5	00162	43S 148E to 66S 171E	04/01/96 to 16/01	G.J.
6	00162	67S 190E to 42S 186E	17/01/96 to 01/02	G.J.
7	00013	38S 210E to 63S 210E	12/10/92 to 28/10	E.F.,P.H.
8	00014	53S 234E to 66S 234E	16/12/92 to 26/12	E.F.,P.H.
9	00081	67S 257E to 26S 257E	27/02/94 to 22/03	E.F.,P.H.
10	00014	54S 272E to 69S 272E	09/01/93 to 17/01	E.F.,P.H.

Table 6.1: Summary of cruise information for the transects illustrated in figure 6.12. The final column, P.I., acknowledges the Principal Investigators as follows: J.S. - J.Swift, E.F. - E.Firing, P.F. - P.Hacker, G.J. - G.Johnson.

Challenor et al (1996) for a cruise across Drakes Passage in November 1992. The cruise was designed to follow the groundtrack of the ERS-1 satellite to enable accurate determination of the dynamic height along that track. The next section describes a technique for determining the mean flow along the ADCP transects shown in figure 6.12, which are not orientated along satellite groundtracks.

6.3.3 Mean flow estimates

If the geostrophic surface current components are known for a particular time at points along a cruise track, the current anomaly measured by the altimeter from the same time and track can be subtracted from the surface current to give the true mean current for the time period over which the current anomaly is referred to. This section investigates the possibility of obtaining profiles of the real mean flow in this way. The task is most straightforward for meridional cruises, due to the use of gridded data. Of the meridional tracks, number 8 has the additional advantage of having two profiles (one for cruising South and one for cruising North), separated by several days. This track will be used to obtain two independent estimates of a mean flow (over the 5 year time period of TPERS maps), which should be the same.

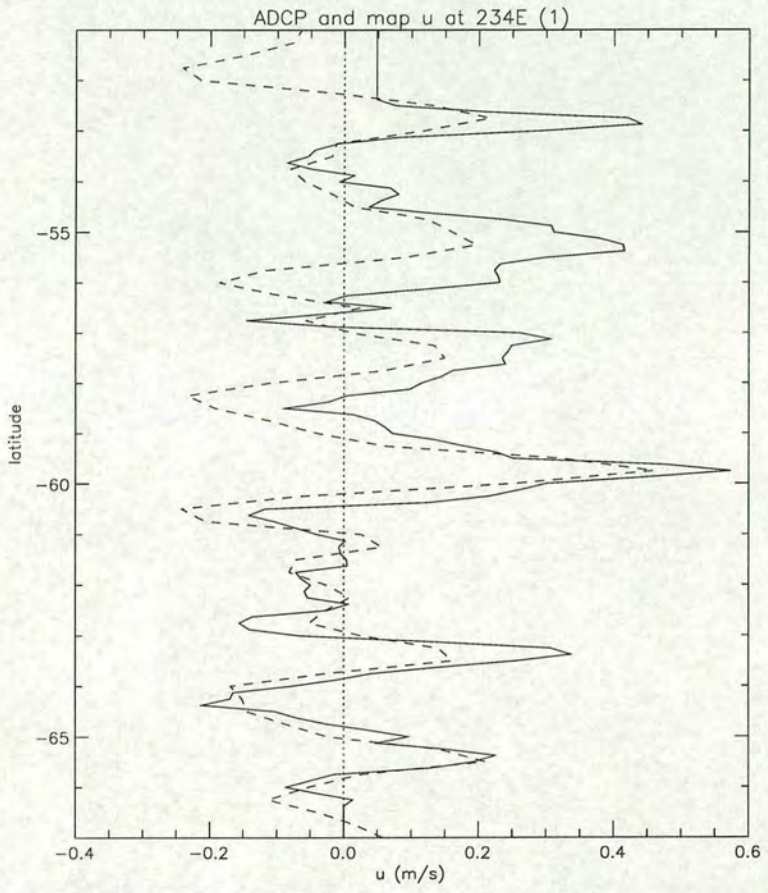

Figure 6.13: Absolute velocity at 100m from ADCP (solid) and map anomaly (dotted) for the southward passage of cruise track 8 (longitude 234°E).

Figure 6.13 shows the absolute zonal velocity at 100m from the ADCP measurement (solid line) and the corrected velocity anomaly from the TPERS maps (dotted line) for cruise track 8 on the southward passage. The time for this cruise is 10 days, which covers one TPERS map. The depth of 100m is chosen to be below the surface mixed layer, and no adjustment for geostrophic shear is used, as it will be seen below that this is small. The absolute current has been smoothed, but variations are still on scales smaller than that resolved in the mapped anomalies. Despite this, the general pattern of the absolute current is reflected by the anomaly which is generally less (more negative). The difference between the two gives an estimate of the mean flow. This difference is typically less than both the absolute current and anomaly and so is sensitive to errors in either. The difference is also sensitive to errors in regions of strong horizontal current shear. Treated with caution, however, the difference may at least indicate the large-scale

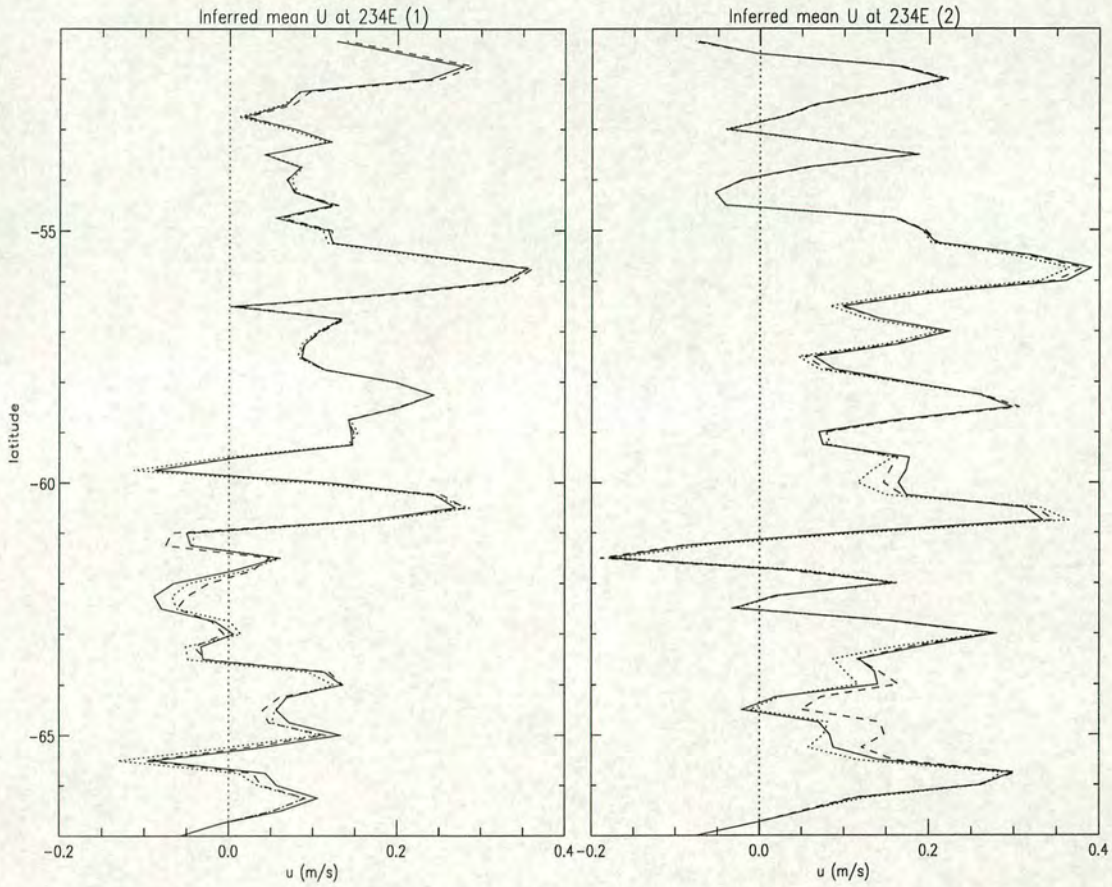

Figure 6.14: Mean zonal velocity calculated from ADCP currents and mapped anomalies for the southward passage of cruise track 8 (left) and the northward passage of cruise track 8 (right). The three lines correspond to ADCP measurements at different depths. The solid line is at 100m, the dashed line 200m and the dotted line 300m.

position and approximate amplitude of jets in the mean flow.

Figure 6.14 shows the mean flow estimates at 234°E, calculated from the southward and northward passages along cruise track 8. The results for the southward passage (1) shows the difference between the velocities shown in figure 6.13. Each graph contains three curves, depicted by a solid, dashed and dotted line. These represent the use of ADCP data from depths of 100m, 200m and 300m respectively. A starting depth of 100m is chosen to be below the surface mixed layer. The close proximity of these curves at most latitudes implies the flow is very barotropic over the upper few hundred metres of this part of the ocean. This means a correction for geostrophic shear is not necessary, and it is sufficient to

take the raw ADCP velocity at any of these depths as the surface geostrophic velocity.

Unfortunately the time difference between the two passages is only about 10 days. This means the two profiles of mean flow are based on two consecutive TPERS anomaly maps. The accuracy of this technique will be poor if the change in the absolute velocity and the change in velocity anomaly over this time are small and comparable to the difference between the two mean flow estimates from figure 6.14. Figure 6.15 (left graph) shows the change in absolute velocity (solid curve) and the change in velocity anomaly (dashed curve) between the two passages (left graph). The difference between the two estimates of mean flow (figure 6.14) is given in the right graph. This is also the difference between the two curves in the left graph. This shows there is significant change in both absolute velocity and velocity anomaly over the 10 days, and at many latitudes this change is comparable to the change in the estimates of mean flow. There are latitudes, however, where the changes in instantaneous velocities are greater than the change in the estimates of mean flow, and here the estimate of mean flow will carry most weight, especially where the mean flow is large. The estimates of mean flow are therefore far from perfect, but indicate a definite jet at 56°S, and probable jets at 58°S and 60.5°S.

The errors involved in using this technique arise from both temporal and spatial factors. The ADCP measurement gives accurate instantaneous velocities (which are measured sequentially over the cruise time). As well as the large-scale components, this will include small-scale ageostrophic features of the absolute current, from small eddies, high-frequency wave activity and tides. None of these are easily measured, and it is certainly not possible to quantify them for the exact time of the ADCP measurement. Even though the ADCP measurements are smoothed, this will not remove ageostrophic components of the current with small timescales but with spatial scales larger than the smoothing scale. Though they are shown to be small, there will also be some differences between the current at 100m and the surface geostrophic current. The mapped anomalies are calculated from 20 days of altimetry measurements, and so some activity on timescales much less than this is filtered out. In addition, the mapped anomalies contain spatial er-

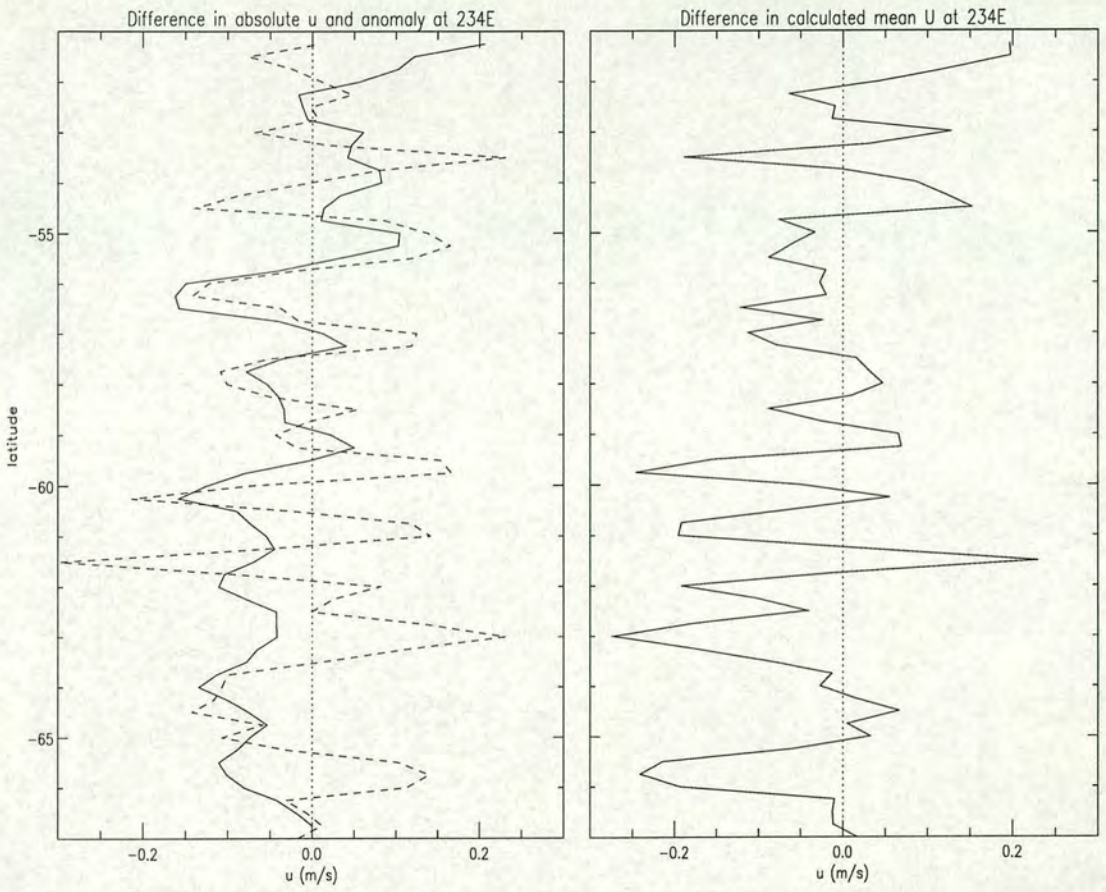

Figure 6.15: Change in ADCP velocity (solid, left graph) and change in map anomaly (dashed, left graph), and the change in estimated mean U (right) for the two passages of cruise track 8.

rors in places away from satellite ground-tracks. It is a combination of these error sources that give rise to the differences illustrated in figure 6.15. These differences can be used to estimate an error for the mean flow estimates. The RMS difference from the right graph of figure 6.15 is 0.16 m/s. This is significant when compared to the estimated jet velocities of 0.30 to 0.40 m/s (figure 6.14). In practice, however, the error will be less than 0.16 m/s where the meridional gradients of the raw profiles (such as figure 6.13) are not too large.

Using results from Challenor et al (1996) (hereafter CRPT), it is possible to make an assessment of temporal smoothing errors in the mapped anomalies. The main result of this work was the calculation of surface geostrophic currents across a track which lay between 55°S, 58°W and 60°S, 55.5°W (see figure 6.12). The currents were calculated for 11 different days between May 1992 and September

1993. ADCP current measurements and CTD measurements were made during a 3 day cruise along this track in November 1992. The cruise followed a ground track of the ERS-1 satellite and was made within a day or two of a satellite pass. The surface geostrophic current across the track was calculated from the ship measurements. The currents on the other ten days were then obtained by making adjustments according to changes measured by the ERS-1 altimeter on passes over the same track and on those other days.

Data from the TPERS maps exist for 6 of the 11 current profiles from CRPT. The anomalies of these 6 profiles (relative to the mean of the six) can be compared to the equivalent anomalies from the maps. The results are shown in Figure 6.16. The top profile shows the mean of the six and the other profiles are the anomalies from CRPT (solid line) and the TPERS maps (dotted line). The anomalies from the appropriate TPERS maps were obtained by differentiating the SSH anomaly along the profile, and subtracting the time-mean of the six profiles. These were then corrected for the bias taken from figure 6.6. In general the agreement is good, with large-scale fluctuations in the "true" anomaly (solid lines) being reflected by the variation in map anomaly. There are, however, smaller scale features in the true anomaly than can be resolved in the maps, and there are notable places where the agreement is poor, such as South of 59°S in profile 018/93. The differences between CRPT and map anomalies indicate temporal smoothing errors and spatial resolution limitations in the mapped anomalies. There will be additional mapping errors away from ground-tracks and this will effect the use of the maps along a meridional profile, for example. Because of the crossover point distribution, however, mapping errors will be fairly small South of about 50°S.

The total surface current for profile 314/92, across Drake Passage, is calculated from the ADCP and CTD measurements only. This surface current can therefore be used with the mapped anomalies to calculate a mean flow across this profile, as was done before for cruise track 8. As discussed above, the errors for this profile will be less than for cruise track 8. The resulting mean flow is shown in figure 6.17. The latitude range is 55° to 60°S and the profile is linear from longitude 58° to 55.5°W. Two eastward (and slightly northward) jets are observed with a magnitude of 60cm/s. The scales are similar to those of jets identified from cruise

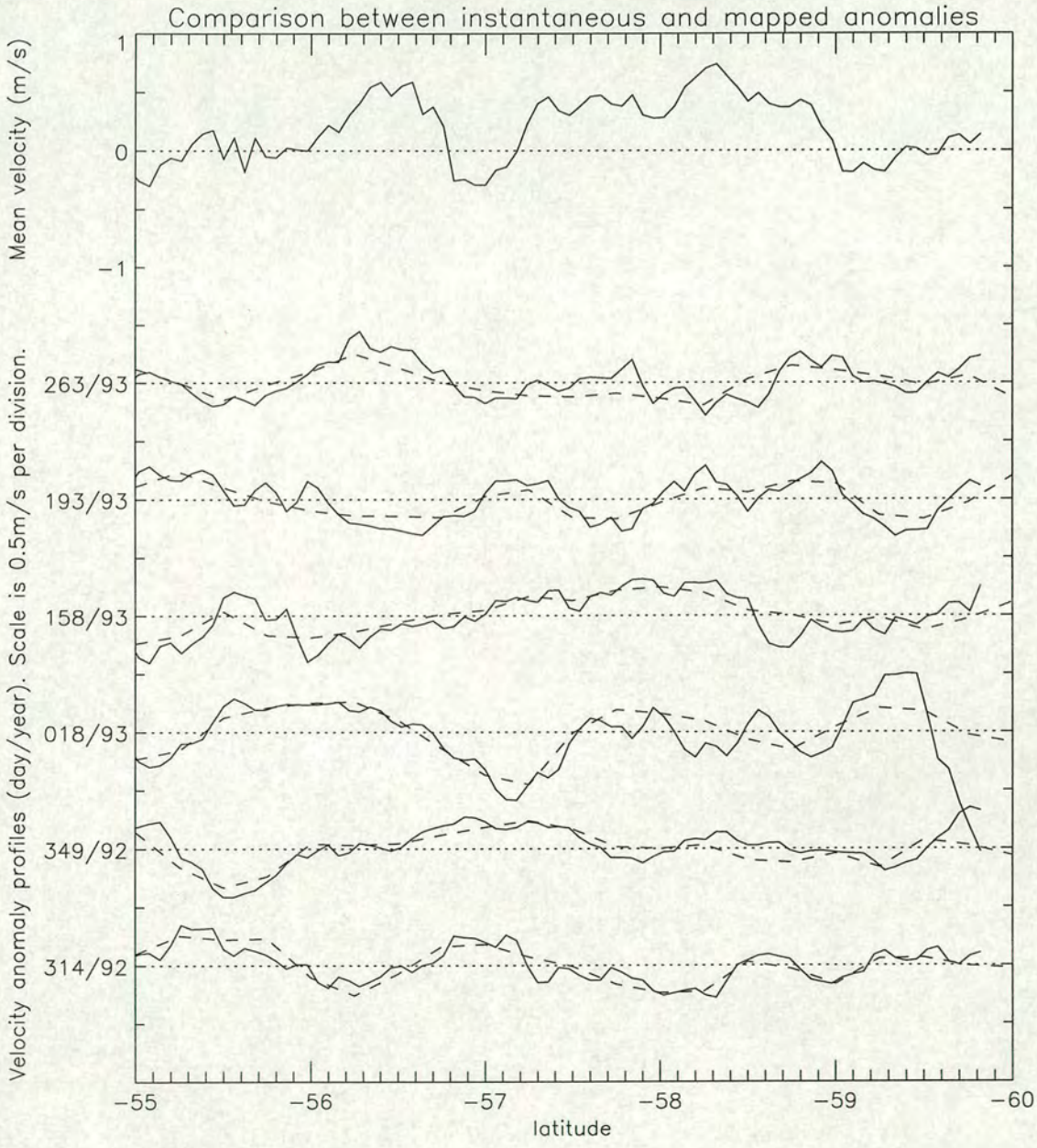

Figure 6.16: Comparison between results from Challenor et al (1996) (solid lines) and the equivalent derived from mapped anomalies (dotted lines) for six currents profiles across a track in Drakes Passage. The top profile shows the mean of the six absolute velocity profiles and the other six profiles show the anomaly from this mean.

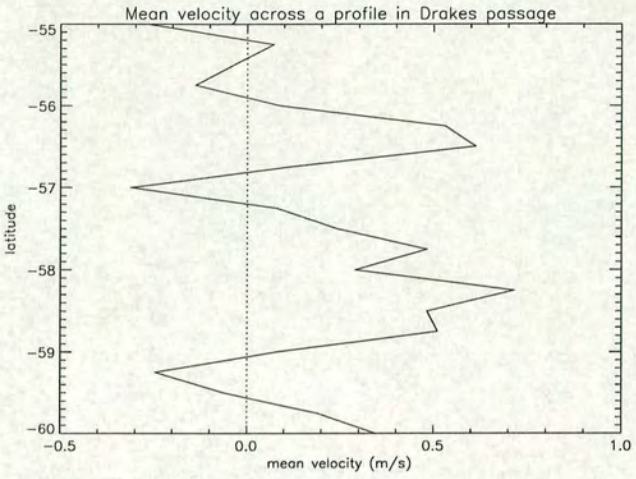

Figure 6.17: Mean velocity in Drake passage, as described in text.

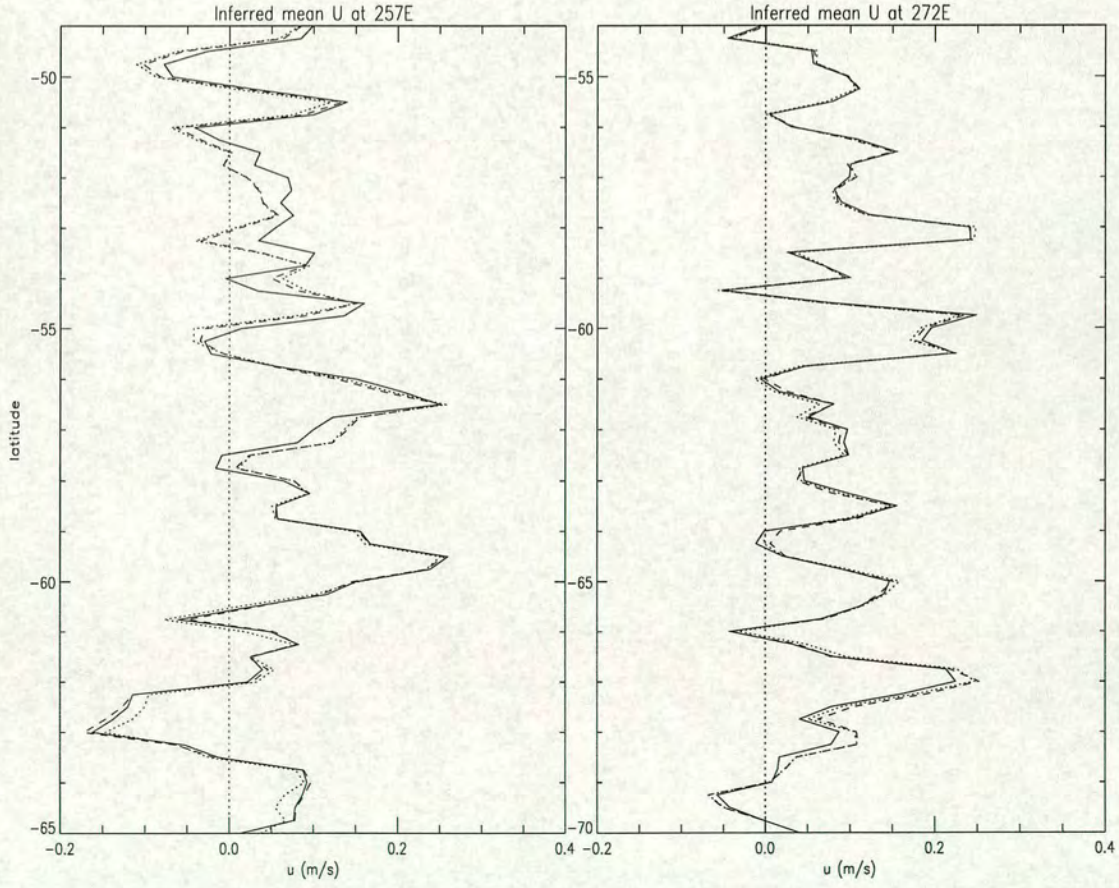

Figure 6.18: Mean zonal velocity calculated from ADCP currents and mapped anomalies for cruise track 9 (left) and cruise track 10 (right). The three lines correspond to ADCP measurements at different depths. The solid line is at 100m, the dashed line 200m and the dotted line 300m. Note the latitude ranges differ by 5°.

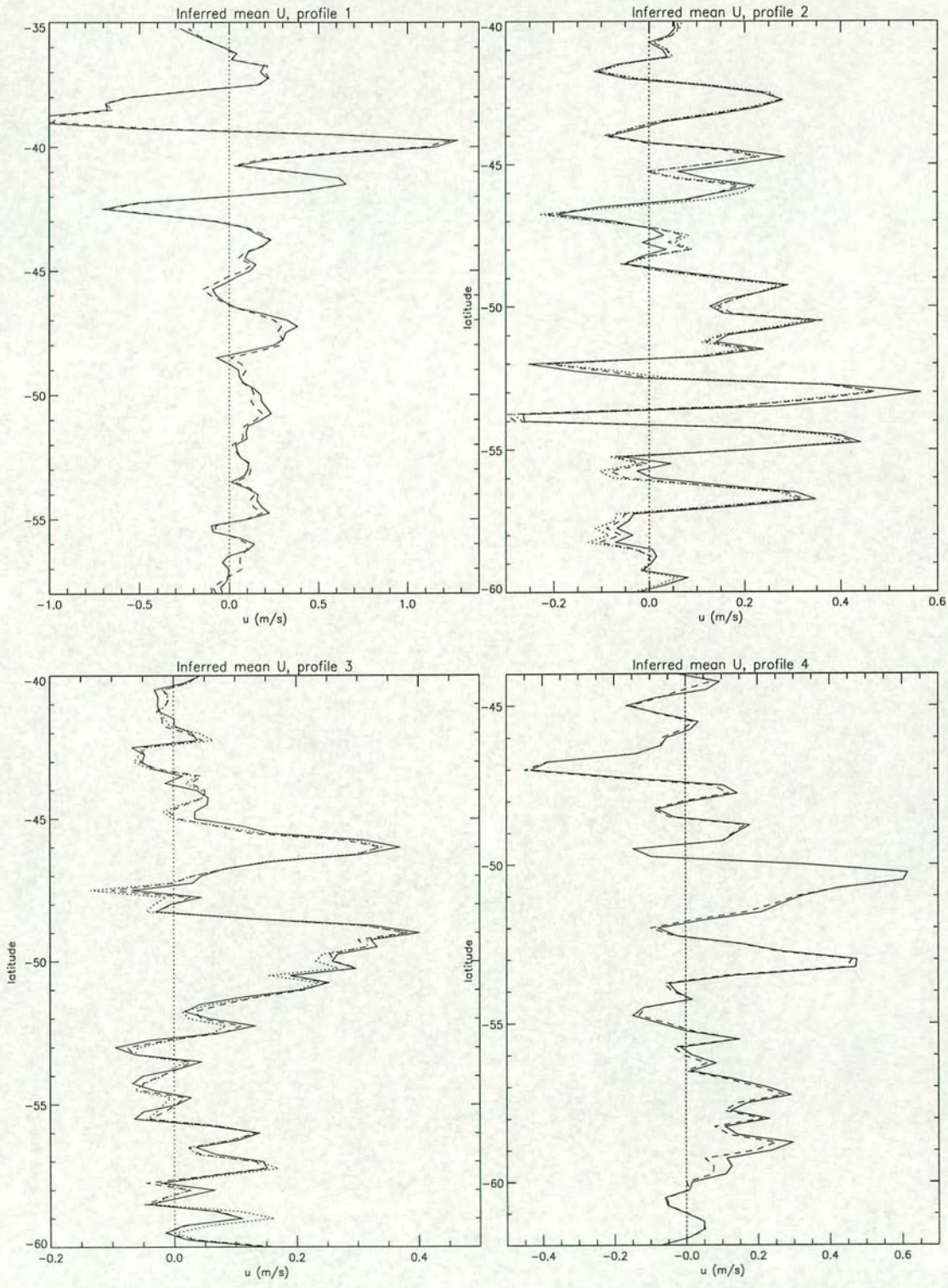

Figure 6.19: Mean zonal velocity calculated from ADCP currents and mapped anomalies for cruise tracks 1 to 4. The three lines correspond to depths of 100m (solid), 200m (dashed) and 300m (dotted).

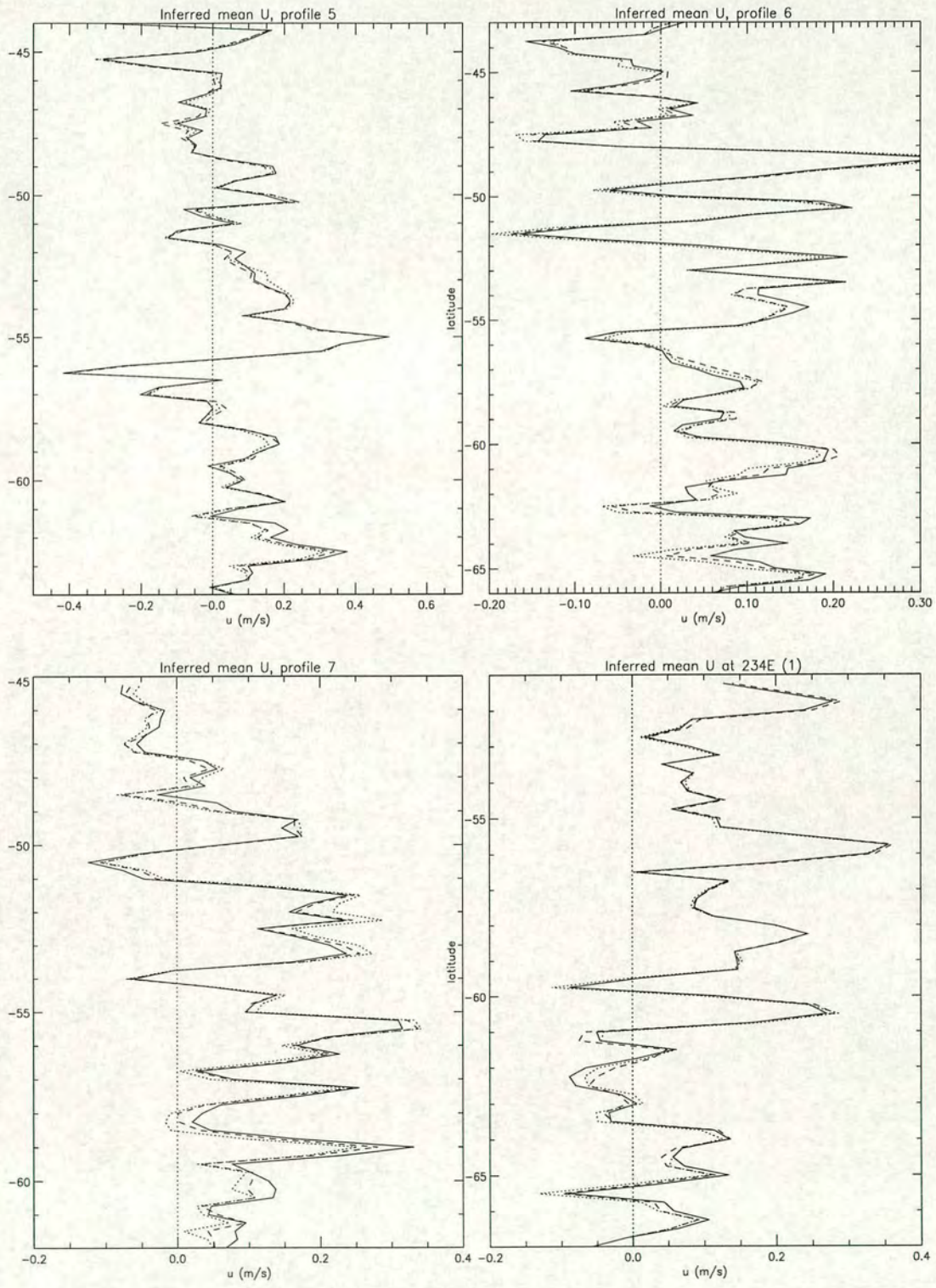

Figure 6.20: Mean zonal velocity calculated from ADCP currents and mapped anomalies for cruise tracks 5 to 8. The three lines correspond to depths of 100m (solid), 200m (dashed) and 300m (dotted).

track 8 (figure 6.14).

The mean flow estimates were calculated for all the transects shown in figure 6.12, though apart from cruise track 8 it is not possible to validate the results. In each case, the calculation was performed using ADCP data at 100m, 200m and 300m. The velocity anomalies from the TPERS maps were corrected using the factor obtained from figure 6.6. Figure 6.18 shows the profiles for cruise tracks 9 and 10. These are meridional profiles downstream of track 8 at 257°E and 272°E respectively. They show eastward jets of up to about 25cm/s. The remaining profiles are shown in figures 6.19 and 6.20. Profile 1 crosses the Agulhas region, and this indicates both an eastward and westward jet of over 1.0m/s. These are the largest currents from this sample, but profiles 2, 4 and 5 show eastward jets over 50cm/s. There are also several jets with speeds between 20 and 40cm/s in all profiles. Jets in the South Pacific are generally slower than elsewhere. These mean zonal flow estimates can be used for comparison in the next section, provided they are treated with caution. The same calculation could be performed for meridional flow, but the mean meridional flow is expected to be small and without a definite jet structure, so the errors are likely to dominate the result.

6.4 The Hughes anisotropy "semivector"

The results from FRAM showed that the eddy orientation angle, θ, gave the position of jets in the mean flow. In addition, the amplitude of the mean flow correlated well with the square root of eddy anisotropy. The best description of the mean flow of the Southern Ocean from eddy quantities would therefore be a representation of the combination of these two results. Hughes (1997) has developed a method of displaying eddy quantities which does exactly that. This representation is a simplification of the velocity variance ellipse and is called the anisotropy semivector for reasons given below. This section follows this work of Hughes, and then presents new results of the anisotropy semivectors in the Southern Ocean, calculated from the TPERS maps.

6.4.1 Formulation

The velocity variance and covariance terms, p, q and r were introduced in section 3.4. These can be combined in a tensor which, following a rotation, can be represented as a velocity variance ellipse. An important quantity which describes the time averaged effect of the velocity anomalies on the mean flow is the Reynolds stress. This is a force, given by $\rho_0\mathbf{M}$, where, for two-dimensional non-divergent flow, $\mathbf{M}$ relates to the tensor terms as follows:

$$-\mathbf{M} = \overline{\mathbf{u}' \cdot \nabla \mathbf{u}'} = (p_x + r_y,\ r_x + q_y). \tag{6.1}$$

Using a well-known vector identity, $\mathbf{M}$ can be broken down into two components as follows:

$$-\mathbf{M} = \overline{\mathbf{u}' \cdot \nabla \mathbf{u}'} = \nabla(p+q)/2 + \hat{\mathbf{k}} \times \overline{\mathbf{u}'\omega'} = \nabla(p+q)/2 + \hat{\mathbf{k}} \times \mathbf{Q}, \tag{6.2}$$

where $\mathbf{Q}$ is the eddy vorticity flux, $\overline{\mathbf{u}'\omega'}$ (where $\omega = \hat{\mathbf{k}}.\nabla \times \mathbf{u}$). One of these components has zero curl, which can be expressed as the gradient of a scalar (the total eddy kinetic energy, $(p+q)/2$). This can be cancelled by a change in the pressure field which has no effect on the mean flow. It is therefore convenient to subtract out this component, and only consider the other, acceleration component of the force, $\mathbf{N}$. This also relates to the tensor terms and is given by

$$\mathbf{N} = \mathbf{M} - (-\nabla(p+q)/2) = -\hat{\mathbf{k}} \times \mathbf{Q} = (s_x + r_y,\ r_x + s_y), \tag{6.3}$$

where $s = (p-q)/2$. Although all the information needed to calculate $\mathbf{N}$ is contained in the velocity variance ellipses, it is not clear how to relate the two quantities from, say, a map of the velocity variance ellipses. It would be possible to present the Reynolds stresses themselves but this requires the differentiation of the tensor terms which introduces large errors when using observed data. $\mathbf{N}$ depends on the quantities r and s, and it is only these terms which are contained in the definition of the eddy anisotropy, ($\sigma_1 - \sigma_2$ - equation 3.12) and the eddy

orientation angle, (θ - equation 3.8). It is possible, therefore, to combine these to produce a quantity which relates to **N**. This quantity is the Hughes anisotropy 'semivector'.

The anisotropy semivector, **A**, has an amplitude relating to the eddy anisotropy and a direction given by the eddy orientation angle, θ. It is defined as

$$\mathbf{A} = \sqrt[4]{r^2 + s^2}\,(\cos\theta, \sin\theta) = (a, b). \tag{6.4}$$

A is called a semivector because the direction, θ, is specified by a formula for 2θ which gives two values of θ, 180 degrees apart. It is not possible to specify over the whole field which of these values to choose, so **A** is a line and not an arrow. The fourth root is chosen for the amplitude so that the quantities r and s relate to a and b in a straightforward way. Given that the direction is specified by $\sin 2\theta = r/A^2$ and $\cos 2\theta = s/A^2$, r and s are given respectively by

$$r = A^2 \sin 2\theta = 2(A\sin\theta)(A\cos\theta) = 2ab, \tag{6.5}$$

$$s = A^2 \cos 2\theta = (A\cos\theta)^2 - (A\sin\theta)^2 = a^2 - b^2. \tag{6.6}$$

Defining $\hat{\mathbf{A}} = \hat{\mathbf{k}} \times \mathbf{A} = (-b, a)$, it is possible to show that **N** relates to **A** as follows:

$$\mathbf{N} = -2(\mathbf{A}\nabla \cdot \mathbf{A} - \hat{\mathbf{A}}\nabla \cdot \hat{\mathbf{A}}). \tag{6.7}$$

The two terms in this equation represent a convergence of **A** ($-\mathbf{A}\nabla \cdot \mathbf{A}$) which corresponds to an eddy force parallel to **A**, and a divergence of $\hat{\mathbf{A}}$ ($\hat{\mathbf{A}}\nabla \cdot \hat{\mathbf{A}}$, equivalent to a curl of -**A**) which corresponds to an eddy force perpendicular to **A**. The interpretation of **A** and this association with **N** will be discussed further in section 6.4.3.

6.4.2 Relationship with E-vectors

Another method of interpreting eddy quantities was developed by Hoskins et al. (1983) (hereafter HJW) in application to the interaction between eddies and the mean flow in the atmosphere. HJW developed a quantity known as the **E** vector which represents the convergence of eddy vorticity flux and is defined as

$$\mathbf{E} = (\overline{v'^2 - u'^2}, -\overline{u'v'}) = (-2s, -r). \tag{6.8}$$

The relationship between the orientation of **E** (which will be designated α) and **A** (θ) is $2\tan\alpha = \tan 2\theta$, so for small angles (near-zonal orientation) $\alpha = \theta$. In terms of a and b, the **E** vector is given as $\mathbf{E} = (b^2 - a^2, -ab)$. The relationship between **A** and **E** is therefore not straightforward when the orientation is non-zonal. **E** describes the momentum flux from the eddies to the mean flow. Where **E** is divergent there is forcing of the mean circulation acting to increase eastward mean flows. Conversely, convergence of **E** indicates a tendency to decrease eastward mean flows. At the centre of eastward zonal jets in the mean flow (if the jet is being forced by the eddies), **E** is expected to be orientated along the jet. Either side of the centre, **E** will tend to point away from the centre. **E** is not a true vector (or semivector), as it will be different when calculated in different (rotated) coordinate systems. This is unlike **A** which, though **A** is a line and not an arrow, transforms as a vector and is independent of the coordinate system used. **E** is a potentially useful indicator of the mean flow but is only valid if approximations are made about the zonality of the flow and eddy structure. These approximations hold for the atmosphere but not for non-zonal currents. **E** is easier to interpret when the zonal approximation is valid, but otherwise **A** must be used. It will be seen in the next section that **A** is also convenient for the visual interpretation of the Reynold's stresses, and hence associations with the mean flow.

6.4.3 Interpretation of results

Before displaying the results of the semivectors for the Southern Ocean, it is necessary to get a feel for their interpretation. Some diagrams from Hughes are

shown in Figure 6.21. These show how typical spatial distributions of **A** relate to the acceleration component of the Reynolds stress, **N**. The direction of **N** shows the direction of the mean force applied to the flow over the period of study. Equation 6.7 showed how **N** related to two terms in **A**. The top part of figure 6.21 demonstrates the nature of these two terms and the resulting force, **N**, when **A** has a constant direction but varying amplitude (five different cases are shown). Where there is most shear in **A**, the divergence is zero and the force points towards higher amplitudes. When there is no shear, the divergence is maximum and the force points to lower amplitudes.

The bottom part of figure 6.21 shows how **N** is orientated for variation in the orientation of **A** along one direction, when **A** has a constant amplitude. This shows how the arrangement of **A** tends to form arrows along the direction of no variation, which point in the direction of **N**. When the arrow formation is blunt, **A** is perpendicular to **N** at the centre of the formation. In this case, on either side of the centre **N** points away from the arrow axis. When the arrow formation is sharp, **A** is parallel to **N** in the centre of the formation and on either side of the centre **N** points towards the arrow axis. Both of these arrow arrangements could be associated with jets in the mean flow, but the additional effects of variation in amplitude are also an important consideration. The associations between **A** and **N** in figure 6.21 do not depend on the orientation of the figure, which may be rotated and mirrored in any way relative to a latitude-longitude grid.

Bearing these theoretical associations in mind, the relationship between **A** and the mean flow can be studied in FRAM. The field of **A** was computed for FRAM by Hughes and is shown in Figure 6.22. The vectors are plotted over the field of mean zonal flow. In many places, the 'blunt arrow' formation can been seen and is aligned with eastward jets in the mean flow. Particularly good examples are at 48°S, 40°E; 58°S, 120°E and 50°S, 195°E. In each case, the amplitude of **A** within the blunt arrow formation decreases away from the centre of the jet. The direction of **N** is then taken from the top part of figure 6.21 so will point westward, acting to decelerate the wings and so sharpen the jets. Evidence of the zonal orientation of **A** in a westward mean flow can be seen at 27°S, 40°E but the sharp arrow formation is perhaps not resolved by the distribution of **A**. The linear

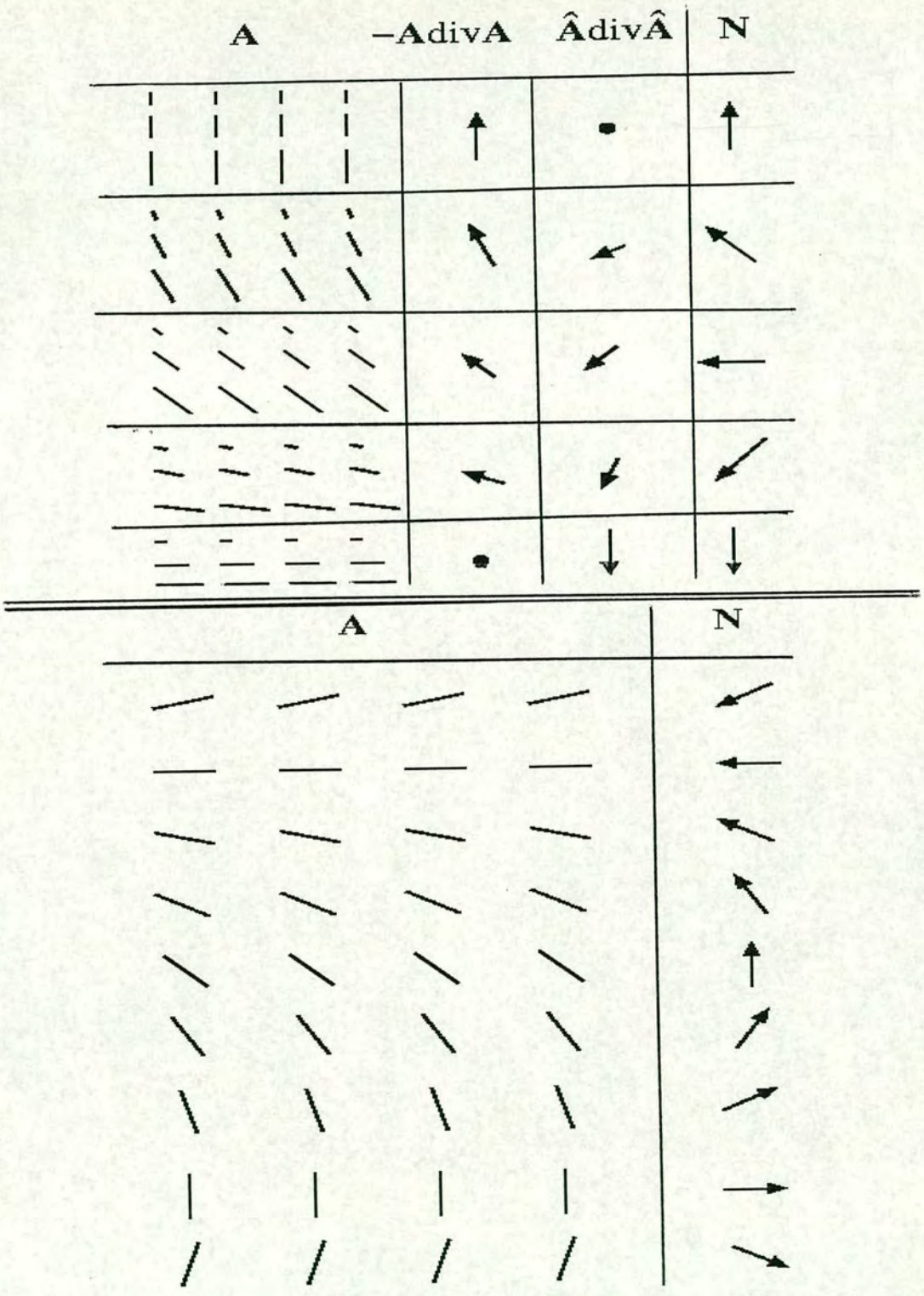

Figure 6.21: Two separate diagrams illustrating the relationship between anisotropy semivectors (**A**) and the acceleration component of the Reynold's stress (**N**), from Hughes (1997). The top diagram shows five different, independent cases where **A** is constant in direction but varying in amplitude (with the two components of **N** given in preceding columns), and the bottom diagram shows the single case where **A** is constant in amplitude and has varying direction.

trend in U may also be important here. The quality of the association between **A** and eastward jets in the mean flow could be enhanced if the jet has accelerated over the period of study. If a deceleration has occurred, a zonal direction of **N** will still be required at the jet centre to maintain the jet, but **A** will decrease in amplitude less in the wings, indicating a spreading of the jet. This is observed in the third example of an eastward jet given above (at 50°S, 195°E).

The results from FRAM show how it is possible, with some confidence, to relate the field of semivectors **A** to features in the mean flow of FRAM. As well as the orientation of **A** being important, the magnitude of **A** (which is proportional to the square root of the eddy anisotropy) was seen to correlate well with the magnitude of U (section 6.1) in certain regions of the Southern Ocean. Without knowing anything about the real mean flow, it is likely the field of **A** from TPERS maps will give an unprecedented idea of mean surface currents in the Southern Ocean. These results are presented below.

6.4.4 Results

The semivectors (**A**) were calculated from velocity anomalies obtained from the TPERS maps. The velocities were filtered to select only variation with periods between 2 and 8 months, using a standard Butterworth filter. This cuts out short period activity that is not represented in FRAM (to enable comparison with the equivalent results in FRAM), and activity on periods close to the annual cycle and longer, so that the results are derived only from activity varying on timescales significantly less than the period of mean flow. The difference between results obtained using the full velocities (as shown in figures 6.7 to 6.9) and the bandpass velocities is mainly seen in the field for θ. With the bandpass velocities, θ is close to $\pm\pi/2$ for most of the region north of the ACC, in all three oceans. There is little difference to the south of, and in the region of the ACC.

Figures 6.23 to 6.28 show the results of **A** for 60° longitude segments of the Southern Ocean between 30°S and 70°S. The semivectors are plotted over the linear trend in u, also calculated from the TPERS maps. This gives an indication of the most active parts of the ACC, and may have an influence on the semivectors.

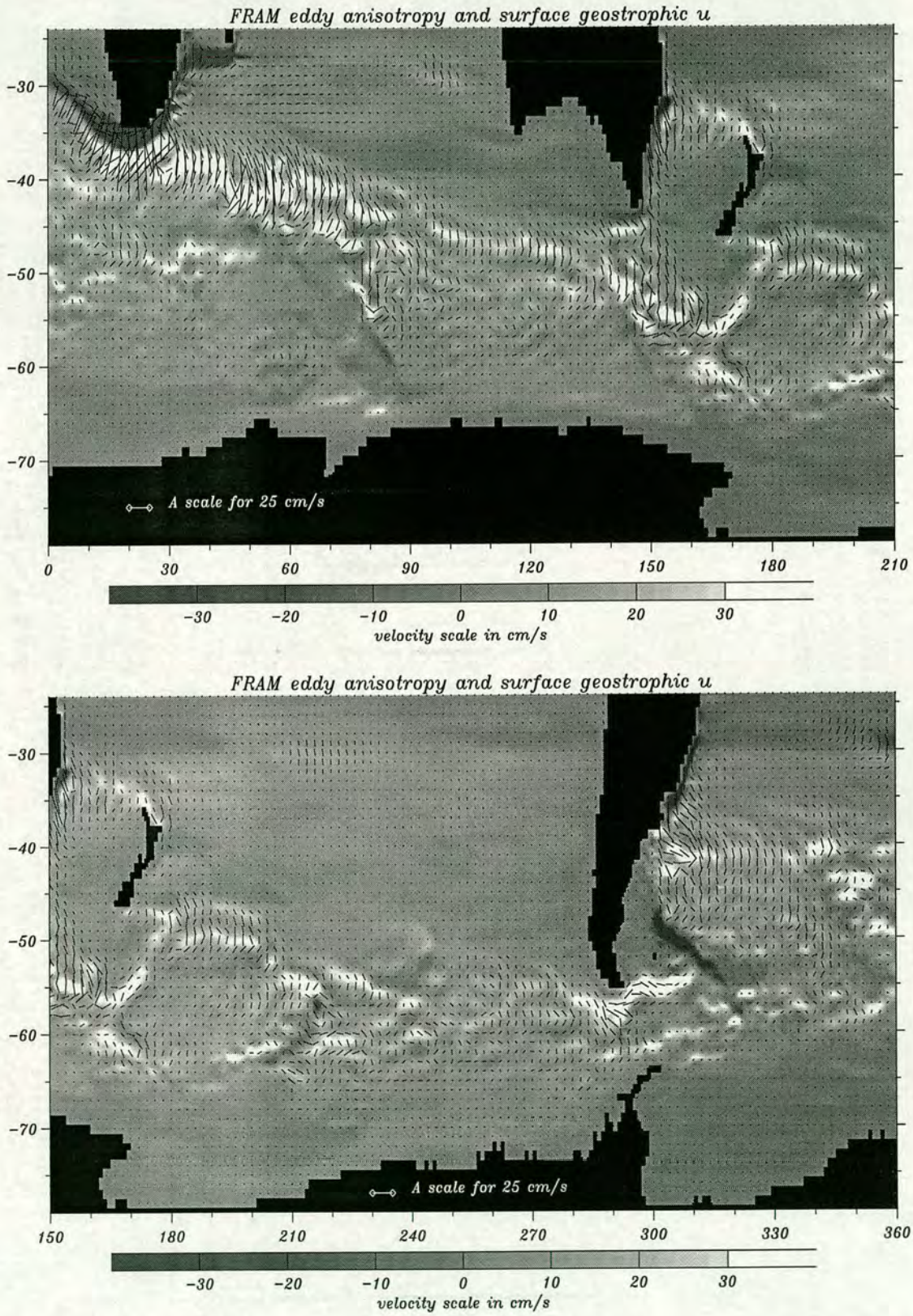

Figure 6.22: Anisotropy semivectors in the Southern Ocean from FRAM, taken from Hughes (1997).

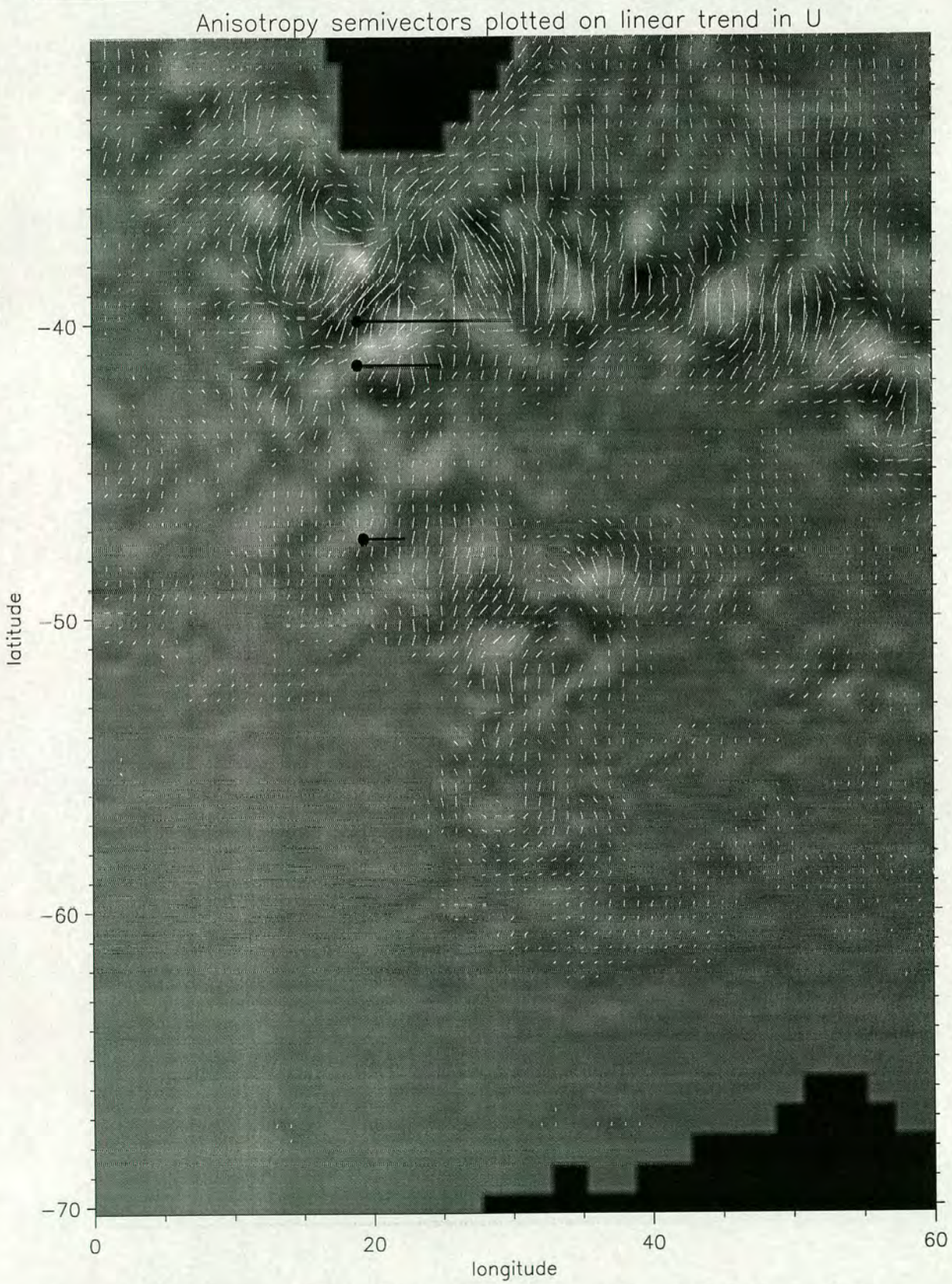

Figure 6.23: Anisotropy semivectors in the Southern Ocean plotted over linear trend in u. Black dots and lines show the position and strength of jets in the mean flow estimates calculated in section 6.3.

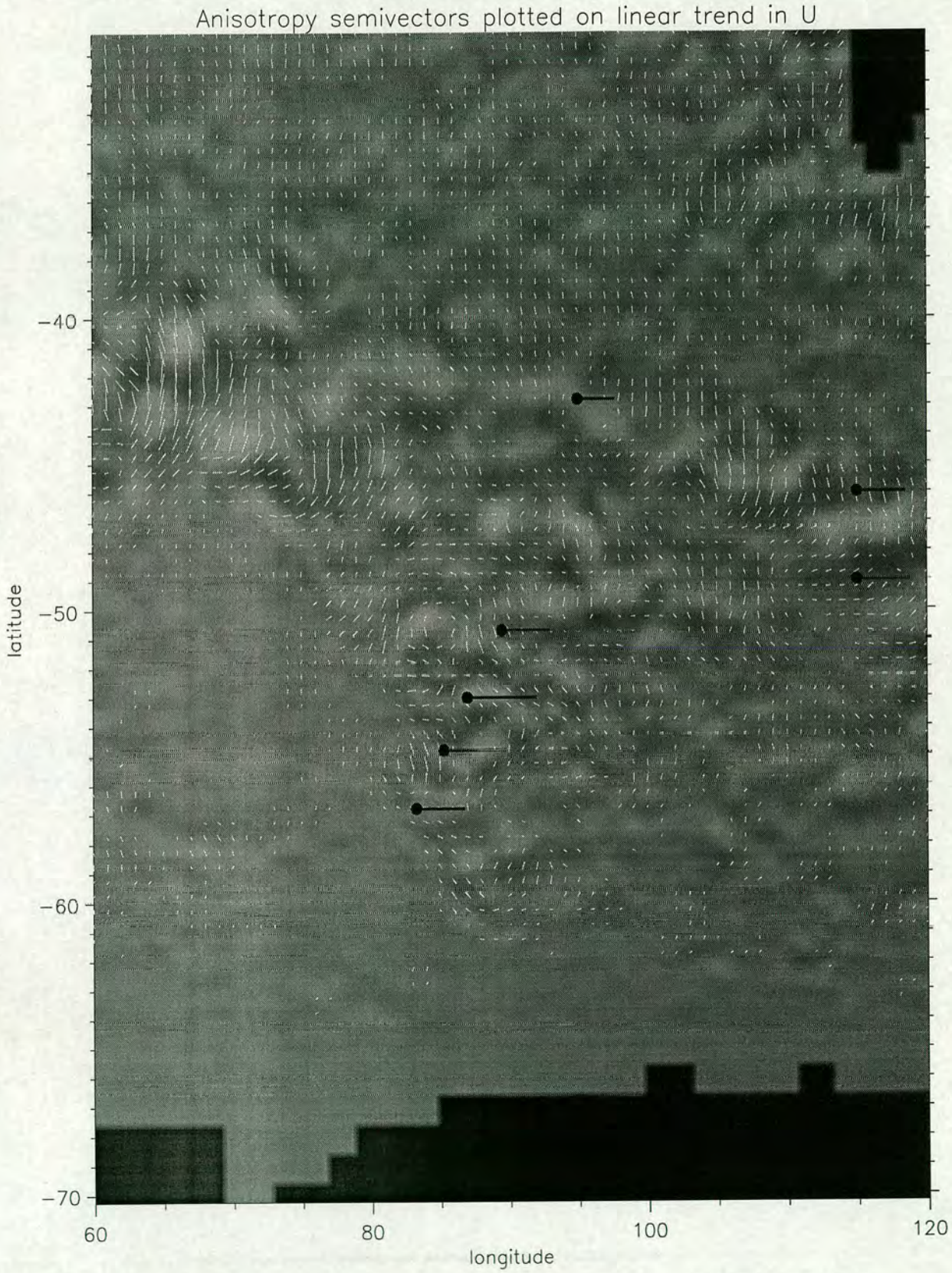

Figure 6.24: Anisotropy semivectors in the Southern Ocean plotted over linear trend in u. Black dots and lines show the position and strength of jets in the mean flow estimates calculated in section 6.3.

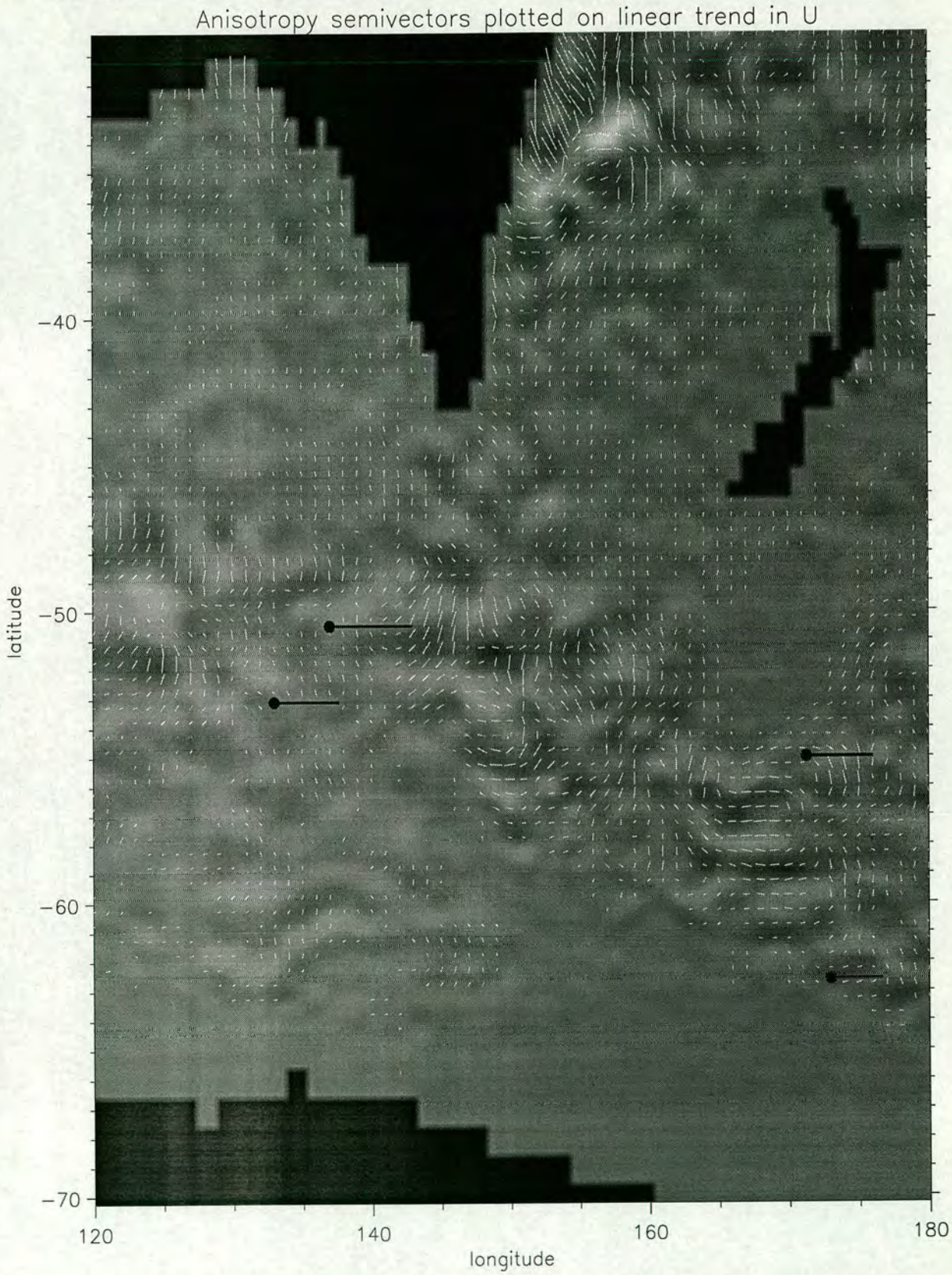

Figure 6.25: Anisotropy semivectors in the Southern Ocean plotted over linear trend in u. Black dots and lines show the position and strength of jets in the mean flow estimates calculated in section 6.3.

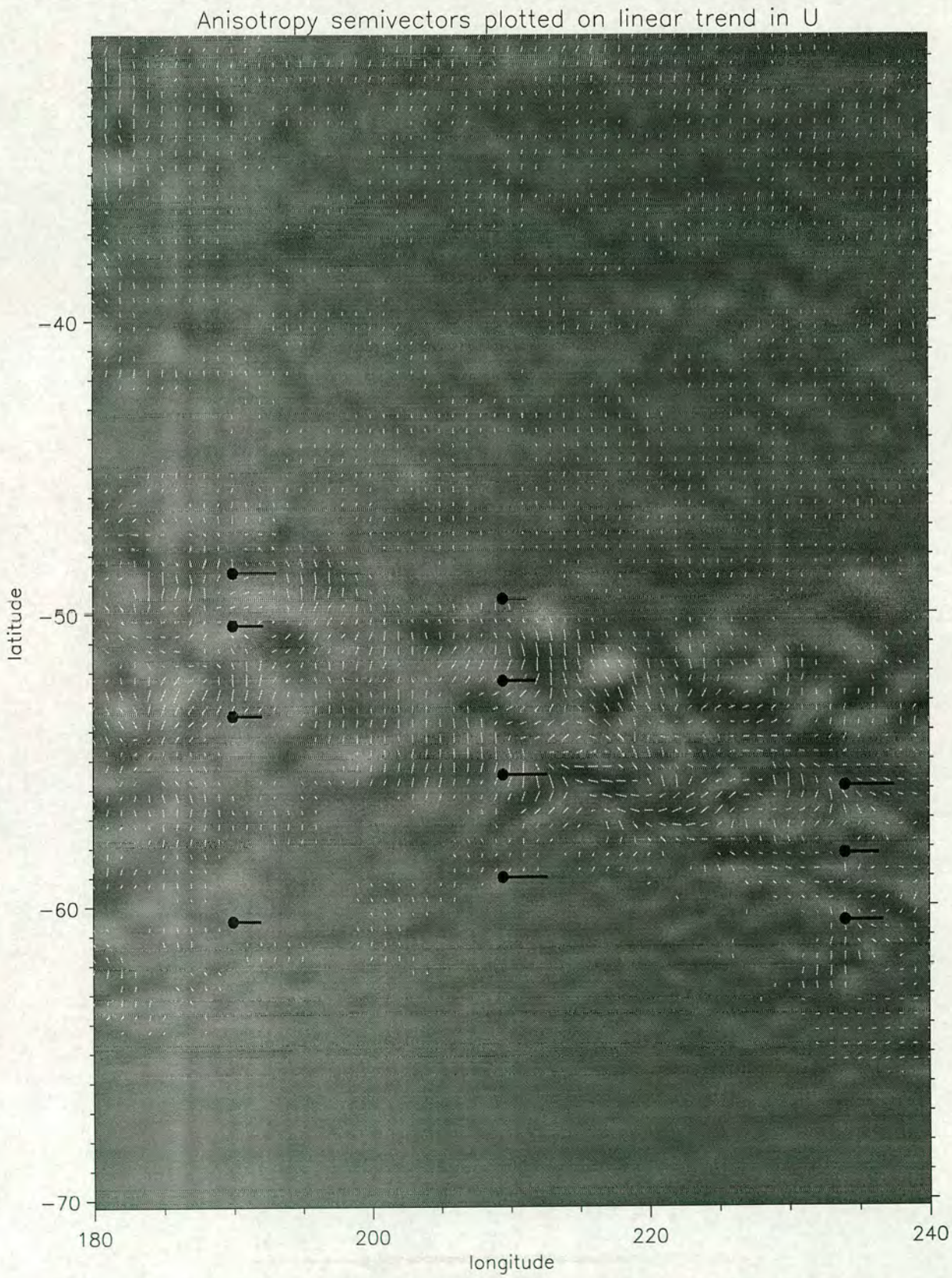

Figure 6.26: Anisotropy semivectors in the Southern Ocean plotted over linear trend in u. Black dots and lines show the position and strength of jets in the mean flow estimates calculated in section 6.3.

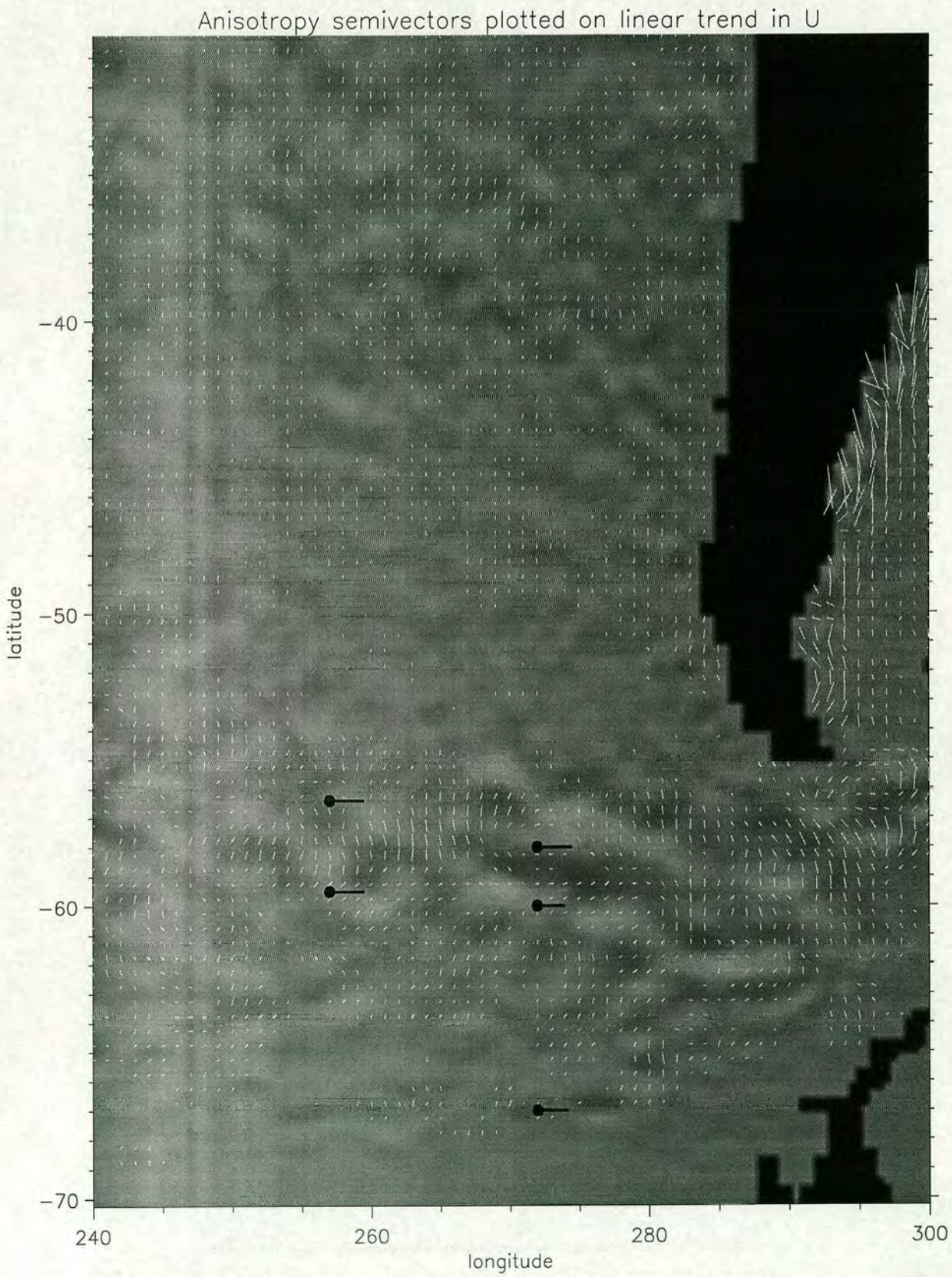

Figure 6.27: Anisotropy semivectors in the Southern Ocean plotted over linear trend in u. Black dots and lines show the position and strength of jets in the mean flow estimates calculated in section 6.3.

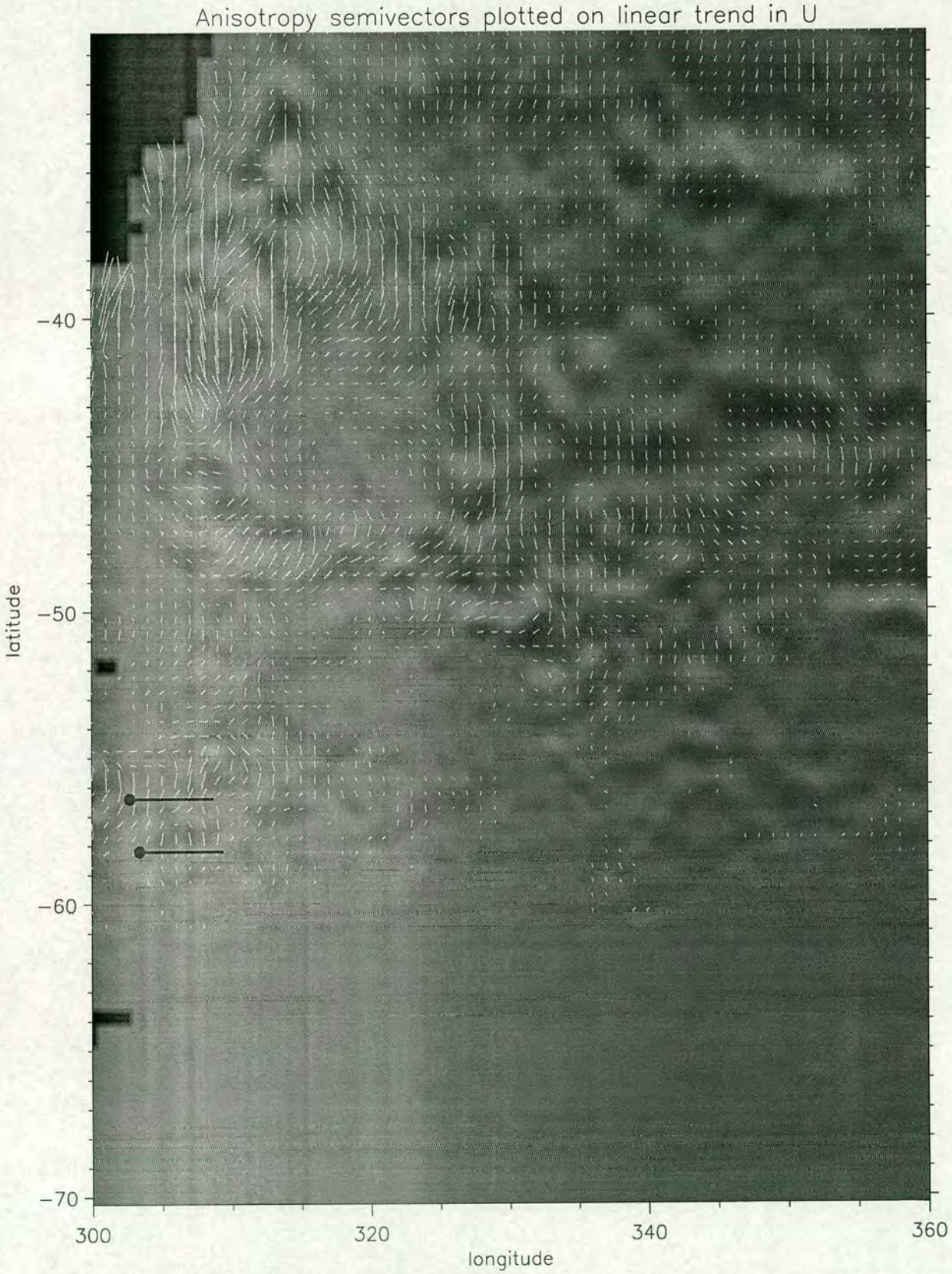

Figure 6.28: Anisotropy semivectors in the Southern Ocean plotted over linear trend in u. Black dots and lines show the position and strength of jets in the mean flow estimates calculated in section 6.3.

The scale for this is given in figure 6.30 as a grey-scale, where dark is strong negative trend, and light is strong positive trend. It is not necessary to know the exact sign when the linear trend is small, as only a strong trend is likely to have an influence. The scale for the length of the semivectors is 5° of latitude equals 1m/s. Semivectors are only shown where their magnitude is greater than 0.02m/s, and they are centred on the position where they are calculated. Superimposed are vectors, marked as black lines originating from the positions given by the black dots, and these show jets from the mean flow estimates from section 6.3. The scaling of these vectors is 10° of longitude equals 1m/s.

Comparison with mean-flow estimates

Figure 6.29 shows how the magnitude of semivectors (**A**) relates to the velocity of jets in the mean-flow estimates (from section 6.3). The results are shown for mean-flow estimates less than 0.4 m/s, as the best comparison is found for this velocity range (see below). Despite some scatter, a linear relationship between the two quantities is evident. Extrapolating by eye, the magnitude of **A** would fall to zero as the mean flow falls to about 0.1m/s. This offset was not observed in FRAM, but then there are no points below 0.18m/s to support it. The correlation for these points is 0.55 and this compares well to correlations between the square root of eddy anisotropy and mean flow in FRAM (section 6.1). If higher velocities are included, the correlation coefficient falls and this is also consistent with the FRAM results. The magnitude of **A** is not seen to increase linearly for velocities greater than 0.4 m/s. With this small sample of points and the errors involved in mean-flow estimates, however, it is not possible to draw definite conclusions about the relationship between the magnitude of **A** and the mean flow, except to note consistencies with FRAM. As well as the magnitude of the semivectors, the orientation is important. This is discussed below.

Effect of trend in u

The semivectors have been plotted over the linear trend in u as a reference for the strength of the ACC, and because the orientation of the semivectors might be

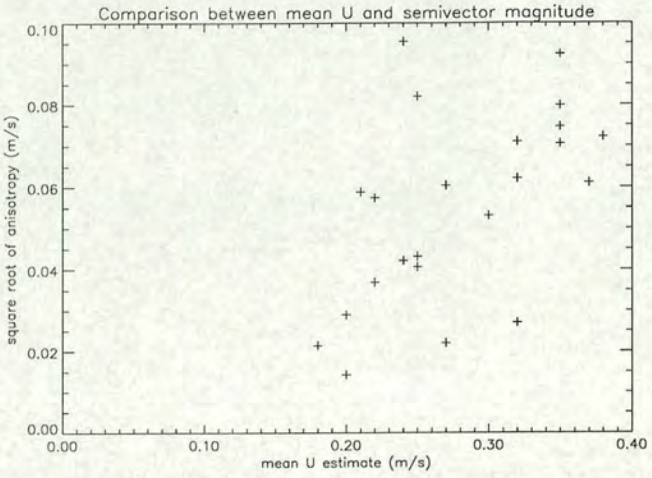

Figure 6.29: Amplitude of semivectors against estimates of U for the jets marked on figures 6.23 to 6.28.

related to the linear trend. The scale for the linear trend is given in figure 6.30, but it is only necessary to distinguish between strong decrease (dark) and strong increase (light) in U. The linear trend was presented for the whole Southern Ocean in figure 6.10. The maximum values were noted to be in the most active parts of the ACC, and this is confirmed by the visual correlation between the magnitude of the semivectors and the magnitude of the linear trend. To test the effect of linear trend on the semivectors, the semivectors were calculated using all data and compared with semivectors calculated from data which had had the linear trend removed. The results could hardly be distinguished from the results in figures 6.23 to 6.28. This means the semivectors relate to the underlying mean flow over the 5 years, and are influenced very little by changes to the flow over that time. This is a useful result. The linear trend is still an indication of activity in the ACC and is therefore a suitable background to the results of semivectors. The trend in u was also seen to relate to some mean jets in FRAM, but with uncertain sign (see section 3.5).

Identification of features

The most readily interpretable features in the semivector fields are the blunt and sharp arrow formations discussed in section 6.4.3. These will point in the direction

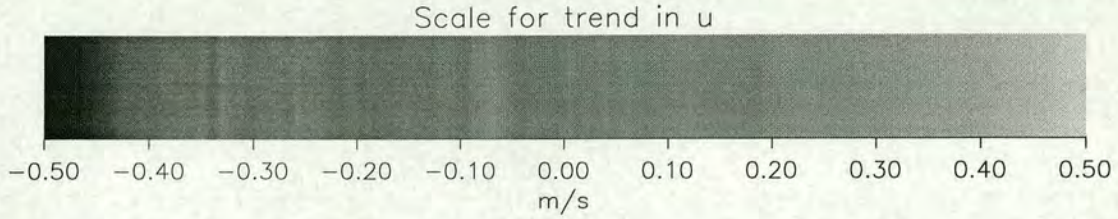

Figure 6.30: Scale for trend in u in results of semivectors

of forcing on the mean flow. In FRAM, blunt arrows were a good indication of near-zonal jets in the mean flow. On figures 6.23 to 6.28, the estimated positions of jets in the mean flow from section 6.3 are marked by black dots (with a line of length proportional to the velocity). In general these jets do not lie within blunt arrow formations, although such formations are evident in the fields. Exceptions to this are jets at (47.5°S, 20°E), (55.5°S, 210°E) and (56.5°S, 302.5°E), and more ambiguously at (55°S, 85°E) and (46°S, 115°E). Some jets lie just to the south of blunt arrows, such as at (53.5°S, 190°E), (52.5°S, 210°E), and (59.5°S, 257°E). Other jets can be associated with sharp arrow formations (47°S, 234°E), and many are in places where the magnitude of $\mathbf{A}$ is less than 0.02m/s. The jet positions cannot be wholly trusted and these examples of jets are not necessarily the most prominent jets in the ACC, but the general indication is that jets in the mean flow are not being forced by the eddies in most cases. This is discussed further in the next section.

As well as the near-zonal arrow formations, other arrow formations are present with a more meridional orientation. Although not illustrated with the FRAM results, it was stated in 6.4.3 that the absolute orientation of the semivectors was unimportant, so the arrow formation should always point in the direction of the forcing of the mean flow. A good example of non-zonal formations is seen in figure 6.25, at 170°E. Just upstream of this longitude, the ACC is confined to 7° of latitude centred on 59°S. Here the semivectors are near zonal in orientation, which implies meridional forcing towards the ACC axis (from figure 6.21) which may be related to the narrowing of the flow. At 170°E an arrow formation is observed to the north of the ACC and with a northward trend. At 58.5°S there is evidence of a westward pointing arrow formation, and just south of this another

eastward arrow can be seen. This gives the picture of a split in the path of the ACC, with the majority of flow moving northeast with a component separating to the south and continuing zonally or even slightly southwards. This is consistent with the mean flow in this region from FRAM.

In the FRAM results, semivectors at the Western boundaries were seen to be inclined from the land mass in a direction given by the mean flow. This is observed in these results on the east coasts of South Africa and Australia. The magnitude of the semivectors appears to relate to the expected mean flow, but the correlations between mean velocities and semivector magnitudes were poor for these regions of FRAM. The arrangement just away from these regions shows forcing of the mean flow towards the boundary, which is consistent with the maintenance of a current at the boundary.

Other interesting features of semivectors are rotational arrangements, seen in several places such as at (51°S, 85°E). This arrangement can be seen in one or two places in the FRAM results, such as at (57°S, 216°E) where the mean flow is westward, and at (62°S, 170°E) where the flow is eastward. These features are hard to interpret and the nature of the forcing on the mean flow is best inferred where there are arrow formations of the semivectors.

6.4.5 Discussion

The new results of Hughes anisotropy semivectors in the Southern Ocean are intended to provide realistic information about the mean flow at the surface, given that this quantity cannot be measured independently. The idea of the semivectors arose from the need to illustrate the way in which dynamically important forces from eddies are acting on the mean flow. Given this, it is intuitive that the mean flow itself is closely related to the forces by which it is sustained, particularly over longer time periods. The Hughes anisotropy semivectors have not previously been presented for the real ocean. This section has shown that the latest mapped anomaly data from both the TOPEX/POSEIDON and ERS satellite altimeters is suitable for the calculation of semivectors. In the FRAM model output, the semivectors could be related to the mean flow. By comparing with

jet positions estimated from work in section 6.3, this same relationship is not seen to hold well in a sample of locations in the real ocean. In FRAM the eddies are acting to accelerate jets in the mean flow, but in the TPERS results this has not been confirmed. The interpretation of semivectors is not a straightforward task, but it has been shown that their amplitude relates well to the mean flow, both in FRAM and for a small sample of real locations. This itself is a good result, and any further information that can be obtained from the orientations of semivectors is a bonus. Ideally more measurements of the real mean flow over this time are required to enable more substantial comparisons to be made. In the absence of these, the semivectors cannot be treated as a perfect diagnostic. They do, however, give valuable information about forcing of the mean flow by eddy activity. As such they may provide a means of relating time dependent currents to the mean flow if the relationship between eddy forcing and jets in the real ocean can be established. The next section looks at a more direct method of calculating eddy forces on the mean flow.

6.5 Reynolds stress and mean temperatures

In view of the quality of the fields of semivector **A** calculated from TPERS maps, it was decided to attempt to calculate the Reynolds stress term, **N**, directly. With awareness of the errors introduced by further differentiating the data, a smoothing method was used to reduce noise in the fields of **A**.

6.5.1 Calculation method

The starting point for the calculation of **N** is the two components of **A**, a and b. At each gridpoint, the direction of minimum change in a and b was established. This was performed by taking 11 points along a line through the gridpoint, separated by the zonal gridpoint spacing. These components are labelled $a1 : a11$ and $b1 : b11$ such that $(a6, b6)$ are the components at the gridpoint in question. For the line taken at an angle to the zonal direction between -90° and 85° (in 5° increments), the value of $(a1 - a6)^2 + (a2 - a6)^2 + ... + (b1 - b6)^2 + ... + (b11 - b6)^2$

was calculated. The direction giving the minimum value was stored (ϕ), and a and b were averaged along that direction over the 11 points. Using these smoothed values of a and b, N was calculated according to the formula

$$\mathrm{N} = -\left((a^2)_x - (b^2)_x + 2(ab)_y,\ 2(ab)_x - (a^2)_y + (b^2)_y\right), \tag{6.9}$$

derived from equations 6.3, 6.5 and 6.6. The components of **N** along and perpendicular to the direction ϕ were then taken. ϕ indicates the direction of least change in the semi-vectors and is therefore expected to indicate the direction of jets in the mean flow, according to observations in FRAM (see figure 6.22).

6.5.2 Results

Figure 6.31 shows the field of N, parallel to the direction ϕ and smoothed over 3 gridpoints zonally and meridionally. Positive (blue) indicates forcing with an eastward component and negative (red) shows forcing with a westward component. Superimposed on the field are contours of mean temperature, as measured by ATSR (Hughes et al, 1998). It is observed in the FRAM atlas (Webb et al, 1991) that strong gradients of mean temperature in FRAM indicate eastward jets in the mean flow (though such gradients are not necessarily associated with all jets). Close contours of mean temperature can therefore be used as an indicator of fronts, which are highly likely to show the position of some jets in the ACC. The results in figure 6.31 show that major jets are generally associated with negative **N** (see for example jets at (40°S, 50°E), (45°S, 70°E), (55°S, 215°E), (58°S, 300°E) and (50°S, 315°E)). This is a very significant result. It means that instead of forcing the jets, as is observed in FRAM, the eddies are generated within the jets and act to decelerate the jets. The jets must therefore be maintained by some other mechanism. This is discussed in 6.5.3, below. The field of **N** also confirms the observations in the field of semivectors that many of the jets identified by ADCP measurements are not being forced by the eddies.

To check the results of **N** are consistent with the field of semivectors, figure 6.32 shows the semivectors plotted over the field of **N** for three enlarged regions; south

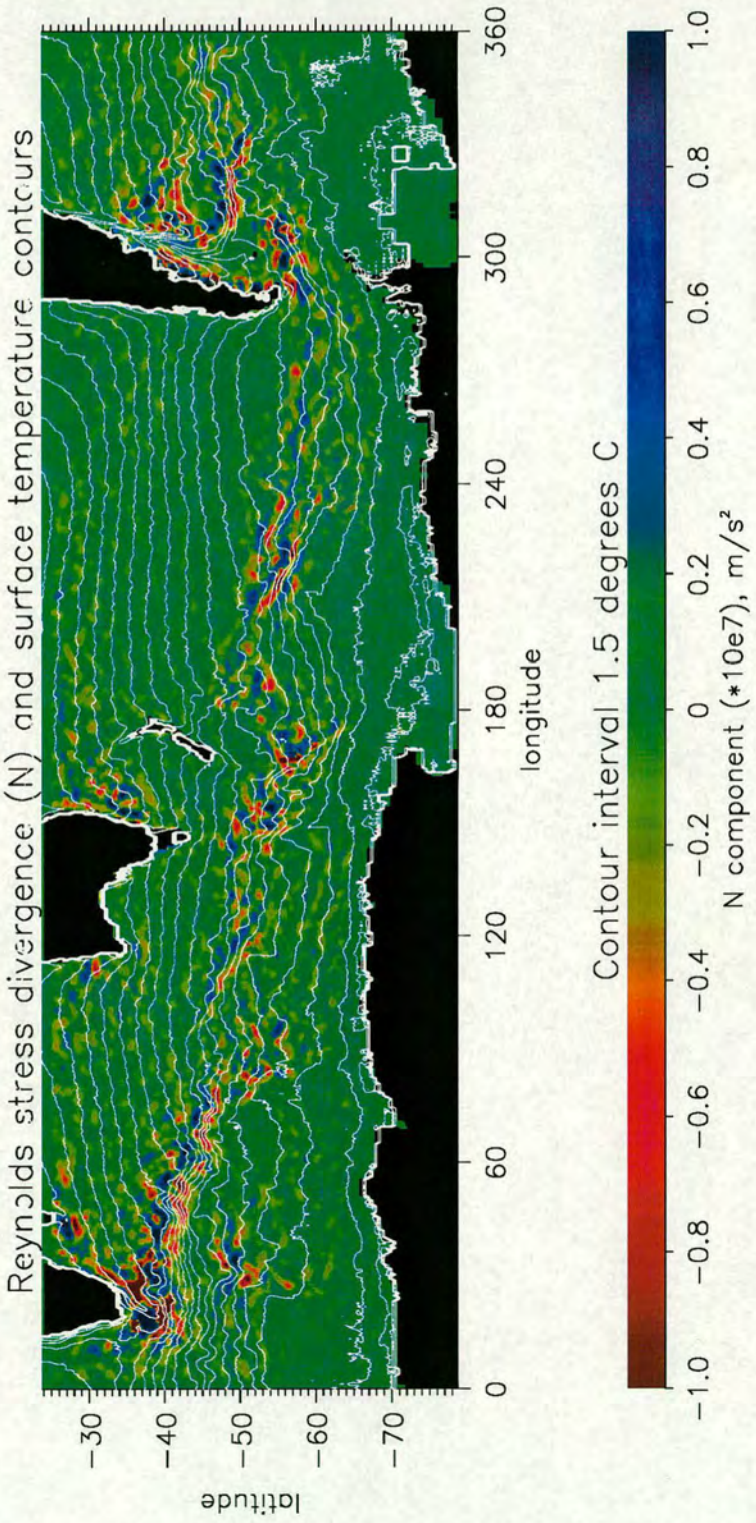

Figure 6.31: Reynolds stress divergence and mean surface temperature contours.

of Australia (top), in the South Pacific (middle), and east of Argentina (bottom). These demonstrate that the arrow formation of semivectors does correspond to the sign of **N**, as shown for the ideal formations in figure 6.21, and this gives confidence in the calculation used to establish **N** from the TPERS maps. This is good news, as the field of **N** is much easier to present and interpret than the semivectors.

6.5.3 Discussion

If jets in the ACC are not being maintained by the action of eddies on the mean flow, some other mechanism must be involved. It is the wind-stress which provides the momentum to drive the ACC, but this is a large-scale forcing which does not explain the position of individual jets. As discussed in chapter 1 and section 4.3 , the bottom topography is known to be important in balancing the momentum input by the wind. From these results, it appears that the position of jets in the real Southern Ocean is being determined by a factor such as topography, and not eddy forcing. Eddies are being generated by instability within the jets and act to oppose the topographic forcing. The interaction between the ACC and topography, as discussed earlier, is not yet fully understood (Hughes et al, 1998). This new result of the Reynolds stress field, obtained using unprecedented resolution of altimeter measurements, will help fuel further research.

In FRAM, eddies were observed to force the jets almost everywhere (see results in figures 3.22 and 6.22). The same relationship between eddies and jets has also been observed in many earlier modelling studies (for example McWilliams et al (1978), McWilliams and Chow (1981)), whose representation of topography is poor or even non-existent. The results in figure 6.31 go against these studies and support the case for misrepresentation of topography being a major cause of model deficiencies (as suggested by Hughes et al (1998)).

Previous work relating to Reynolds stresses in the Southern Ocean is presented by Johnson et al (1992) and Morrow et al (1994). Johnson et al calculated Reynolds stresses using two and a half years of Geosat data (1986 to 1989), which they presented for the region (50-66°S, 190-280°E). They observed large

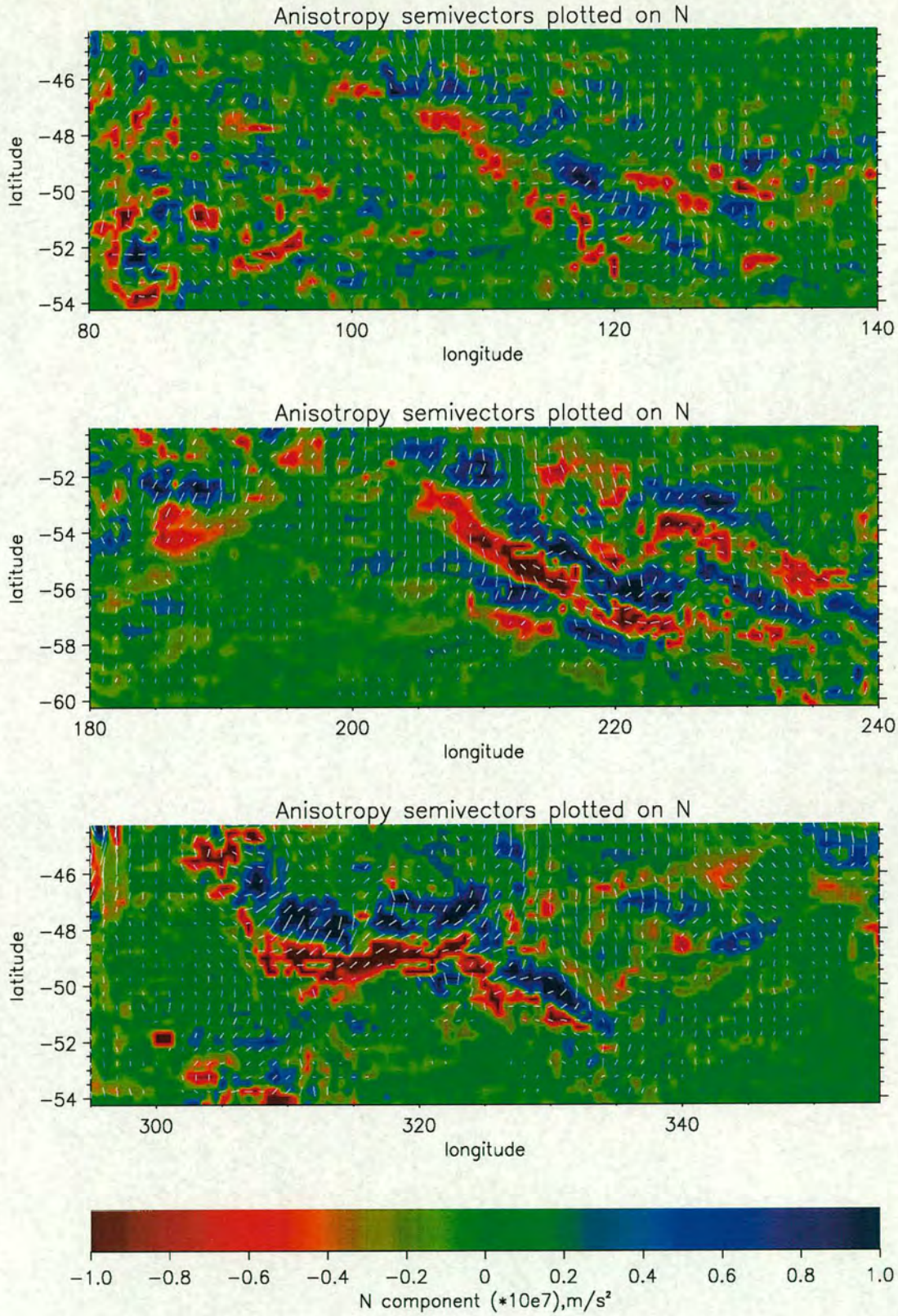

Figure 6.32: Semivectors plotted over the field of Reynolds stress divergence (**N**) for a region south of Australia (top), part of the South Pacific (middle), and east of South America (bottom).

regional variability which appeared to be related to topography, implying a strong influence by topography on the mean flow as suggested here. They also concluded that the Reynolds stress was tending to accelerate the mean flow, contrary to the results presented here. Their resolution of 1.5° meridional and 6° zonal, however, is insufficient to fully resolve the narrow jet features observed here, such as at (55°S, 215°E), and it could be that the positive Reynolds stress either side of the jet is dominating the results at this resolution. This is further supported by their observation that the region of greatest stress did not correspond with the position of the polar or sub-antarctic front, as determined by ship measurements. They suggest a reason for this is that the current might have two preferred paths for crossing the Pacific Antarctic Ridge, as observed here. Though the resolution of the Geosat data is likely to be the reason for the differences, the possibility of different behaviour at the earlier time period must not be ruled out.

The work of Morrow et al was mentioned in section 2.3. They also used Geosat data to calculate velocity variance ellipses and Reynolds stresses for the whole Southern Ocean. Results of the eddy force on the mean flow were presented for the region (30-60°S, 0-180°E), for the along stream component (as figure 6.31) and cross stream component. These show qualitively similar results for the region downstream of Agulhas, with positive eddy forcing north of negative eddy forcing. The resolution of the Geosat data, however, means those results are fairly sparse. Morrow et al conclude, like Johnson et al, that the eddies are acting to accelerate jets in the mean flow, contrary to the results of figure 6.31. As well as resolution differences (Morrow et al use 3° averages of eddy statistics from crossover points), there may also be problems with their comparison with the mean flow. They use the Gordon atlas (Gordon and Molinelli, 1982) to establish the position of jets and, though many jets are in the same place as indicated by the temperature gradients, a major difference is around (40°S, 30-50°E) where there are few data points in the atlas. Here the atlas puts the jet about 2°N of the large temperature gradient, and this makes the difference between acceleration and deceleration of the flow according to the Reynolds stresses. This is also where the eddy forces are largest and so could account for the different conclusion. Further discussion of these issues is found in Hughes and Ash (1999).

6.6 Summary

In the previous chapter, data at TOPEX/POSEIDON crossover points was found to have limitations when calculating the eddy quantities introduced in section 3.4. The study of eddy quantities was extended at the start of this chapter, where it was shown that the eddy anisotropy compared well to the surface mean flow in certain regions of the FRAM output. Correlations between eddy quantities and mean zonal flow were calculated in FRAM and shown to be particularly good in the southeast Pacific.

Mapped anomaly data from a combination of the TOPEX/POSEIDON and ERS1/2 altimeters was obtained for a period of 5 years from October 1992 to October 1997, with one map every ten days. It was shown that smooth fields of the eddy quantities could be calculated from this data. In particular the eddy orientation angle could be calculated and this had not been possible with the data at crossover points.

ADCP measurements from ship cruises were used in conjunction with mapped anomalies to obtain estimates of the real mean flow at specific locations. Whilst there are limitations with the accuracy of the technique, some jets in the mean flow were tentatively identified. A means of representing the eddy quantities developed by Hughes was presented. This was then used to display the eddy forcing information for the Southern Ocean in unprecedented detail. Specific features were identified in the results and compared with the available estimates of real mean flow. The relationship between eddy forcing and mean flow at this sample of locations did not support the results from FRAM output, where eddies act to force the major eastward jets.

Finally, a smoothing method was used to calculate the field of Reynolds stress divergence. When compared with surface temperature contours, this confirmed the observation in the field of semivectors that the eddy forcing acts to oppose major jets in the mean flow, contrary to results from FRAM and previous work on the Southern Ocean. Differences were blamed on resolution problems and sparse hydrographic data in parts of the Southern Ocean.

Chapter 7

Conclusions

7.1 Summary of principal results

The work presented in this thesis has described a study of near-surface dynamics in the Southern Ocean. This was performed using output from an oceanographic model, and satellite measurements of the sea surface height. Rossby waves were identified and their phase speeds measured, and the time-averaged effect of the eddy activity was calculated and, where possible, compared to the mean flow. Original work is contained in chapters 3 to 6, and will be summarised here.

Chapter 3 described the analysis of output from the Fine Resolution Antarctic Model (FRAM). Principal components analysis was used to highlight the presence of Rossby waves of different frequencies. A prominent waveguide was identified south of Australia, and this region was used to study the relationship between Rossby wave phase speeds and the mean flow. The phase speeds were found to be insensitive to local velocity of mean flow, and this was shown to be due to a balance between effective beta and the mean zonal flow within the jet. This could not be confirmed in the real ocean (chapter 5), where the mean flow is not known. It therefore remains a model observation. Phase speeds were found to increase in proportion to frequency and this was shown to be consistent with theory. A study of time-average eddy quantities showed a clear relationship between the orientation angle of velocity variance ellipses and the axes of jets in the mean flow. Following from the findings of chapter 3, chapter 4 described the use

FRAM output to investigate the possibility of retrieving information about the mean flow from the measurement of Rossby waves. It was concluded that our current understanding of the theory of Rossby wave propagation is insufficient to quantitively relate Rossby waves to the mean flow.

Chapter 5 introduced data from the TOPEX/POSEIDON satellite mission and used techniques developed for the analysis of FRAM output (chapter 3) to study the real Southern Ocean. High accuracy of individual measurements was chosen at the expense of spatial resolution, by studying data only at crossover points on the satellite ground-track. A suitable means of presenting data at crossover points was developed and used throughout the chapter. Principal components analysis in the frequency domain enabled regions associated with Rossby wave propagation at specific frequencies to be identified. These regions are variable in size, but smaller than about 20° in longitude and 4° in latitude. They are widely distributed throughout the observed part of the Southern Ocean, but are notably fewer in number at higher frequencies (periods less than 100 days). Longitude-time diagrams of data at crossover points were shown to indicate coherent propagation of Rossby waves at many of the locations identified by the principal components analysis. Using a combination of the Fast Fourier Transform and the Radon Transform, mean zonal phase speeds were measured at seven such locations, and presented for the period range 87 to 348 days. For regions within or close to the ACC, phase speeds are eastwards between 1.0 and 4.0 cm/s. They compare well with the results from FRAM (chapter 3), increasing approximately linearly with frequency. For regions outside the ACC, phase speeds are westwards between 1.0 and 5.0 cm/s. This is consistent with previous measurements of Rossby wave phase speeds in other oceans, though speeds are higher than those predicted by linear theory, as has been previously noted (see section 2.4). The eddy variance and anisotropy (equivalent to the size and eccentricity of the velocity variance ellipse respectively) were calculated from the crossover data, but the eddy orientation angle could not be calculated accurately due to sensitivity of the calculation to crossover angle.

Data in the form of mapped anomalies of sea surface height (from a combination of the TOPEX/POSEIDON, ERS1 and ERS2 satellite altimeters) was introduced

in chapter 6. This was used to calculate the eddy quantities at high spatial resolution, including the eddy orientation angle. Acoustic Doppler Current Profiler measurements from selected ship cruises in the Southern Ocean were used in combination with the anomaly data to estimate the strength and position of jets in the mean flow across eleven profiles. A method of representing the eddy forcing on the mean flow, known as 'anisotropy semivectors', was developed by Hughes (1997). This was used to illustrate the eddy forcing on the mean flow for the entire Southern Ocean (South of 30°S) in unprecedented detail. A consistent relationship between anisotropy semivectors and jets in the mean-flow had been identified in FRAM, but the same relationship was not observed in the real ocean when using a sample of mean-flow estimates derived from ship data. Using a smoothing method, the magnitude of the eddy forcing of the mean flow (the Reynolds stress divergence) was calculated from the semivectors. This was compared with frontal positions at the surface, which could be inferred from mean surface temperature contours derived by satellite and which provide an indication of mean jets in the ACC. For the most prominent eastward jets, the eddy forcing is observed to be negative (westward), and this is opposite to the forcing in FRAM and other models. In FRAM, the jets are seen to be forced over time by the eddies. In the real ocean it seems the eddies are generated by instability within the jets, which may therefore be forced by the topography. The reason for this difference is probably the poor representation of ocean topography in FRAM and other models which display the same characteristics. This new result of eddy forcing is also contrary to some previous work, but this previous work has been based on atlas data which suffers from poor hydrographic coverage in some key regions.

7.2 Discussion and suggestions for further work

An original aim of this thesis was to infer the mean flow from time dependent velocities. Time dependent velocities have been studied in detail to give comprehensive Rossby wave and eddy characteristics from the latest set of altimetric measurements. It has not been possible, however, to use these results to predict

a field for the mean flow near the surface over the time period which has been studied. This is because of deficiencies in our understanding of the relationships between Rossby waves, eddy quantities and the mean flow. Much theoretical progress has been made (as mentioned in chapter 2), and this kind of observational and model study will certainly help bridge the gap between theory and reality.

The results obtained here are only from the Southern Ocean. Because the ACC is so different from other ocean currents, it is not possible to assume that the same results would apply elsewhere in the world ocean. Many of the techniques used, however, could easily be applied to other oceans. The analysis presented in chapter 5 used data at groundtrack crossover points. Due to the distribution of the data, this analysis could only be applied to the equivalent latitudes in the northern hemisphere (i.e. between about 30° and 65°N). Phase speed measurements were only considered accurate south of 50°S and could therefore only be applied to the most northern parts of the Atlantic and Pacific oceans. However, because of the quality of the data as mapped anomalies, used in chapter 6, the analysis in chapter 5 could be repeated with this form of data, and then applied at all latitudes between ±81° (though outside ±66° there is only ERS data which has coarser temporal resolution and also suffers from seasonal presence of sea ice). Equivalent results from the mapped anomalies could be compared with the work presented here to assess whether the reduced accuracy of gradients in sea surface height is outweighed by the improved spatial resolution. This is likely to be the case at many latitudes.

The analysis presented in chapter 6, could also be applied at other latitudes where the data is available. The eddy quantities could be calculated and compared with the flow in more heavily sampled regions such as the North Atlantic. Comparison between the eddy quantities and output from an ocean model in that region would help confirm the results given here in terms of differences between models and reality. There are also many more current profile (ADCP) tracks outside the Southern Ocean. Where these cross known currents, the technique in section 6.3 could be applied to establish estimates of mean flow. This is especially useful when there is more than one current profile for the same track, particularly if the

measurement times differ by a month or more.

Much of the work in this thesis has used the FRAM model of the Southern Ocean for the development of techniques and comparison with observations. Though this is a sophisticated model, it is now several years old. It would be useful to repeat some of the work with a more recent model, such as the OCCAM global ocean model. The analysis presented in chapter 3 could easily be repeated using different model output, and compared with the results from FRAM. The results of this thesis have highlighted the need for improving the representation of topography in ocean models, however, as this may currently limit their use for investigating the interaction between eddies and the mean flow.

As future satellite missions improve our knowledge of the geoid, it will become possible to obtain a direct measure of the mean flow from altimetry. This will enable research to build upon the results given here, and so help towards a full understanding of the relationship between eddy activity and the mean flow in the Southern Ocean.

References

Anderson, D.L.T. and A.E. Gill, Spin-up of a stratified ocean, with applications to upwelling, *Deep-Sea Res., 22,* 583-596, 1975.

Anderson, D.L.T. and P.D. Killworth, Spin-up of a stratified ocean, with topography, *Deep-Sea Res., 24,* 709-732, 1977.

Anderson, D.L.T. and P.D. Killworth, Non-linear propagation of long internal Rossby waves, *Deep-Sea Res., 26,* 1033-1050, 1979.

Annenkov, S.Yu. and V.I. Shrira, On zonal waveguides for Rossby waves in the world ocean, *Oceanology, 32,* 1-5, 1992.

AVISO, AVISO user handbook: merged TOPEX/POSEIDON products, AVI-NT-02-101-CN, edition 2.1, 1992.

Badger, J., Mechanisms for rapid synoptic development, Ph.D. thesis, Department of Meteorology, University of Reading, 1997.

Barnett, T.P., Interaction of the monsoon and pacific trade wind system at interannual time scales, Part I: The equatorial zone, *Mon. Weather Rev., 111,* 756-773, 1983.

Bryan, K. and Cox, M.D., The circulation of the world ocean: a numerical study. Part I, a homogeneous model, *J. Phys. Oceanogr., 2,* 319-335, 1972.

Challenor, P.G., J.F. Read, R.T. Pollard and R.T. Tokmakian, Measuring surface currents in drake passage from altimetry and hydrography, *J. Phys. Oceanogr., 26,* 2748-2759, 1996.

Chelton, D.B. and M.G. Schlax, Global observations of oceanic rossby waves, *Science, 272,* 234-238, 1996.

Chelton, D.B., R.A. de Szoeke, M.G. Schlax, K.E. Naggar and N. Siwertz, Geographical variability of the first baroclinic Rossby radius of deformation, *J. Phys. Oceanogr., 28,* 433-460, 1998.

Cipollini, P., D. Cromwell and G.D. Quartly, Variability of Rossby wave propagation in the North Atlantic from TOPEX/POSEIDON altimetry. Proceedings of the IEEE international geoscience and remote sensing symposium (IGARSS '96), Lincoln (Nebraska), 27-31 May 1996, 1996.

Cipollini, P., D. Cromwell and G.D. Quartly, Observations of Rossby wave propagation in the Northeast Atlantic with TOPEX/POSEIDON altimetry, *Adv. in Space Res.,* in press, 1997a.

Cipollini, P., D. Cromwell, M.S. Jones, G.D. Quartly and P.G. Challenor, Concurrent altimeter and infrared observations of Rossby wave propagation near 34°N in the Northeast Atlantic, *Geophys. Res. Letters, 24,* 889-892, 1997b.

Clarke, A.J., Dynamics of large-scale wind-driven variations in the Antarctic Circumpolar Current, *J. Phys. Oceanogr., 12,* 1092-1105, 1982.

Cox, M.D., A primitive equation, three-dimensional model of the Ocean. GFDL Ocean Group Technical Report No. 1 [Available from Geophysical Fluid Dynamics Laboratory/NOAA, Princeton University, Princeton NJ 08542], 1984.

Dickinson, R.E., Planetary Rossby waves propagating vertically through weak westerly wind wave guides, *J. Atmos. Sciences, 25,* 984-1002, 1968.

Dickinson, R.E., Propagators of atmospheric motions. 2. Excitation by switch-on sources, *Rev. Geophys., 7,* 515-538, 1969a.

Dickinson, R.E., Vertical propagation of planetary Rossby waves through an atmosphere with Newtonian cooling, *J. Geophys. Res., 74,* 929-938, 1969b.

Dickinson, R.E., Theory of planetary wave-zonal flow interaction, *J. Atmos. Sciences, 26,* 73-81, 1969c.

Dickinson, R.E., Development of a Rossby wave critical level, *J. Atmos. Sciences, 27,* 627-633, 1970.

Dickinson, R.E., Rossby waves - Long-period oscillations of oceans and atmospheres, *Ann. Rev. Fluid Mech., 10,* 159-195, 1978.

Drazin, P.G., D.N. Beaumont and S.A. Coaker, On Rossby waves modified by basic shear, and barotropic instability, *J. Fluid Mech., 124,* 439-456, 1982.

Emery, W.J. and L. Magaard, Baroclinic Rossby waves as inferred from temperature fluctuations in the eastern Pacific, *J. Mar. Res., 34,* 365-385, 1976.

FRAM Group, An eddy-resolving model of the Southern Ocean, *Eos Trans. AGU, 72,* 169-175, 1991.

Garcia, R.R. and J.E. Geisler, Vertical structure of stationary planetary waves in the presence of altitude-dependent zonal winds and dissipation, *J. Geophys. Res., 79,* 5613-24, 1974.

Gaspar, P., F. Ogor, P.Y. LeTraon and O.Z. Zanife, Estimating the sea-state bias of the Topex and Posedion altimeters from crossover differences, *J. Geophys. Res., 99 C12,* 24981-24994, 1994.

Geisler, J.E. and R.E. Dickinson, Numerical study of an interacting Rossby wave and barotropic zonal flow near a critical level, *J. Atmos. Sciences, 31,* 946-955, 1974.

Gille, S.T., The Southern Ocean momentum balance: Evidence for topographic effects from numerical model output and altimeter data, *J. Phys. Oceanogr., 27,* 2219-2232, 1997.

Glazman, R.E., A. Fabrikant and A. Greysukh, Statistics of spatial-temporal variations of sea surface height based on TOPEX altimeter measurements, *Int. J. Remote Sens., 17,* 2647-2666, 1996.

Gordon, A., and P. Tchernia, Waters of the continental margin off Adelie coast, Antarctica, *Antacrtic Oceanology II: The Australian-New Zealand Sector. Antarctic Research Series, 19,* 59-69, 1972.

Gordon, A.L. and E. Molinelli, Southern Ocean Atlas, Columbia University Press, 200pp, 1982.

Gwilliam, C.S., A.C. Coward, B.A. de Cuevas, D.J. Webb, E. Rourke, S.R. Thompson and K. Döös, The OCCAM global ocean model, *Proc. Second UNAM-Cray Supercomputing Conf.: Numerical Simulations in the Environmental and Earth Sciences,* Mexico City, Mexico, Cray Research, 1997.

Harris, J.L., Southern Ocean circulation from hydrographic data: a finite difference inverse model, Ph.D. thesis, Institute of Antarctic and Southern Ocean Studies, University of Tasmania, 1996.

Haynes, P.H., The effect of barotropic instability on the nonlinear evolution of a Rossby-wave critical layer, *J. Fluid Mech., 207,* 231-266, 1989.

Hellerman, S. and M. Rosenstein, Normal monthly wind stress over the world ocean with error estimates, *J. Phys. Oceanogr., 13,* 1093-1104, 1983.

Hoskins, B.J., James, I.N. and G.H. White, The shape, propagation and mean-flow interaction of large-scale weather systems, *J. Atmos. Sciences, 40,* 1595-1612, 1983.

Hoskins, B.J. and T. Ambrizzi, Rossby wave propagation on a realistic longitudinally varying flow, *J. Atmos. Sciences, 50,* 1661-1671, 1993.

Hough, S.S., On the application of harmonic analysis to the dynamical theory of the tides, Part I, On Laplace's 'oscillations of the first species', and on the dynamics of ocean currents, *Philos. Trans. R. Soc. London, Ser. A, 189,* 201-257, 1897.

Hough, S.S., On the application of harmonic analysis to the dynamical theory of the tides, Part II, On the general integration of Laplace's dynamical equations, *Philos. Trans. R. Soc. London, Ser. A, 191,* 139-185, 1898.

Hughes, C.W., The effect of topography on ocean flow, D.Phil. thesis, University of Oxford, 1992.

Hughes, C.W., Rossby waves in the Southern Ocean: a comparison of TOPEX/POSEIDON altimetry with model predictions, *J. Geophys. Res., 100 C8,* 15933-15950, 1995.

Hughes, C.W., The antarctic circumpolar current as a waveguide for rossby waves, *J. Phys. Oceanogr., 26,* 1375-1387, 1996.

Hughes, C.W., On the graphical representation of eddy vecocity covariances, *Ocean Modelling, 114,* 9-12 (unpublished manuscript), 1997.

Hughes, C.W. and P.D. Killworth, On the effects of bottom topography in the large-scale circulation of the Southern Ocean, *J. Phys. Oceanogr., 25,* 2485-2497, 1995.

Hughes, C.W., M.S. Jones and S. Carnochan, The use of transient features to identify eastward currents in the Southern Ocean, *J. Geophys. Res., 103 C2,* 2929-2943, 1998.

Hughes, C.W. and E.R. Ash, Eddy forcing of the mean flow in the Southern Ocean, *J. Geophys. Res., submitted,* 1999.

Johnson, T.J., R.H. Stewart, C.K. Shum and B.D. Tapley, Distribution of Reynolds stress carried by mesoscale variability in the Antarctic Circumpolar Current, *Geophys. Res. Letters, 19,* 1201-1204, 1992.

Kamenkovich, I.V. and J. Pedlosky, Radiating instability of nonzonal ocean currents, *J. Phys. Oceanogr., 26,* 622-643, 1996.

Kang, Y.Q., J.M. Price and L. Magaard, On stable and unstable Rossby waves in non-zonal oceanic shear flow, *J. Phys. Oceanogr., 12,* 528-537, 1982.

Kessler, W.S., Observations of long Rossby waves in the northern tropical Pacific, *NOAA Tech. Memo. ERL PMEL-86,* 169pp., Pac. Mar. Environ. Lab., Natl. Oceanic and Atmos. Admin., Washington, D.C., 1989.

Kessler, W.S., Observations of long Rossby waves in the northern tropical Pacific, *J. Geophys. Res., 95,* 5183-5217, 1990.

Killworth, P.D., On the propagation of stable baroclinic Rossby waves through a mean shear flow, *Deep-Sea Res., 26A,* 998-1031, 1979.

Killworth, P.D. and M.E. McIntyre, Do Rossby wave critical layers absorb, reflect or over-reflect?, *J. Fluid Mech., 161,* 449-492, 1985.

Killworth, P.D., An equivalent-barotropic mode in the Fine Resolution Antarctic Model, *J. Phys. Oceanogr., 22,* 1379-1387, 1992.

Killworth, P.D. and M.M. Nanneh, Isopycnal momentum budget of the Antarctic Circumpolar Current in the Fine Resolution Antarctic Model, *J. Phys. Oceanogr., 24,* 1201-1223, 1994.

Killworth, P.D., D.B. Chelton and R.A. de Szoeke, The speed of observed and theoretical long extra-tropical planetary waves, *J. Phys. Oceanogr., 27,* 1946-1966, 1997.

Krupitsky, A., V.M. Kamenkovich, N. Naik and M.A. Cane, A linear equivalent barotropic model of the antarctic circumpolar current with realistic coastlines and bottom topography, *J. Phys. Oceanogr., 26,* 1803-1824, 1996.

Kuo, H.-L., Dynamic instability of two-dimensional nondivergent flow in a barotropic atmosphere, *J. Meteorol., 6,* 105-122, 1949.

Le Provost, C., M.L. Genco, F. Lynard, P. Vincent and P. Canceil, Spectroscopy of the world ocean tides from a finite-element hydrographic model, *J. Geophys. Res., 99,* 24777-24797, 1994.

Le Traon, P.Y. and J.-F. Minster, Sea level variability and semiannual Rossby waves in the South Atlantic subtropical gyre, *J. Geophys. Res., 98,* 12315-12326, 1993.

Le Traon, P.Y., F. Nadal and N. Ducet, An improved mapping method of multisatellite altimeter data, *J. Atmos. and Oce. Tech., 15,* 522-534, 1998.

Levitus, S., Climatological atlas of the world ocean, NOAA Professional Paper, No. 113, 173pp, 1982.

Levitus, S. and T. Boyer, World ocean atlas 1994, Vol 4: Temperature, NOAA Atlas NESDIS 4, U.S. Govt. Printing Office, 150pp, 1994.

Levitus, S., R. Burgett and T. Boyer, World ocean atlas 1994, Vol 3: Salinity, NOAA Atlas NESDIS 3, U.S. Govt. Printing Office, 150pp, 1994.

Lighthill, M.J., Waves in fluids, Cambridge Press, pp504, 1978.

Longuet-Higgins, M.S., Planetary waves on a rotating sphere, *Proc. R. Soc. London Ser. A, 279,* 446-473, 1964a.

Longuet-Higgins, M.S., On group velocity and energy flux in planetary wave motions, *Deep-Sea Res. 11,* 35-43, 1964b.

Longuet-Higgins, M.S., Planetary waves on a rotating sphere, II, *Proc. R. Soc. London Ser. A, 294,* 40-54, 1965a.

Longuet-Higgins, M.S., The response of a stratified ocean to stationary or moving wind-systems, *Deep-Sea Res. 12,* 923-973, 1965b.

Longuet-Higgins, M.S., Some dynamical aspects of ocean currents, *Quart. J. Royal Met. Soc. 91,* 425-457, 1965c.

Mantyla, A.W. and J.L. Reid, Abyssal characteristics of the world ocean waters, *Deep-Sea Res. 30,* 805-833, 1983.

Margules, M., Luftbewegungen in einer rotierenden Sphäroidschale (II. Teil), *Sitzungsber. Kais. Akad. Wiss. Wien, Math.-Nat. Cl. 102,* Abt. IIA, 11-56, 1893. [English transl.: "Air motion in a rotating spherical shell, by Max Margules" (B. Haurwitz, transl.), Natl. Cent. Atmos. Res. Tech. Note NCAR/TN-156 + STR.]

Marshall, D., Topographic steering of the antarctic circumpolar current, *J. Phys. Oceanogr., 25,* 1636-1650, 1995.

Marshall, J., D. Olbers, H. Ross and D. Wolf-Gladrow, Potential vorticity constraints on the dynamics and hydrography of the Southern Ocean, *J. Phys. Oceanogr., 23,* 465-487, 1993.

Maslowe, S.A., Critical layers in shear flows, *Ann. Rev. Fluid Mech., 18,* 405-432, 1986.

Matano, R.P. and S.G.H. Philander, On the decay of the meanders of eastward currents, *J. Phys. Oceanogr., 24,* 298-304, 1994.

McIntyre, M.E. and W.A. Norton, Dissipative wave-mean interactions and the transport of vorticity or potential vorticity, *J. Fluid Mech., 212,* 403-435, 1990.

McWilliams, J.C. and G.R. Flierl, Optimal, quasi-geostrophic wave analysis of MODE array data, *Deep Sea Res., 23,* 285-300, 1976.

McWilliams, J.C., W.R. Holland and J.H.S. Chow, A description of numerical Antarctic Circumpolar Currents, *Dyn. Atmos. Oceans, 2,* 213-291, 1978.

McWilliams, J.C. and J.H.S. Chow, Equilbrium geostrophic turbulence I: a reference solution in a β-plane channel, *J. Phys. Oceanogr., 11,* 921-949, 1981.

Meinardus, W., Ergebnisse der Seefahrt des Gauss, *Dtsch. Sudpol. Exped. 1901-1903, 3,* 531, 1923.

Mekki, O.M. and J.F. McKenzie, The propagation of atmospheric Rossby-gravity waves in latitudinally sheared zonal flows, *Phil. Trans. Roy. Soc. London. Ser. A, 287, no. 1340,* 115-143, 1977.

Moore, J.K., M.R. Abbott and J.G. Richman, Location and dynamics of the Antarctic Polar Front from satellite sea surface temperature data, *J. Geophys. Res., 104 C2,* 3059-3073, 1999.

Morrow, R., R. Coleman, J. Church and D. Chelton, Surface eddy momentum flux and velocity variances in the Southern Ocean from Geosat altimetry, *J. Phys. Oceanogr., 24,* 2050-2071, 1994.

Morse, P.M. and H. Feshbach, Methods of theoretical physics, McGraw-Hill, pp997, 1953.

Munk, W.H. and E. Palmén, Note on the dynamics of the Antarctic Circumpolar Current, *Tellus, 3,* 53-55, 1951.

Nerem, R.S., E.J. Schrama, C.J. Koblinsky and B.D. Beckley, A preliminary evaluation of ocean topography from the TOPEX/POSEIDON mission, *J. Geophys. Res., 99,* 24565-24583, 1994,

Nowlin, W.D., Jr. and J.M. Klinck, The physics of the antarctic circumpolar current, *Rev. Geophys., 24(3),* 469-491, 1986.

Orsi, A.H., W.D. Nowlin Jr and T. Whitworth III, On the circulation and stratification of the Weddell Gyre, *Deep-Sea Res., 40(1),* 169-203, 1993.

Orsi, A.H., T. Whitworth III and W.D. Nowlin Jr, On the meridional extent and fronts of the Antarctic Circumpolar Current, *Deep-Sea Res., Part I, 42,* 641-673, 1995.

Panetta, R.L., Zonal jets in wide baroclinically unstable regions: persistence and scale selection, *J. Atmos. Sci., 50,* 2073-2106, 1993.

Pedlosky, J., On the radiation of meso-scale energy in the mid-ocean, *Deep-Sea Res., 24,* 591-600, 1977.

Pedlosky, J., Geophysical fluid dynamics (2nd edition), Springer Verlag, pp710, 1987.

Pickard, G.L. and W.J. Emery, Descriptive Physical Oceanography (5th edition), Pergamon Press, pp320, 1990.

Platzman, G.W., The Rossby wave, *Quart. J. Royal Met. Soc., 94 401,* 225-248, 1968.

Polito, P.S. and P. Cornillon, Long baroclinic Rossby waves detected by TOPEX/POSEIDO
J. Geophys. Res., 102 C2, 3215-3235, 1997.

Price, J.M. and L. Magaard, Interannual baroclinic Rossby waves in the mid-latitude North Atlantic, *J. Phys. Oceanogr., 16,* 2061-2070, 1986.

Rhines, P.B., Waves and turbulence on a β-plane, *J. Fluid Mech., 69,* 417-443, 1975.

Rintoul, S.R., Mass, heat, oxygen and nutrient fluxes in the Atlantic Ocean determined by Inverse Methods, Ph.D. thesis, Woods Hole Oceanographic Institution, Massachusetts Institute of Technology, 1988.

Roether, W., R. Schlitzer, A. Putzka, P. Beining, K. Bulsiwicz, G. Rohardt and F. Delahoyde, A chloroflouromethane and hydrographic section across Drake Passage: deep water ventilation and meridional property transport, *J. Geophys. Res., 98 C8,* 14423-14435, 1993.

Rogel, P., J.-F. Minster, E. Blayo, J.-M. Molines and J. Verron, Propagation of the dominant sea level signals in the North Atlantic from TOPEX/POSEIDON altimeter data, *J. Geophys. Res.*

Rossby, C.-G. and collaborators, Relation between variations in the intensity of the zonal circulation of the atmosphere and the displacements of the semi-permanent centers of action, *Ibid, 2,* 38-55, 1939.

Rossby, C.-G., Planetary flow patterns in the atmosphere, *Quart. J. Royal Met. Soc., 66,* supplement, 68-87, 1940.

Schlax, M.G. and D.B. Chelton, Detecting aliased tidal errors in altimeter height measurements, *J. Geophys. Res., 99,* 12603-12612, 1994.

Schulman, E.E., The Antarctic Circumpolar Current, paper presented at Summer Computer Simulation Conference, Natl. Sci. Found., Denver, Colo., June 1970.

Shum, C.K., J.C. Ries and B.D. Tapley, The accuracy and applications of satellite altimetry, *Geophys. J. Int., 121,* 321-336, 1995.

Sievers, H.A. and J.W.D. Nowlin, The stratification and water masses at Drake Passage, *J. Geophys. Res., 89 C6,* 10489-10514, 1984.

Spall, M.A., Rossby wave radiation in the Cape Verde Frontal Zone, *J. Phys. Oceanogr., 22,* 796-807, 1992.

Stammer, D., Global characteristics of ocean variability estimated from regional TOPEX/POSEIDON altimeter measurements, *J. Phys. Oceanogr., 27,* 1743-1769, 1997.

Stevens, D.P. and P.D. Killworth, The distribution of kinetic energy in the Southern Ocean. A comparison between observations and an eddy resolving general circulation model, *Philos. Trans. R. Soc. London B, 338,* 251-257, 1992.

Stewartson, K., The evolution of the critical layer of a Rossby wave, *Geophys. Astrophys. Fluid Dynamics, 9,* 185-200, 1978.

Stommel, H., The westward intensification of wind-driven ocean currents, *Trans. American Geophys. Union, 29,* 202-206, 1948.

Sverdrup, H.U., M.W. Johnson and R.H. Fleming, The oceans: their physics, chemistry and general biology, Prentice Hall, 1087pp, 1942

Tchernia, P., Descriptive regional oceanography, Pergamon Press, Oxford, England, pp253, 1980.

Thomson, R., Topographic Rossby waves at a site north of the Gulf Stream, *Deep Sea Res., 18,* 1-19, 1971.

Tokmakian, R.T. and P.G. Challenor, Observations in the Canary basin and the Azores frontal region using Geosat data, *J. Geophys. Res., 98,* 4761-4773, 1993.

Treguier, A.M. and J.C. McWilliams, Topographic influence on wind-driven stratified flow in a β-plane channel: An idealised model for the Antarctic Circumpolar Current, *J. Phys. Oceanogr., 20,* 321-343, 1990.

Treguier, A.M. and R.L. Panetta, Multiple zonal jets in a quasigeostrophic model of the Antarctic Circumpolar Current, *J. Phys. Oceanogr., 24,* 2263-2277, 1994.

Vassie, J.M., A.J. Harrison, P.L. Woodworth, S.A. Harangozo, M.J. Smithson and S.R. Thompson, On the temporal variability of the transport between Amsterdam and Kerguelen islands, *J. Geophys. Res., 99 C1,* 937-949, 1994.

Wang, L. and C.J. Koblinsky, Low-frequency in regions of the Kuroshio extension and the gulf stream, *J. Geophys. Res., 100,* 18313-18331, 1995.

Warn, T. and H. Warn, On the development of a Rossby wave critical level, *J. Atmos. Sci., 33,* 2021-024, 1976.

Warn, T. and H. Warn, The evolution of a nonlinear critical level, *Stud. Appl. Math., 59,* 37-71, 1978.

Webb, D.J., P.D. Killworth, A.C. Coward and S.R. Thompson, The FRAM atlas of the Southern Ocean, NERC, Swindon, 1991.

Wells, N.C. and B.A. De Cuevas, Depth-integrated vorticity budget of the Southern Ocean from a general circulation model, *J. Phys. Oceanogr., 25,* 2569-2582, 1995.

White, W.B., Annual forcing of baroclinic long waves in the tropical North Pacific, *J. Phys. Oceanogr., 7,* 50-61, 1977.

White, W.B., The resonant response of interannual baroclinic Rossby waves to wind forcing in the eastern midlatitude North Pacific, *J. Phys. Oceanogr., 15,* 404-415, 1985.

White, W.B. and J.F.T. Saur, Sources of interannual baroclinic Rossby waves in the eastern subtropical North Pacific, *J. Phys. Oceanogr., 13,* 531-544, 1983.

Williams, G.P., Planetary circulations. I: Barotropic representation of Jovian and terrestrial turbulence, *J. Atmos. Sci., 35,* 1399-1426, 1978.

WOCE Data Products Committe, WOCE global data, version 1.0, WOCE international project office, WOCE report 158/98, Southampton, UK, 1998.

Wolf, J.-O., E. Maier-Reimer, and D. Olbers, Wind-driven flow over topography in a zonal β-plane channel: A quasi-geostrophic model of the Antarctic Circumpolar Current, *J. Phys. Oceanogr., 21,* 236-264, 1991.

Wunsch, C., The work done by the wind on the oceanic general circulation, *J. Phys. Oceanogr., 28,* 2332-2340, 1998.